DYNAMIC MODELING, VALIDATION, AND CONTROL FOR VAPOR COMPRESSION SYSTEMS

BY

HERSCHEL PANGBORN

THESIS

Submitted in partial fulfillment of the requirements
for the degree of Master of Science in Mechanical Engineering
in the Graduate College of the
University of Illinois at Urbana-Champaign, 2015

Urbana, Illinois

Adviser:

Professor Andrew Alleyne

Abstract

This thesis traces the complete process of model-based control design for vapor compression systems (VCSs), from nonlinear model development to linearization and control formulation. Addressing gaps in the previous literature, the equations behind each model and control approach are clearly stated and emphasis is placed on conducting experimental validation at every stage.

Both finite volume and switched moving boundary approaches for nonlinear control-oriented heat exchanger modeling are presented, illustrating the key differences in the method of discretization between these approaches. Practical considerations for the numerical implementation of these approaches in simulation are also provided. A detailed linearization of the switched moving boundary approach leads to the creation of a family of four-component linear models for different modes of operation of a VCS. The nonlinear and linear models are then validated with experimental data to reveal the tradeoffs of each. Furthermore, an augmentation to the switched moving boundary method is derived which captures the effects of air humidity. Experimental validation demonstrates that this augmented model more accurately predicts both air-side and refrigerant-side outputs at high humidity in addition to providing accurate predictions of liquid condensate formation and air outlet humidity.

Finally, the value of the linear VCS models is demonstrated by their application in model-based control. A switched LQR approach is shown in both simulation and experimental application to be capable of driving the system between operational modes in order to regulate about a desired nominal operating condition. In particular, the experiments demonstrate improved robustness at low evaporator superheat of the switched LQR approach as compared to a decentralized PI approach.

To my friends, family, and teachers

Acknowledgments

I would first like to thank my advisor, Dr. Andrew Alleyne, for his invaluable guidance during the last two years. I could not imagine a better mentor as I begin my own career in research, and am honored to have the opportunity to continue studying under his tutelage. I would also like to thank the past and present members of the Alleyne Research group, especially Tim, Justin, Matt, Katie, Lindsey, and Bryan. My research has benefitted greatly from many discussions and collaborations with these individuals, and their friendship has truly enriched my time at UIUC.

I must also thank my family. My parents' enduring support and love have given me the confidence to pursue my passions. My sisters have always been kind enough to include their younger brother in their lives, and in doing so taught me how to create the life I dream of living.

None of my successes would be possible without Courtney at my side. She not only joined me in the 600 mile trek west to pursue my goals, but has supported me through many long nights and weekends of work.

Lastly, I would like to acknowledge the support of a University of Illinois at Urbana-Champaign graduate fellowship, the United States Air Force, and the National Science Foundation Graduate Research Fellowship. This support has empowered me to pursue research that I believe in.

Table of Contents

List of Symbols

A	Area
c_p	Constant Pressure Specific Heat Capacity
h	Specific Enthalpy
k	Sample Time Index
L	Length (Chapter 2-3)
m	Mass
$\dot{m}$	Mass Flow Rate
NTU	Number of Transfer Units
o	Valve Opening Input
P	Pressure
p	Perimeter
$\dot{Q}$	Heat Transfer Rate
q	Refrigerant Quality
RH	Relative Humidity
s	Entropy
T	Temperature
tot	Total
u	Input
V	Volume (Chapter 2-3)
v	Rotational Speed
x	State Vector
y	Output Vector

α	Heat or Mass Transfer Coefficient
β	Mass Transfer Parameter Adjustment Factor
$\bar{\gamma}$	Mean Void Fraction
ζ	Normalized Control Volume Length
λ	Latent Heat of Condensation
η	Surface Effectiveness
η_{isen}	Isentropic Efficiency
η_{vol}	Volumetric Efficiency
ρ	Density
τ	Time Constant
ω	Humidity Ratio

List of Subscripts

a	Air Mixture
a_{dry}	Dry Air
c	Condenser
cs	Cross Sectional
CV	Control Volume
$comp$	Compressor
d	Dew (Chapter 5) / Disturbance (Chapter 6)
$diff$	Difference
e	Evaporator
EEV	Electronic Expansion Valve
f	Saturated Liquid
g	Saturated Gas
i	Control Volume Index
in	Inlet
$isen$	Isentropic
k	Time Step Index
l	Liquid Water
$meas$	Measured

N	Total Number of Control Volumes
n	Row Index
o	Nominal (Steady-State) Operating Condition
out	Outlet
r	Refrigerant
s	Surface
sat	Saturation
SC	Subcool
SH	Superheat
sys	System
TP	Two-Phase
vol	Volumetric
w	Heat Exchanger Wall
z	Length along Refrigerant Flow Direction

List of Abbreviations

CV	Control Volume
EEV	Electronic Expansion Valve
FV	Finite Volume
HTC	Heat Transfer Coefficient
HVAC	Heating, Ventilation, and Air Conditioning
LMI	Linear Mixed Inequality
LQR	Linear Quadratic Regulator
MB	Moving Boundary
MPC	Model Predictive Control
MSS	Minimum Stable Superheat
NTU	Number of Transfer Units
P-h	Pressure-Enthalpy
PI	Proportional-Integral
RH	Relative Humidity
RTF	Real Time Factor
RTO	Real Time Optimizer
SMB	Switched Moving Boundary
VCS	Vapor Compression System

Chapter 1

Introduction

The use of vapor compression systems (VCSs) is now ubiquitous for the transportation of thermal energy between physical locations. Among the many applications of VCSs is air conditioning and refrigeration in both residential and commercial sectors. The U.S. Energy Information Administration reported in 2009 that almost 87% of residences in the United States contain at least one air conditioning unit, representing nearly 100 million homes [1]. According to the U.S. Department of Energy, these air conditioners are responsible for about 6% of a household's energy use on average [2]. The widespread use of these systems in the commercial sector is also clear. Commercial buildings are one of the major sources of energy consumption in the U.S., at just under 20% of national energy consumption. Almost half of this commercial energy consumption is used for lighting, space heating, and space cooling [3]. VCSs are also essential for the refrigerated transportation of perishable goods. The International Institute of Refrigeration reported in 2002 that more than 1 million refrigerated road vehicles were in use, transporting $1.2 trillion dollars of cargo [4]. For all these applications, improving the performance and efficiency of VCSs brings both economic and environmental benefits.

1.1 Vapor Compression Systems

In VCSs, a cycling refrigerant serves as a means by which to move energy. The most basic VCS consists of four primary components: An evaporator, a compressor, a condenser, and an expansion device. For the purpose of this work, additional components such as accumulators and receivers are not considered. These components are present in many current systems but we choose to bypass their inclusion here to focus on some of the basic understanding associated with a canonical VCS system. Extending the results of this thesis to systems with other components and configurations is left to future work.

The evaporator and condenser are specialized heat exchangers, transferring energy between two mediums without allowing them to come into direct contact. In each heat exchanger, the flow of the refrigerant is said to occur on the "refrigerant side" of the component. The other medium with which the component exchanges energy, often air or a single-phase fluid, is said to be on the "secondary side."

In the case of a basic refrigerant-to-air system, for which air is the medium on the secondary side of both heat exchangers, up to four actuator inputs can be used to control operation of the VCS. These are: The speed of the fan blowing air across the external surfaces of the evaporator, the rotational speed of the compressor, the speed of the fan blowing air across the external surfaces of the condenser, and the degree of opening of the expansion device. While not treated in this work, in some systems the fan speeds may be fixed, leaving only two actuator inputs. The heat exchanger fans and compressor all consume electrical power in driving these actuators. Depending on the type of expansion device used, this component may or may not consume electrical power as well.

Figure 1.1 shows a schematic and typical Pressure-Enthalpy (P-h) diagram of a basic VCS. Refrigerant flowing through the evaporator at low pressure absorbs energy from the evaporator secondary side, typically undergoing a phase change from two-phase to superheated vapor in the process. The refrigerant then flows into the compressor, where it is pressurized into a high-temperature superheated vapor. Next, the refrigerant enters the condenser, where it rejects energy to the condenser secondary side, typically changing to a subcooled liquid phase in the process. After exiting the condenser, the refrigerant flows through the expansion device, where its temperature and pressure are reduced, causing a phase change to a two-phase liquid before the refrigerant again enters the evaporator, completing the cycle. In this way, the refrigerant is used as a means to "pump" energy from the evaporator secondary side to the condenser secondary side.

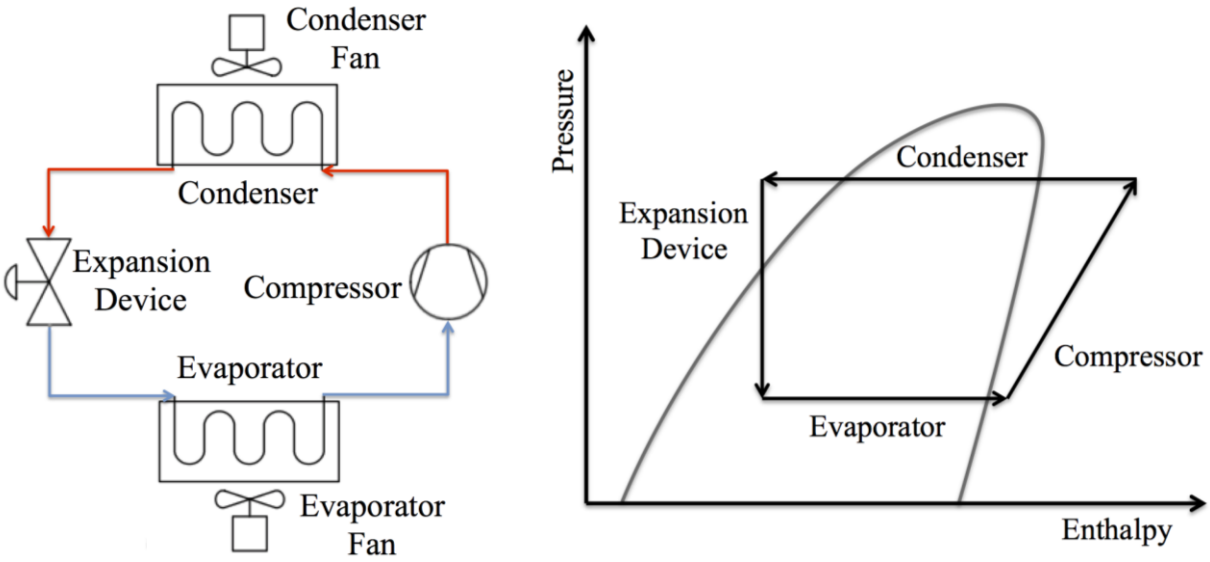

Figure 1.1 VCS Schematic (left) and P-h Diagram (right)

While the phases at the entrance and exit of each heat exchanger are typically as shown in Figure 1.1 during nominal operation, this is not the case at all times. Startup or shutdown conditions, large disturbances on the secondary-side, or faults in control can all result in off-nominal phase flow combinations in the heat exchangers.

1.2 Modeling and Control of VCSs

While many of the characteristics of a VCS are determined by its physical design, the control algorithm used to select actuator inputs during operation can have an immense effect on the ability of the system to achieve a given performance criteria (for example, a desired cooling capacity of one of the heat exchangers) while minimizing the electrical energy consumed by the actuators and minimizing component wear. The development of effective control algorithms is often improved when preceded by the creation of mathematical models that capture the salient dynamics of the system while maintaining a level of simplicity that permits relevant analytical tools to be used. Such models are called “control-oriented” models. Various forms of these models can serve as a means of better understanding the system, can be used as plants on which to evaluate candidate control approaches prior to experimental testing, and can also be directly embedded into control algorithms.

The above uses of control-oriented modeling motivate a significant portion of this thesis. Several modeling approaches, including both nonlinear and linear formations, are derived and

compared. For the use of these models as plants on which to test control designs, we improve upon the relevant previous literature in three ways. First, the use of state-of-the-art model formulations brings enhanced accuracy and numerical robustness over previous efforts. Second, the comparison of simulation results with experimental data allows for a characterization of the relative accuracy of each approach, revealing tradeoffs associated with the use of each. Third, a significant gap observed in the accuracy of the models is closed. Specifically, their ability to maintain accuracy under humid air conditions is improved through a more nuanced treatment of the air-side calculations.

We further demonstrate the use of control-oriented models by directly embedding linear models for multiple modes of operation into a control algorithm. The resulting controller is able to direct the system across a wide range of operating conditions. There are again three broad ways in which the relevant previous literature is improved upon. First, a more detailed formulation for both the linear models and the control framework is provided. Second, emphasis is placed on developing a framework suited to real-world implementation. This comes with an understanding that under the ideal conditions often presented in simulation, robustness to model error, disturbances, and sensor noise may not be as thoroughly tested. Successful experimental application of the control framework demonstrates the success of this control approach. Third, previous discussions on the stability of the closed-loop system are revisited.

1.3 Organization of Thesis

The remainder of this thesis is organized as follows. Chapter 2 presents nonlinear first principles models for four standard VCS components: An evaporator, a condenser, an electronic expansion valve (EEV), and a compressor. For the evaporator and condenser, two methods of spatial discretization are discussed. These are the finite volume (FV) and switched moving boundary (SMB) approaches. The latter approach includes a different mode for each combination of refrigerant phases in the heat exchangers. The SMB heat exchanger models, as well as the EEV and compressor models, are then linearized in Chapter 3. In Chapter 4, FV, SMB, and linear models are validated with experimental data and the tradeoffs of each modeling approach are discussed. As an aside, Chapter 5 presents and experimentally validates an augmentation to the air-side modeling of the SMB heat exchangers that uses the additional input of air inlet humidity to predict the air outlet humidity and condensate mass flow rate. These

modified models are shown to more accurately predict other outputs of interest when the system is operating under high humidity conditions. Returning to the linear models, Chapter 6 presents a switched LQR approach for control of VCSs across a wide range of desired operating conditions, including with and without evaporator superheat. This approach is demonstrated both in simulation and in experimental validation. Chapter 7 provides conclusions and identifies opportunities for future work.

Chapter 2

Nonlinear Model Formulations

This chapter presents an overview and derivation of the nonlinear, control-oriented, and physics-based models that have been developed for VCSs. Work included here and in further chapters has been published in [5]. Section 2.1 summarizes the literature on the most common approaches to control-oriented heat exchanger modeling. Section 2.2 provides formulations of these approaches and discusses several important considerations that must be made in their implementation. Section 2.3 overviews the other component models required for VCS simulation.

2.1 Heat Exchanger Model Formulations in the Literature

Of the components typically incorporated in a VCS, the heat exchangers are the most complex to model due to the highly nonlinear nature of the thermal dynamics that take place and the timescale separation between thermal and mechanical dynamics [6].

In recent literature, two approaches have been dominant for control-oriented physics-based modeling of heat exchangers. These are often referred to as the finite volume (FV) and the moving boundary (MB) lumped parameter methods. Both methods involve spatially discretizing the heat exchanger into control volumes (CVs) and calculating a set of average, or "lumped," parameters for each volume. The discussion that follows on the historical development of these methods draws significantly from the literature review in [6].

2.1.1 Finite Volume Approach

The FV approach, dating to [7] and [8], involves discretizing the heat exchanger spatially into an arbitrary number of equally sized CVs, as shown in Figure 2.1. The refrigerant flow in each volume may switch between superheated, two-phase, and subcooled phases as model inputs

and states change. In [9] it is demonstrated that in energy transport modeling, increasing the spatial discretization from low values improves accuracy, but as the approximation converges to the true solution, further increases in discretization bring negligible improvements in accuracy. Similarly, increasing the number CVs of a FV heat exchanger model increases the accuracy up to some limit [10]. This reveals the inherent tradeoff between accuracy and computational cost, as increasing the discretization also increases the number of states to compute.

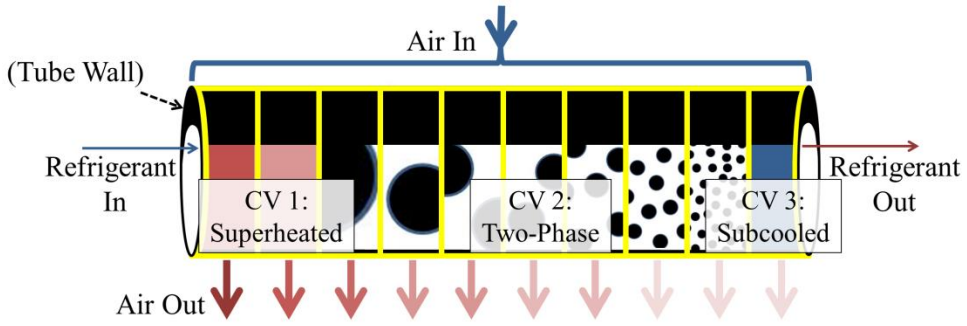

Figure 2.1 FV Model with 10 CVs for a Cross-Flow Refrigerant-to-Air Condenser

2.1.2 Moving Boundary Approach

The MB formulation results from the desire to maintain a reasonable level of accuracy without resorting to the high level of discretization often required of FV models, and therefore achieve a better balance between accuracy and computational cost. In this approach the heat exchanger is divided into CVs corresponding to each refrigerant phase, as shown in Figure 2.2. Unlike with the FV approach, the size of volumes can vary with time as phase flow lengths change. The calculation of lumped parameters for the two-phase region of the heat exchanger is often facilitated by incorporation of a mean void fraction assumption as proposed in [11], which describes the ratio of the vapor volume to the total volume along the length of the two-phase region. The use of void fraction correlations such as that in [12] further supports this. Allowing refrigerant phase regions to completely disappear and reappear without the occurrence of numerical issues is a property of Switched MB (SMB) models [13], including recent work in [14] that presents and validates a SMB model capable of describing the startup and shutdown dynamics of VCSs.

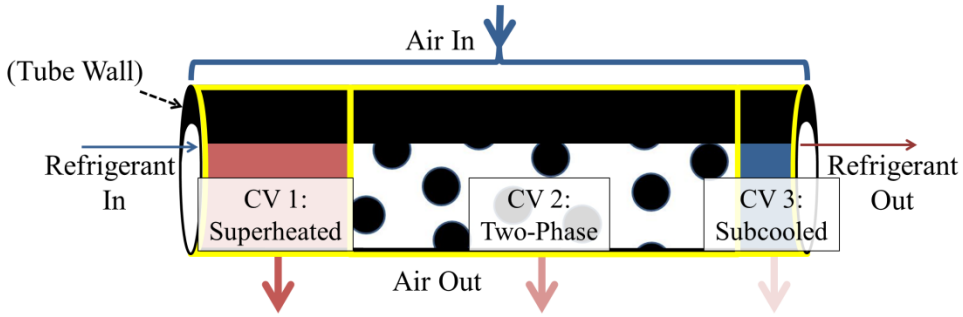

Figure 2.2 MB Model with Three CVs for a Cross-Flow Refrigerant-to-Air Condenser

2.1.3 FV vs. MB Comparisons in the Literature

Despite the considerable volume of work that has been devoted to advancing the FV and MB modeling approaches, few direct comparisons between the two are available. To the authors' knowledge, the only publications including such a discussion are [15] and [16].

In [15], the FV and MB approaches are compared for modeling shell-and-tube heat exchangers incorporated in a centrifugal chiller system, with data validation from a 300kW test stand. A MB model and a 15 volume FV model were found to have essentially equal accuracy, but the MB model simulated about three times faster. The real time factor (RTF) of the FV model was 1.2 on average, meaning that the simulation ran slower than real time given the computational resources available at the time. Eq. (2.1) provides the formula used to calculate RTF.

$$RTF = \frac{length\ of\ \ time\ taken\ to\ run\ simulation}{length\ of\ \ time\ that\ is\ simulated} \tag{2.1}$$

The formulations used in [15] resulted in a MB model that was less robust to start-up and load-change transients than the FV model. A linear profile in enthalpy was assumed in the two-phase flow region of both models. This resulted in issues with charge estimation in the MB model due to an inability to account for the highly nonlinear distribution of mass along the length of that region that is known to occur. Incorporation of mean void fraction is suggested as a method by which to better estimate a lumped density for the two-phase region.

In [16], simulation results of FV and MB models are shown to match very closely for outputs of evaporator pressure, superheat, and air outlet temperature in response to steps in valve and compressor actuators. No comparison to experimental results is provided, although it is

stated that the difference between the models falls within the error typical of validation data. Variation in FV model outputs and simulation speed for different levels of discretization are also shown. For a 500s simulation using non-compiled MATLAB/Simulink® and a 4th order Runge-Kutta solver of fixed step 0.01s, the MB model had a RTF of 0.06, while the FV model had a RTF ranging from 0.06 when simulated with one CV to 141.23 when simulated with 100 CVs. MB, FV, and three different SMB formulations are compared for conditions in which evaporator superheat is lost. This demonstrates the ability of SMB and FV formulations to function correctly when the presence of a given phase in the heat exchanger is lost or regained. The MB model is unable to function correctly under these conditions, undergoing a numerical failure as a result of attempting to invert a singular matrix. A structure from conservation equations is provided for the FV and MB models, and broad comments on the use of stiff differential equation solvers to address timescale separation and the need to avoid discontinuities in fluid property tables and other correlations are given.

Despite the evidence in [15] and [16] to the contrary, there exists a perception in the field that the higher level of discretization available in the FV approach allows it provide significantly more accurate simulation results than the MB or SMB approaches, as acknowledged in [6], [14], and [17]. This conventional wisdom is depicted graphically in Figure 2.3. Following experimental validation and comparison of these approaches in Chapter 4, we discuss a revised notion of the tradeoffs in Section 4.5.

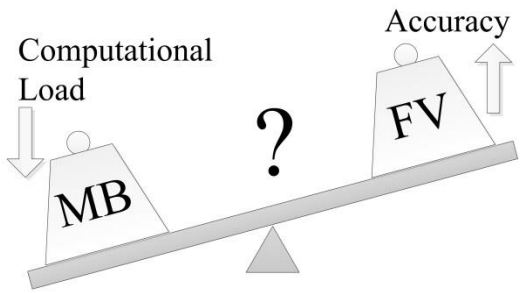

Figure 2.3 Conventional Wisdom of FV vs. MB Tradeoffs

2.2 Heat Exchanger Model Derivations

While several of the elements associated with heat exchanger modeling may be found in the existing literature, it is important to briefly revisit them in this section. In this manner the reader is aware of the precise nature of the models being used in the validation and comparison

results which are a key contribution of this work. Both the FV and the SMB approaches can be derived by applying conservation equations to each CV of the heat exchanger. As should be clear from the introduction, many derivations of these approaches are available in the literature. Therefore, we present here only a summary of the formulations used in this work and some specifics that are not commonly addressed in literature but can be very useful in practice for implementing the models in simulation. These formulations are directly applicable only to a cross-flow, refrigerant-to-air heat exchanger.

The following assumptions are made about the heat exchanger in simplifying the conservation equations:

1. The refrigerant flows through a long, thin, circular, and uniform horizontal tube.
2. The refrigerant flows only in the longitudinal direction.
3. Axial heat conduction in the refrigerant is negligible.
4. Momentum change and viscous friction in the refrigerant are negligible.

Assumption 4 above implies that the heat exchanger is isobaric, rendering analysis of conservation of momentum unnecessary. This assumption is widely applied in MB formulations throughout the literature and often used in FV formulations [6]. In [18], it was found that FV heat exchanger models with and without incorporation of the momentum equation are both acceptably accurate in describing dynamic and steady-state behavior for applications in model-based control design. It is also assumed in these models that no water vapor is present in the ambient air, or that the effects of any water vapor that is present are negligible. This assumption is revisited in Chapter 5.

Applying the above assumptions to conservation of refrigerant mass, refrigerant energy, and tube wall energy yields Eqs. (2.2)-(2.4), respectively.

$$A_{cs,r}\frac{\partial \rho_r}{\partial t}+\frac{\partial \dot{m}_r}{\partial z}=0 \tag{2.2}$$

$$A_{cs,r}\frac{\partial(\rho h-P)_r}{\partial t}+\frac{\partial(\dot{m}h)_r}{\partial z}=p\alpha_r(T_w-T_r) \tag{2.3}$$

$$\left(A_{cs}\rho c_p\right)_w\frac{\partial T_w}{\partial t}=p\alpha_r(T_r-T_w)+p\alpha_a(T_a-T_w) \tag{2.4}$$

2.2.1 Finite Volume

In deriving the finite volume model, we treat the heat exchanger as an arbitrary number of equally sized CVs. Each volume has an inlet and outlet refrigerant flow internal to the tube and an inlet and outlet air flow external to the tube, as shown in Figure 2.4. The derivation follows from that presented in [19] for a single-phase heat exchanger.

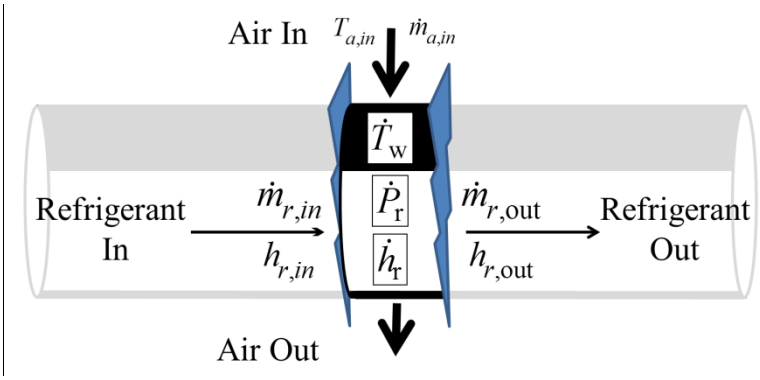

Figure 2.4 One FV Control Volume

We first express the three conservation equations for just one CV, denoted by *i*. The following steps are applied to Eqs. (2.2)-(2.4):

1. Integrate over the length of the CV (from 0 to L_v) and apply Leibniz's rule
2. Denote $\rho_{r,i}$ $h_{r,i}$ $T_{r,i}$ $T_{w,i}$ $T_{a,i}$ $\alpha_{r,i}$, and $\alpha_{a,i}$ as average values for the CV
3. Express the derivative of density as a function of pressure and enthalpy derivatives, as shown in Eq. (2.5)

$$\dot{\rho}_{r,i} = \left(\frac{\partial \rho}{\partial P}\Big|_h \right)_{r,i} \dot{P}_r + \left(\frac{\partial \rho}{\partial h}\Big|_P \right)_{r,i} \dot{h}_{r,i} \tag{2.5}$$

These steps yield further simplified forms of conservation of refrigerant mass, refrigerant energy, and tube wall energy, given respectively in Eqs. (2.6)-(2.8).

$$V_{CV} \left[\left(\frac{\partial \rho}{\partial P}\Big|_h \right)_{r,i} \dot{P}_r + \left(\frac{\partial \rho}{\partial h}\Big|_P \right)_{r,i} \dot{h}_{r,i} \right] = \dot{m}_{r,in} - \dot{m}_{r,out} \tag{2.6}$$

$$V_{CV}\left[\left(\frac{\partial\rho}{\partial P}\Big|_h\right)_{r,i} h_{r,i} - 1\right]\dot{P}_r + V_{CV}\left[\left(\frac{\partial\rho}{\partial h}\Big|_P\right)_{r,i} h_{r,i} + \rho_{r,i}\right]\dot{h}_{r,i} = \left(\dot{m}h\right)_{r,in} - \left(\dot{m}h\right)_{r,out} + A_{s,CV}\alpha_{r,i}(T_{w,i} - T_{r,i}) \tag{2.7}$$

$$\left(mc_p\right)_{w,CV}\dot{T}_{w,i} = A_{s,CV}\alpha_{r,i}(T_{r,i} - T_{w,i}) + A_{s,CV}\alpha_{a,i}(T_{a,i} - T_{w,i}) \tag{2.8}$$

In implementation, the energy transferred between the air and the wall will be calculated via the effectiveness number transfer unit (e-NTU) method described by Eqs. (2.9) and (2.10).

$$NTU = \left(\frac{\alpha A_s}{\dot{m}C_p}\right)_a \tag{2.9}$$

$$\dot{Q}_{a,i} = \frac{(\dot{m}C_p)_a}{n}\left(T_{a,in} - \left[T_{w,i} + (T_{a,in} - T_{w,i})e^{-NTU}\right]\right) \tag{2.10}$$

Therefore, the term: $A_{s,CV}\alpha_{a,i}(T_{a,i} - T_{w,i})$ in Eq. (2.8) will be replaced by $\dot{Q}_{a,i}$, as in Eq. (2.11).

$$\left(mc_p\right)_{w,CV}\dot{T}_{w,i} = A_{s,cv}\alpha_{r,i}(T_{r,i} - T_{w,i}) + \dot{Q}_{a,i} \tag{2.11}$$

Combining the conservation equations in matrix form yields:

$$\begin{pmatrix} V_{CV}\left(\frac{\partial\rho}{\partial P}\Big|_h\right)_{r,i} & V_{CV}\left(\frac{\partial\rho}{\partial h}\Big|_P\right)_{r,i} & 0 \\ V_{CV}\left[\left(\frac{\partial\rho}{\partial P}\Big|_h\right)_{r,i} h_{r,i} - 1\right] & V_{CV}\left[\left(\frac{\partial\rho}{\partial h}\Big|_P\right)_{r,i} h_{r,i} + \rho_{r,i}\right] & 0 \\ 0 & 0 & (mC_p)_{w,CV} \end{pmatrix} \begin{pmatrix} \dot{P}_r \\ \dot{h}_{r,i} \\ \dot{T}_{w,i} \end{pmatrix} = \begin{pmatrix} \dot{m}_{r,in} - \dot{m}_{r,out} \\ \left(\dot{m}h\right)_{r,in} - \left(\dot{m}h\right)_{r,out} + A_{s,CV}\alpha_{r,i}(T_{w,i} - T_{r,i}) \\ A_{s,CV}\alpha_{r,i}(T_{r,i} - T_{w,i}) + \dot{Q}_{a,i} \end{pmatrix}. \tag{2.12}$$

The next task is to extend the formulation from one CV to an arbitrary number of connected volumes. In doing so, the intermediate mass flow rates between volumes will be made part of the state vector. For example, for the three CVs shown in Figure 2.5, conservation of refrigerant mass can be expressed as:

$$\begin{pmatrix} V_{CV}\left(\frac{\partial\rho}{\partial P}\big|_h\right)_{r,1} & & & 1 & 0 \\ V_{CV}\left(\frac{\partial\rho}{\partial P}\big|_h\right)_{r,2} & I_{3x3}\times V_{CV}\left(\frac{\partial\rho}{\partial h}\big|_P\right)_{r,i} & & -1 & 1 \\ V_{CV}\left(\frac{\partial\rho}{\partial P}\big|_h\right)_{r,3} & & & 0 & -1 \end{pmatrix} \begin{pmatrix} \dot{P}_r \\ \dot{h}_{r,1} \\ \dot{h}_{r,2} \\ \dot{h}_{r,3} \\ \dot{m}_{r,1;2} \\ \dot{m}_{r,2;3} \end{pmatrix} = \begin{pmatrix} \dot{m}_{r,in} \\ 0 \\ -\dot{m}_{r,out} \end{pmatrix}. \tag{2.13}$$

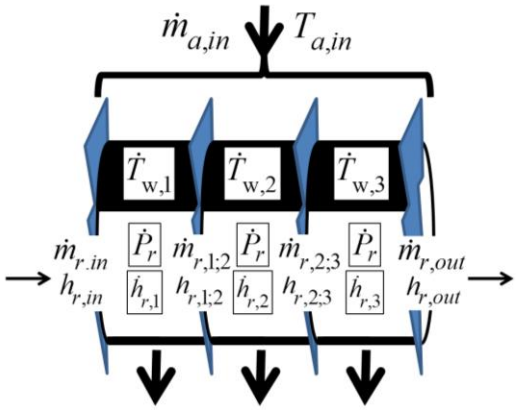

Figure 2.5 States Existing at and between a Three Control Volume FV Model

Conservation of refrigerant energy for the three CVs can be expressed as:

$$\begin{pmatrix} V_{CV}\left[\left(\frac{\partial\rho}{\partial P}\big|_h\right)_{r,1} h_{r,1} - 1\right] & & h_{r,1;2} & 0 \\ V_{CV}\left[\left(\frac{\partial\rho}{\partial P}\big|_h\right)_{r,2} h_{r,2} - 1\right] & V_{CV}Z & -h_{r,1;2} & h_{r,2;3} \\ V_{CV}\left[\left(\frac{\partial\rho}{\partial P}\big|_h\right)_{r,3} h_{r,3} - 1\right] & & 0 & -h_{r,2;3} \end{pmatrix} \begin{pmatrix} \dot{P}_r \\ \dot{h}_{r,1} \\ \dot{h}_{r,2} \\ \dot{h}_{r,3} \\ \dot{m}_{r,1;2} \\ \dot{m}_{r,2;3} \end{pmatrix}$$

$$= \begin{pmatrix} \dot{m}_{r,in}h_{r,in} + A_{s,CV}\alpha_{r,1}(T_{w,1} - T_{r,1}) \\ A_{s,CV}\alpha_{r,2}(T_{w,2} - T_{r,2}) \\ -\dot{m}_{r,out}h_{r,out} + A_{s,CV}\alpha_{r,3}(T_{w,3} - T_{r,3}) \end{pmatrix} \tag{2.14}$$

with $Z = diag\left(h_{r,1}\left(\frac{\partial\rho}{\partial h}\big|_P\right)_{r,1} + \rho_{r,1} \quad , \quad h_{r,2}\left(\frac{\partial\rho}{\partial h}\big|_P\right)_{r,2} + \rho_{r,2} \quad , \quad h_{r,3}\left(\frac{\partial\rho}{\partial h}\big|_P\right)_{r,3} + \rho_{r,3}\right)$.

Lastly, conservation of tube wall energy for the three CVs can be expressed as:

$$(mC_p)_{w,cv}\begin{pmatrix}\dot{T}_{w,1}\\ \dot{T}_{w,2}\\ \dot{T}_{w,3}\end{pmatrix}=\begin{pmatrix}A_{s,CV}\alpha_{r,1}(T_{r,1}-T_{w,1})+\dot{Q}_{a,1}\\ A_{s,CV}\alpha_{r,2}(T_{r,2}-T_{w,2})+\dot{Q}_{a,2}\\ A_{s,CV}\alpha_{r,3}(T_{r,3}-T_{w,3})+\dot{Q}_{a,3}\end{pmatrix}. \tag{2.15}$$

Eqs. (2.13)-(2.15) for a three control volume FV model can be easily extended to an arbitrary number of CVs. Eqs. (2.13) and (2.14) must be stacked and solved together, while Eq. (2.15) can be solved independently. These can be generalized as in Eqs. (2.16)-(2.17).

$$Z_1\begin{pmatrix}\dot{P}_r & \dot{h}_{r1} & \cdots & \dot{h}_{r,N} & \dot{m}_{r,1;2} & \cdots & \dot{m}_{r,N-1;N}\end{pmatrix}^T=Z_2 \tag{2.16}$$

$$Z_3\begin{pmatrix}\dot{T}_{w,1} & \cdots & \dot{T}_{w,N}\end{pmatrix}^T=Z_4 \tag{2.17}$$

There are *3N* states to solve in the matrix equations. Although only *2N+1* of these necessitate integration because integrals of the intermediate mass flow rates are not used elsewhere in the model, integration of *N* additional states associated with mass flow is implemented as part of a filter that improves the numerical robustness and speed of the model, as discussed in Section 2.2.4. While not done in the formulation presented here, it is shown in [16] that the intermediate mass flow rates could be eliminated through algebraic manipulations of the conservation equations. In this work, a linear profile assumption on the intermediate mass flow rates resulting from Eq. (2.16) is used to find a lumped mass flow rate for each CV, which is necessary for computing the refrigerant-side heat transfer coefficient (HTC). Because the inlet and outlet mass flow rates are inputs to the heat exchanger models, they can be included in the calculation, as shown in Eq. (2.18).

$$\begin{pmatrix}\dot{m}_{r,1} & \cdots & \dot{m}_{r,N}\end{pmatrix}\approx\frac{\begin{pmatrix}\dot{m}_{r,in} & \dot{m}_{r,1;2} & \cdots & \dot{m}_{r,N-1;N}\end{pmatrix}+\begin{pmatrix}\dot{m}_{r,1;2} & \cdots & \dot{m}_{r,N-1;N} & \dot{m}_{r,out}\end{pmatrix}}{2} \tag{2.18}$$

Note that both intermediate enthalpies and lumped enthalpies exist in Eq. (2.14). One way to address this issue would be to assume a linear enthalpy profile across each CV and interpolate the lumped enthalpies calculated in the previous time step to estimate the intermediate enthalpies, as in Eq. (2.19). However, this can create numerical issues in the form of high frequency oscillations under some simulation conditions. These oscillations reduce the

allowable time step size of the variable step solver, decreasing the speed of the simulation. Instead, the outlet enthalpy of each volume is assumed to be equal to the lumped enthalpy for that volume calculated in the previous time step. The outlet enthalpy from the heat exchanger can be extrapolated from those of the last two CVs as in Eq. (2.20) without the occurrence of high frequency oscillations in the numerical solution.

$$h_{r,i;i+1} \approx \frac{h_{r,i+1} - h_{r,i}}{2} \tag{2.19}$$

$$h_{r,out} \approx h_{r,N} + \frac{(h_{r,N} - h_{r,N-1})}{2} \tag{2.20}$$

2.2.2 Switched Moving Boundary

In formulating the SMB model, we define one CV for each refrigerant phase region in the heat exchanger. Because these regions may completely disappear and reappear, the formulation requires a set of equations for each possible combination of phases present in the heat exchanger, as well as switching criteria and pseudo-state equations that smoothly transition the model between these sets. The formulation used in this work was developed in [20] and has three possible combinations of phases in the evaporator and four in the condenser, as depicted in Figure 2.6.

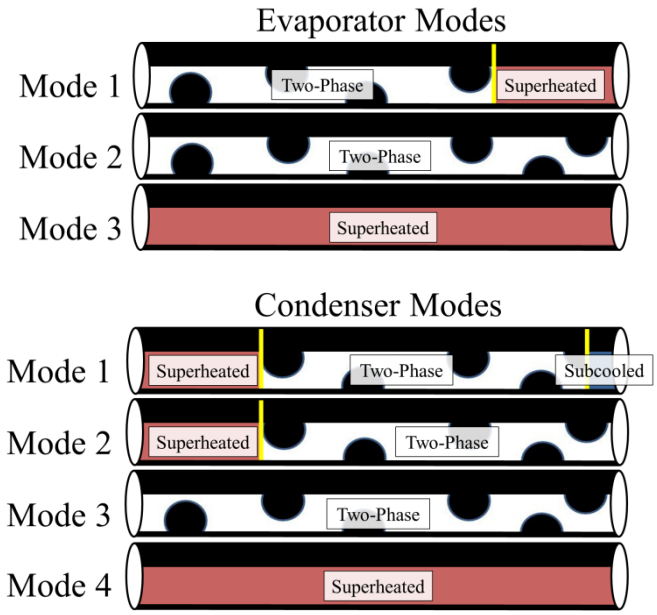

Figure 2.6 SMB Evaporator and Condenser Modes

The primary differences between simplification of the conservation equations for the SMB derivation and that for the FV model are a change in integration limits and the fact that the lengths of CVs are variable. We present here only the derivation of conservation equations for the two-phase CV of Mode 1 of the condenser as an example of how this model is formulated, as well as an overview of the switching criteria for all modes. The following steps are applied to Eqs.(2.2)-(2.4):

1. Integrate over the length of the CV (from 0 L_{SH} to L_{SH+TP}) and apply Leibniz's rule
2. Denote $\rho_{r,TP}$ $h_{r,TP}$ $T_{r,TP}$ $T_{w,TP}$ $T_{\mathrm{a},TP}$ $\alpha_{r,TP}$, and $\alpha_{a,TP}$ as lumped values for the CV
3. Apply the product rule as needed
4. Normalize the lengths of each CV by the total length of the heat exchanger

These steps yield further simplified forms of conservation of refrigerant mass, refrigerant energy, and tube wall energy, given respectively in Eqs. (2.21)-(2.23).

$$\zeta_{TP}\dot{\rho}_{r,TP}+\left(\rho_{r,g}-\rho_{r,f}\right)\dot{\zeta}_{SH}+(\rho_{r,TP}-\rho_{r,f})\dot{\zeta}_{TP}=\frac{\dot{m}_{r,SH;TP}-\dot{m}_{r,TP;SC}}{V_{total}} \tag{2.21}$$

$$\begin{aligned}&\zeta_{TP}\frac{d(\rho h)_{r,TP}}{dt}-\zeta_{TP}\dot{P}_r+\left[(\rho h)_{r,TP}-(\rho h)_{r,f}\right]\dot{\zeta}_{TP}+\left[(\rho h)_{r,g}-(\rho h)_{r,f}\right]\dot{\zeta}_{SH}\\&=\frac{\left(\dot{m}h\right)_{r,SH;TP}-\left(\dot{m}h\right)_{r,TP;SC}+A_{\mathrm{s},total}\zeta_{TP}\alpha_{r,i}(T_{w,i}-T_{r,i})}{V_{total}}\end{aligned} \tag{2.22}$$

$$\begin{aligned}&\zeta_{TP}\dot{T}_{w,TP}+\left(T_{w,SH}-T_w|_{L_{SH}+L_{TP}}\right)\dot{\zeta}_{TP}+\left(T_w|_{L_{SH}}-T_w|_{L_{SH}+L_{TP}}\right)\dot{\zeta}_{SH}\\&=\frac{A_{\mathrm{s},total}\zeta_{TP}\left[\alpha_{r,i}(T_{r,i}-T_{w,i})+\alpha_{a,i}(T_{a,i}-T_{w,i})\right]}{\left(mc_p\right)_w}\end{aligned} \tag{2.23}$$

The conservation equations for the superheated and subcooled CVs contribute six more equations to the three given above in Eqs. (2.21)-(2.23). Through algebraic manipulations, these nine equations can be combined to remove the intermediate mass flow rates $\dot{m}_{r,SH;TP}$ and $\dot{m}_{r,TP;SC}$.

The use of mean void fraction allows the model to describe the system using the nine states of: Pressure, the wall temperature of each CV, the normalized length of two CVs, enthalpy

of the superheated and subcooled CVs, and mean void fraction of the two-phase CV. This state vector is shown symbolically in Section 2.2.2.2 as Eq. (2.40).

The derivative of refrigerant densities in the superheated and subcooled volumes is calculated using Eq. (2.5). In the two-phase volume, density and enthalpy are calculated from mean void fraction via:

$$\rho_{TP} = \bar{\gamma}\rho_g + (1-\bar{\gamma})\rho_f \tag{2.24}$$

$$h_{TP} = \frac{\bar{\gamma}(h\rho)_g + (1-\bar{\gamma})(h\rho)_f}{\bar{\gamma}\rho_g + (1-\bar{\gamma})\rho_f} \tag{2.25}$$

Derivatives of density and enthalpy with respect to time, pressure, and mean void fraction can be found by differentiating Eqs. (2.24)-(2.25). These can then be combined with the conservation equations to describe the system by the desired states [20].

The general principles involved in formulating Mode 1 of the condenser can be extended to describe the other modes of both the condenser and evaporator. Not covered in detail here is the use of profile assumptions in the last CV of each mode to calculate outlet properties. In the most common modes of operation, the log mean temperature approach found in [21] is used to calculate outlet properties of superheated and subcooled volumes and mean void fraction is used to calculate outlet properties of two-phase volumes; however different approaches are used for modes involved in shutdown and startup modeling. Pseudo-state equations used to "track" states that become inactive when the CV they describe is no longer present in the refrigerant flow are also not covered in depth here. The reader is referred to [20] for these details. As with the FV model, the e-NTU method of Eqs. (2.9)-(2.10) is used to calculate the energy transferred between the air and the tube wall.

Developing switching criteria that transition the model between modes smoothly is a significant challenge of SMB modeling. Most of the switches are triggered when states and their derivatives meet a set of conditions, as detailed in Figure 2.7. Note that $\bar{\gamma}_{full}$ for the evaporator refers to mean void fraction calculated with the outlet as fully evaporated, and $\bar{\gamma}_{full}$ for the condenser refers to mean void fraction calculated with the inlet and outlet as fully evaporated and fully condensed, respectively. $\zeta_{\min}$ is a small nonzero number that can be tuned for the differential equation solver used to run the model.

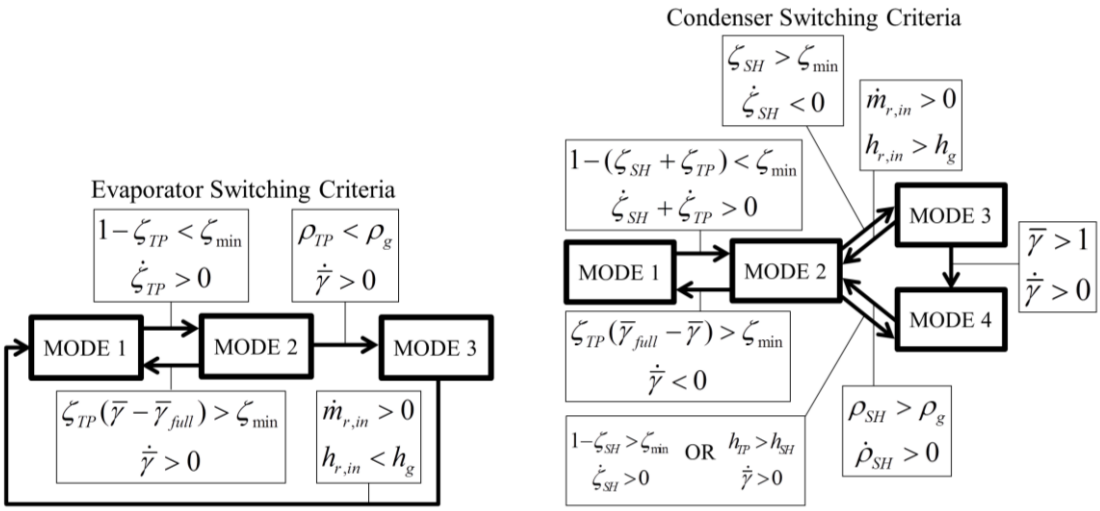

Figure 2.7 SMB Switching Criteria by Mode

2.2.2.1 Evaporator Formulation

As shown in Figure 2.6, the nonlinear SMB evaporator includes three modes to capture different combinations of phase flow. The remainder of this work will use only Mode 1, which represents an evaporator with both two-phase flow and superheated flow, and Mode 2, which represents an evaporator with only two-phase flow. Therefore, we present here only the final forms of these nonlinear modes.

Both modes follow the general nonlinear descriptor form:

$$\begin{aligned} Z_1(x_e,u_e)\dot{x}_e &= Z_2(x_e,u_e) \\ \mathrm{y}_e &= Z_3(x_e,u_e) \end{aligned} \tag{2.26}$$

with

$$\begin{aligned} u_e &= \begin{pmatrix} \dot{m}_{r,in} & \dot{m}_{r,out} & h_{r,in} & T_{a,in} & \dot{m}_{a,in} \end{pmatrix}^T \\ y_e &= \begin{pmatrix} P & h_{r,out} & T_{r,out} & SH & T_{a,out} & \dot{Q} \end{pmatrix}^T \end{aligned} . \tag{2.27}$$

The state vector of the evaporator is given by:

$$x_e = \begin{pmatrix} \zeta_1 & P & h_{r,2} & T_{w,1} & T_{w,2} & \bar{\gamma} \end{pmatrix}^T , \tag{2.28}$$

however for some modes the full state vector does not appear in the descriptor form, in which case the remaining states are tracked using pseudo-state equations.

2.2.2.1.1 Mode 1: Two-Phase and Superheated Zones

For Mode 1, also referred to as the "2-zone" evaporator model, the full state vector of Eq. (2.28) is used and Z_1 is given by:

$$Z_1 = \begin{pmatrix} z_{11} & z_{12} & z_{13} & 0 & 0 & z_{16} \\ z_{21} & z_{22} & z_{23} & 0 & 0 & 0 \\ z_{31} & z_{32} & z_{33} & 0 & 0 & z_{36} \\ z_{41} & 0 & 0 & z_{44} & 0 & 0 \\ z_{51} & 0 & 0 & 0 & z_{55} & 0 \\ 0 & z_{62} & 0 & 0 & 0 & z_{66} \end{pmatrix} \tag{2.29}$$

with elements as indicated in Table 2.1.

Table 2.1 Mode 1 Matrix Elements of Z_1

z_{11}	$V_{tot}\left(\rho_1 - \rho_2\right)$
z_{12}	$V_{tot}\left(\zeta_1 \frac{\partial \rho_1}{\partial P}\Big\|_{\bar{\gamma}} + \zeta_2 \frac{\partial \rho_2}{\partial P}\Big\|_{h_{r,2}}\right)$
z_{13}	$V_{tot}\zeta_2 \frac{\partial \rho_2}{\partial h_{r,2}}\Big\|_P$
z_{16}	$V_{tot}\zeta_1 \frac{\partial \rho_1}{\partial \bar{\gamma}}\Big\|_P$
z_{21}	$V_{tot}\rho_2(h_{r,v} - h_{r,2})$
z_{22}	$V_{tot}\zeta_2\left((h_{r,2} - h_{r,v})\frac{\partial \rho_2}{\partial P}\Big\|_{h_{r,2}} - 1\right)$
z_{23}	$V_{tot}\zeta_2\left((h_{r,2} - h_{r,v})\frac{\partial \rho_2}{\partial h_{r,2}}\Big\|_P + \rho_2\right)$
z_{31}	$V_{tot}\left(\rho_1 h_{r,1} - \rho_2 h_{r,v}\right)$

Table 2.1 (cont.)

z_{32}	$V_{tot}\left[\zeta_1\left(h_{r,1}\frac{\partial\rho_1}{\partial P}\Big\vert_{\bar{\gamma}}+\rho_1\frac{\partial h_{r,1}}{\partial P}\Big\vert_{\bar{\gamma}}-1\right)+\zeta_2 h_{r,v}\frac{\partial\rho_2}{\partial P}\Big\vert_{h_{r,2}}\right]$
z_{33}	$V_{tot}\zeta_2 h_{r,v}\frac{\partial\rho_2}{\partial h_{r,2}}\Big\vert_P$
z_{36}	$V_{tot}\zeta_1\left(h_{r,1}\frac{\partial\rho_1}{\partial\bar{\gamma}}\Big\vert_P+\rho_1\frac{\partial h_{r,1}}{\partial\bar{\gamma}}\Big\vert_P\right)$
z_{41}	$m_w c_p(T_{w_1}-T_w\vert_{L_1})$
z_{44}	$m_w c_{p,w}\zeta_1$
z_{51}	$m_w c_p(T_w\vert_{L_1}-T_{w_2})$
z_{55}	$m_w c_{p,w}\zeta_2$
z_{62}	$\frac{\partial\bar{\gamma}_{full}}{\partial P}$
z_{66}	-1

In Table 2.1, $T_w\vert_{L_1}$ is given by:

$$T_w\vert_{L_1}=\begin{cases}T_{w,2}\ \ if\ \ \dot{\zeta}_1\geq 0\\ T_{w,1}\ \ if\ \ \dot{\zeta}_1<0\end{cases}. \tag{2.30}$$

and $\bar{\gamma}_{full}$ is as defined in the paragraph above Figure 2.7.

Z_2 and Z_3 are given by:

$$Z_2 = \begin{pmatrix} \dot{m}_{r,in} - \dot{m}_{r,out} \\ \dot{m}_{r,out}(h_{r,v} - h_{r,out}) + A_s\zeta_2\alpha_{r,2}(T_{w,2} - T_{r,2}) \\ \dot{m}_{r,in}h_{r,in} - \dot{m}_{r,out}h_{r,v} + A_s\zeta_1\alpha_{r,1}(T_{w,1} - T_{r,1}) \\ A_s\zeta_1\alpha_{r,1}(T_{r,1} - T_{w,1}) + \zeta_1\dot{m}_{a,in}c_{p,a}\left\{T_{a,in} - \left[T_{w,1} + (T_{a,in} - T_{w,1})e^{-NTU}\right]\right\} \\ A_s\zeta_2\alpha_{r,2}(T_{r,1} - T_{w.2}) + \zeta_2\dot{m}_{a,in}c_{p,a}\left\{T_{a,in} - \left[T_{w,2} + (T_{a,in} - T_{w,2})e^{-NTU}\right]\right\} \\ K(\bar{\gamma} - \bar{\gamma}_{full}) \end{pmatrix} \tag{2.31}$$

$$Z_3 = \begin{pmatrix} P \\ 2h_{r,2} - h_{r,g} \\ f(2h_{r,2} - h_{r,g}, P) \\ f(2h_{r,2} - h_{r,g}, P) - T_{sat}(P) \\ \zeta_1\left(T_{w,1} + (T_{a,in} - T_{w,1})e^{-NTU}\right) + \zeta_2\left(T_{w,2} + (T_{a,in} - T_{w,2})e^{-NTU}\right) \\ \dot{m}_{a,in}c_{p,a}\left(\zeta_1\left(T_{w,1} + (T_{a,in} - T_{w,1})e^{-NTU}\right) + \zeta_2\left(T_{w,2} + (T_{a,in} - T_{w,2})e^{-NTU}\right) - T_{a,in}\right) \end{pmatrix}. \tag{2.32}$$

2.2.2.1.2 Mode 2: Two-Phase Zone Only

For Mode 2, also referred to as the "1-zone" evaporator model, the full state vector of Eq. (2.28) is reduced to:

$$x_e = \begin{pmatrix} P & T_{w,1} & \bar{\gamma} \end{pmatrix}^T \tag{2.33}$$

and Z_1, Z_2, and Z_3 are given by:

$$Z_1 = \begin{pmatrix} V_{tot}\frac{\partial\rho_1}{\partial P}\Big|_{\bar{\gamma}} & 0 & V_{tot}\frac{\partial\rho_1}{\partial\bar{\gamma}}\Big|_P \\ V_{tot}\left(h_{r,1}\frac{\partial\rho_1}{\partial P}\Big|_{\bar{\gamma}} + \rho_1\frac{\partial h_{r,1}}{\partial P}\Big|_{\bar{\gamma}} - 1\right) & 0 & V_{tot}\left(\rho_1\frac{\partial h_{r,1}}{\partial\bar{\gamma}}\Big|_P + h_{r,1}\frac{\partial\rho_1}{\partial\bar{\gamma}}\Big|_P\right) \\ 0 & m_w c_{p,w} & 0 \end{pmatrix} \tag{2.34}$$

$$Z_2 = \begin{pmatrix} \dot{m}_{r,in} - \dot{m}_{r,out} \\ \dot{m}_{r,in}h_{r,in} - \dot{m}_{r,out}h_{r,out} + A_s\alpha_{r,1}(T_{w,1} - T_{r,1}) \\ A_s\alpha_{r,1}(T_{r,1} - T_{w,1}) + \dot{m}_{a,in}c_{p,a}\left\{T_{a,in} - \left[T_{w,1} + (T_{a,in} - T_{w,1})e^{-NTU}\right]\right\} \end{pmatrix} \tag{2.35}$$

$$Z_3 = \begin{pmatrix} P \\ q_{out} h_{r,g} + (1 - q_{out})\, \mathrm{h}_{r,f} \\ f(P) \\ 0 \\ T_{w,1} + (T_{a,in} - T_{w,1}) e^{-NTU} \\ \dot{m}_{a,in} c_{p,a} \left(T_{w,1} + (T_{a,in} - T_{w,1}) e^{-NTU} - T_{a,in} \right) \end{pmatrix}. \tag{2.36}$$

In addition, this mode makes use of the following pseudo-state equations:

$$\begin{aligned} \dot{\zeta}_1 &= k(\zeta_{1,track} - \zeta_1) \\ \dot{h}_{r,2} &= k(h_{r,v} - h_{r,2}) \\ \dot{T}_{w_2} &= k(T_{w,1} - T_{w,2}) \end{aligned} \tag{2.37}$$

where $k = 5$ is chosen to ensure that the tracking dynamics are sufficiently fast as compared to the system dynamics, and $\zeta_{1,track} = 0.999$.

2.2.2.2 Condenser Formulation

As shown in Figure 2.6, the nonlinear SMB condenser includes four modes to capture different combinations of phase flow. The remainder of this work will use only Mode 1, which represents a condenser with superheated, two-phase, and subcooled flow, and Mode 2, which represents a condenser with only superheated and two-phase flow. Therefore, we again present here only the final forms of these nonlinear modes.

Both modes follow the general nonlinear descriptor form:

$$\begin{aligned} Z_1(x_c, u_c)\dot{x}_c &= Z_2(x_c, u_c) \\ \mathrm{y}_c &= Z_3(x_c, u_c) \end{aligned} \tag{2.38}$$

with

$$\begin{aligned} u_c &= \begin{pmatrix} \dot{m}_{r,in} & \dot{m}_{r,out} & h_{r,in} & T_{a,in} & \dot{m}_{a,in} \end{pmatrix}^T \\ y_c &= \begin{pmatrix} P & h_{r,out} & T_{r,out} & SC & T_{a,out} & \dot{Q} \end{pmatrix}^T \end{aligned}. \tag{2.39}$$

The state vector of the condenser is given by:

$$x_c = \begin{pmatrix} \zeta_1 & \zeta_2 & P & h_{r,1} & h_{r,3} & \bar{\gamma} & T_{w,1} & T_{w,2} & T_{w,3} \end{pmatrix}^T, \tag{2.40}$$

however for some modes the full state vector does not appear in the descriptor form, in which case the remaining states are tracked using pseudo-state equations.

2.2.2.2.1 Mode 1: Superheated, Two-Phase, and Subcooled Zones

For Mode 1, also referred to as the "3-zone" condenser model, the full state vector of Eq. (2.40) is used and Z_1 is given by:

$$Z_1 = \begin{pmatrix} z_{11} & 0 & z_{13} & z_{14} & 0 & 0 & 0 & 0 & 0 \\ z_{21} & z_{22} & z_{23} & z_{24} & z_{25} & z_{26} & 0 & 0 & 0 \\ z_{31} & z_{32} & z_{33} & z_{34} & z_{35} & z_{36} & 0 & 0 & 0 \\ z_{41} & z_{42} & z_{43} & 0 & z_{45} & 0 & 0 & 0 & 0 \\ 0 & 0 & 0 & 1 & 0 & 0 & 0 & 0 & 0 \\ 0 & 0 & z_{63} & 0 & 0 & 1 & 0 & 0 & 0 \\ z_{71} & 0 & 0 & 0 & 0 & 0 & z_{77} & 0 & 0 \\ z_{81} & z_{82} & 0 & 0 & 0 & 0 & 0 & z_{88} & 0 \\ z_{91} & z_{92} & 0 & 0 & 0 & 0 & 0 & 0 & z_{99} \end{pmatrix} \tag{2.41}$$

with elements as indicated in Table 2.2.

Table 2.2 Mode 1 Matrix Elements of Z_1

z_{11}	$V_{tot}\rho_1\left(h_{r,1}-h_{r,g}\right)$
z_{13}	$V_{tot}\zeta_1\left(\left(h_{r,1}-h_{r,g}\right)\frac{\partial\rho_1}{\partial P}\Big\vert_{h_{r,1}}-1\right)$
z_{14}	$V_{tot}\zeta_1\left(\rho_1+\left(h_{r,1}-h_{r,g}\right)\frac{\partial\rho_1}{\partial h_{r,1}}\Big\vert_{P}\right)$
z_{21}	$V_{tot}(\rho_1-\rho_3)$
z_{22}	$V_{tot}(\rho_2-\rho_3)$
z_{23}	$V_{tot}\left(\zeta_1\frac{\partial\rho_1}{\partial P}\Big\vert_{h_{r,1}}+\zeta_2\frac{\partial\rho_2}{\partial P}\Big\vert_{\bar{\gamma}}+\zeta_3\frac{\partial\rho_3}{\partial P}\Big\vert_{h_{r,3}}\right)$

Table 2.2 (cont.)

z_{24}	$V_{tot}\zeta_1 \frac{\partial \rho_1}{\partial h_{r,1}}\Big\vert_P$
z_{25}	$V_{tot}\zeta_3 \frac{\partial \rho_3}{\partial h_{r,3}}\Big\vert_P$
z_{26}	$V_{tot}\zeta_2 \frac{\partial \rho_2}{\partial \bar{\gamma}}\Big\vert_P$
z_{31}	$V_{tot}\left(\rho_1 h_{r,g} - \rho_3 h_{r,f}\right)$
z_{32}	$V_{tot}\left(\rho_2 h_{r,2} - \rho_3 h_{r,f}\right)$
z_{33}	$V_{tot}\left(\zeta_1 h_{r,g} \frac{\partial \rho_1}{\partial P}\Big\vert_{h_{r,1}} + \zeta_2\left(\rho_2 \frac{\partial h_2}{\partial P}\Big\vert_{\bar{\gamma}} + h_{r,2} \frac{\partial \rho_2}{\partial P}\Big\vert_{\bar{\gamma}} - 1\right) + \zeta_3 h_{r,f} \frac{\partial \rho_3}{\partial P}\Big\vert_{h_{r,3}}\right)$
z_{34}	$V_{tot}\zeta_1 h_{r,g} \frac{\partial \rho_1}{\partial h_{r,1}}\Big\vert_P$
z_{35}	$V_{tot}\zeta_3 h_{r,g} \frac{\partial \rho_3}{\partial h_{r,3}}\Big\vert_P$
z_{36}	$V_{tot}\zeta_2\left(h_{r,2} \frac{\partial \rho_2}{\partial \bar{\gamma}}\Big\vert_P + \rho_2 \frac{\partial h_{r,2}}{\partial \bar{\gamma}}\Big\vert_P\right)$
z_{41}	$V_{tot}\rho_3\left(h_{r,f} - h_{r,3}\right)$
z_{42}	$V_{tot}\rho_3\left(h_{r,f} - h_{r,3}\right)$
z_{43}	$V_{tot}\zeta_3\left(\left(h_{r,3} - h_{r,f}\right)\frac{\partial \rho_3}{\partial P}\Big\vert_{h_{r,3}} - 1\right)$

Table 2.2 (cont.)

z_{45}	$V_{tot}\zeta_3\left(\left(h_{r,3}-h_{r,f}\right)\frac{\partial\rho_3}{\partial h_{r,3}}\Big\|_P+\rho_3\right)$
z_{63}	$-\frac{\partial\overline{\gamma}_{full}}{\partial P}$
z_{71}	$c_{p,w}m_w(T_{w,1}-T_{w\|L_1})$
z_{77}	$c_{p,w}m_w\zeta_1$
z_{81}	$c_{p,w}m_w(T_{w\|L_1}-T_{w\|L_2})$
z_{82}	$c_{p,w}m_w(T_{w,2}-T_{w\|L_2})$
z_{88}	$c_{p,w}m_w\zeta_2$
z_{91}	$c_{p,w}m_w(T_{w\|L_2}-T_{w,3})$
z_{92}	$c_{p,w}m_w(T_{w\|L_2}-T_{w,3})$
z_{99}	$c_{p,w}m_w\zeta_3$

In Table 2.2, $T_w|_{L_1}$ and $T_w|_{L_2}$ are given by:

$$T_w|_{L_1}=\begin{cases}T_{w,2} \ if \ \dot{\zeta}_1>0\\ T_{w,1} \ if \ \dot{\zeta}_1\le 0\end{cases}$$
$$T_w|_{L_2}=\begin{cases}T_{w,3} \ if \ \dot{\zeta}_1+\dot{\zeta}_2>0\\ T_{w,2} \ if \ \dot{\zeta}_1+\dot{\zeta}_2\le 0\end{cases}. \qquad (2.42)$$

and $\overline{\gamma}_{full}$ is as defined in the paragraph above Figure 2.7.

Z_2 and Z_3 are given by:

$$Z_2 = \begin{pmatrix} \dot{m}_{r,in}(h_{r,in} - h_{r,g}) + A_s\zeta_1\alpha_{r,1}(T_{w,1} - T_{r,1}) \\ \dot{m}_{r,in} - \dot{m}_{r,out} \\ \dot{m}_{r,in}h_{r,g} - \dot{m}_{r,out}h_{r,f} + A_s\zeta_2\alpha_{r,2}(T_{w,2} - T_{r,2}) \\ \dot{m}_{r,out}(h_{r,f} - h_{r,out}) + A_s\zeta_3\alpha_{r,3}(T_{w,3} - T_{r,3}) \\ 5\left(\frac{h_{r,in} + h_{r,g}}{2} - h_{r,1}\right) \\ 5(\bar{\gamma}_{full} - \bar{\gamma}) \\ \dot{m}_{a,in}c_{p,a}\zeta_1\left(T_{a,in} - \left(T_{w,1} + (T_{a,in} - T_{w,1})e^{-NTU}\right)\right) - \alpha_a A_s\zeta_1(T_{w,1} - T_{r,1}) \\ \dot{m}_{a,in}c_{p,a}\zeta_2\left(T_{a,in} - \left(T_{w,2} + (T_{a,in} - T_{w,2})e^{-NTU}\right)\right) - \alpha_a A_s\zeta_2(T_{w,2} - T_{r,2}) \\ \dot{m}_{a,in}c_{p,a}\zeta_3\left(T_{a,in} - \left(T_{w,3} + (T_{a,in} - T_{w,3})e^{-NTU}\right)\right) - \alpha_a A_s\zeta_3(T_{w,3} - T_{r,3}) \end{pmatrix} \quad (2.43)$$

$$Z_3 = \begin{pmatrix} P \\ h_{r,3} \\ f(h_{r,3}, P) \\ f(h_{r,3}, P) - T_{sat}(P) \\ \zeta_1\left(T_{w,1} + (T_{a,in} - T_{w,1})e^{-NTU}\right) + \zeta_2\left(T_{w,2} + (T_{a,in} - T_{w,2})e^{-NTU}\right) + \zeta_3\left(T_{w,3} + (T_{a,in} - T_{w,3})e^{-NTU}\right) \\ \dot{m}_{a,in}c_{p,a}\begin{pmatrix} T_{a,in} - \zeta_1\left(T_{w,1} + (T_{a,in} - T_{w,1})e^{-NTU}\right) \\ -\zeta_2\left(T_{w,2} + (T_{a,in} - T_{w,2})e^{-NTU}\right) - \zeta_3\left(T_{w,3} + (T_{a,in} - T_{w,3})e^{-NTU}\right) \end{pmatrix} \end{pmatrix} . \quad (2.44)$$

2.2.2.2.2 Mode 2: Superheated and Two-Phase Zones Only

For Mode 2, also referred to as the "2-zone" condenser model, the full state vector of Eq. (2.40) is reduced to:

$$x_c = \begin{pmatrix} \zeta_1 & P & h_{r,1} & \bar{\gamma} & T_{w,1} & T_{w,2} \end{pmatrix}^T \quad (2.45)$$

and Z_1 is given by:

$$Z_1 = \begin{pmatrix} z_{11} & z_{12} & z_{13} & z_{14} & 0 & 0 \\ z_{21} & z_{22} & z_{23} & z_{24} & 0 & 0 \\ z_{31} & z_{32} & z_{33} & 0 & 0 & 0 \\ 0 & 0 & 1 & 0 & 0 & 0 \\ z_{51} & 0 & 0 & 0 & z_{55} & 0 \\ z_{61} & 0 & 0 & 0 & 0 & z_{66} \end{pmatrix} \tag{2.46}$$

with elements as indicated in Table 2.3.

Table 2.3 Mode 2 Matrix Elements of Z_1

z_{11}	$V_{tot}(\rho_1 - \rho_2)$
z_{12}	$V_{tot}\left(\zeta_1 \frac{\partial \rho_1}{\partial P}\Big\|_{h_{r,1}} + \zeta_2 \frac{\partial \rho_2}{\partial P}\Big\|_{\bar{\gamma}}\right)$
z_{13}	$V_{tot}\zeta_1 \frac{\partial \rho_1}{\partial h_{r,1}}\Big\|_P$
z_{14}	$V_{tot}\zeta_2 \frac{\partial \rho_2}{\partial \bar{\gamma}}\Big\|_P$
z_{21}	$V_{tot}\left(\rho_1 h_{r,1} - \rho_2 h_{r,g}\right)$
z_{22}	$V_{tot}\left(\zeta_1\left(h_{r,1}\frac{\partial \rho_1}{\partial P}\Big\|_{h_{r,1}} - 1\right) + \zeta_2 h_{r,g}\frac{\partial \rho_2}{\partial P}\Big\|_{\bar{\gamma}}\right)$
z_{23}	$V_{tot}\zeta_1\left(\rho_1 + h_{r,1}\frac{\partial \rho_1}{\partial h_{r,1}}\Big\|_P\right)$
z_{24}	$V_{tot}\zeta_2 h_{r,g}\frac{\partial \rho_2}{\partial \bar{\gamma}}\Big\|_P$
z_{31}	$V_{tot}\rho_2(h_{r,g} - h_{r,2})$

Table 2.3 (cont.)

z_{32}	$V_{tot}\zeta_2\left(\left(h_{r,2}-h_{r,g}\right)\frac{\partial\rho_2}{\partial P}\Big\vert_{\bar{\gamma}}+\rho_2\frac{\partial h_{r,2}}{\partial P}\Big\vert_{\bar{\gamma}}-1\right)$
z_{33}	$V_{tot}\zeta_2\left(\rho_2\frac{\partial h_{r,2}}{\partial\bar{\gamma}}\Big\vert_P+(h_{r,2}-h_{r,g})\frac{\partial\rho_2}{\partial\bar{\gamma}}\Big\vert_P\right)$
z_{51}	$m_w c_{p_w}(T_{w_1}-T_{w\vert L_1})$
z_{55}	$m_w c_{p_w}\zeta_1$
z_{61}	$m_w c_{p_w}(T_{w\vert L_1}-T_{w_2})$
z_{66}	$m_w c_{p_w}\zeta_2$

Z_2, and Z_3 are given by:

$$Z_2=\begin{pmatrix}\dot{m}_{r,in}-\dot{m}_{r,out}\\ \dot{m}_{r,in}h_{r,in}-\dot{m}_{r,out}h_{r,g}+A_s\zeta_1\alpha_{r,1}(T_{w_1}-T_{r_1})\\ \dot{m}_{r,out}(h_{r,g}-h_{r,o})+A_s\zeta_2\alpha_{r,2}(T_{w_2}-T_{r_2})\\ 5\left(\frac{h_{r,in}+h_{r,g}}{2}-h_{r,1}\right)\\ \dot{m}_{a,in}c_{p,a}\zeta_1\left(T_{a,in}-\left(T_{w,1}+(T_{a,in}-T_{w,1})e^{-NTU}\right)\right)-\alpha_{r,1}A_s\zeta_1(T_{w,1}-T_{r,1})\\ \dot{m}_{a,in}c_{p,a}\zeta_2\left(T_{a,in}-\left(T_{w,2}+(T_{a,in}-T_{w,2})e^{-NTU}\right)\right)-\alpha_{r,2}A_s\zeta_2(T_{w,2}-T_{r,2})\end{pmatrix} \tag{2.47}$$

$$Z_3=\begin{pmatrix}P\\ q_{out}h_{r,g}+(1-q_{out})h_{r,f}\\ f(P)\\ 0\\ \zeta_1\left(T_{w,1}+(T_{a,in}-T_{w,1})e^{-NTU}\right)+\zeta_2\left(T_{w,2}+(T_{a,in}-T_{w,2})e^{-NTU}\right)\\ \dot{m}_{a,in}c_{p,a}\left(T_{a,in}-\zeta_1\left(T_{w,1}+(T_{a,in}-T_{w,1})e^{-NTU}\right)-\zeta_2\left(T_{w,2}+(T_{a,in}-T_{w,2})e^{-NTU}\right)\right)\end{pmatrix}. \tag{2.48}$$

In addition, this mode makes use of the following pseudo-state equations:

$$\begin{aligned}\dot{\zeta}_2 &= -\dot{\zeta}_1 \\ \dot{h}_{r,3} &= k(h_{r,f} - h_{r,3}) \\ \dot{T}_{w_2} &= k(T_{w,2} - T_{w,3})\end{aligned} \tag{2.49}$$

where $k = 5$ is chosen to ensure that the tracking dynamics are sufficiently fast as compared to the system dynamics.

2.2.3 Property Table Correlations

Both the FV and the SMB models rely upon a number of lookup tables and empirical correlations in order to function correctly. In the models presented in this work, as is done frequently in heat exchanger modeling, fluid properties such as such as density, temperature, and specific heat capacity of the refrigerant and air are interpolated from property lookup tables generated using the REFPROP database released by NIST, detailed in [22]. Zivi's local void fraction correlation is used in the SMB model where necessary. Air-side HTCs are calculated using the Colburn j factor, as in [17]. Superheated and subcooled refrigerant-side HTCs are found using a Gnielinski correlation [23]. Two-phase refrigerant-side HTCs for the condenser are found using the correlation by Dobson and Chato [24], while those for the evaporator are found using the correlation from Wattelet et al [25].

As is stated in [16], care must be taken to ensure that discontinuities in property tables and correlations do not cause numerical errors. As an example of the issues that can arise from discontinuities, we consider the calculation of refrigerant-side HTCs in the FV condenser. A HTC is calculated for each CV at every time step, and varies with the pressure, enthalpy, and mass flow rate of the refrigerant. Figure 2.8 shows the profile of HTCs in the condenser for fixed pressure and mass flow rate. In the original profile, it is clear that sharp changes in derivatives exist at the saturation points where the method being used to compute the HTCs switches between the Gnielinksi and the Dobston-Chato correlations, and at the peak value of HTC. For some combinations of operating conditions and number of CVs, the presence of these discontinuities can cause numerical errors which slow or interfere with execution of the model. As also shown in Figure 2.8, a simple smoothing function can be implemented to remove the

discontinuities. This results in faster and more robust simulations, and has negligible effects on model accuracy. For the FV model used in this work, a three-dimensional lookup table of smoothed values of HTC is computed and stored for both the evaporator and the condenser prior to simulations.

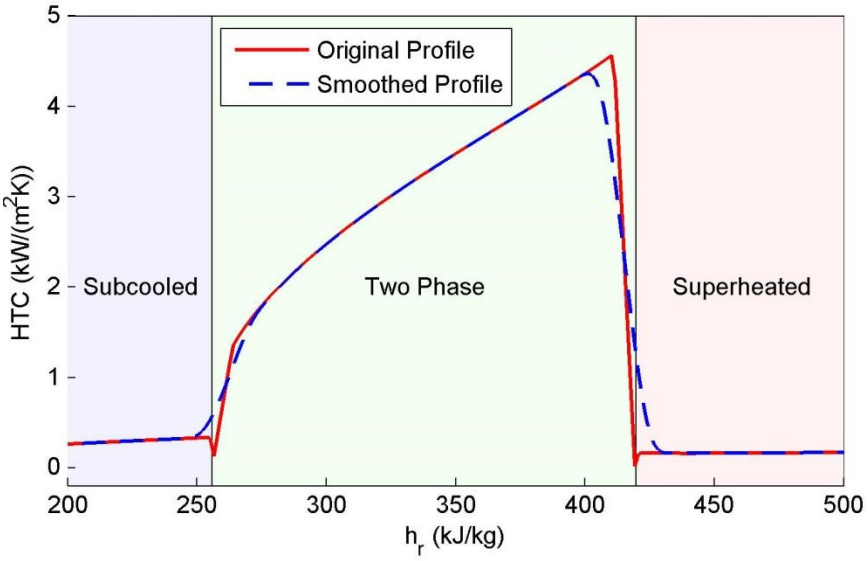

Figure 2.8 Condenser Heat Transfer Coefficient Profile ($P = 1000kPa$, $\dot{m} = 0.0062kg/s$)

2.2.4 Differential Equation Solvers

The models presented here are simulated using the MATLAB/Simulink® 'ode23tb' solver in Chapter 4. This solver is variable step, dynamically changing the step size of the simulation to maintain error within a specified tolerance. This solver is also suited for "stiff" systems in which the dynamics evolve on a wide range of timescales. One measure of stiffness is the stiffness ratio, defined as:

$$S = \frac{\max\left|\text{Real}(\lambda_k)\right|}{\min\left|\text{Real}(\lambda_k)\right|} \tag{2.50}$$

where (λ_k) is the set of eigenvalues for the system of differential equation. Even when a stiff solver is used, the step size allowable to ensure a given tolerance decreases as the stiffness increases. Therefore, it is desirable to reduce the stiffness ratio of a model in order to achieve faster simulation. This can be accomplished by increasing the time constants of the fastest dynamics of the system, which for the FV model are associated with the refrigerant mass flow

rates. These time constants can be increased by implementing a low pass filter on the refrigerant mass flow rate of each volume of the form:

$$\dot{m}_{r,i}^{filt}(s) = \frac{1}{Ks+1}\dot{m}_{r,i}(s) \tag{2.51}$$

where K is a positive constant. Incorporating Eq. (2.51) can reduce the heat exchanger stiffness ratio by orders of magnitude, improving not only the speed of the model, but also its robustness with respect to the ability of any given solver to solve the model under constraints of time step size and allowable error tolerance.

2.3 Other System Components

To complete the basic 4-component VCS simulation, models for a compressor and an expansion device are required. The models are provided inputs of the pressure calculated by the upstream and downstream heat exchangers, the inlet enthalpy from the upstream heat exchanger, and an actuator command. For the compressor, this command is a rotational speed. For the valve, which is an electronic expansion valve (EEV) in this work, the actuator command is the percent opening of the valve orifice. The compressor and valve models calculate the outlet enthalpy and refrigerant mass flow rate using both interpolation of empirically derived lookup tables and first principles equations.

2.3.1 Electronic Expansion Valve

The nonlinear EEV model follows directly from [19]. The EEV takes four inputs: valve opening input, inlet pressure, outlet pressure, and inlet enthalpy. The input vector is expressed as:

$$u_{EEV} = \begin{pmatrix} o_{EEV} & P_{in} & P_{out} & h_{in} \end{pmatrix}^T . \tag{2.52}$$

Using static relationships only, the EEV model calculates the refrigerant mass flow rate. The component is assumed to be isenthalpic, so the outlet enthalpy equals the inlet enthalpy. The output vector is expressed as:

$$y_{EEV} = \begin{pmatrix} \dot{m}_{EEV} & h_{out} \end{pmatrix}^T . \tag{2.53}$$

The nonlinear input-output relationship is:

$$\begin{pmatrix} \dot{m}_{EEV} \\ h_{out} \end{pmatrix} = \begin{pmatrix} C_d \sqrt{\rho_{in}(P_{in} - P_{out})} \\ h_{in} \end{pmatrix} \tag{2.54}$$

where C_d is the discharge coefficient, calculated from a semi-empirical map as a function of the valve opening input and pressure differential:

$$C_d = f(o_{EEV}, P_{in} - P_{out}) \ . \tag{2.55}$$

2.3.2 Compressor

The nonlinear compressor model follows directly from [20]. The compressor takes four inputs: compressor rotational speed, inlet pressure, outlet pressure, and inlet enthalpy. The input vector is expressed as:

$$u_{comp} = \begin{pmatrix} v_{comp} & P_{in} & P_{out} & h_{in} \end{pmatrix}^T \ . \tag{2.56}$$

Using static relationships only, the compressor model calculates the refrigerant mass flow rate. The outlet enthalpy is calculated first as a static relationship, and then passed through a first order filter to account for the heat capacitance of the compressor shell. The output vector is expressed as:

$$y_{comp} = \begin{pmatrix} \dot{m}_{comp} & h_{out} \end{pmatrix}^T \ . \tag{2.57}$$

The static nonlinear input-output relationship is:

$$\begin{pmatrix} \dot{m}_{comp} \\ h_{out,sattic} \end{pmatrix} = \begin{pmatrix} v_{comp} V_{comp} \rho_{in} \eta_{vol} \\ h_{in} + \frac{1}{\eta_{isen}} (h_{out,isen} - h_{in}) \end{pmatrix} \tag{2.58}$$

where η_{vol} and η_{isen} are the volumetric and isentropic efficiencies of the compressor, respectively, calculated from a semi-empirical map as functions of the compressor speed and pressure ratio:

$$\begin{aligned} \eta_{vol} &= f(v_{comp}, \frac{P_{out}}{P_{in}}) \\ \eta_{isen} &= f(v_{comp}, \frac{P_{out}}{P_{in}}) \end{aligned} \tag{2.59}$$

and $h_{out,isen}$ is the isentropic outlet enthalpy, calculated as:

$$h_{out,isen} = f(P_{out}, s_{in}) \ . \tag{2.60}$$

The dynamic outlet enthalpy is then given by:

$$\dot{h}_{out} = \frac{1}{\tau}(h_{out,static} - h_{out}) \tag{2.61}$$

where τ is the time constant of the first order filter.

Chapter 3

Linear Model Formulations

The nonlinear nature of the models presented in Chapter 2 limit the extent to which they can be implemented in model-based control design. Instead, these models are more suited for use in simulation as a plant on which candidate control approaches can be evaluated prior to experimental testing. In developing such control approaches it is desirable to have linearized models, allowing designers to make use of the well-established theoretical results on linear model-based control. This chapter develops such models. Sections 3.1 and 3.2 derive linear evaporator and condenser models, respectively, via linearization of the SMB heat exchanger formulations of Section 2.2.2. Sections 3.3 and 3.4 derive linear EEV and compressor models, respectively, via linearization of the nonlinear components of Section 2.3. Section 3.5 shows how these individual linear component models can be combined to form a single linear model representing a four-component VCS.

3.1 Evaporator

As in [19] and [26], Eq. (2.26) is linearized about an arbitrary set of nominal steady-state operating conditions for each mode, defined as $x_{e,o}$, $u_{e,o}$, and $y_{e,o}$, giving:

$$\begin{aligned} Z_1(x_{e,o}, u_{e,o})\dot{x}_e &\approx A\Delta x_e + B\Delta u_e \\ y_e &\approx C\Delta x_e + \mathrm{D}\,\Delta u_e + y_{e,o} \end{aligned} \tag{3.1}$$

where $\Delta x_e = x_e - x_{e,o}$, $\Delta u_e = u_e - u_{e,o}$, and

$$
\begin{aligned}
A &= \frac{\partial Z_2(x,u)}{\partial x}\Big|_{x_o,u_o} \\
B &= \frac{\partial Z_2(x,u)}{\partial u}\Big|_{x_o,u_o} \\
C &= \frac{\partial Z_3(x,u)}{\partial x}\Big|_{x_o,u_o} \\
D &= \frac{\partial Z_3(x,u)}{\partial u}\Big|_{x_o,u_o}
\end{aligned}
\tag{3.2}
$$

We note that $\dot{x}_{e,o} = 0$ because the nominal operating condition is at steady-state. We also mention that while most entries of the linearized matrices are found purely mathematically, some are modified based on intuition or trial and error to improve accuracy in relation to the nonlinear model or to remove negligible terms.

3.1.1 Mode 1: Two-Phase and Superheated Zones

For Mode 1 of the evaporator, *A*, *B*, *C*, and *D* are given by:

$$
A = \begin{pmatrix}
0 & 0 & 0 & 0 & 0 & 0 \\
\frac{\partial (Z_2)_2}{\partial \zeta_1} & \frac{\partial (Z_2)_2}{\partial P} & \frac{\partial (Z_2)_2}{\partial h_2} & 0 & \frac{\partial (Z_2)_2}{\partial T_{w_3}} & 0 \\
\frac{\partial (Z_2)_3}{\partial \zeta_1} & \frac{\partial (Z_2)_3}{\partial P} & 0 & \frac{\partial (Z_2)_3}{\partial T_{w_1}} & 0 & 0 \\
\frac{\partial (Z_2)_4}{\partial \zeta_1} & \frac{\partial (Z_2)_4}{\partial P} & 0 & \frac{\partial (Z_2)_4}{\partial T_{w_1}} & 0 & 0 \\
\frac{\partial (Z_2)_5}{\partial \zeta_1} & \frac{\partial (Z_2)_5}{\partial P} & \frac{\partial (Z_2)_5}{\partial h_2} & 0 & \frac{\partial (Z_2)_5}{\partial T_{w_3}} & 0 \\
0 & \frac{\partial (Z_2)_6}{\partial P} & 0 & 0 & 0 & \frac{\partial (Z_2)_6}{\partial \bar{\gamma}}
\end{pmatrix}\Bigg|_{x_o,u_o}
\tag{3.3}
$$

$$B=\begin{pmatrix} \frac{\partial(Z_2)_1}{\partial \dot{m}_{r,in}} & \frac{\partial(Z_2)_1}{\partial \dot{m}_{r,out}} & 0 & 0 & 0 \\ 0 & \frac{\partial(Z_2)_2}{\partial \dot{m}_{r,out}} & 0 & 0 & 0 \\ \frac{\partial(Z_2)_3}{\partial \dot{m}_{r,in}} & \frac{\partial(Z_2)_3}{\partial \dot{m}_{r,out}} & \frac{\partial(Z_2)_3}{\partial h_{r,in}} & 0 & 0 \\ 0 & 0 & 0 & \frac{\partial(Z_2)_4}{\partial T_{a,in}} & \frac{\partial(Z_2)_4}{\partial \dot{m}_{a,in}} \\ 0 & 0 & 0 & \frac{\partial(Z_2)_5}{\partial T_{a,in}} & \frac{\partial(Z_2)_5}{\partial \dot{m}_{a,in}} \\ 0 & 0 & \frac{\partial(Z_2)_6}{\partial h_{r,in}} & 0 & 0 \end{pmatrix}\Bigg|_{x_o,u_o} \tag{3.4}$$

$$C=\begin{pmatrix} 0 & \frac{\partial(Z_3)_1}{\partial P} & 0 & 0 & 0 & 0 \\ 0 & \frac{\partial(Z_3)_2}{\partial P} & \frac{\partial(Z_3)_2}{\partial h_2} & 0 & 0 & 0 \\ 0 & \frac{\partial(Z_3)_3}{\partial P} & \frac{\partial(Z_3)_3}{\partial h_2} & 0 & 0 & 0 \\ 0 & \frac{\partial(Z_3)_4}{\partial P} & \frac{\partial(Z_3)_4}{\partial P} & 0 & 0 & 0 \\ \frac{\partial(Z_3)_5}{\partial \zeta_1} & 0 & 0 & 0 & \frac{\partial(Z_3)_5}{\partial T_{w_2}} & \frac{\partial(Z_3)_5}{\partial \bar{\gamma}} \\ \frac{\partial(Z_3)_6}{\partial \zeta_1} & 0 & 0 & 0 & \frac{\partial(Z_3)_6}{\partial T_{w_2}} & \frac{\partial(Z_3)_6}{\partial \bar{\gamma}} \end{pmatrix}\Bigg|_{x_o,u_o} \tag{3.5}$$

$$D=\begin{pmatrix} 0 & 0 & 0 & 0 & 0 \\ 0 & 0 & 0 & 0 & 0 \\ 0 & 0 & 0 & 0 & 0 \\ 0 & 0 & 0 & 0 & 0 \\ 0 & 0 & 0 & \frac{\partial(Z_3)_5}{\partial T_{a,in}} & \frac{\partial(Z_3)_5}{\partial \dot{m}_{a,in}} \\ 0 & 0 & 0 & \frac{\partial(Z_3)_6}{\partial T_{a,in}} & \frac{\partial(Z_3)_6}{\partial \dot{m}_{a,in}} \end{pmatrix}\Bigg|_{x_o,u_o} . \tag{3.6}$$

Table 3.1: Mode 1 Matrix Elements of *A*

$\frac{\partial(Z_2)_2}{\partial\zeta_1}$	$-A_s\alpha_{r,2}(T_{w,2}-T_{r,2})$
$\frac{\partial(Z_2)_2}{\partial P}$	$2\dot{m}_{r,out}\frac{\partial h_{r,v}}{\partial P}-A_s\zeta_2\alpha_{r,2}\frac{\partial T_{r,2}}{\partial P}$
$\frac{\partial(Z_2)_2}{\partial h_{r,2}}$	$-2\dot{m}_{r,out}-A_s\zeta_2\alpha_{r,2}\frac{\partial T_{r,2}}{\partial h_{r,2}}$
$\frac{\partial(Z_2)_2}{\partial T_{w_3}}$	$A_s\zeta_2\alpha_{r,2}$
$\frac{\partial(Z_2)_3}{\partial\zeta_1}$	$A_s\alpha_{r,1}(T_{w,1}-T_{r,1})$
$\frac{\partial(Z_2)_3}{\partial P}$	$-\dot{m}_{r,out}\frac{\partial h_{r,v}}{\partial P}-A_s\zeta_1\alpha_{r,1}\frac{\partial T_{r,1}}{\partial P}$
$\frac{\partial(Z_2)_3}{\partial T_{w_1}}$	$A_s\zeta_1\alpha_{r,1}$
$\frac{\partial(Z_2)_4}{\partial\zeta_1}$	$A_s\alpha_{r,1}(T_{r,1}-T_{w,1})+\dot{m}_{a,in}c_{p,a}\left\{T_{a,i}-\left[T_{w,1}+(T_{a,i}-T_{w,1})e^{-NTU}\right]\right\}$
$\frac{\partial(Z_2)_4}{\partial P}$	$A_s\zeta_1\alpha_{r,1}\frac{\partial T_{r,1}}{\partial P}$
$\frac{\partial(Z_2)_4}{\partial T_{w_1}}$	$-A_s\zeta_1\alpha_{r,1}-\zeta_1\dot{m}_{a,in}c_{p,a}(1-e^{-NTU})$
$\frac{\partial(Z_2)_5}{\partial\zeta_1}$	$-A_s\alpha_{r,2}(T_{r,2}-T_{w,2})-\dot{m}_{a,in}c_{p,a}\left\{T_{a,in}-\left[T_{w,2}+(T_{a,in}-T_{w,2})e^{-NTU}\right]\right\}$
$\frac{\partial(Z_2)_5}{\partial P}$	$A_s\zeta_2\alpha_{r,2}\frac{\partial T_{r,2}}{\partial P}$
$\frac{\partial(Z_2)_5}{\partial h_{r,2}}$	$A_s\zeta_2\alpha_{r,2}\frac{\partial T_{r,2}}{\partial h_{r,2}}$

Table 3.1 (cont.)

$\frac{\partial(Z_2)_5}{\partial T_{w_3}}$	$-A_s\zeta_2\alpha_{r,2}-\zeta_2\dot{m}_{a,in}c_{p,a}(1-e^{-NTU})$
$\frac{\partial(Z_2)_6}{\partial P}$	$-K\frac{\partial\bar{\gamma}_{full}}{\partial P}$
$\frac{\partial(Z_2)_6}{\partial\bar{\gamma}}$	K

Table 3.2: Mode 1 Matrix Elements of *B*

$\frac{\partial(Z_2)_1}{\partial\dot{m}_{r,in}}$	1
$\frac{\partial(Z_2)_1}{\partial\dot{m}_{r,out}}$	-1
$\frac{\partial(Z_2)_2}{\partial\dot{m}_{r,out}}$	$2(h_{r,v}-h_{r,2})$
$\frac{\partial(Z_2)_3}{\partial\dot{m}_{r,in}}$	$h_{r,in}$
$\frac{\partial(Z_2)_3}{\partial\dot{m}_{r,out}}$	$-h_{r,v}$
$\frac{\partial(Z_2)_3}{\partial h_{r,in}}$	$\dot{m}_{r,in}$
$\frac{\partial(Z_2)_4}{\partial T_{a,in}}$	$\zeta_1\dot{m}_{a,in}c_{p,a}\left(1-e^{-NTU}\right)$
$\frac{\partial(Z_2)_4}{\partial\dot{m}_{a,in}}$	$\zeta_1 c_{p,a}\left\{T_{a,in}-\left[T_{w,1}+(T_{a,in}-T_{w,1})e^{-NTU}\right]\right\}$ $+\dot{m}_{a,in}\zeta_1 c_{p,a}(T_{a,in}-T_{w,1})e^{-NTU}NTU\left(\frac{1}{\alpha_a}\frac{\partial\alpha_a}{\partial\dot{m}_{a,in}}-\frac{1}{\dot{m}_{a,in}}\right)$
$\frac{\partial(Z_2)_5}{\partial T_{a,in}}$	$\zeta_2\dot{m}_{a,i}c_{p,a}\left(1-e^{-NTU}\right)$

Table 3.2 (cont.)

$\frac{\partial(Z_2)_5}{\partial \dot{m}_{a,in}}$	$\zeta_2 c_{p,a}\left\{T_{a,in}-\left[\mathrm{T}_{w,2}+(T_{a,in}-T_{w,2})e^{-NTU}\right]\right\}$ $+\dot{m}_{a,in}\zeta_2 c_{p,a}(T_{a,in}-T_{w,1})e^{-NTU}NTU\left(\frac{1}{\alpha_a}\frac{\partial \alpha_a}{\partial \dot{m}_{a,in}}-\frac{1}{\dot{m}_{a,in}}\right)$
$\frac{\partial(Z_2)_6}{\partial h_{r,in}}$	$-K\frac{\partial \overline{\gamma}_{full}}{\partial h_{r,in}}$

Table 3.3: Mode 1 Matrix Elements of *C*

$\frac{\partial(Z_3)_1}{\partial P}$	1
$\frac{\partial(Z_3)_2}{\partial P}$	$-\frac{\partial h_{r,g}}{\partial P}$
$\frac{\partial(Z_3)_2}{\partial h_{r,2}}$	2
$\frac{\partial(Z_3)_3}{\partial P}$	$2\frac{dT_{r,2}}{dP}-\frac{dT_{r,1}}{dP}$
$\frac{\partial(Z_3)_3}{\partial h_{r,2}}$	$2\frac{dT_{r,2}}{dh_{r,2}}$
$\frac{\partial(Z_3)_4}{\partial P}$	$2\frac{dT_{r,2}}{dP}-2\frac{dT_{r,1}}{dP}$
$\frac{\partial(Z_3)_4}{\partial P}$	$2\frac{dT_{r,2}}{dh_{r,2}}$
$\frac{\partial(Z_3)_5}{\partial \zeta_1}$	$\left(T_{w,1}+(T_{a,in}-T_{w,1})e^{-NTU}\right)-\left(T_{w,1}+(T_{a,in}-T_{w,1})e^{-NTU}\right)$
$\frac{\partial(Z_3)_5}{\partial T_{w_2}}$	$\zeta_1(1-e^{-NTU})$
$\frac{\partial(Z_3)_5}{\partial \overline{\gamma}}$	$\zeta_2(1-e^{-NTU})$

Table 3.3 (cont.)

$\frac{\partial(Z_3)_6}{\partial\zeta_1}$	$\dot{m}_{a,in}c_{p,a}\frac{\partial(Z_3)_5}{\partial\zeta_1}$
$\frac{\partial(Z_3)_6}{\partial T_{w_2}}$	$\dot{m}_{a,in}c_{p,a}\frac{\partial(Z_3)_5}{\partial T_{w_2}}$
$\frac{\partial(Z_3)_6}{\partial\bar{\gamma}}$	$\dot{m}_{a,in}c_{p,a}\frac{\partial(Z_3)_5}{\partial\bar{\gamma}}$

Table 3.4: Mode 1 Matrix Elements of *D*

$\frac{\partial(Z_3)_5}{\partial T_{a,in}}$	$\zeta_1 e^{-NTU}+\zeta_2 e^{-NTU}$
$\frac{\partial(Z_3)_5}{\partial\dot{m}_{a,in}}$	$-\left[\zeta_1(T_{a,in}-T_{w,1})+\zeta_2(T_{a,in}-T_{w,2})\right]e^{-NTU}NTU\left(\frac{1}{\alpha_a}\frac{\partial\alpha_a}{\partial\dot{m}_{a,in}}-\frac{1}{\dot{m}_{a,in}}\right)$
$\frac{\partial(Z_3)_6}{\partial T_{a,in}}$	$\dot{m}_{a,in}c_{p,a}\left(\frac{\partial(Z_3)_5}{\partial T_{a,in}}-1\right)$
$\frac{\partial(Z_3)_6}{\partial\dot{m}_{a,in}}$	$c_{p,a}\left(\zeta_1\left(T_{w,1}+(T_{a,in}-T_{w,1})e^{-NTU}\right)+\zeta_2\left(T_{w,2}+(T_{a,in}-T_{w,2})e^{-NTU}\right)-T_{a,in}+\dot{m}_{a,in}\frac{\partial(Z_3)_5}{\partial\dot{m}_{a,in}}\right)$

3.1.2 Mode 2: Two-Phase Zone Only

For Mode 2 with the state vector of Eq. (2.33), *A*, *B*, *C*, and *D* are given by:

$$A=\left.\begin{pmatrix} & & \\ 0 & 0 & 0 \\ \frac{\partial(Z_2)_2}{\partial P} & \frac{\partial(Z_2)_2}{\partial T_{w,1}} & \frac{\partial(Z_2)_2}{\partial\bar{\gamma}} \\ \frac{\partial(Z_2)_3}{\partial P} & \frac{\partial(Z_2)_3}{\partial T_{w,1}} & 0 \end{pmatrix}\right|_{x_o,u_o} \tag{3.7}$$

$$B = \left(\begin{array}{ccccc} \frac{\partial (Z_2)_1}{\partial \dot{m}_{r,in}} & \frac{\partial (Z_2)_1}{\partial \dot{m}_{r,out}} & 0 & 0 & 0 \\ \frac{\partial (Z_2)_2}{\partial \dot{m}_{r,in}} & \frac{\partial (Z_2)_2}{\partial \dot{m}_{r,out}} & \frac{\partial (Z_2)_2}{\partial h_{r,in}} & 0 & 0 \\ 0 & 0 & 0 & \frac{\partial (Z_2)_3}{\partial T_{a,in}} & \frac{\partial (Z_2)_3}{\partial \dot{m}_{a,in}} \end{array} \right) \Bigg|_{x_o, u_o} \tag{3.8}$$

$$C = \left(\begin{array}{ccc} \frac{\partial (Z_3)_1}{\partial P} & 0 & 0 \\ \frac{\partial (Z_3)_2}{\partial P} & 0 & \frac{\partial (Z_3)_2}{\partial \overline{\gamma}} \\ \frac{\partial (Z_3)_3}{\partial P} & 0 & 0 \\ 0 & 0 & 0 \\ 0 & \frac{\partial (Z_3)_5}{\partial T_{w,1}} & 0 \\ 0 & \frac{\partial (Z_3)_6}{\partial T_{w,1}} & 0 \end{array} \right) \Bigg|_{x_o, u_o} \tag{3.9}$$

$$D = \left(\begin{array}{ccccc} 0 & 0 & 0 & 0 & 0 \\ 0 & 0 & \frac{\partial (Z_3)_2}{\partial h_{r,in}} & 0 & 0 \\ 0 & 0 & 0 & 0 & 0 \\ 0 & 0 & 0 & 0 & 0 \\ 0 & 0 & 0 & \frac{\partial (Z_3)_5}{\partial T_{a,in}} & \frac{\partial (Z_3)_5}{\partial \dot{m}_{a,in}} \\ 0 & 0 & 0 & \frac{\partial (Z_3)_6}{\partial T_{a,in}} & \frac{\partial (Z_3)_6}{\partial \dot{m}_{a,in}} \end{array} \right) \Bigg|_{x_o, u_o} \tag{3.10}$$

Table 3.5: Mode 2 Matrix Elements of *A*

$\frac{\partial(Z_2)_2}{\partial P}$	$-\dot{m}_{r,out}\frac{\partial h_{r,out}}{\partial P}-A_s\zeta_1\alpha_{r,1}\frac{\partial T_{r,1}}{\partial P}$
$\frac{\partial(Z_2)_2}{\partial T_{w,1}}$	$A_s\zeta_1\alpha_{r,1}$
$\frac{\partial(Z_2)_2}{\partial \bar{\gamma}}$	$-\dot{m}_{r,out}\frac{\partial h_{r,out}}{\partial \bar{\gamma}}$
$\frac{\partial(Z_2)_3}{\partial P}$	$A_s\alpha_{r,1}\frac{\partial T_{r,1}}{\partial P}$
$\frac{\partial(Z_2)_3}{\partial T_{w,1}}$	$-A_s\alpha_{r,1}-\dot{m}_{a,in}c_{p,a}(1-e^{-NTU})$

Table 3.6: Mode 2 Matrix Elements of *B*

$\frac{\partial(Z_2)_1}{\partial \dot{m}_{r,in}}$	1
$\frac{\partial(Z_2)_1}{\partial \dot{m}_{r,out}}$	-1
$\frac{\partial(Z_2)_2}{\partial \dot{m}_{r,in}}$	$h_{r,in}$
$\frac{\partial(Z_2)_2}{\partial \dot{m}_{r,out}}$	$-h_{r,out}$
$\frac{\partial(Z_2)_2}{\partial h_{r,in}}$	$\dot{m}_{r,in}-\dot{m}_{r,out}\frac{\partial h_{r,out}}{\partial h_{r,in}}$
$\frac{\partial(Z_2)_3}{\partial T_{a,in}}$	$\dot{m}_{a,in}c_{p,a}(1-e^{-NTU})$
$\frac{\partial(Z_2)_3}{\partial \dot{m}_{a,in}}$	$c_{p,a}\left\{T_{a,in}-\left[T_{w,1}+(T_{a,in}-T_{w,1})e^{-NTU}\right]\right\}$ $+\dot{m}_{a,in}c_{p,a}(T_{a,in}-T_{w,1})e^{-NTU}NTU\left(\frac{1}{\alpha_a}\frac{\partial \alpha_a}{\partial \dot{m}_{a,in}}-\frac{1}{\dot{m}_{a,in}}\right)$

Table 3.7: Mode 2 Matrix Elements of *C*

$\frac{\partial(Z_3)_1}{\partial P}$	1
$\frac{\partial(Z_3)_2}{\partial P}$	$\frac{\partial q_{out}}{\partial P}(h_{r,g}-h_{r,f})+q_{out}\left(\frac{\partial h_{r,g}}{\partial P}-\frac{\partial h_{r,f}}{\partial P}\right)+\frac{\partial h_{r,f}}{\partial P}$
$\frac{\partial(Z_3)_2}{\partial \bar{\gamma}}$	$\frac{\partial q_{out}}{\partial \bar{\gamma}}(h_{r,g}-h_{r,f})$
$\frac{\partial(Z_3)_3}{\partial P}$	$\frac{\partial T_{r,1}}{\partial P}$
$\frac{\partial(Z_3)_5}{\partial T_{w,1}}$	$1-e^{-NTU}$
$\frac{\partial(Z_3)_6}{\partial T_{w,1}}$	$\dot{m}_{a,in}c_{p,a}\frac{\partial(Z_3)_5}{\partial T_{w,1}}$

Table 3.8: Mode 2 Matrix Elements of *D*

$\frac{\partial(Z_3)_2}{\partial h_{r,in}}$	$\frac{\partial x_{out}}{\partial h_{r,in}}(h_{r,g}-h_{r,f})$
$\frac{\partial(Z_3)_5}{\partial T_{a,in}}$	e^{-NTU}
$\frac{\partial(Z_3)_5}{\partial \dot{m}_{a,in}}$	$-(T_{a,in}-T_{w,1})e^{-NTU}NTU\left(\frac{1}{\alpha_a}\frac{\partial \alpha_a}{\partial \dot{m}_{a,in}}-\frac{1}{\dot{m}_{a,in}}\right)$
$\frac{\partial(Z_3)_6}{\partial T_{a,in}}$	$\dot{m}_{a,in}c_{p,a}\left(\frac{\partial(Z_3)_5}{\partial T_{a,in}}-1\right)$
$\frac{\partial(Z_3)_6}{\partial \dot{m}_{a,in}}$	$c_{p,a}\left(T_{w,1}+(T_{a,in}-T_{w,1})e^{-NTU}-T_{a,in}+\dot{m}_{a,in}\frac{\partial(Z_3)_5}{\partial \dot{m}_{a,in}}\right)$

To incorporate the pseudo-state equations, the system is augmented as follows:

$$\dot{x}_e \approx \begin{pmatrix} Z_1^{-1}A & 0_{3x3} \\ W & \end{pmatrix} \Delta x_e + \begin{pmatrix} Z_1^{-1}B \\ 0_{3x5} \end{pmatrix} \Delta u_e$$
$$y_e \approx \begin{pmatrix} C & 0_{6x3} \end{pmatrix} \Delta x_e + \mathrm{D}\,\Delta u_e + y_{e,o} \tag{3.11}$$

where

$$W = \begin{pmatrix} 0 & 0 & 0 & -K & 0 & 0 \\ K\dfrac{\partial h_{r,g}}{\partial P} & 0 & 0 & 0 & -K & 0 \\ 0 & K & 0 & 0 & 0 & -K \end{pmatrix}. \tag{3.12}$$

This gives the augmented state vector:

$$x_e = \begin{pmatrix} P & T_{w,1} & \bar{\gamma} & \zeta_1 & h_{r,2} & T_{w,2} \end{pmatrix}^T. \tag{3.13}$$

The ordering of these states can easily be changed to recover the full state vector of Eq. (2.28).

3.1.3 Nonlinear and Linear Model Comparison

Figure 3.1 shows the output response of the nonlinear SMB and linear 2-zone evaporator models to a step in each input. The states of each model are plotted in Figure 3.2. For this simulation, the linear model was linearized about the nominal steady-state operating conditions of the nonlinear model, which are reached before and after each input step.

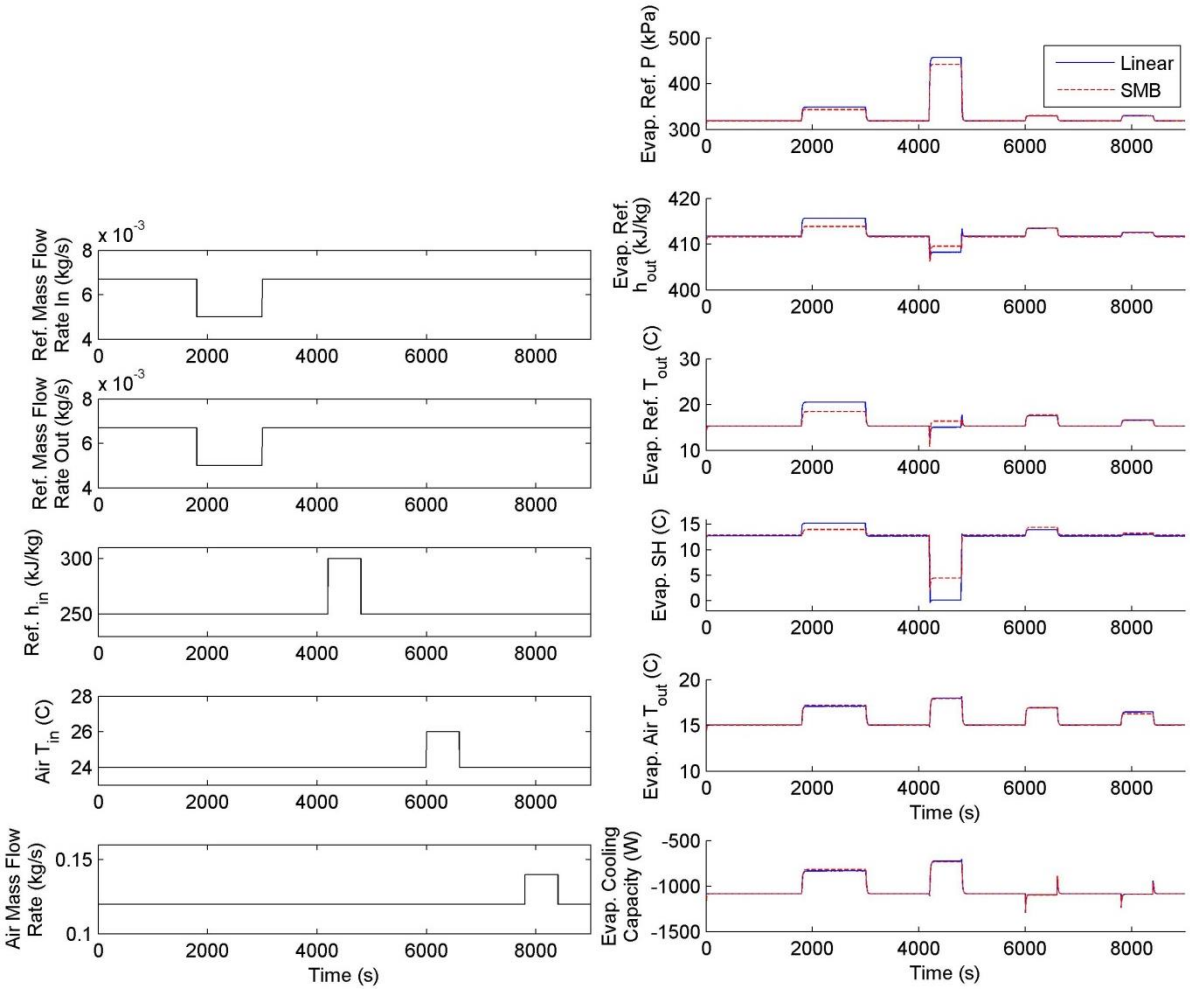

Figure 3.1 Nonlinear and Linear 2-Zone Evaporator Comparison—Inputs (left) and Outputs (right)

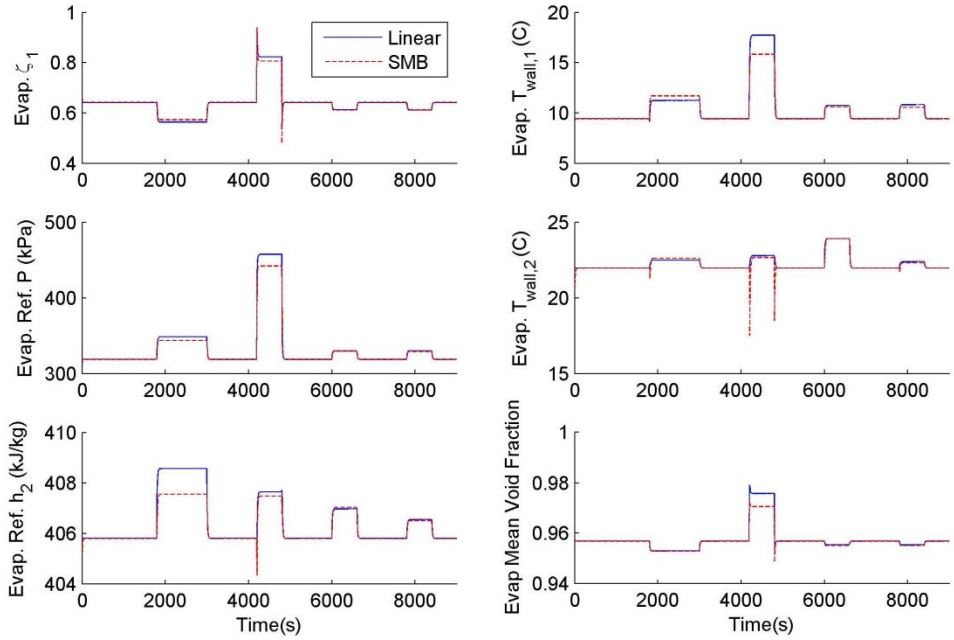

Figure 3.2 Nonlinear and Linear 2-Zone Evaporator Comparison—States

Figure 3.3 shows the output response of the nonlinear SMB and linear 1-zone evaporator models to a step in each input. The changing inputs at the start of the simulation are used to trigger a switch of the nonlinear model into the correct mode. The nonlinear model remains in this mode for the remainder for the simulation. Note that the output of evaporator superheat is not shown in Figure 3.3. Because the refrigerant is two-phase at the evaporator outlet in this mode, the superheat is zero at all times. The states of each model are plotted in Figure 3.4, and the pseudo-states are plotted in Figure 3.5. For this simulation, the linear model was again linearized about the nominal steady-state operating conditions of the nonlinear model, which are reached before and after each input step.

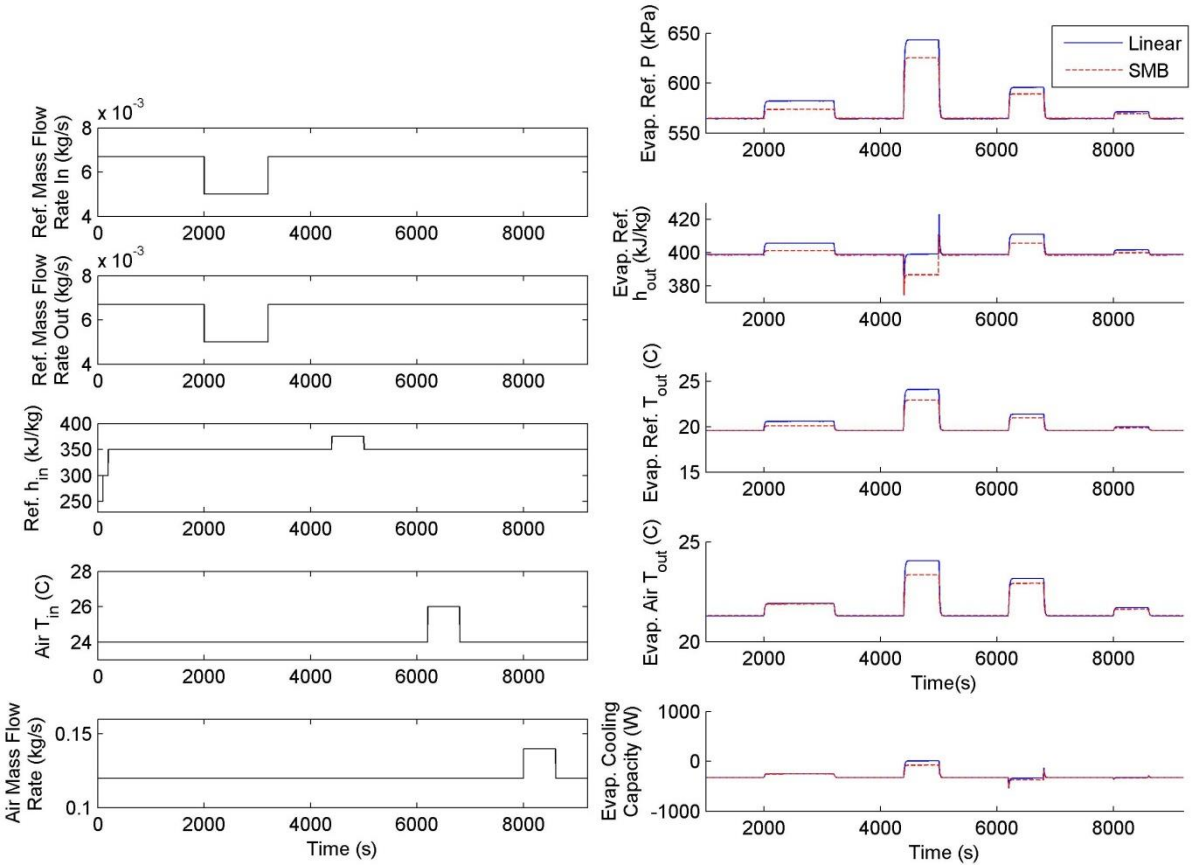

Figure 3.3 Nonlinear and Nonlinear 1-Zone Evaporator Comparison—Inputs (left) and Outputs (right)

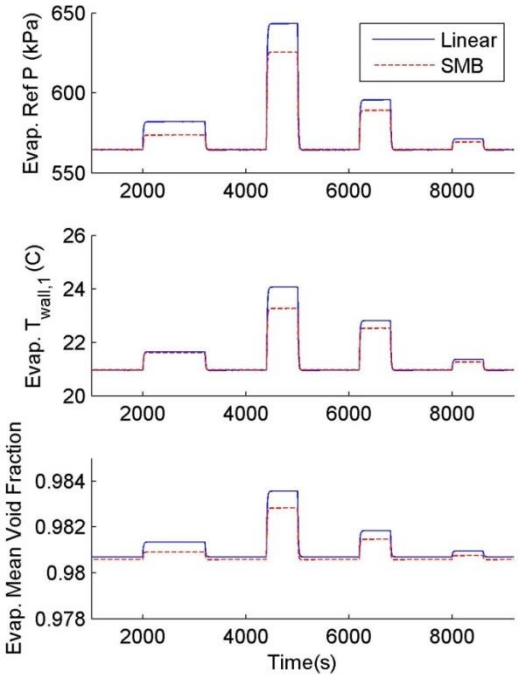

Figure 3.4 Nonlinear and Nonlinear 1-Zone Evaporator Comparison—States

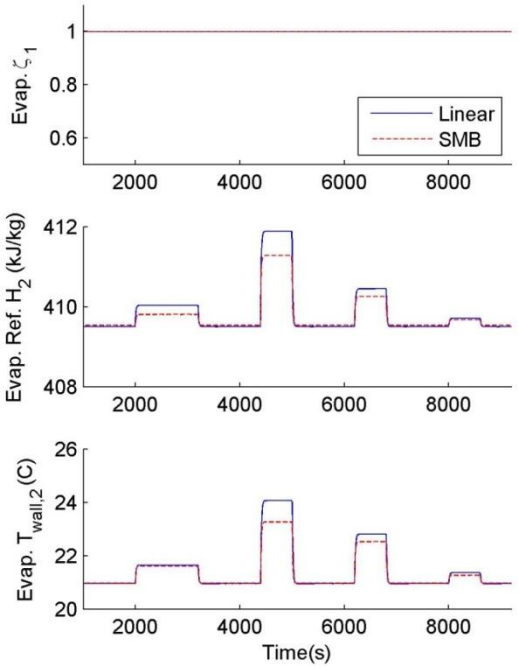

Figure 3.5 Nonlinear and Nonlinear 1-Zone Evaporator Comparison—Pseudo-States

Although not all gains are matched perfectly, it is clear that both the 2-zone and 1-zone linear evaporator models match their nonlinear equivalents closely.

3.2 Condenser

As in [19] and [26], Eq. (2.38) is linearized about an arbitrary set of nominal steady-state operating conditions for each mode, defined as $x_{c,o}$, $u_{c,o}$, and $y_{c,o}$, giving:

$$\begin{aligned} Z_1(x_{c,o}, u_{c,o})\dot{x}_c &\approx A\Delta x_c + B\Delta u_c \\ y_c &\approx C\Delta x_c + D\Delta u_c + y_{c,o} \end{aligned} \tag{3.14}$$

where $\Delta x_c = x_c - x_{c,o}$, $\Delta u_c = u_c - u_{c,o}$, and

$$\begin{aligned} A &= \frac{\partial Z_2(x,u)}{\partial x}\Big|_{x_o,u_o} \\ B &= \frac{\partial Z_2(x,u)}{\partial u}\Big|_{x_o,u_o} \\ C &= \frac{\partial Z_3(x,u)}{\partial x}\Big|_{x_o,u_o} \\ D &= \frac{\partial Z_3(x,u)}{\partial u}\Big|_{x_o,u_o} \end{aligned} \tag{3.15}$$

We note that $\dot{x}_{c,o} = 0$ because the nominal operating condition is at steady-state. We also mention that while most entries of the linearized matrices are found purely mathematically, some are modified based on intuition or trial and error to improve accuracy in relation to the nonlinear model or remove negligible terms.

3.2.1 Mode 1: Superheated, Two-Phase, and Subcooled Zones

For Mode 1 of the condenser, *A*, *B*, *C*, and *D* are given by:

$$A=\begin{pmatrix}
\frac{\partial(Z_2)_1}{\partial\zeta_1} & 0 & \frac{\partial(Z_2)_1}{\partial P} & \frac{\partial(Z_2)_1}{\partial h_{r,1}} & 0 & 0 & \frac{\partial(Z_2)_1}{\partial T_{w,1}} & 0 & 0 \\
0 & 0 & 0 & 0 & 0 & 0 & 0 & 0 & 0 \\
0 & \frac{\partial(Z_2)_3}{\partial\zeta_2} & \frac{\partial(Z_2)_3}{\partial P} & 0 & 0 & 0 & 0 & \frac{\partial(Z_2)_3}{\partial T_{w,2}} & 0 \\
\frac{\partial(Z_2)_4}{\partial\zeta_1} & \frac{\partial(Z_2)_4}{\partial\zeta_2} & \frac{\partial(Z_2)_4}{\partial P} & 0 & \frac{\partial(Z_2)_4}{\partial h_{r,3}} & 0 & 0 & 0 & \frac{\partial(Z_2)_4}{\partial T_{w,3}} \\
0 & 0 & \frac{\partial(Z_2)_5}{\partial P} & \frac{\partial(Z_2)_5}{\partial h_{r,1}} & 0 & 0 & 0 & 0 & 0 \\
0 & 0 & \frac{\partial(Z_2)_6}{\partial P} & 0 & 0 & \frac{\partial(Z_2)_6}{\partial\bar{\gamma}} & 0 & 0 & 0 \\
\frac{\partial(Z_2)_7}{\partial\zeta_1} & 0 & \frac{\partial(Z_2)_7}{\partial P} & \frac{\partial(Z_2)_7}{\partial h_{r,1}} & 0 & 0 & \frac{\partial(Z_2)_7}{\partial T_{w,1}} & 0 & 0 \\
0 & \frac{\partial(Z_2)_8}{\partial\zeta_2} & \frac{\partial(Z_2)_8}{\partial P} & 0 & 0 & 0 & 0 & \frac{\partial(Z_2)_8}{\partial T_{w,2}} & 0 \\
\frac{\partial(Z_2)_9}{\partial\zeta_1} & \frac{\partial(Z_2)_9}{\partial\zeta_2} & \frac{\partial(Z_2)_9}{\partial P} & 0 & \frac{\partial(Z_2)_9}{\partial h_{r,3}} & 0 & 0 & 0 & \frac{\partial(Z_2)_9}{\partial T_{w,3}}
\end{pmatrix}\Bigg|_{x_o,u_o}$$

(3.16)

$$B = \left(\begin{array}{ccccc} \frac{\partial (Z_2)_1}{\partial \dot{m}_{r,in}} & 0 & \frac{\partial (Z_2)_1}{\partial h_{r,in}} & 0 & 0 \\ \frac{\partial (Z_2)_2}{\partial \dot{m}_{r,in}} & \frac{\partial (Z_2)_2}{\partial \dot{m}_{r,out}} & 0 & 0 & 0 \\ \frac{\partial (Z_2)_3}{\partial \dot{m}_{r,in}} & \frac{\partial (Z_2)_3}{\partial \dot{m}_{r,out}} & 0 & 0 & 0 \\ 0 & \frac{\partial (Z_2)_4}{\partial \dot{m}_{r,out}} & 0 & 0 & 0 \\ 0 & 0 & \frac{\partial (Z_2)_5}{\partial h_{r,in}} & 0 & 0 \\ 0 & 0 & 0 & 0 & 0 \\ 0 & 0 & 0 & \frac{\partial (Z_2)_7}{\partial T_{a,in}} & \frac{\partial (Z_2)_7}{\partial \dot{m}_{a,in}} \\ 0 & 0 & 0 & \frac{\partial (Z_2)_8}{\partial T_{a,in}} & \frac{\partial (Z_2)_8}{\partial \dot{m}_{a,in}} \\ 0 & 0 & 0 & \frac{\partial (Z_2)_9}{\partial T_{a,in}} & \frac{\partial (Z_2)_9}{\partial \dot{m}_{a,in}} \end{array} \right) \Bigg|_{x_o, u_o} \tag{3.17}$$

$$C = \left(\begin{array}{ccccccccc} 0 & 0 & \frac{\partial (Z_3)_1}{\partial P} & 0 & 0 & 0 & 0 & 0 & 0 \\ 0 & 0 & 0 & 0 & \frac{\partial (Z_3)_2}{\partial h_{r,3}} & 0 & 0 & 0 & 0 \\ 0 & 0 & \frac{\partial (Z_3)_3}{\partial P} & 0 & \frac{\partial (Z_3)_3}{\partial h_{r,3}} & 0 & 0 & 0 & 0 \\ 0 & 0 & \frac{\partial (Z_3)_4}{\partial P} & 0 & \frac{\partial (Z_3)_4}{\partial h_{r,3}} & 0 & 0 & 0 & 0 \\ \frac{\partial (Z_3)_5}{\partial \zeta_1} & \frac{\partial (Z_3)_5}{\partial \zeta_2} & 0 & 0 & 0 & 0 & \frac{\partial (Z_3)_5}{\partial T_{w,1}} & \frac{\partial (Z_3)_5}{\partial T_{w,2}} & \frac{\partial (Z_3)_5}{\partial T_{w,3}} \\ \frac{\partial (Z_3)_6}{\partial \zeta_1} & \frac{\partial (Z_3)_6}{\partial \zeta_2} & 0 & 0 & 0 & 0 & \frac{\partial (Z_3)_6}{\partial T_{w,1}} & \frac{\partial (Z_3)_6}{\partial T_{w,2}} & \frac{\partial (Z_3)_6}{\partial T_{w,3}} \end{array} \right) \Bigg|_{x_o, u_o} \tag{3.18}$$

$$D = \begin{pmatrix} 0 & 0 & 0 & 0 & 0 \\ 0 & 0 & 0 & 0 & 0 \\ 0 & 0 & 0 & 0 & 0 \\ 0 & 0 & 0 & 0 & 0 \\ 0 & 0 & 0 & \frac{\partial (Z_3)_5}{\partial T_{a,in}} & \frac{\partial (Z_3)_5}{\partial \dot{m}_{a,in}} \\ 0 & 0 & 0 & \frac{\partial (Z_3)_6}{\partial T_{a,in}} & \frac{\partial (Z_3)_6}{\partial \dot{m}_{a,in}} \end{pmatrix} \Bigg|_{x_o, u_o} . \tag{3.19}$$

Table 3.9: Mode 1 Matrix Elements of *A*

$\frac{\partial (Z_2)_1}{\partial \zeta_1}$	$A_s \alpha_{r,1} (T_{w,1} - T_{r,1})$
$\frac{\partial (Z_2)_1}{\partial P}$	$\dot{m}_{r,in} \left(\frac{\partial h_{r,in}}{\partial P} - \frac{\partial h_{r,g}}{\partial P} \right) - A_s \zeta_1 \alpha_{r,1} \frac{\partial T_{r,1}}{\partial P}$
$\frac{\partial (Z_2)_1}{\partial h_{r,1}}$	$-A_s \zeta_1 \alpha_{r,1} \frac{\partial T_{r,1}}{\partial h_{r,1}}$
$\frac{\partial (Z_2)_1}{\partial T_{w,1}}$	$A_s \zeta_1 \alpha_{r,1}$
$\frac{\partial (Z_2)_3}{\partial \zeta_2}$	$A_s \alpha_{r,2} (T_{w,2} - T_{r,2})$
$\frac{\partial (Z_2)_3}{\partial P}$	$\dot{m}_{r,in} \frac{\partial h_{r,g}}{\partial P} - \dot{m}_{r,out} \frac{\partial h_{r,f}}{\partial P} - A_s \zeta_2 \alpha_{r,2} \frac{\partial T_{r,2}}{\partial P}$
$\frac{\partial (Z_2)_3}{\partial T_{w,2}}$	$A_s \zeta_2 \alpha_{r,2}$
$\frac{\partial (Z_2)_4}{\partial \zeta_1}$	$-A_s \alpha_{r,3} (T_{w,3} - T_{r,3})$
$\frac{\partial (Z_2)_4}{\partial \zeta_2}$	$-A_s \alpha_{r,3} (T_{w,3} - T_{r,3})$
$\frac{\partial (Z_2)_4}{\partial P}$	$\dot{m}_{r,out} \frac{\partial h_{r,f}}{\partial P} - \dot{m}_{r,out} \frac{\partial h_{r,out}}{\partial P} - A_s \zeta_3 \alpha_{r,3} \frac{\partial T_{r,3}}{\partial P}$

Table 3.9 (cont.)

$\frac{\partial (Z_2)_4}{\partial h_{r,3}}$	$-\dot{m}_{r,out} - A_s \zeta_3 \alpha_{r,3} \frac{\partial T_{r,3}}{\partial h_{r,3}}$
$\frac{\partial (Z_2)_4}{\partial T_{w,3}}$	$A_s \zeta_3 \alpha_{r,3}$
$\frac{\partial (Z_2)_5}{\partial P}$	$\frac{5}{2}\left(\frac{\partial h_{r,in}}{\partial P} + \frac{\partial h_{r,g}}{\partial P}\right) - 5\frac{\partial h_{r,1}}{\partial P}$
$\frac{\partial (Z_2)_5}{\partial h_{r,1}}$	-5
$\frac{\partial (Z_2)_6}{\partial P}$	$5\frac{\partial \bar{\gamma}_{full}}{\partial P}$
$\frac{\partial (Z_2)_6}{\partial \bar{\gamma}}$	-5
$\frac{\partial (Z_2)_7}{\partial \zeta_1}$	$\dot{m}_{a,in} c_{p,a} \left(T_{a,i} - \left(T_{w,1} + (T_{a,in} - T_{w,1}) e^{-NTU}\right)\right) - \alpha_{r,1} A_s (T_{w,1} - T_{r,1})$
$\frac{\partial (Z_2)_7}{\partial P}$	$\alpha_{r,1} A_s \zeta_1 \frac{\partial T_{r,1}}{\partial P}$
$\frac{\partial (Z_2)_7}{\partial h_{r,1}}$	$\alpha_{r,1} A_s \zeta_1 \frac{\partial T_{r,1}}{\partial h_{r,1}}$
$\frac{\partial (Z_2)_7}{\partial T_{w,1}}$	$\dot{m}_{a,in} c_{p,a} \zeta_1 (e^{-NTU} - 1) - \alpha_{r,1} A_s \zeta_1$
$\frac{\partial (Z_2)_8}{\partial \zeta_2}$	$\dot{m}_{a,in} c_{p,a} \left(T_{a,in} - \left(T_{w,2} + (T_{a,in} - T_{w,2}) e^{-NTU}\right)\right) - \alpha_{r,2} A_s (T_{w,2} - T_{r,2})$
$\frac{\partial (Z_2)_8}{\partial P}$	$\alpha_{r,2} A_s \zeta_2 \frac{\partial T_{r,2}}{\partial P}$
$\frac{\partial (Z_2)_8}{\partial T_{w,2}}$	$\dot{m}_{a,in} c_{p,a} \zeta_2 (e^{-NTU} - 1) - \alpha_{r,2} A_s \zeta_2$
$\frac{\partial (Z_2)_9}{\partial \zeta_1}$	$-\dot{m}_{a,in} c_{p,a} \left(T_{a,in} - \left(T_{w,3} + (T_{a,in} - T_{w,3}) e^{-NTU}\right)\right) + \alpha_{r,3} A_s (T_{w,3} - T_{r,3})$

Table 3.9 (cont.)

$\frac{\partial (Z_2)_9}{\partial \zeta_2}$	$-\dot{m}_{a,in} c_{p,a} \left(T_{a,in} - \left(T_{w,3} + (T_{a,in} - T_{w,3}) e^{-NTU} \right) \right) + \alpha_{r,3} A_s (T_{w,3} - T_{r,3})$
$\frac{\partial (Z_2)_9}{\partial P}$	$\alpha_{r,3} A_s \zeta_3 \frac{\partial T_{r,3}}{\partial P}$
$\frac{\partial (Z_2)_9}{\partial h_{r,3}}$	$\alpha_{r,3} A_s \zeta_3 \frac{\partial T_{r,3}}{\partial h_{r,3}}$
$\frac{\partial (Z_2)_9}{\partial T_{w,3}}$	$\dot{m}_{a,in} c_{p,a} \zeta_3 (e^{-NTU} - 1) - \alpha_{r,3} A_s \zeta_3$

Table 3.10: Mode 1 Matrix Elements of *B*

$\frac{\partial (Z_2)_1}{\partial \dot{m}_{r,in}}$	$h_{r,in} - h_{r,g}$
$\frac{\partial (Z_2)_1}{\partial h_{r,in}}$	$\dot{m}_{r,in}$
$\frac{\partial (Z_2)_2}{\partial \dot{m}_{r,in}}$	1
$\frac{\partial (Z_2)_2}{\partial \dot{m}_{r,out}}$	-1
$\frac{\partial (Z_2)_3}{\partial \dot{m}_{r,in}}$	$h_{r,g}$
$\frac{\partial (Z_2)_3}{\partial \dot{m}_{r,out}}$	$-h_{r,f}$
$\frac{\partial (Z_2)_4}{\partial \dot{m}_{r,out}}$	$\mathrm{h}_{r,f} - h_{r,o}$
$\frac{\partial (Z_2)_5}{\partial h_{r,in}}$	$\frac{5}{2}$
$\frac{\partial (Z_2)_7}{\partial T_{a,in}}$	$\dot{m}_{a,in} c_{p,a} \zeta_1 (1 - e^{-NTU})$

Table 3.10 (cont.)

$\frac{\partial (Z_2)_7}{\partial \dot{m}_{a,in}}$	$c_{p,a}\zeta_1\left(T_{a,in}-\left(T_{w,1}+(T_{a,in}-T_{w,1})e^{-NTU}\right)\right)$ $+\dot{m}_{a,in}\zeta_1 c_{p,a}(T_{a,in}-T_{w,1})e^{-NTU}NTU\left(\frac{1}{\alpha_a}\frac{\partial \alpha_a}{\partial \dot{m}_{a,in}}-\frac{1}{\dot{m}_{a,in}}\right)$
$\frac{\partial (Z_2)_8}{\partial T_{a,in}}$	$\dot{m}_{a,in}c_{p,a}\zeta_2(1-e^{-NTU})$
$\frac{\partial (Z_2)_8}{\partial \dot{m}_{a,in}}$	$c_{p,a}\zeta_2\left(T_{a,in}-\left(T_{w,2}+(T_{a,in}-T_{w,2})e^{-NTU}\right)\right)$ $+\dot{m}_{a,in}\zeta_2 c_{p,a}(T_{a,in}-T_{w,2})e^{-NTU}NTU\left(\frac{1}{\alpha_a}\frac{\partial \alpha_a}{\partial \dot{m}_{a,in}}-\frac{1}{\dot{m}_{a,in}}\right)$
$\frac{\partial (Z_2)_9}{\partial T_{a,in}}$	$\dot{m}_{a,in}c_{p,a}\zeta_3(1-e^{-NTU})$
$\frac{\partial (Z_2)_9}{\partial \dot{m}_{a,in}}$	$c_{p,a}\zeta_3\left(T_{a,in}-\left(T_{w,3}+(T_{a,in}-T_{w,3})e^{-NTU}\right)\right)$ $+\dot{m}_{a,in}\zeta_3 c_{p,a}(T_{a,in}-T_{w,3})e^{-NTU}NTU\left(\frac{1}{\alpha_a}\frac{\partial \alpha_a}{\partial \dot{m}_{a,in}}-\frac{1}{\dot{m}_{a,in}}\right)$

Table 3.11: Mode 1 Matrix Elements of *C*

$\frac{\partial (Z_3)_1}{\partial P}$	1
$\frac{\partial (Z_3)_2}{\partial h_{r,3}}$	1
$\frac{\partial (Z_3)_3}{\partial P}$	$\frac{\partial T_{r,3}}{\partial P}$
$\frac{\partial (Z_3)_3}{\partial h_{r,3}}$	$\frac{\partial T_{r,3}}{\partial h}$
$\frac{\partial (Z_3)_4}{\partial P}$	$\frac{\partial T_{sat}}{\partial P}-\frac{\partial T_{r,3}}{\partial P}$
$\frac{\partial (Z_3)_4}{\partial h_{r,3}}$	$-\frac{\partial T_{r,3}}{\partial h}$

Table 3.11 (cont.)

$\frac{\partial (Z_3)_5}{\partial \zeta_1}$	$\left(T_{w,1} + (T_{a,in} - T_{w,1})e^{-NTU}\right) - \left(T_{w,3} + (T_{a,in} - T_{w,3})e^{-NTU}\right)$
$\frac{\partial (Z_3)_5}{\partial \zeta_2}$	$\left(T_{w,2} + (T_{a,in} - T_{w,2})e^{-NTU}\right) - \left(T_{w,3} + (T_{a,in} - T_{w,3})e^{-NTU}\right)$
$\frac{\partial (Z_3)_5}{\partial T_{w,1}}$	$\zeta_1(1 - e^{-NTU})$
$\frac{\partial (Z_3)_5}{\partial T_{w,2}}$	$\zeta_2(1 - e^{-NTU})$
$\frac{\partial (Z_3)_5}{\partial T_{w,3}}$	$\zeta_3(1 - e^{-NTU})$
$\frac{\partial (Z_3)_6}{\partial \zeta_1}$	$-\dot{m}_{a,in} c_{p,a} \frac{\partial (Z_3)_5}{\partial \zeta_1}$
$\frac{\partial (Z_3)_6}{\partial \zeta_2}$	$-\dot{m}_{a,in} c_{p,a} \frac{\partial (Z_3)_5}{\partial \zeta_2}$
$\frac{\partial (Z_3)_6}{\partial T_{w,1}}$	$-\dot{m}_{a,in} c_{p,a} \frac{\partial (Z_3)_5}{\partial T_{w,1}}$
$\frac{\partial (Z_3)_6}{\partial T_{w,2}}$	$-\dot{m}_{a,in} c_{p,a} \frac{\partial (Z_3)_5}{\partial T_{w,2}}$
$\frac{\partial (Z_3)_6}{\partial T_{w,3}}$	$-\dot{m}_{a,in} c_{p,a} \frac{\partial (Z_3)_5}{\partial T_{w,3}}$

Table 3.12: Mode 1 Matrix Elements of *D*

$\frac{\partial (Z_3)_5}{\partial T_{a,in}}$	$\zeta_1 e^{-NTU} + \zeta_2 e^{-NTU} + \zeta_3 e^{-NTU}$
$\frac{\partial (Z_3)_5}{\partial \dot{m}_{a,in}}$	$-\left[\zeta_1(T_{a,in} - T_{w_1}) + \zeta_2(T_{a,in} - T_{w_2}) + \zeta_3(T_{a,in} - T_{w_3})\right] e^{-NTU} NTU \left(\frac{1}{\alpha_a}\frac{\partial \alpha_a}{\partial \dot{m}_{a,in}} - \frac{1}{\dot{m}_{a,in}}\right)$
$\frac{\partial (Z_3)_6}{\partial T_{a,in}}$	$-\dot{m}_{a,in} c_{p,a} \left(\frac{\partial (Z_3)_5}{\partial T_{a,in}} - 1\right)$

Table 3.12 (cont.)

$\frac{\partial (Z_3)_6}{\partial \dot{m}_{a,in}}$	$-c_{p,a}\left(\zeta_1\left(T_{w,1}+(T_{a,in}-T_{w,1})e^{-NTU}\right)\right.$ $+\zeta_2\left(T_{w,2}+(T_{a,in}-T_{w,2})e^{-NTU}\right)$ $\left.+\zeta_3\left(T_{w,3}+(T_{a,in}-T_{w,3})e^{-NTU}\right)-T_{a,in}+\dot{m}_{a,in}\frac{\partial (Z_3)_5}{\partial \dot{m}_{a,in}}\right)$

3.2.2 Mode 2: Superheated and Two-Phase Zones Only

For Mode 2 of the condenser, *A*, *B*, *C*, and *D* are given by:

$$A=\left.\begin{pmatrix} 0 & 0 & 0 & 0 & 0 & 0 \\ \frac{\partial (Z_2)_2}{\partial \zeta_1} & \frac{\partial (Z_2)_2}{\partial P} & \frac{\partial (Z_2)_2}{\partial h_{r,1}} & 0 & \frac{\partial (Z_2)_2}{\partial T_{w,1}} & 0 \\ 0 & \frac{\partial (Z_2)_3}{\partial P} & 0 & \frac{\partial (Z_2)_3}{\partial \bar{\gamma}} & 0 & \frac{\partial (Z_2)_3}{\partial T_{w,2}} \\ 0 & \frac{\partial (Z_2)_4}{\partial P} & \frac{\partial (Z_2)_4}{\partial h_{r,1}} & 0 & 0 & 0 \\ \frac{\partial (Z_2)_5}{\partial \zeta_1} & \frac{\partial (Z_2)_5}{\partial P} & \frac{\partial (Z_2)_5}{\partial h_{r,1}} & 0 & \frac{\partial (Z_2)_5}{\partial T_{w,1}} & 0 \\ 0 & \frac{\partial (Z_2)_6}{\partial P} & 0 & 0 & 0 & \frac{\partial (Z_2)_6}{\partial T_{w,2}} \end{pmatrix}\right|_{x_o,u_o} \tag{3.20}$$

$$B=\left.\begin{pmatrix} \frac{\partial (Z_2)_1}{\partial \dot{m}_{r,in}} & \frac{\partial (Z_2)_1}{\partial \dot{m}_{r,out}} & 0 & 0 & 0 \\ \frac{\partial (Z_2)_2}{\partial \dot{m}_{r,in}} & \frac{\partial (Z_2)_2}{\partial \dot{m}_{r,out}} & \frac{\partial (Z_2)_2}{\partial h_{r,in}} & 0 & 0 \\ 0 & \frac{\partial (Z_2)_3}{\partial \dot{m}_{r,out}} & 0 & 0 & 0 \\ 0 & 0 & \frac{\partial (Z_2)_4}{\partial h_{r,in}} & 0 & 0 \\ 0 & 0 & 0 & \frac{\partial (Z_2)_5}{\partial T_{a,in}} & \frac{\partial (Z_2)_5}{\partial \dot{m}_{a,in}} \\ 0 & 0 & 0 & \frac{\partial (Z_2)_6}{\partial T_{a,in}} & \frac{\partial (Z_2)_6}{\partial \dot{m}_{a,in}} \end{pmatrix}\right|_{x_o,u_o} \tag{3.21}$$

$$C = \begin{pmatrix} 0 & \frac{\partial (Z_3)_1}{\partial P} & 0 & 0 & 0 & 0 \\ 0 & \frac{\partial (Z_3)_2}{\partial P} & 0 & \frac{\partial (Z_3)_2}{\partial \bar{\gamma}} & 0 & 0 \\ 0 & \frac{\partial (Z_3)_3}{\partial P} & 0 & 0 & 0 & 0 \\ 0 & 0 & 0 & 0 & 0 & 0 \\ \frac{\partial (Z_3)_5}{\partial \zeta_1} & 0 & 0 & 0 & \frac{\partial (Z_3)_5}{\partial T_{w,1}} & \frac{\partial (Z_3)_5}{\partial T_{w,2}} \\ \frac{\partial (Z_3)_6}{\partial \zeta_1} & 0 & 0 & 0 & \frac{\partial (Z_3)_6}{\partial T_{w,1}} & \frac{\partial (Z_3)_6}{\partial T_{w,2}} \end{pmatrix}\Bigg|_{x_o,u_o} \tag{3.22}$$

$$D = \begin{pmatrix} 0 & 0 & 0 & 0 & 0 \\ 0 & 0 & 0 & 0 & 0 \\ 0 & 0 & 0 & 0 & 0 \\ 0 & 0 & 0 & 0 & 0 \\ 0 & 0 & 0 & \frac{\partial (Z_3)_5}{\partial T_{a,in}} & \frac{\partial (Z_3)_5}{\partial \dot{m}_{a,in}} \\ 0 & 0 & 0 & \frac{\partial (Z_3)_6}{\partial T_{a,in}} & \frac{\partial (Z_3)_6}{\partial T_{a,in}} \end{pmatrix}\Bigg|_{x_o,u_o} \tag{3.23}$$

Table 3.13: Mode 1 Matrix Elements of *A*

$\frac{\partial (Z_2)_2}{\partial \zeta_1}$	$A_s \alpha_{r,1}(T_{w,1} - T_{r,1})$
$\frac{\partial (Z_2)_2}{\partial P}$	$-\dot{m}_{r,out}\frac{\partial h_{r,g}}{\partial P} - A_s \zeta_1 \alpha_{r,1}\frac{\partial T_{r,1}}{\partial P}$
$\frac{\partial (Z_2)_2}{\partial h_{r,1}}$	$-A_s \zeta_1 \alpha_{r,1}\frac{\partial T_{r,1}}{\partial h_{r,1}}$
$\frac{\partial (Z_2)_2}{\partial T_{w,1}}$	$A_s \zeta_1 \alpha_{r,1}$
$\frac{\partial (Z_2)_3}{\partial P}$	$\dot{m}_{r,out}\frac{\partial h_{r,g}}{\partial P} - \dot{m}_{r,out}\frac{\partial h_{r,out}}{\partial P} - A_s \zeta_2 \alpha_{r,2}\frac{\partial T_{r,2}}{\partial P}$

Table 3.13 (cont.)

$\frac{\partial (Z_2)_3}{\partial \bar{\gamma}}$	$-\dot{m}_{r,out} \frac{\partial h_{r,out}}{\partial \bar{\gamma}}$
$\frac{\partial (Z_2)_3}{\partial T_{w,2}}$	$A_s \zeta_2 \alpha_{r,2}$
$\frac{\partial (Z_2)_4}{\partial P}$	$\frac{5}{2}\frac{\partial h_{r,g}}{\partial P} - 5\frac{\partial h_{r,1}}{\partial P}$
$\frac{\partial (Z_2)_4}{\partial h_{r,1}}$	-5
$\frac{\partial (Z_2)_5}{\partial \zeta_1}$	$\dot{m}_{a,in} c_{p,a} \left(T_{a,in} - \left(T_{w,1} + (T_{a,in} - T_{w,1}) e^{-NTU} \right) \right) - \alpha_{r,1} A_s (T_{w,1} - T_{r,1})$
$\frac{\partial (Z_2)_5}{\partial P}$	$\alpha_{r,1} A_s \zeta_1 \frac{\partial T_{r,1}}{\partial P}$
$\frac{\partial (Z_2)_5}{\partial h_{r,1}}$	$\alpha_{r,1} A_s \zeta_1 \frac{\partial T_{r,1}}{\partial h_{r,1}}$
$\frac{\partial (Z_2)_5}{\partial T_{w,1}}$	$\dot{m}_{a,in} c_{p,a} \zeta_1 (e^{-NTU} - 1) - \alpha_{r,1} A_s \zeta_1$
$\frac{\partial (Z_2)_6}{\partial P}$	$\alpha_{r,2} A_s \zeta_2 \frac{\partial T_{r,2}}{\partial P}$
$\frac{\partial (Z_2)_6}{\partial T_{w,2}}$	$\dot{m}_{a,in} c_{p,a} \zeta_2 (e^{-NTU} - 1) - \alpha_{r,2} A_s \zeta_2$

Table 3.14: Mode 1 Matrix Elements of *B*

$\frac{\partial (Z_2)_1}{\partial \dot{m}_{r,in}}$	1
$\frac{\partial (Z_2)_1}{\partial \dot{m}_{r,out}}$	-1
$\frac{\partial (Z_2)_2}{\partial \dot{m}_{r,in}}$	$h_{r,in}$

Table 3.14 (cont.)

$\frac{\partial (Z_2)_2}{\partial \dot{m}_{r,out}}$	$-h_{r,g}$
$\frac{\partial (Z_2)_2}{\partial h_{r,in}}$	$\dot{m}_{r,in}$
$\frac{\partial (Z_2)_3}{\partial \dot{m}_{r,out}}$	$h_{r,g} - h_{r,out}$
$\frac{\partial (Z_2)_4}{\partial h_{r,in}}$	$\frac{5}{2}$
$\frac{\partial (Z_2)_5}{\partial T_{a,in}}$	$\dot{m}_{a,in} c_{p,a} \zeta_1 (1 - e^{-NTU})$
$\frac{\partial (Z_2)_5}{\partial \dot{m}_{a,in}}$	$c_{p,a}\zeta_1 \left(T_{a,in} - \left(T_{w,1} + (T_{a,in} - T_{w,1}) e^{-NTU} \right) \right)$ $+\dot{m}_{a,in}\zeta_1 c_{p,a} (T_{a,in} - T_{w,1}) e^{-NTU} NTU \left(\frac{1}{\alpha_a} \frac{\partial \alpha_a}{\partial \dot{m}_{a,in}} - \frac{1}{\dot{m}_{a,in}} \right)$
$\frac{\partial (Z_2)_6}{\partial T_{a,in}}$	$\dot{m}_{a,in} c_{p,a} \zeta_2 (1 - e^{-NTU})$
$\frac{\partial (Z_2)_6}{\partial \dot{m}_{a,in}}$	$c_{p,a}\zeta_2 \left(T_{a,in} - \left(T_{w,2} + (T_{a,in} - T_{w,2}) e^{-NTU} \right) \right)$ $+\dot{m}_{a,in}\zeta_2 c_{p,a} (T_{a,in} - T_{w,2}) e^{-NTU} NTU \left(\frac{1}{\alpha_a} \frac{\partial \alpha_a}{\partial \dot{m}_{a,in}} - \frac{1}{\dot{m}_{a,in}} \right)$

Table 3.15: Mode 1 Matrix Elements of *C*

$\frac{\partial (Z_3)_1}{\partial P}$	1
$\frac{\partial (Z_3)_2}{\partial P}$	$\frac{\partial q_{out}}{\partial P}(h_{r,g} - h_{r,f}) + q_{out}\left(\frac{\partial h_{r,g}}{\partial P} - \frac{\partial h_{r,f}}{\partial P} \right) + \frac{\partial h_{r,f}}{\partial P}$
$\frac{\partial (Z_3)_2}{\partial \bar{\gamma}}$	$\frac{\partial q_{out}}{\partial \bar{\gamma}}(h_{r,g} - h_{r,f})$
$\frac{\partial (Z_3)_3}{\partial P}$	$\frac{\partial T_{r,2}}{\partial P}$

Table 3.15 (cont.)

$\frac{\partial (Z_3)_5}{\partial \zeta_1}$	$T_{w,1} + (T_{a,1} - T_{w,1}) e^{-NTU}$
$\frac{\partial (Z_3)_5}{\partial T_{w,1}}$	$\zeta_1 (1 - e^{-NTU})$
$\frac{\partial (Z_3)_5}{\partial T_{w,2}}$	$\zeta_2 (1 - e^{-NTU})$
$\frac{\partial (Z_3)_6}{\partial \zeta_1}$	$-\dot{m}_{a,in} c_{p,a} \frac{\partial (Z_3)_5}{\partial \zeta_1}$
$\frac{\partial (Z_3)_6}{\partial T_{w,1}}$	$-\dot{m}_{a,in} c_{p,a} \frac{\partial (Z_3)_5}{\partial T_{w,1}}$
$\frac{\partial (Z_3)_6}{\partial T_{w,2}}$	$-\dot{m}_{a,in} c_{p,a} \frac{\partial (Z_3)_5}{\partial T_{w,2}}$

Table 3.16: Mode 1 Matrix Elements of *D*

$\frac{\partial (Z_3)_5}{\partial T_{a,in}}$	$\zeta_1 e^{-NTU} + \zeta_2 e^{-NTU}$
$\frac{\partial (Z_3)_5}{\partial \dot{m}_{a,in}}$	$-\left[\zeta_1 (T_{a,in} - T_{w,1}) + \zeta_2 (T_{a,in} - T_{w,2})\right] e^{-NTU} NTU \left(\frac{1}{\alpha_a} \frac{\partial \alpha_a}{\partial \dot{m}_{a,in}} - \frac{1}{\dot{m}_{a,in}} \right)$
$\frac{\partial (Z_3)_6}{\partial T_{a,in}}$	$-\dot{m}_{a,in} c_{p,a} \left(\frac{\partial (Z_3)_5}{\partial T_{a,in}} - 1 \right)$
$\frac{\partial (Z_3)_6}{\partial \dot{m}_{a,in}}$	$-c_{p,a} \left(\zeta_1 \left(T_{w,1} + (T_{a,in} - T_{w,1}) e^{-NTU} \right) + \zeta_2 \left(T_{w,2} + (T_{a,in} - T_{w,2}) e^{-NTU} \right) - T_{a,in} + \dot{m}_{a,in} \frac{\partial (Z_3)_5}{\partial \dot{m}_{a,in}} \right)$

To incorporate the pseudo-state equations, the system is augmented as follows:

$$\dot{x}_c \approx \begin{pmatrix} Z_1^{-1} A & 0_{6x3} \\ W & \end{pmatrix} \Delta x_c + \begin{pmatrix} Z_1^{-1} B \\ 0_{3x5} \end{pmatrix} \Delta u_c \qquad (3.24)$$

$$y_c \approx \begin{pmatrix} C & 0_{6x3} \end{pmatrix} \Delta x_c + D \Delta u_c + y_{c,o}$$

where

$$W = \begin{pmatrix} 0 & 0 & 0 & 0 & 0 & 0 & 0 & 0 & 0 \\ 0 & K\dfrac{\partial h_{r,f}}{\partial P} & 0 & 0 & 0 & 0 & 0 & -K & 0 \\ 0 & 0 & 0 & 0 & 0 & K & 0 & 0 & -K \end{pmatrix}. \tag{3.25}$$

This gives the augmented state vector:

$$x_e = \begin{pmatrix} \zeta_1 & P & h_{r,1} & \bar{\gamma} & T_{w,1} & T_{w,2} & \zeta_2 & h_{r,1} & T_{w,3} \end{pmatrix}^T \tag{3.26}$$

The ordering of these states can easily be changed to recover the full state vector of Eq. (2.28).

3.2.3 Nonlinear and Linear Model Comparison

Figure 3.6 shows the output response of the nonlinear SMB and linear 3-zone condenser models to a step in each input. The states of each model are plotted in Figure 3.7. For this simulation, the linear model was linearized about the nominal steady-state operating conditions of the nonlinear model, which are reached before and after each input step. As with the linear evaporator, although not all gains are matched perfectly, it is clear that the 3-zone linear condenser model matches its nonlinear equivalent closely.

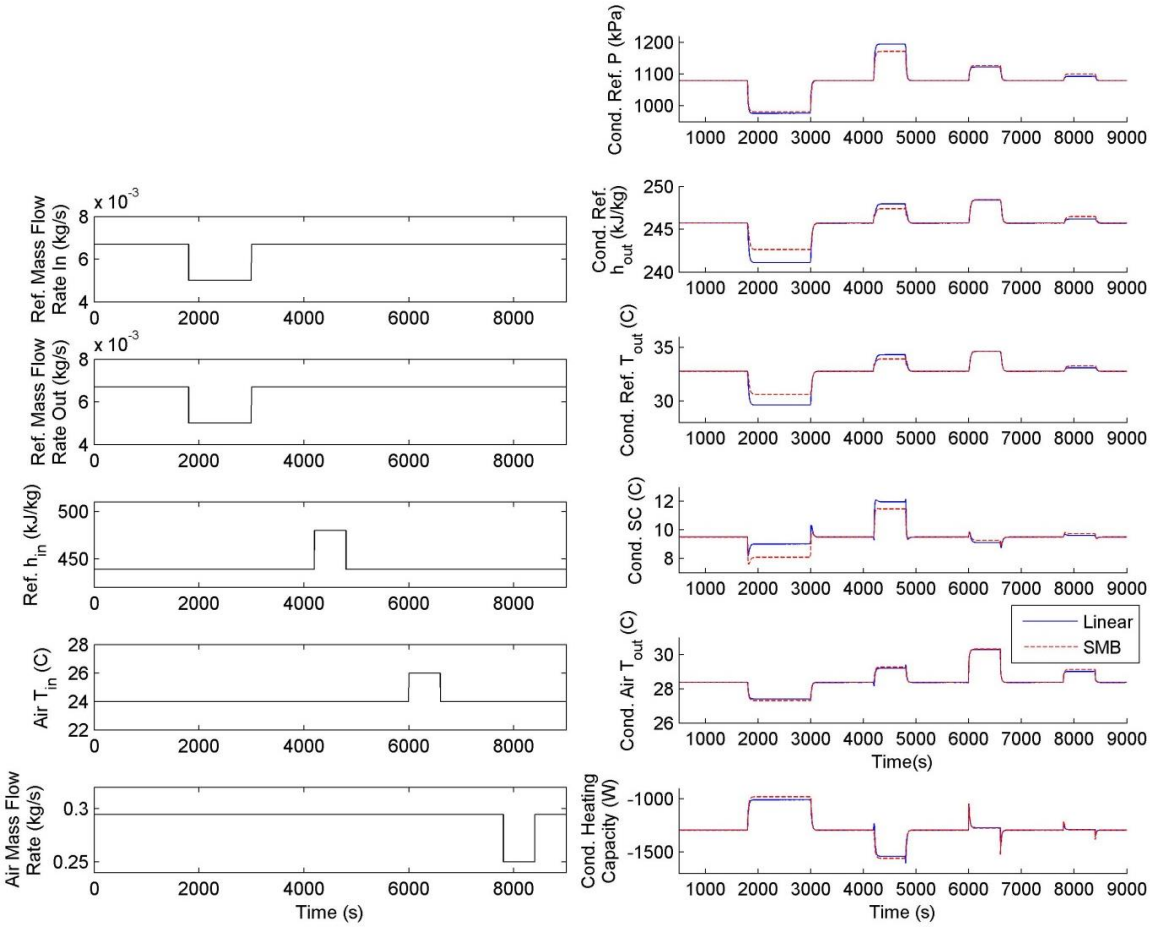

Figure 3.6 Nonlinear and Linear 3-zone Condenser Comparison—Inputs (left) and Outputs (right)

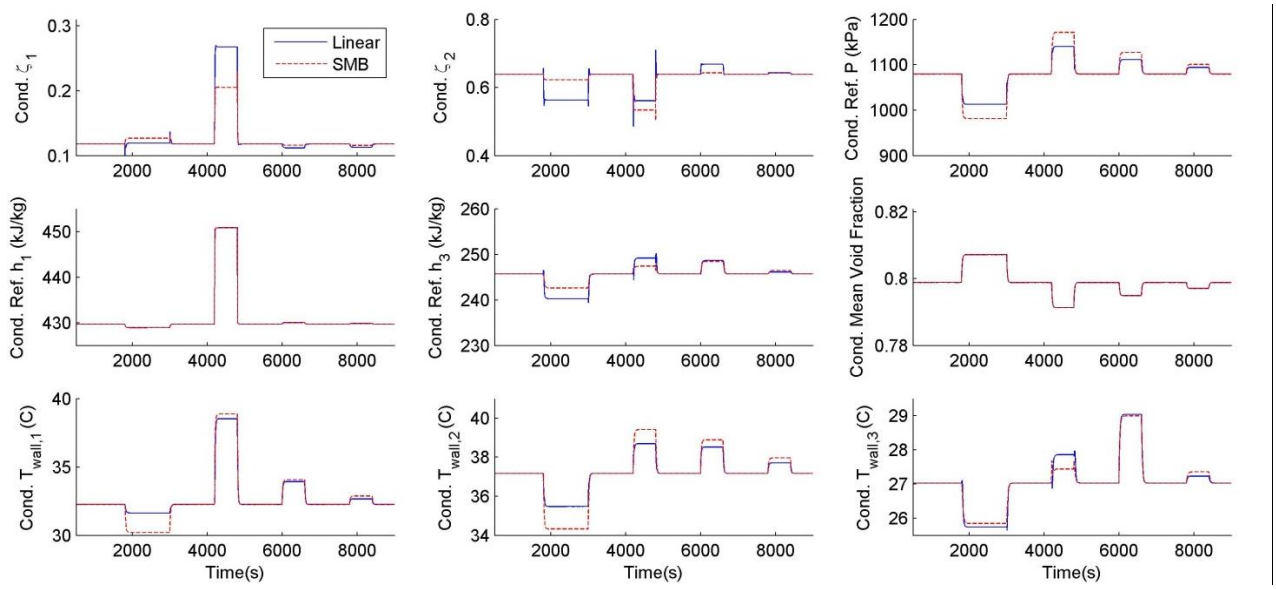

Figure 3.7 Nonlinear and Linear 3-zone Condenser Comparison—States

Figure 3.8 shows the output response of the nonlinear SMB and linear 2-zone condenser models to a step in each input. The changing inputs at the start of the simulation are used to trigger a switch of the nonlinear model into the correct mode. The nonlinear model remains in this mode for the remainder for the simulation. The states of each model are plotted in Figure 3.9. As this figure shows, the linear condenser is far from matching its nonlinear equivalent, diverging from the nominal conditions. Despite significant efforts to improve functionality through modification of the linearized equations and state vector, a suitable linear model of this mode could not be found. Such a model is reportedly used for model-based control in [26], but no equations are given. Deriving a stable and accurate 2-zone linear condenser model is left to future work.

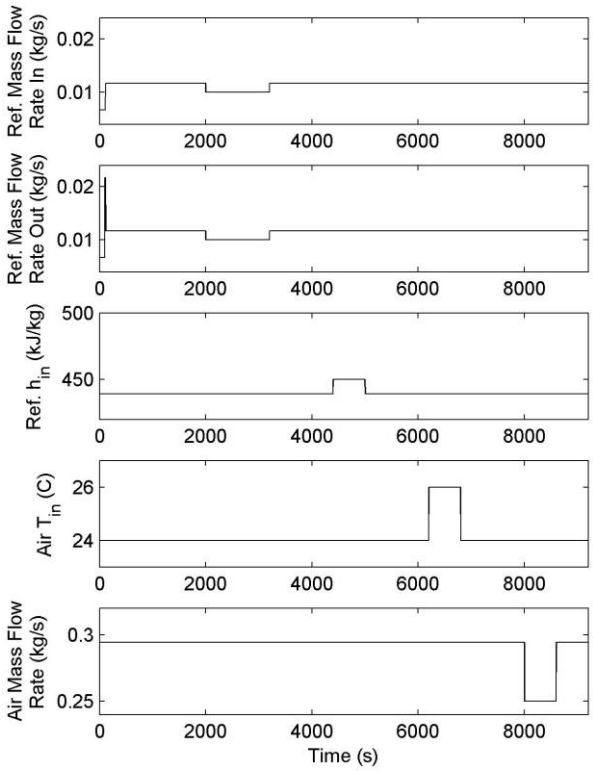

Figure 3.8 Nonlinear and Linear 2-zone Condenser Comparison—Inputs

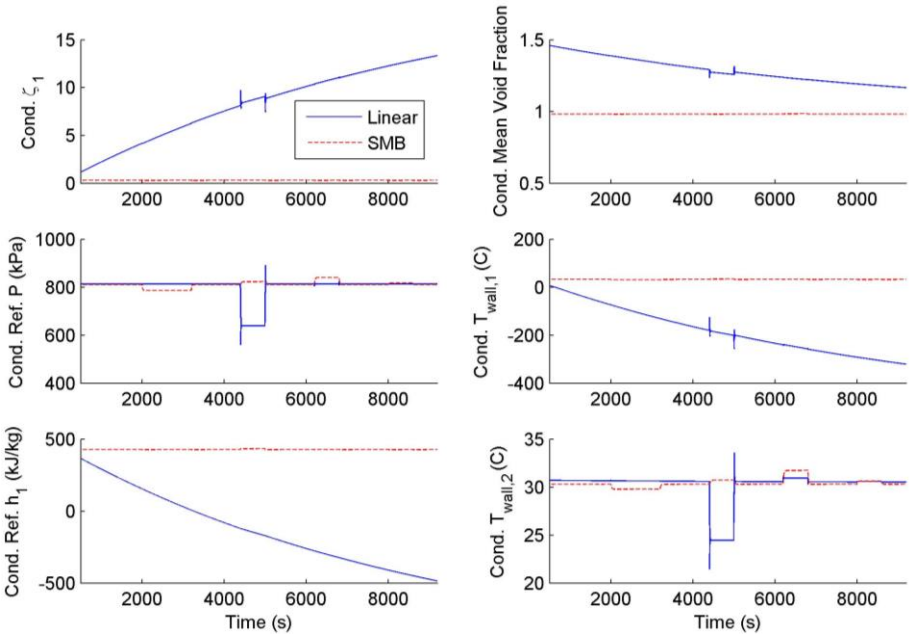

Figure 3.9 Nonlinear and Linear 2-zone Condenser Comparison—States

3.3 Electronic Expansion Valve

As described in Section 2.3.1, the nonlinear model is of the form:

$$y_{EEV} = f(u_{EEV}) \ . \tag{3.27}$$

Linearizing the nonlinear model about an arbitrary set of nominal operating conditions defined as $y_{EEV,o}$, $u_{EEV,o}$ the linear model takes the form:

$$y_{EEV} \approx D_{EEV}\Delta u_{EEV} + y_{EEV,o} \tag{3.28}$$

where

$$\Delta u_{EEV} = u_{EEV} - u_{EEV,o} \tag{3.29}$$

and D_{EEV} is the Jacobian of f evaluated at $u_{EEV,o}$:

$$D_{EEV} = \frac{\partial f}{\partial u_{EEV}}\Big|_{u_o} = \begin{pmatrix} \frac{\partial \dot{m}_v}{\partial u_v} & \frac{\partial \dot{m}_v}{\partial P_{in}} & \frac{\partial \dot{m}_v}{\partial P_{out}} & \frac{\partial \dot{m}_v}{\partial h_{in}} \\ 0 & 0 & 0 & \frac{\partial h_{out}}{\partial h_{in}} \end{pmatrix}\Big|_{u_o} \ . \tag{3.30}$$

The elements of D_{EEV} are given by Table 3.17.

Table 3.17 Matrix Elements of D_{EEV}

$\frac{\partial \dot{m}_{EEV}}{\partial o_{EEV}}$	$\frac{\partial C_d}{\partial o_{EEV}}\sqrt{\rho_{in}(P_{in}-P_{out})}$
$\frac{\partial \dot{m}_{EEV}}{\partial P_{in}}$	$\sqrt{\rho_{in}(P_{in}-P_{out})}\frac{\partial C_d}{\partial P_{in}} + \frac{C_d}{2\sqrt{\rho_{in}(P_{in}-P_{out})}}\left(\frac{\partial \rho}{\partial P_{in}}\Big\|_{h_{in}}(P_{in}-P_{out}) + \rho_{in}\right)$
$\frac{\partial \dot{m}_{EEV}}{\partial P_{out}}$	$\sqrt{\rho_{in}(P_{in}-P_{out})}\frac{\partial C_d}{\partial P_{out}} - \frac{C_d\rho_{in}}{2\sqrt{\rho_{in}(P_{in}-P_{out})}}$
$\frac{\partial \dot{m}_{EEV}}{\partial h_{in}}$	$\frac{C_d(P_{in}-P_{out})}{2\sqrt{\rho_{in}(P_{in}-P_{out})}}\frac{\partial \rho}{\partial h_{in}}\Big\|_{P_{in}}$
$\frac{\partial h_{out}}{\partial h_{in}}$	1

This linearization is slightly adapted from that given in [19]. The main difference is that here, partial derivatives of the discharge coefficient are taken with respect to either P_{in} or P_{out}, as opposed to always being taken with respect to $(P_{in} - P_{out})$.

3.3.1 Nonlinear and Linear Model Comparison

Figure 3.10 shows the response of the nonlinear and linear EEV models to a step in each input of approximately 15% the nominal value. The models clearly match closely.

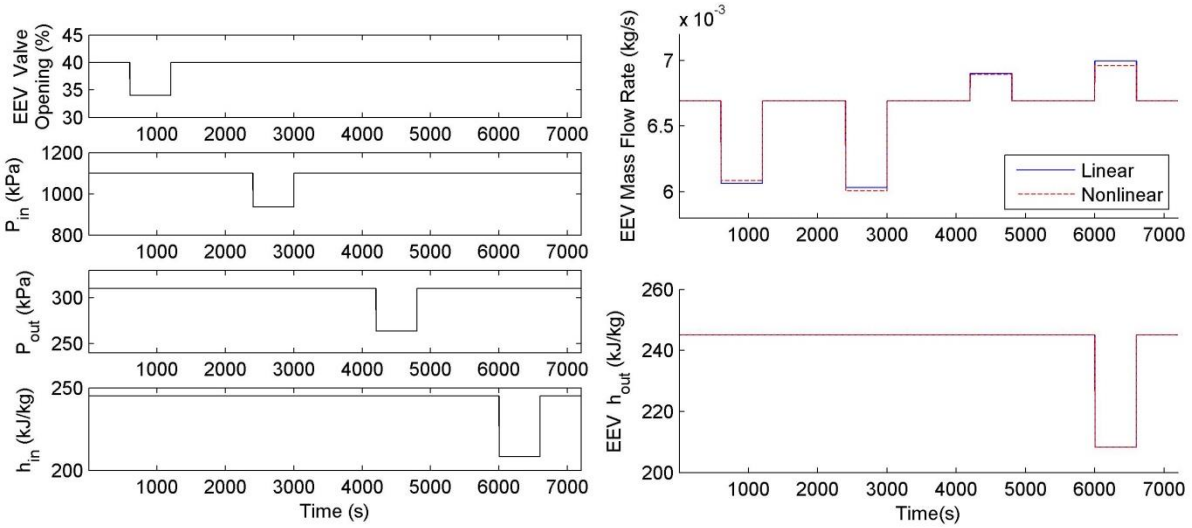

Figure 3.10 Nonlinear and Linear EEV Comparison—Inputs (left) and Outputs (right)

3.4 Compressor

3.4.1 Static Linear Model

We first present a linear model that neglects the dynamic imposed on compressor's outlet enthalpy in the nonlinear model. As described in Section 2.3.2, the static outputs of the nonlinear model are of the form:

$$y_{comp} = f(u_{comp}) \ . \tag{3.31}$$

Linearizing the nonlinear model about an arbitrary set of nominal operating conditions defined as $y_{comp,o}$ and $u_{comp,o}$, the linear model takes the form:

$$y_{comp} \approx D_{comp}\Delta u_{comp} + y_{comp,o} \tag{3.32}$$

where

$$\Delta u_{comp} = u_{comp} - u_{comp,o} \tag{3.33}$$

and D_{comp} is the Jacobian of f evaluated at $u_{comp,o}$:

$$D_{comp} = \frac{\partial f}{\partial u_{comp}}\Big|_{u_o} = \begin{pmatrix} \frac{\partial \dot{m}_{comp}}{\partial v_{comp}} & \frac{\partial \dot{m}_{comp}}{\partial P_{in}} & \frac{\partial \dot{m}_{comp}}{\partial P_{out}} & \frac{\partial \dot{m}_{comp}}{\partial h_{in}} \\ \frac{\partial h_{out}}{\partial v_{comp}} & \frac{\partial h_{out}}{\partial P_{in}} & \frac{\partial h_{out}}{\partial P_{out}} & \frac{\partial h_{out}}{\partial h_{in}} \end{pmatrix}\Big|_{u_o} . \tag{3.34}$$

The elements of D_{comp} are given by Table 3.18.

Table 3.18 Matrix Elements of D_{comp}

$\frac{\partial \dot{m}_{comp}}{\partial v_{comp}}$	$V_{comp}\rho_{in}\left(v_{comp}\frac{\partial \eta_{vol}}{\partial v_{comp}} + \eta_{vol}\right)$
$\frac{\partial \dot{m}_{comp}}{\partial P_{in}}$	$v_{comp}V_{comp}\left(-\rho_{in}\frac{\partial \eta_{vol}}{\partial P_{ratio}}\frac{P_{ratio}}{P_{in}} + \eta_{vol}\frac{\partial \rho}{\partial P_{in}}\Big\|_{h_{in}}\right)$
$\frac{\partial \dot{m}_{comp}}{P_{out}}$	$v_{comp}V_{comp}\rho_{in}\frac{\partial \eta_{vol}}{\partial P_{ratio}}\frac{1}{P_{in}}$
$\frac{\partial \dot{m}_{comp}}{\partial h_{in}}$	$_{comp}V_{comp}\eta_{vol}\frac{\partial \rho}{\partial h_{in}}\Big\|_{P_{in}}$
$\frac{\partial h_{out}}{\partial v_{comp}}$	$\left(\frac{h_{in} - h_{out,isen}}{\eta_{isen}^{\ 2}}\right)\frac{\partial \eta_{isen}}{\partial v_{comp}}$
$\frac{\partial h_{out}}{\partial P_{in}}$	$\left(\frac{h_{out,isen} - h_{in}}{\eta_{isen}^{\ 2}}\right)\frac{\partial \eta_{vol}}{\partial P_{ratio}}\frac{P_{ratio}}{P_{in}} + \frac{1}{\eta_{isen}}\frac{\partial h_{out,isen}}{\partial s}\Big\|_{P_{out}}\frac{\partial s}{\partial P_{in}}\Big\|_{h_{in}}$
$\frac{\partial h_{out}}{P_{out}}$	$\left(\frac{h_{in} - h_{out,isen}}{\eta_{isen}^{\ 2}}\right)\frac{\partial \eta_{vol}}{\partial P_{ratio}}\frac{1}{P_{in}} + \frac{1}{\eta_{isen}}\frac{\partial h_{out,isen}}{\partial P_{out}}\Big\|_{s}$
$\frac{\partial h_{out}}{\partial h_{in}}$	$\frac{1}{\eta_{isen}}\frac{\partial h_{out,isen}}{\partial s}\Big\|_{P_{out}}\frac{\partial s}{\partial h_{in}}\Big\|_{P_{in}} + 1 - \frac{1}{\eta_{isen}}$

This linearization follows directly from [19].

3.4.2 Dynamic Linear Model

In order to include the dynamic imposed on compressor's outlet enthalpy in the nonlinear model, the elements of D_{comp} can be assembled into the following state-space form:

$$\begin{aligned}
\dot{x}_{comp} &\approx A\Delta x_{comp} + B\Delta u_{comp} \\
&= \begin{pmatrix} 0 & 0 \\ 0 & -\dfrac{1}{\tau} \end{pmatrix} \Delta x_{comp} + \begin{pmatrix} 0 & 0 & 0 & 0 \\ \dfrac{\partial h_{out}}{\partial v_{comp}} & \dfrac{\partial h_{out}}{\partial P_{in}} & \dfrac{\partial h_{out}}{\partial P_{out}} & \dfrac{\partial h_{out}}{\partial h_{in}} \end{pmatrix}\Bigg|_{u_o} \Delta u_{comp} \\
y_{comp} &\approx C\Delta x_{comp} + D\Delta u_{comp} + y_{comp,o} \\
&= \begin{pmatrix} 0 & 0 \\ 0 & \dfrac{1}{\tau} \end{pmatrix} \Delta x_{comp} + \begin{pmatrix} \dfrac{\partial \dot{m}_{comp}}{\partial v_{comp}} & \dfrac{\partial \dot{m}_{comp}}{\partial P_{in}} & \dfrac{\partial \dot{m}_{comp}}{\partial P_{out}} & \dfrac{\partial \dot{m}_{comp}}{\partial h_{in}} \\ 0 & 0 & 0 & 0 \end{pmatrix}\Bigg|_{u_o} \Delta u_{comp} + y_{comp,o}
\end{aligned} \tag{3.35}$$

where x_{comp} is the state vector $\begin{pmatrix} \dot{m}_{comp} & \bar{h}_{out} \end{pmatrix}^T$ and $\Delta x_{comp} = x_{comp} - x_{comp,o}$. The overbar on the state $\bar{h}_{out}$ is meant to emphasize that this state, while associated with the compressor outlet enthalpy, does not correspond exactly to that output. It can easily be seen from the last line of Eq. (3.35) that the two are related by:

$$h_{out} = \frac{1}{\tau}(\bar{h}_{out} - h_{out,o}) + h_{out,o}\,. \tag{3.36}$$

3.4.3 Nonlinear and Linear Model Comparison

Figure 3.11 shows the response of the nonlinear and linear compressor models to a step in each input of approximately 15% the nominal value. The nonlinear and dynamic linear models both capture the first order time constant on outlet enthalpy, while the static model does not.

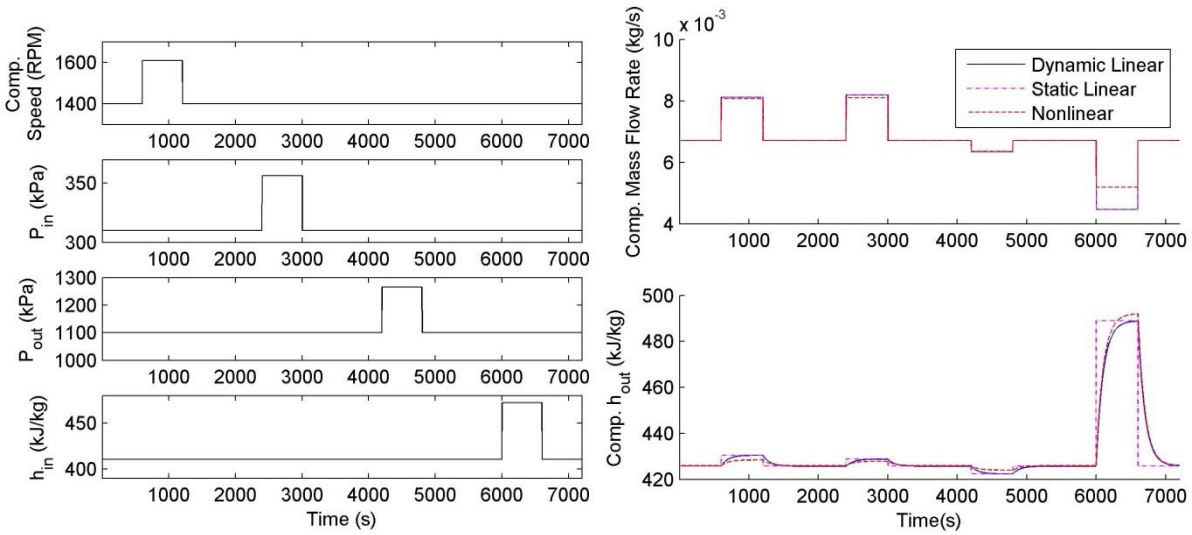

Figure 3.11 Nonlinear and Linear Compressor Comparison—
Inputs (left) and Outputs (right)

3.5 Linear Model Combination

In order to combine the individual component linear models into a single linear model that represents a complete four-component VCS, the component models are first combined in pairs to generate linear models that represent each half of the system. The two subsystems are then combined to generate a complete linear VCS model. The approach used here mirrors that presented in Appendix A of [41]. We show simulation results in this section only for the first modes of the evaporator and condenser, however models including the other heat exchanger modes can easily be generated as well.

3.5.1 EEV/Evaporator Combination

In combining the linear EEV and evaporator models, the dynamic pressure calculated by the evaporator becomes an internal feedback signal to the EEV, as shown in Figure 3.12.

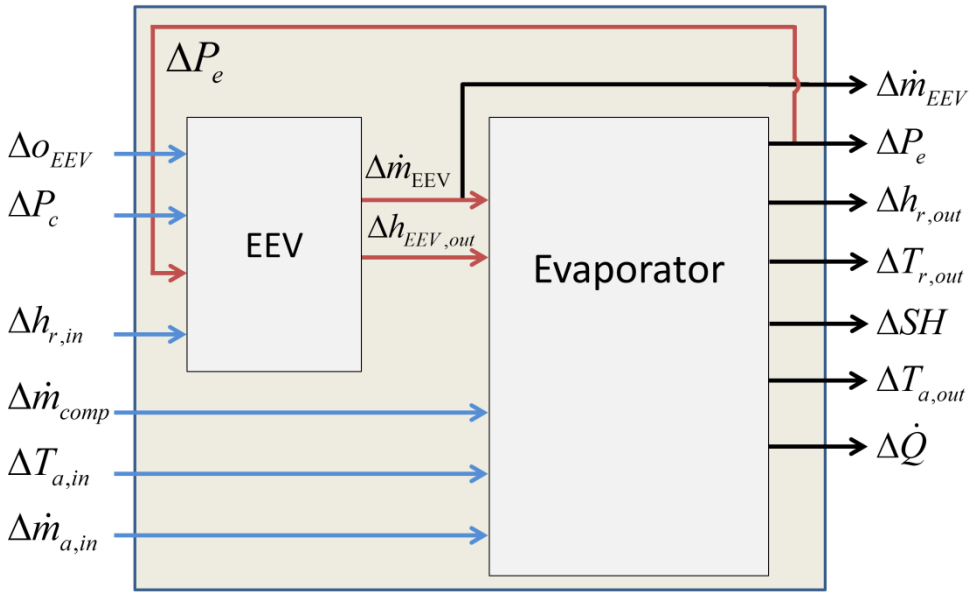

Figure 3.12 EEV and Evaporator Combination

As can be seen in Figure 3.12, the $\dot{m}_{r,in}$ and $h_{r,in}$ inputs of the evaporator model are provided by the internal feedforward from $\dot{m}_{EEV}$ and $h_{EEV,out}$. The n^{th} row of Eq. (3.1) can be written as:

$$\left(\dot{x}_e\right)_n = \begin{pmatrix} a_1 & \cdots & a_{n6} \end{pmatrix} \begin{pmatrix} \Delta\zeta_1 \\ \Delta P_e \\ \Delta h_2 \\ \Delta T_{w_1} \\ \Delta T_{w_2} \\ \Delta\bar{\gamma} \end{pmatrix} + \begin{pmatrix} b_{n1} & \cdots & b_{n5} \end{pmatrix} \begin{pmatrix} \Delta\dot{m}_{EEV} \\ \Delta\dot{m}_{comp} \\ \Delta h_{EEV,out} \\ \Delta T_{a,in} \\ \Delta\dot{m}_{a,in} \end{pmatrix}. \tag{3.37}$$

where $a_{n1\cdots n6}$ and $b_{n1\cdots n5}$ represent the nth rows of $Z_1^{-1}A$ and $Z_1^{-1}B$, respectively. From Eqs. (3.28) and (3.30), we see that $\Delta\dot{m}_{EEV}$ and $\Delta h_{EEV,out}$ in Eq. (3.37) can be expressed in terms of the EEV model's inputs:

$$\Delta\dot{m}_{EEV} = \begin{pmatrix} \hat{d}_{11} & \cdots & \hat{d}_{14} \end{pmatrix} \begin{pmatrix} \Delta o_v \\ \Delta P_c \\ \Delta P_e \\ \Delta h_{r,in} \end{pmatrix} \tag{3.38}$$

$$\Delta h_{EEV,out} = \hat{d}_{24}\Delta h_{r,in}$$

where $\hat{d}$ indicates elements of D_{EEV}.

Substituting Eq. (3.38) into Eq. (3.37), we can write the state space equation for the combined model as:

$$\begin{aligned}\left(\dot{x}_e\right)_n = &\begin{pmatrix} a_{n1} & \cdots & a_{n6} \end{pmatrix}\begin{pmatrix} \Delta\zeta_1 \\ \Delta P_e \\ \Delta h_2 \\ \Delta T_{w_1} \\ \Delta T_{w_2} \\ \Delta\bar{\gamma} \end{pmatrix} + \begin{pmatrix} b_{n2} & b_{n4} & b_{n5} \end{pmatrix}\begin{pmatrix} \Delta\dot{m}_{comp} \\ \Delta T_{a,in} \\ \Delta\dot{m}_{a,in} \end{pmatrix} \\ &+ b_{n1}\begin{pmatrix} \hat{d}_{11} & \cdots & \hat{d}_{14} \end{pmatrix}\begin{pmatrix} \Delta o_v \\ \Delta P_c \\ \Delta P_e \\ \Delta h_{r,in} \end{pmatrix} + b_{n3}\hat{d}_{24}\Delta h_{r,in}\end{aligned} \tag{3.39}$$

Reorganizing the terms in Eq. (3.39) , the final state space form becomes:

$$\begin{aligned}\left(\dot{x}_e\right)_n = &\begin{pmatrix} a_{n1} & a_{n2} + b_{n1}\hat{d}_{13} & a_{n3} & \cdots & a_{n6} \end{pmatrix}\begin{pmatrix} \Delta\zeta_1 \\ \Delta P_e \\ \Delta h_2 \\ \Delta T_{w_1} \\ \Delta T_{w_2} \\ \Delta\bar{\gamma} \end{pmatrix} \\ &+ \begin{pmatrix} b_{n1}\hat{d}_{11} & b_{n1}\hat{d}_{12} & b_{n1}\hat{d}_{14} + b_{n3}\hat{d}_{24} & b_{n2} & b_{n4} & b_{n5} \end{pmatrix}\begin{pmatrix} \Delta o_v \\ \Delta P_c \\ \Delta h_{r,in} \\ \Delta\dot{m}_{comp} \\ \Delta T_{a,in} \\ \Delta\dot{m}_{a,in} \end{pmatrix}\end{aligned} \tag{3.40}$$

Recognizing that $h_{r,in}$ for the EEV is equal to $h_{c,r,out}$, Eq. (3.40) can be written compactly for all rows of $\dot{x}_e$ as:

$$\dot{x}_e = \bar{A}\Delta x_e + \bar{B}\Delta\bar{u}_e \tag{3.41}$$

where $\bar{u}_e$ is the input vector for the combined EEV/evaporator model, given by:

$$\begin{pmatrix} o_v & P_c & h_{c,r,out} & \dot{m}_{comp} & T_{a,in} & \dot{m}_{a,in} \end{pmatrix}^T . \tag{3.42}$$

Following a parallel process for the outputs of Eq. (3.1), we find that:

$$\left(\Delta y_e\right)_n = \begin{pmatrix} c_{n1} & c_{n2} + d_{n1}\hat{d}_{13} & c_{n3} & c_{n4} & c_{n5} & c_{n6} \end{pmatrix} \begin{pmatrix} \Delta\zeta_1 \\ \Delta P_e \\ \Delta h_2 \\ \Delta T_{w_1} \\ \Delta T_{w_2} \\ \Delta\bar{\gamma} \end{pmatrix} +$$

$$\begin{pmatrix} d_{n1}\hat{d}_{11} & d_{n1}\hat{d}_{12} & d_{n1}\hat{d}_{14} + d_{n3}\hat{d}_{24} & d_{n2} & d_{n4} & d_{n5} \end{pmatrix} \begin{pmatrix} \Delta o_v \\ \Delta P_c \\ \Delta h_{r,in} \\ \Delta\dot{m}_{comp} \\ \Delta T_{a,in} \\ \Delta\dot{m}_{a,in} \end{pmatrix}$$

where $c_{n1\cdots n6}$ and $d_{n1\cdots n5}$ represent the n^{th} rows of C and D, respectively. This can be written compactly as:

$$\Delta y_e = \bar{C}\Delta x_e + \bar{D}\Delta\bar{u}_e . \tag{3.43}$$

3.5.1.1 Nonlinear and Linear Model Comparison

Figure 3.13 shows the response of the first six outputs of the nonlinear and linear combined EEV/2-zone evaporator models. The seventh output (the cooling capacity) is shown in Figure 3.14. The states of each model are plotted in Figure 3.15. For this simulation, the linear model was linearized about the nominal steady-state operating conditions of the nonlinear model, which are reached before and after each input step. Just as with the individual component models, the combined EEV/evaporator linear and nonlinear models match closely.

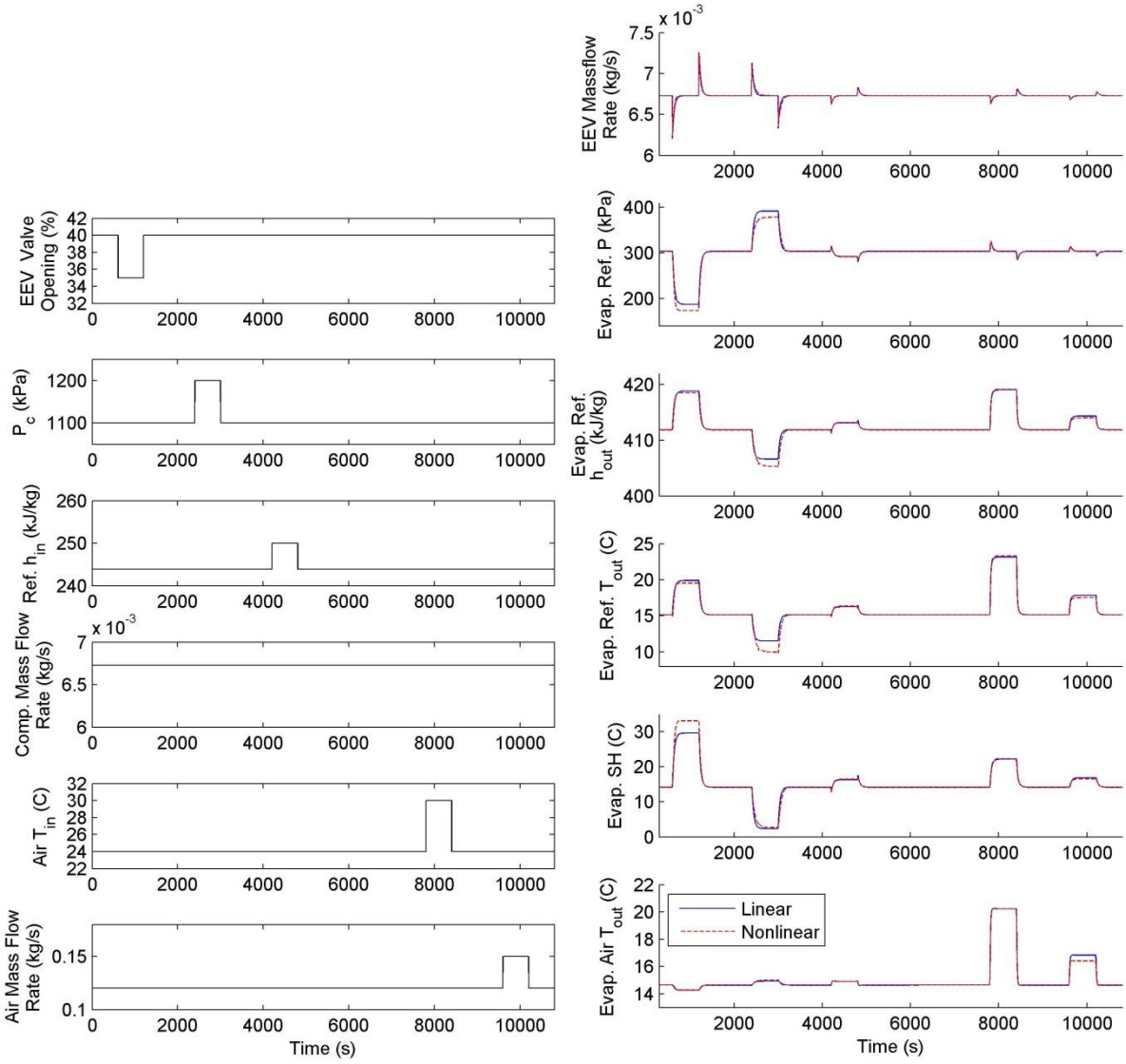

Figure 3.13 Nonlinear and Linear EEV/2-zone Evaporator Comparison—Inputs (left) and First Six Outputs (right)

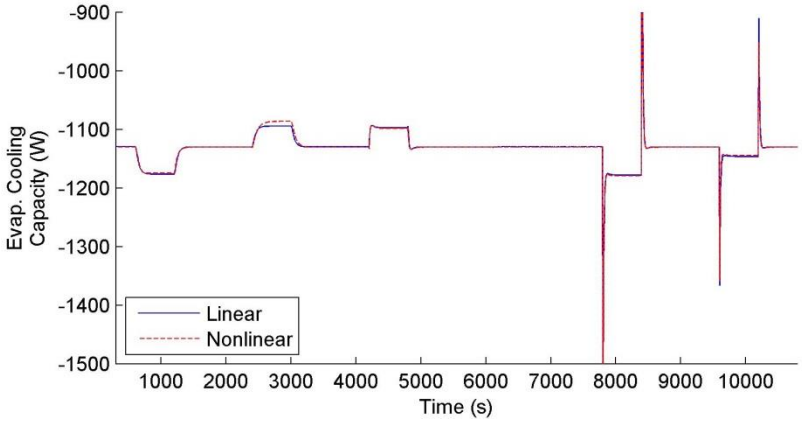

Figure 3.14 Nonlinear and Linear EEV/2-zone Evaporator Comparison—Cooling Capacity Output (right)

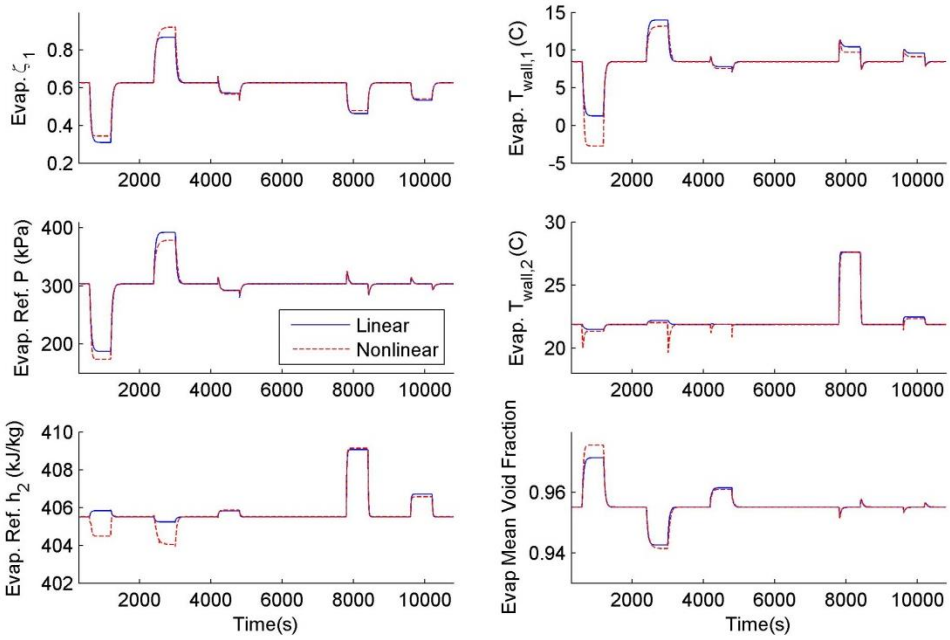

Figure 3.15 Nonlinear and Linear EEV/2-zone Evaporator Comparison—States

3.5.2 Compressor/Condenser Combination

In Section 3.4, two versions of a linear compressor are derived. The first is purely static, while the second includes a dynamic state for the outlet enthalpy. While the static version can be combined with the condenser in a manner similar to how the EEV and evaporator are combined, the dynamic version necessitates a different approach.

3.5.2.1 Static Compressor with Condenser

In combining the static linear compressor and linear evaporator models, the dynamic pressure calculated by the condenser becomes an internal feedback signal to the compressor, as shown in Figure 3.16.

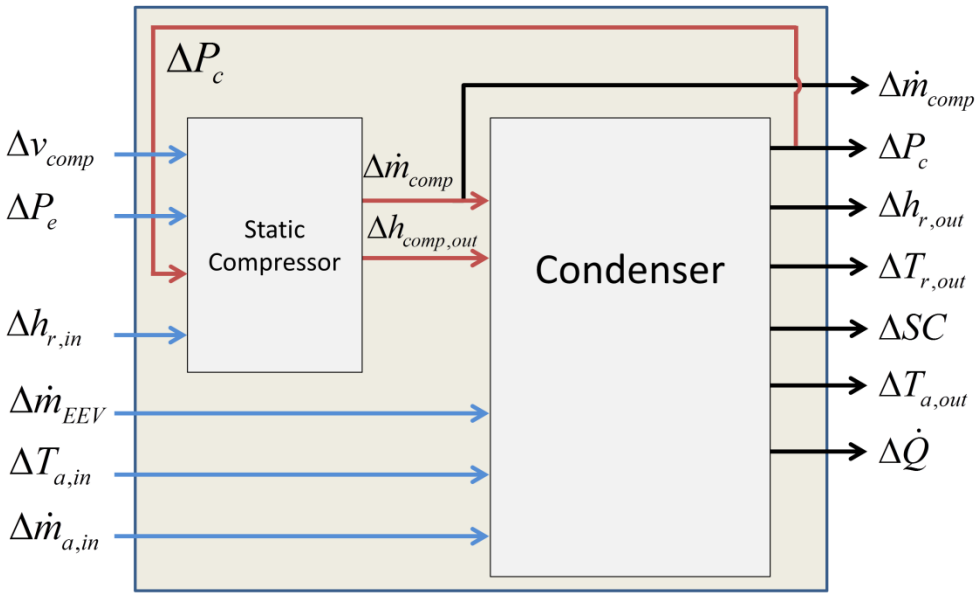

Figure 3.16 Static Compressor and Condenser Combination

As can be seen in Figure 3.16, the $\dot{m}_{r,in}$ and $h_{r,in}$ inputs of the evaporator model are provided by the internal feedforward from $\dot{m}_{comp}$ and $h_{comp,out}$. The n^{th} row of Eq. (3.14) can then be written as:

$$\left(\dot{x}_c\right)_n = \begin{pmatrix} a_1 & \cdots & a_{n9} \end{pmatrix} \begin{pmatrix} \Delta\zeta_1 \\ \Delta\zeta_2 \\ \Delta P_c \\ \Delta h_1 \\ \Delta h_3 \\ \Delta\bar{\gamma} \\ \Delta T_{w_1} \\ \Delta T_{w_2} \\ \Delta T_{w_3} \end{pmatrix} + \begin{pmatrix} b_{n1} & \cdots & b_{n5} \end{pmatrix} \begin{pmatrix} \Delta\dot{m}_{comp} \\ \Delta\dot{m}_{EEV} \\ \Delta h_{comp,out} \\ \Delta T_{a,in} \\ \Delta\dot{m}_{a,in} \end{pmatrix}. \tag{3.44}$$

where $a_{n1\cdots n9}$ and $b_{n1\cdots n5}$ represent the nth rows of $Z_1^{-1}A$ and $Z_1^{-1}B$, respectively. From Eqs. (3.32) and (3.34), we see that $\Delta\dot{m}_{r,comp}$ and $\Delta h_{comp,out}$ in Eq. (3.44) can be expressed in terms of the compressor model's inputs:

$$\begin{aligned}\Delta\dot{m}_{r,comp} &= \begin{pmatrix}\hat{d}_{11} & \cdots & \hat{d}_{14}\end{pmatrix}\begin{pmatrix}\Delta v_{comp}\\ \Delta P_e\\ \Delta P_c\\ \Delta h_{r,in}\end{pmatrix}\\ \Delta h_{comp,out} &= \begin{pmatrix}\hat{d}_{21} & \cdots & \hat{d}_{24}\end{pmatrix}\begin{pmatrix}\Delta v_{comp}\\ \Delta P_e\\ \Delta P_c\\ \Delta h_{r,in}\end{pmatrix}\end{aligned} \tag{3.45}$$

where $\hat{d}$ indicates elements of D_{comp}.

Substituting Eq. (3.45) into (3.44), we can write the state space equation for the combined model as:

$$\begin{aligned}\left(\dot{x}_c\right)_n = &\begin{pmatrix}a_{n1} & \cdots & a_{n9}\end{pmatrix}\begin{pmatrix}\Delta\zeta_1\\ \Delta\zeta_2\\ \Delta P_c\\ \Delta h_1\\ \Delta h_3\\ \Delta\overline{\gamma}\\ \Delta T_{w_1}\\ \Delta T_{w_2}\\ \Delta T_{w_3}\end{pmatrix} + \begin{pmatrix}b_{n2} & b_{n4} & b_{n5}\end{pmatrix}\begin{pmatrix}\Delta\dot{m}_{EEV}\\ \Delta T_{a,in}\\ \Delta\dot{m}_{a,in}\end{pmatrix}\\ &+b_{n1}\begin{pmatrix}\hat{d}_{11} & \cdots & \hat{d}_{14}\end{pmatrix}\begin{pmatrix}\Delta v_{comp}\\ \Delta P_e\\ \Delta P_c\\ \Delta h_{r,in}\end{pmatrix} + b_{n3}\begin{pmatrix}\hat{d}_{21} & \cdots & \hat{d}_{24}\end{pmatrix}\begin{pmatrix}\Delta v_{comp}\\ \Delta P_e\\ \Delta P_c\\ \Delta h_{r,in}\end{pmatrix}\end{aligned} \tag{3.46}$$

Reorganizing the terms in Eq. (3.46), the final state space form becomes:

$$\left(\dot{x}_c\right)_n = \begin{pmatrix} a_{n1} & a_{n2} + b_{n1}\hat{d}_{13} + b_{n3}\hat{d}_{23} & a_{n3} & \cdots & a_{n9} \end{pmatrix} \begin{pmatrix} \Delta\zeta_1 \\ \Delta\zeta_2 \\ \Delta P_c \\ \Delta h_1 \\ \Delta h_3 \\ \Delta\bar{\gamma} \\ \Delta T_{w_1} \\ \Delta T_{w_2} \\ \Delta T_{w_3} \end{pmatrix}$$

$$+ \begin{pmatrix} b_{n1}\hat{d}_{11} + b_{n3}\hat{d}_{21} & b_{n1}\hat{d}_{12} + b_{n3}\hat{d}_{22} & b_{n1}\hat{d}_{14} + b_{n3}\hat{d}_{24} & b_{n2} & b_{n4} & b_{n5} \end{pmatrix} \begin{pmatrix} \Delta v_{comp} \\ \Delta P_e \\ \Delta h_{r,in} \\ \Delta\dot{m}_{EEV} \\ \Delta T_{a,in} \\ \Delta\dot{m}_{a,in} \end{pmatrix} \quad (3.47)$$

Recognizing that $h_{r,in}$ for the compressor is equal to $h_{e,r,out}$, Eq. (3.47) can be written compactly for all rows of $\dot{x}_c$ as:

$$\dot{x}_c = \bar{A}\Delta x_c + \bar{B}\Delta\bar{u}_c \quad (3.48)$$

where $\bar{u}_c$ is the input vector for the combined condenser/compressor model, given by:

$$\begin{pmatrix} v_{comp} & P_e & h_{e,r,out} & \dot{m}_{EEV} & T_{a,in} & \dot{m}_{a,in} \end{pmatrix}^T. \quad (3.49)$$

Following a parallel process for the outputs of Eq. (3.14), we find that:

$$\left(\Delta y_c\right)_n = \begin{pmatrix} c_{n1} & c_{n2} + d_{n1}\hat{d}_{13} + d_{n3}\hat{d}_{23} & c_{n3} & \cdots & c_{n9} \end{pmatrix} \begin{pmatrix} \Delta\zeta_1 \\ \Delta\zeta_2 \\ \Delta P_c \\ \Delta h_1 \\ \Delta h_3 \\ \Delta\bar{\gamma} \\ \Delta T_{w_1} \\ \Delta T_{w_2} \\ \Delta T_{w_3} \end{pmatrix}$$

$$+ \begin{pmatrix} d_{n1}\hat{d}_{11} + d_{n3}\hat{d}_{21} & d_{n1}\hat{d}_{12} + d_{n3}\hat{d}_{22} & d_{n1}\hat{d}_{14} + d_{n3}\hat{d}_{24} & d_{n2} & d_{n4} & d_{n5} \end{pmatrix} \begin{pmatrix} \Delta v_{comp} \\ \Delta P_e \\ \Delta h_{r,in} \\ \Delta\dot{m}_{EEV} \\ \Delta T_{a,in} \\ \Delta\dot{m}_{a,in} \end{pmatrix}$$

where $c_{n1\cdots n9}$ and $d_{n1\cdots n5}$ represent the n^{th} rows of C and D, respectively. This can be written compactly as:

$$\Delta y_c = \bar{C}\Delta x_c + \bar{D}\Delta\bar{u}_c . \tag{3.50}$$

3.5.2.2 Dynamic Compressor with Condenser

Combining the dynamic compressor model with the condenser requires a method for feedback interconnection of two dynamic models. This can be done using the Redheffer star product, which is included in MATLAB as the embedded function ‘lft’. The interconnection of the compressor and condenser can be arranged as depicted in Figure 3.17, which is compatible with the system structure required by ‘lft’.

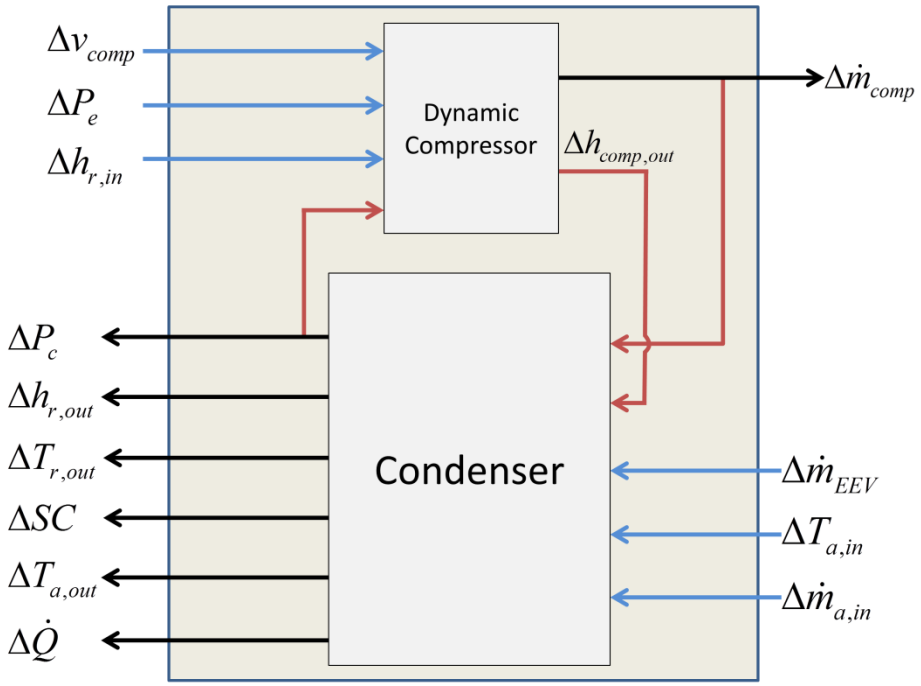

Figure 3.17: Dynamic Compressor and Condenser Combination

The Redheffer Star Product then produces a system of the form:

$$\begin{aligned} \dot{\bar{x}}_c &= \bar{A}\Delta\bar{x}_c + \bar{B}\Delta\bar{u}_c \\ \Delta y_c &= \bar{C}\Delta\bar{x}_c + \bar{D}\Delta\bar{u}_c \end{aligned} \tag{3.51}$$

where

$$\bar{x}_c = \begin{pmatrix} \dot{m}_{comp} & \bar{h}_{comp,out} & \zeta_1 & \zeta_2 & P & h_{r,1} & h_{r,3} & \bar{\gamma} & T_{w,1} & T_{w,2} & T_{w,3} \end{pmatrix}^T. \tag{3.52}$$

Because $\dot{m}_{comp}$ contains no dynamics (i.e. its relevant elements of $\bar{A}$, $\bar{B}$, and $\bar{C}$ are all zeros), it can be removed from the state vector to obtain the system that behaves identically:

$$\begin{aligned} \dot{\bar{\bar{x}}}_c &= \bar{\bar{A}}\Delta\bar{\bar{x}}_c + \bar{\bar{B}}\Delta\bar{\bar{u}}_c \\ y_c &= \bar{\bar{C}}\Delta\bar{\bar{x}}_c + \bar{\bar{D}}\Delta\bar{\bar{u}}_c \end{aligned} \tag{3.53}$$

with

$$\bar{\bar{x}}_c = \begin{pmatrix} \bar{h}_{comp,out} & \zeta_1 & \zeta_2 & P & h_{r,1} & h_{r,3} & \bar{\gamma} & T_{w,1} & T_{w,2} & T_{w,3} \end{pmatrix}^T. \tag{3.54}$$

We again note that the overbar on $\bar{h}_{comp,out}$ is meant to emphasize that this state, while associated with the compressor outlet enthalpy dynamic, does not correspond exactly to that output. Rather, the two are related by Eq. (3.36).

3.5.2.3 Nonlinear and Linear Model Comparison

Figure 3.18 shows the response of the first six outputs of the nonlinear and linear combined compressor/3-zone condenser models. The seventh output (the heating capacity) is shown in Figure 3.19. The states of each model (excluding that associated with the compressor outlet enthalpy) are plotted in Figure 3.20. For this simulation, the linear model was linearized about the nominal steady-state operating conditions of the nonlinear model, which are reached before and after each input step. The linear models with a dynamic and static compressor behave very similarly in this case. However, the differences will become more apparent when the model is combined with the linear EEV/evaporator and receives feedback from the other half of the VCS, as discussed in Section 3.5.3.1.

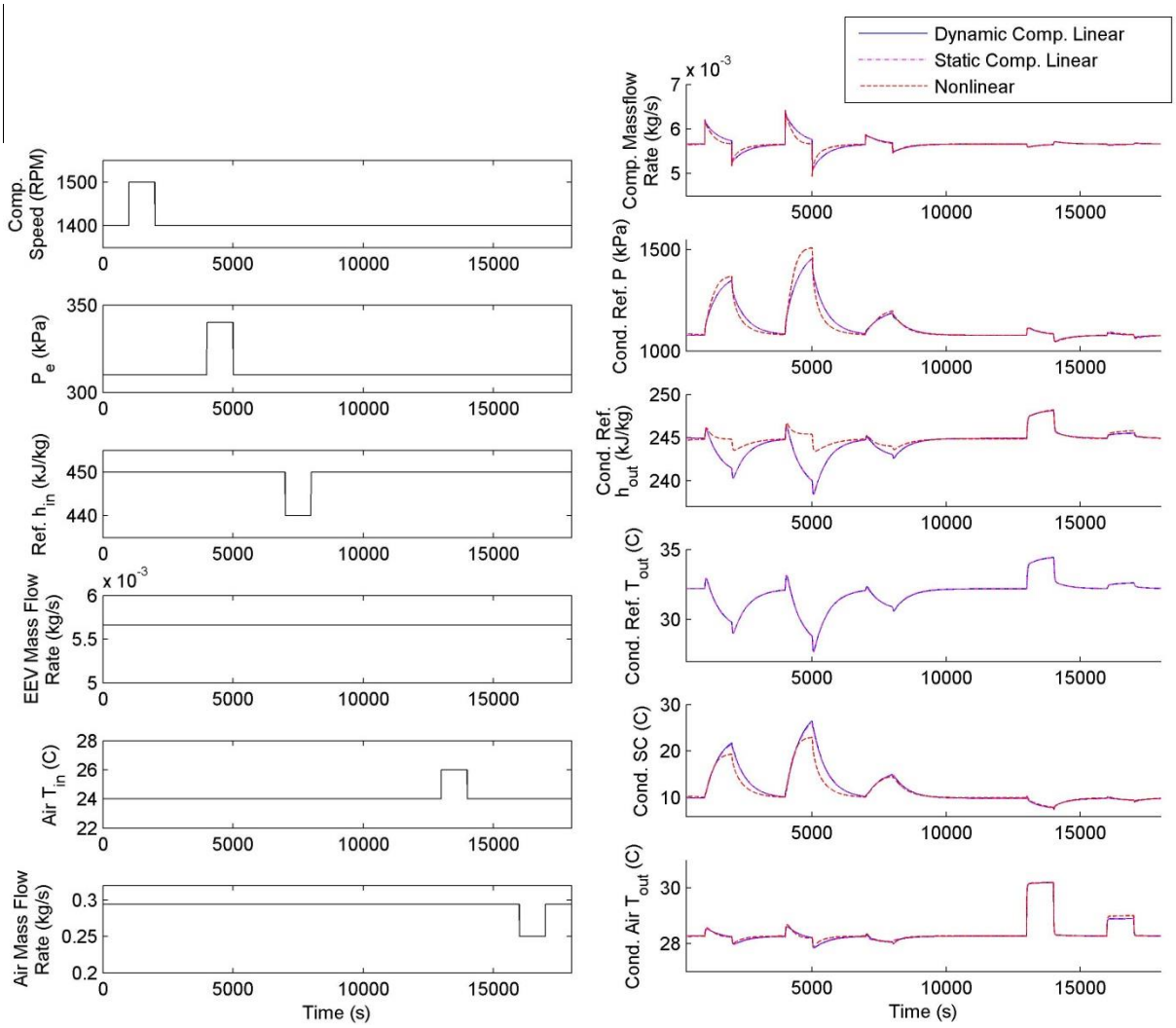

Figure 3.18 Nonlinear and Linear Compressor/3-zone Condenser Comparison—Inputs (left) and First Six Outputs (right)

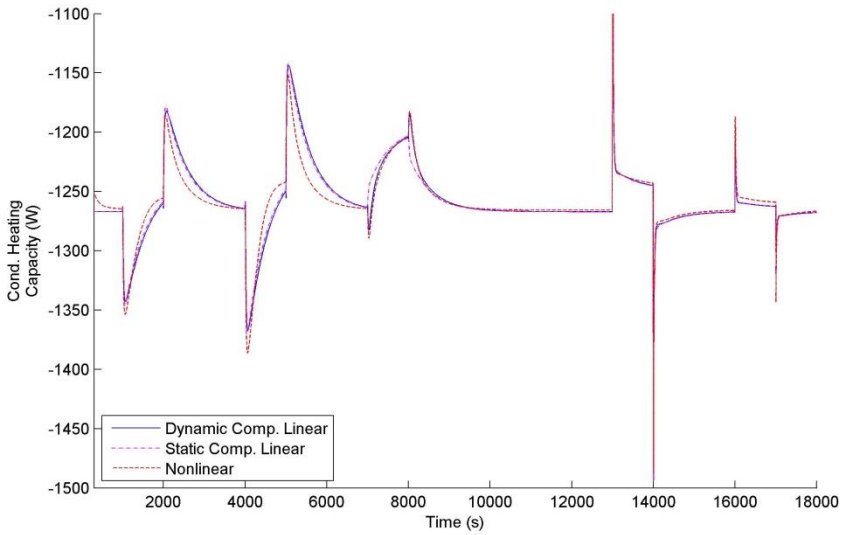

Figure 3.19 Nonlinear and Linear Compressor/3-zone Condenser Comparison—Heating Capacity Output

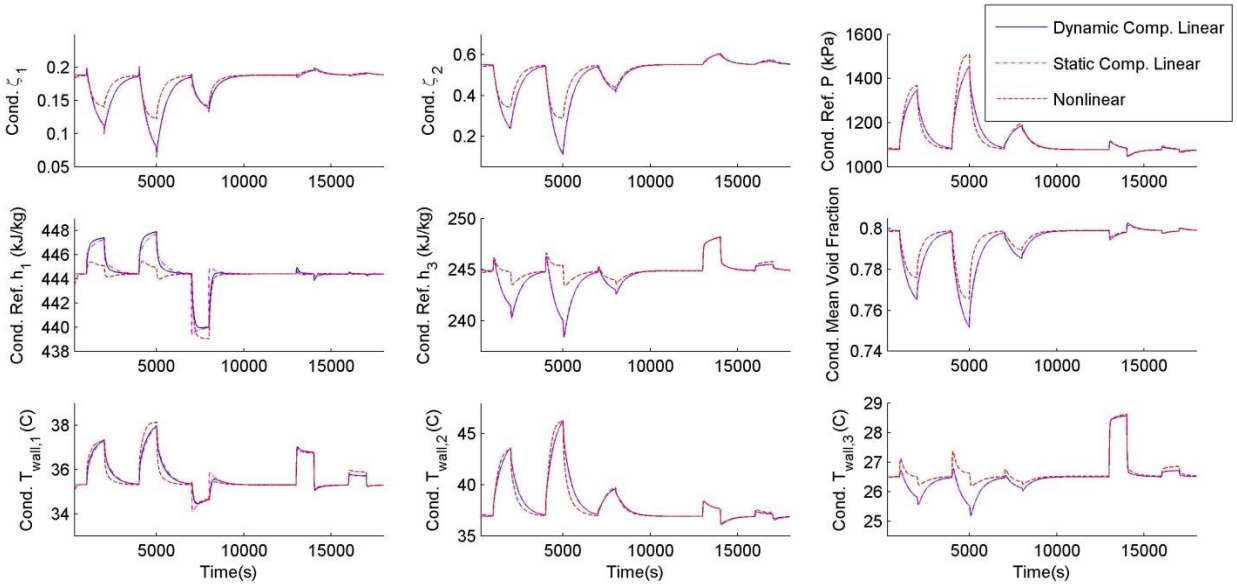

Figure 3.20 Nonlinear and Linear Compressor/3-zone Condenser Comparison —States

3.5.3 Full System Assembly

The Redheffer Star Product and embedded MATLAB function ‘lft’ are again used to combine the EEV/evaporator and compressor/condenser subsystem models into a linear four-component VCS model. Figure 3.21 depicts this interconnection of the two subsystems. Note

that the ordering of inputs and outputs of the subsystems has been adjusted in order to group the feedback signals together.

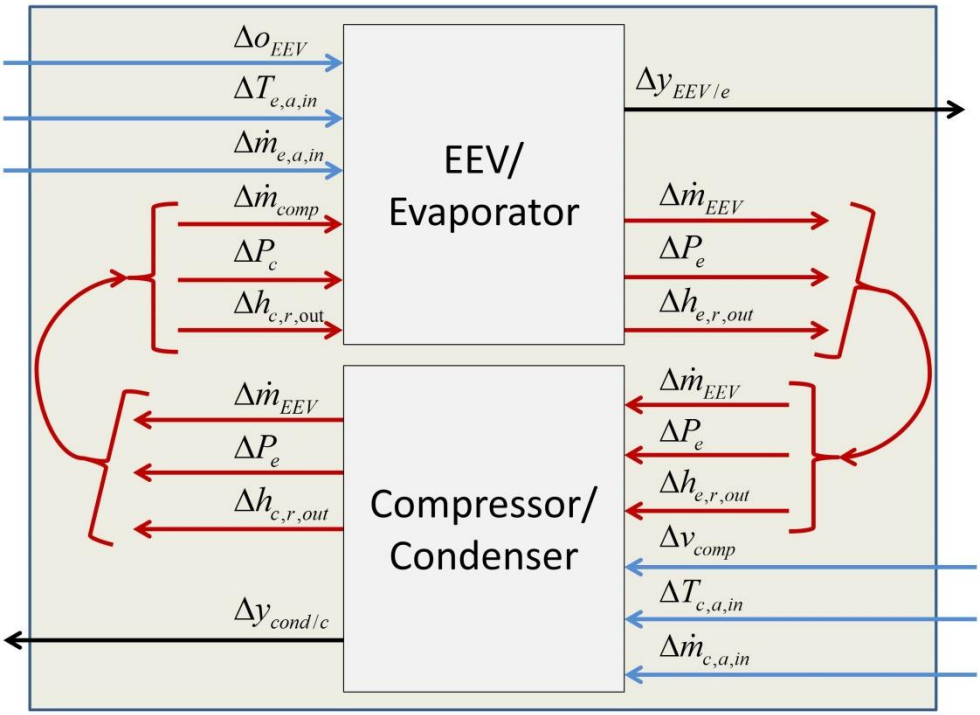

Figure 3.21: Subsystem Interconnection

The resulting linear four-component VCS model takes the form

$$\begin{aligned} \dot{x}_{sys} &= A_{sys}\Delta x_{sys} + B_{sys}\Delta u_{sys} \\ \Delta y_{sys} &= C_{sys}\Delta x_{sys} + D_{sys}\Delta u_{sys} \end{aligned} \tag{3.55}$$

where

$$\begin{aligned} u_{sys} &= \begin{pmatrix} o_{EEV} & T_{e,a,in} & \dot{m}_{e,a,in} & v_{comp} & T_{c,a,in} & \dot{m}_{c,a,in} \end{pmatrix}^T \\ y_{sys} &= \begin{pmatrix} y_{EEV/e} & y_{cond/c} \end{pmatrix}^T \\ &= \begin{pmatrix} \dot{m}_{EEV} & P_e & h_{e,r,out} & T_{e,r,out} & SH & T_{e,a,out} & \dot{Q}_e & \dot{m}_{comp} & P_c & h_{c,r,out} & T_{c,r,out} & SC & T_{c,a,out} & \dot{Q}_c \end{pmatrix}^T \end{aligned} \tag{3.56}$$

and

$$x_{sys} = \begin{pmatrix} x_e & x_c \end{pmatrix}^T \quad \text{or} \quad x_{sys} = \begin{pmatrix} x_e & \bar{\bar{x}}_c \end{pmatrix}^T . \tag{3.57}$$

The ‘or’ in Eq. (3.57) is determined by whether the static or dynamic compressor model is used, the difference being that $\bar{\bar{x}}_c$ includes one additional state for the compressor outlet enthalpy dynamic.

3.5.3.1 Nonlinear and Linear ‘3-2’ Model Comparison

We now compare a nonlinear VCS model using the SMB heat exchangers with the full system linear model described above. We first consider the case where the nonlinear and linear heat exchangers operate in Mode 1 at all times. The linear model is therefore generated by the combination of the linear Mode 1 evaporator and linear Mode 1 condenser models with the linear compressor and EEV, and linearized about the nominal steady-state operating conditions of the nonlinear model reached before and after each input step. Because Mode 1 for the condenser includes three refrigerant phase zones (superheated, two-phase, and subcooled) and Mode 1 of the evaporator includes two refrigerant phase zones (two-phase and superheated), we refer to this as the ‘3-2’ VCS mode.

Figure 3.22 shows the sequence of inputs used to compare the nonlinear and linear VCS models. The inputs are chosen such that the nonlinear system at all times remains in the ‘3-2’ mode. Figure 3.23 shows the output response of the first six outputs of each heat exchanger, and Figure 3.24 shows the seventh output. Figure 3.25 and Figure 3.26 show the states of the evaporator and condenser, respectively.

It is clear from these figures that the nonlinear and linear models match fairly well. Although not all gains of the linear model match the nonlinear model, the outputs and states consistently step in the correct direction. The difference between the linear models with and without the compressor enthalpy dynamic is visible in the subplot of $h_{r,1}$ in Figure 3.26. The former matches the time constant of the response in the nonlinear model, while the latter has a faster response. However, this difference is small enough that for most applications of the linear model, including the estimation and control design of Chapter 6, the added accuracy due to including the compressor enthalpy dynamic is not worth the added model complexity that it brings.

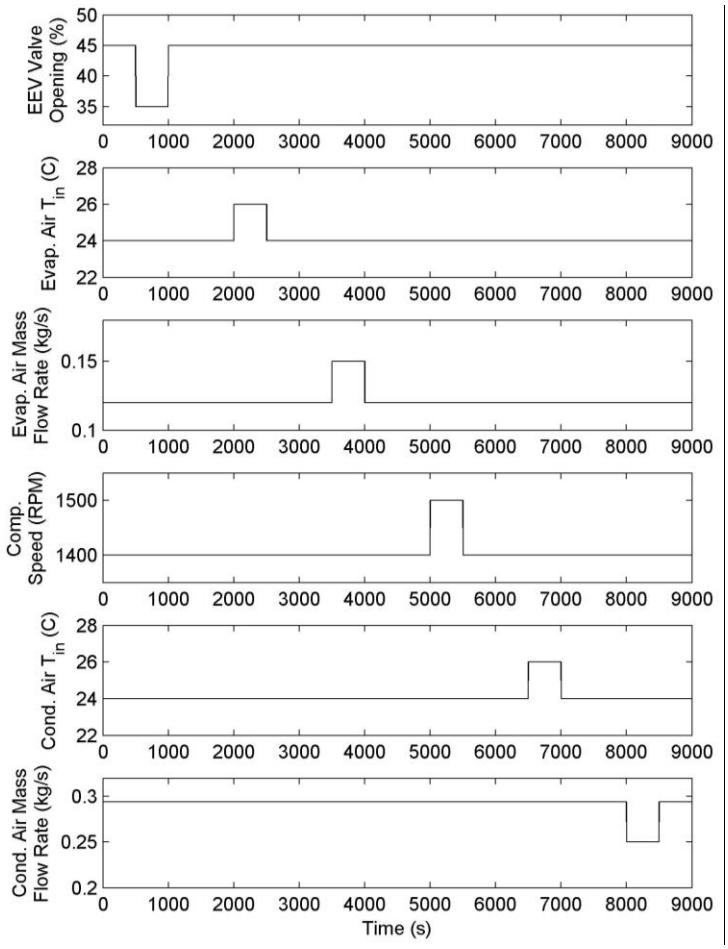

Figure 3.22 Nonlinear and Linear VCS Comparison—Inputs

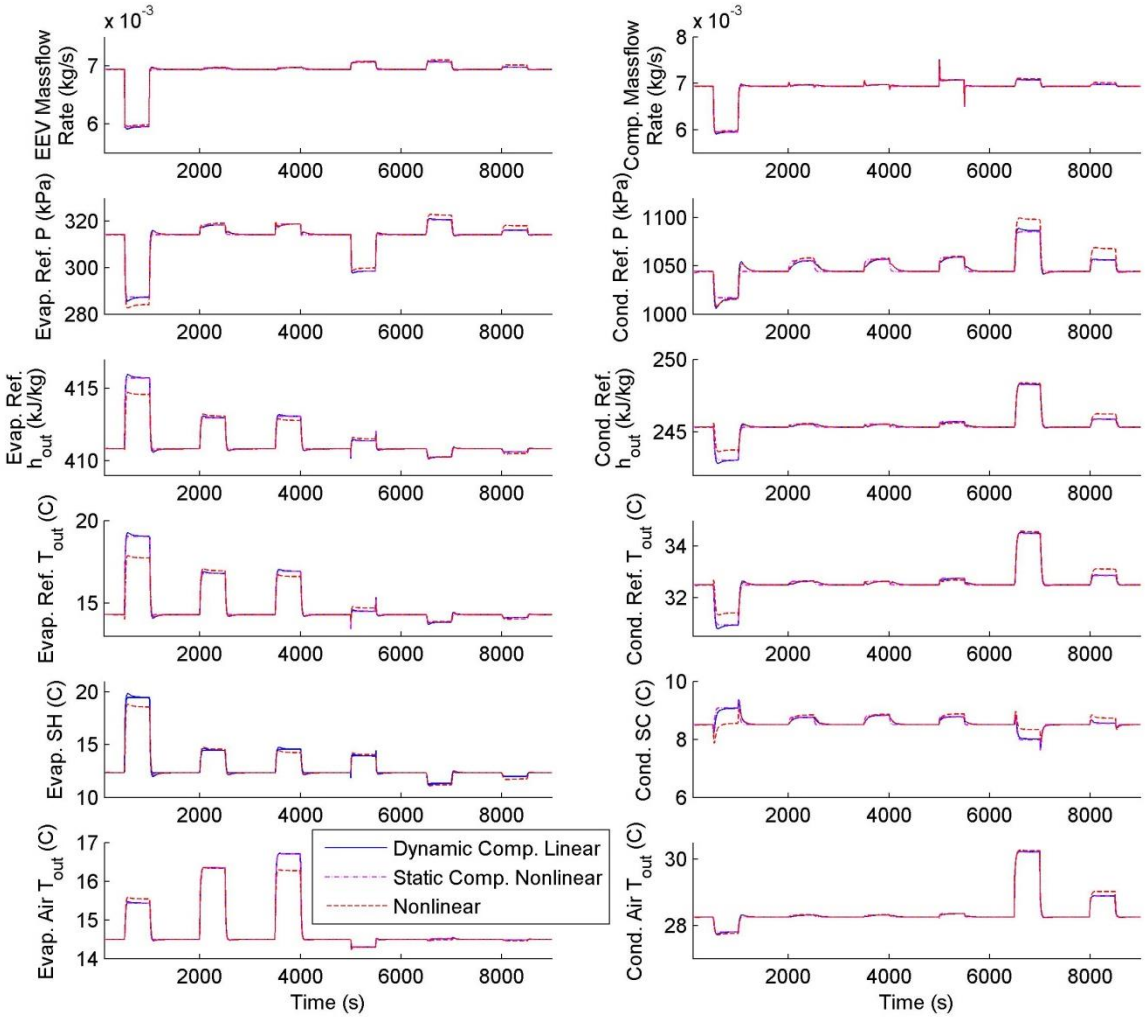

Figure 3.23 Nonlinear and Linear VCS Comparison—First Six Outputs of Each Heat Exchanger

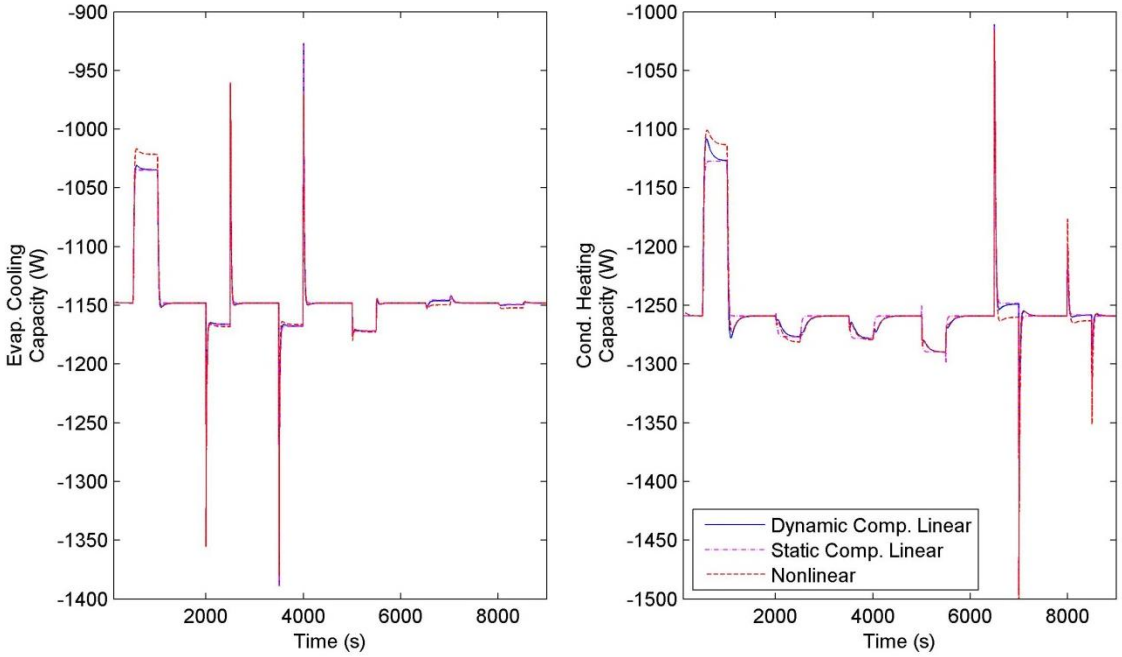

Figure 3.24 Nonlinear and Linear VCS Comparison—Seventh Heat Exchanger Output

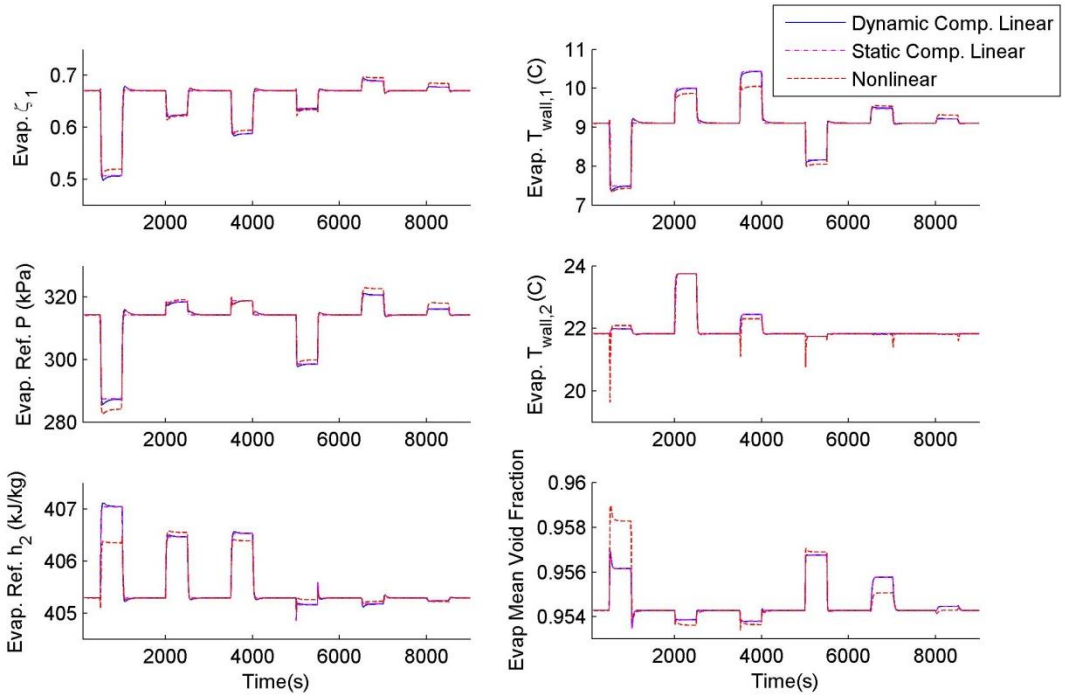

Figure 3.25 Nonlinear and Linear VCS Comparison—Evaporator States

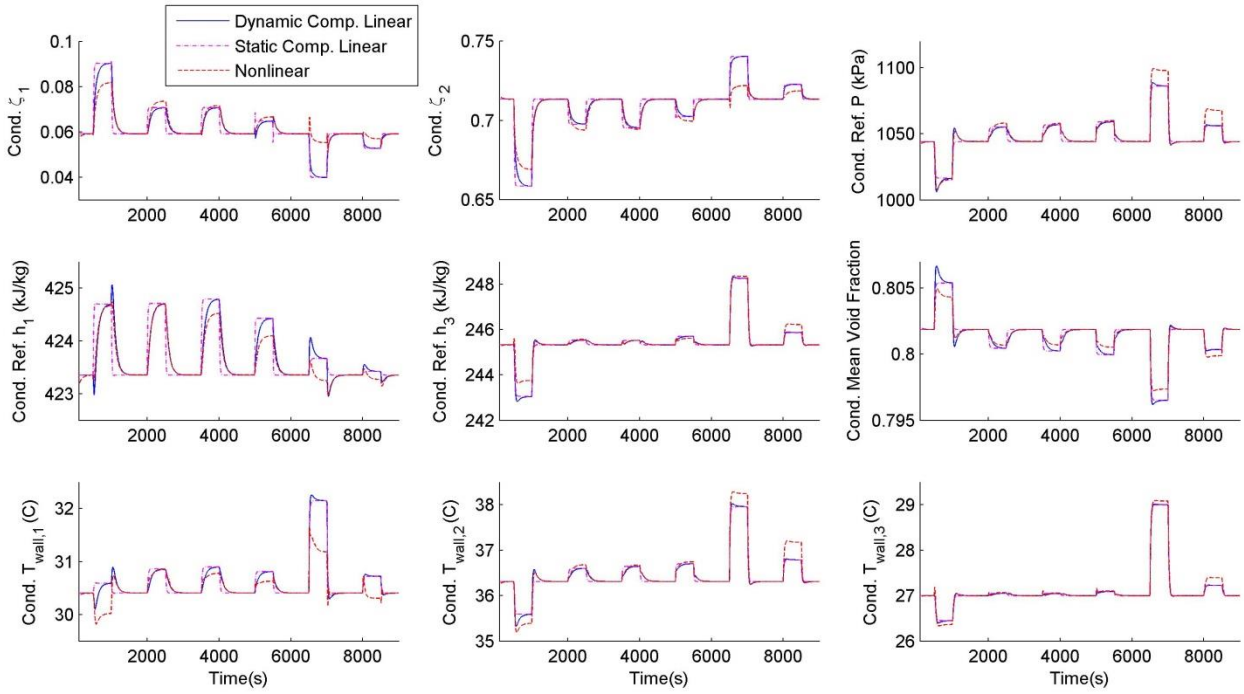

Figure 3.26 Nonlinear and Linear VCS Comparison—Condenser States

3.5.3.2 Nonlinear and Linear '3-1' Model Comparison

We next consider the case where the condenser operates in Mode 1 at all times and the evaporator operates in Mode 2 at all times. The linear model is therefore generated by the combination of the linear Mode 1 condenser models and linear Mode 2 evaporator with the linear compressor and EEV, and linearized about the nominal steady-state operating conditions of the nonlinear model reached before and after each input step. Because Mode 1 for the condenser includes three refrigerant phase zones (superheated, two-phase, and subcooled) and Mode 2 of the evaporator includes only a two-phase zone, we refer to this as the '3-1' VCS mode.

Figure 3.27 shows the sequence of inputs used to compare the nonlinear and linear VCS models. The inputs are chosen such that the nonlinear system remains in the '3-1' mode through all the input steps. Figure 3.28 shows the output response of the first six outputs of each heat exchanger, and Figure 3.29 shows the seventh output. Figure 3.30 and Figure 3.31 show the states of the evaporator and condenser, respectively.

We can see from these figures that the linear models with and without the compressor enthalpy dynamic are essentially equivalent. It is also clear that the match between the linear and nonlinear models is worse than for the '3-2' model. The gains of the linear model do not tend to

match the nonlinear model as closely, although the outputs and states generally step in the correct direction. This increased mismatch is due to highly nonlinear behavior known to be associated with the two-phase refrigerant that has been exposed at the outlet of the evaporator in the absence of a superheated zone. This nonlinearity can be seen, for example, at high and low quality values of refrigerant heat transfer coefficient, plotted in Figure 2.8. Although this might at first imply that the linear '3-1' model is not sufficiently accurate to be of any value, we recall that the motivation for creating the linear models is not for use in open-loop VCS simulations, but instead for their incorporation into model-based state estimation and control designs. We show in Chapter 6 that through the use of designs that include feedback from the plant and are robust to model error, the linear '3-1' model can be quite effective for these purposes.

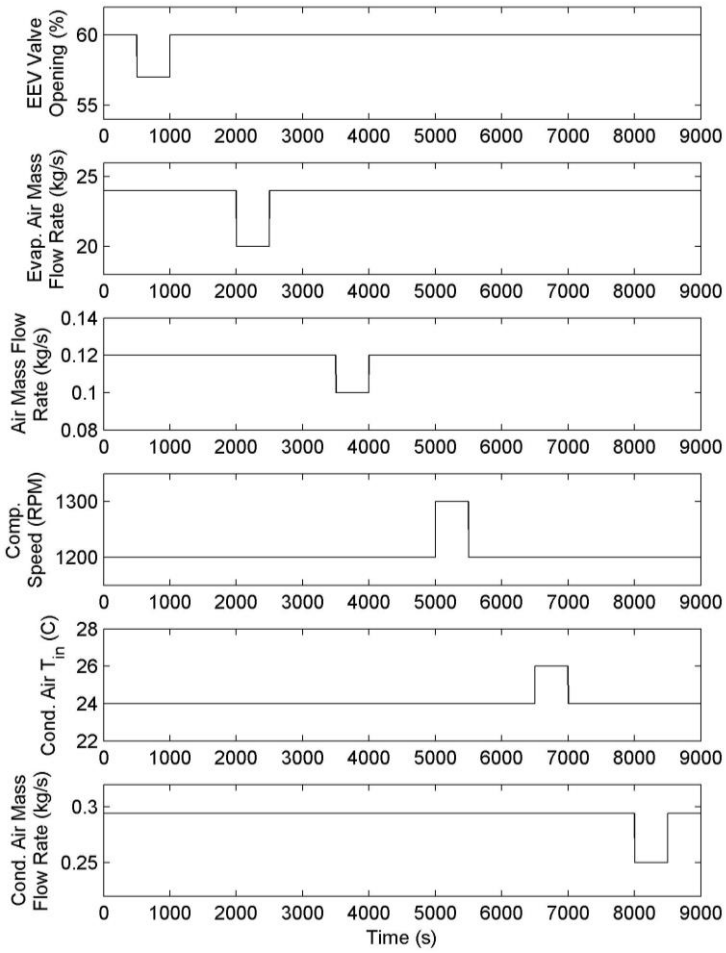

Figure 3.27 Nonlinear and Linear VCS Comparison—Inputs

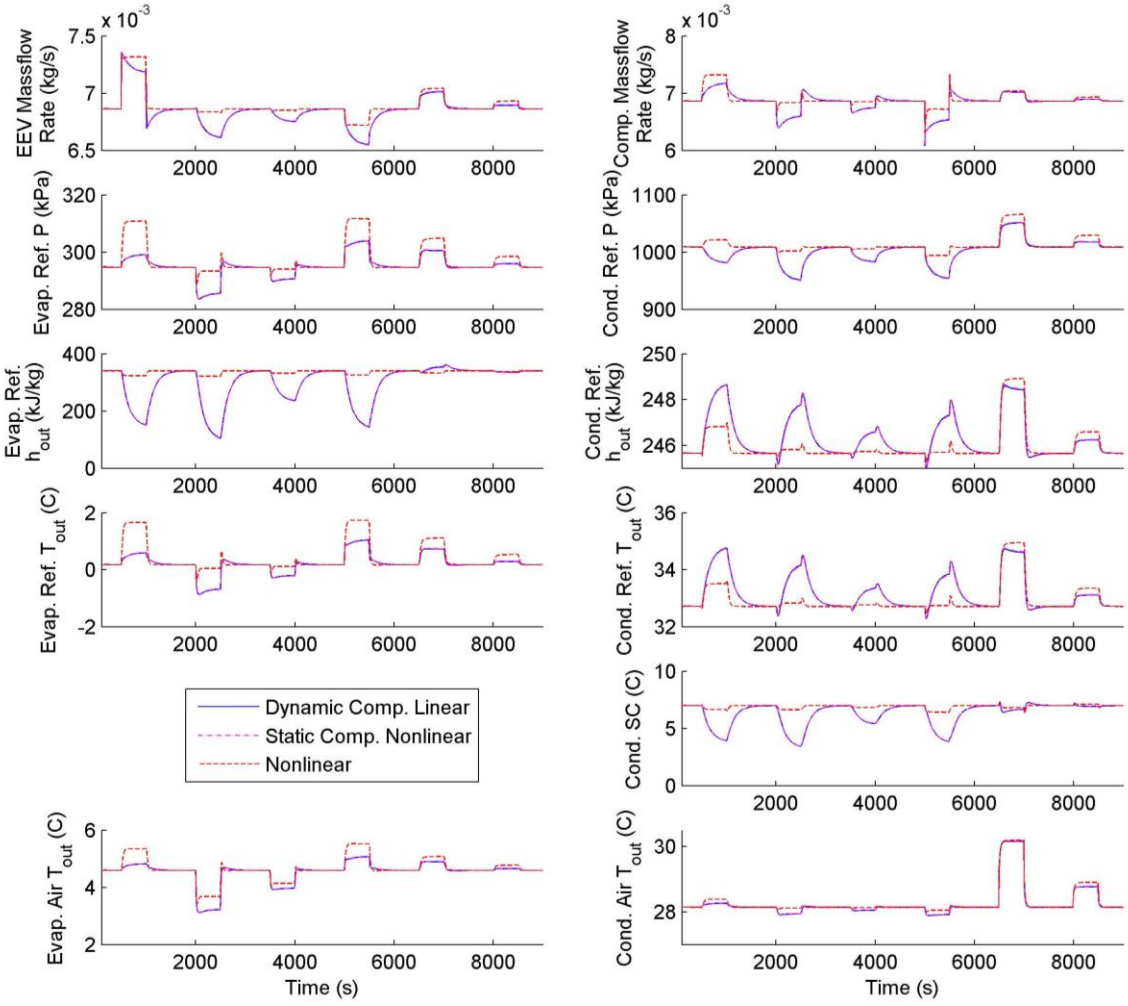

Figure 3.28 Nonlinear and Linear VCS Comparison—First Six Outputs of Each Heat Exchanger

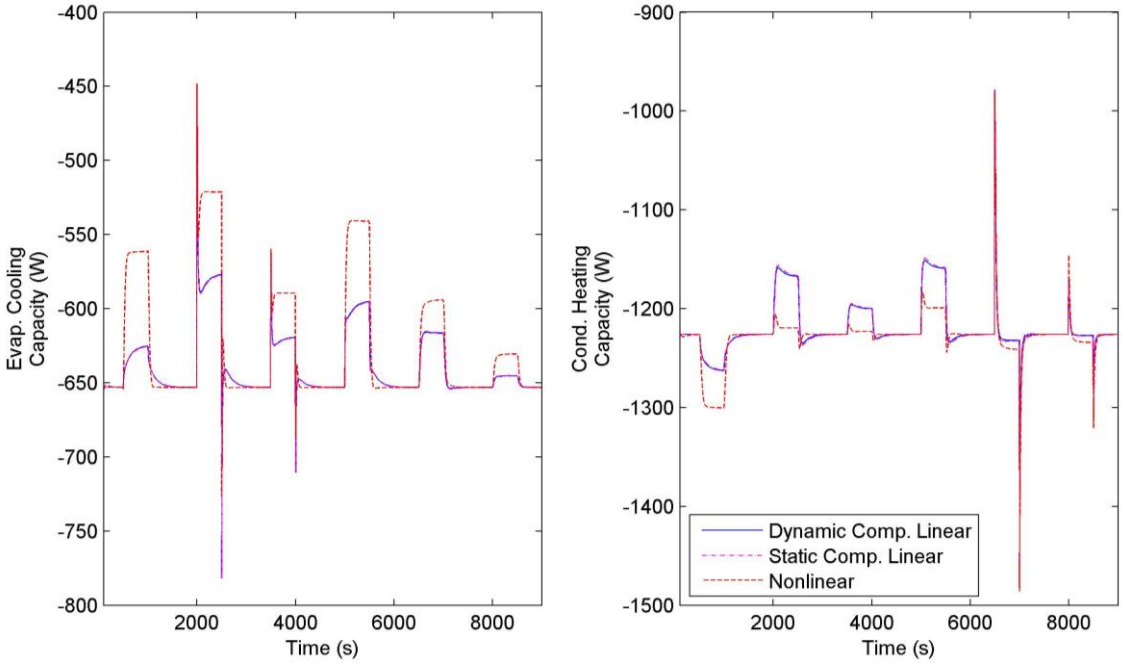

Figure 3.29 Nonlinear and Linear VCS Comparison—Seventh Heat Exchanger Output

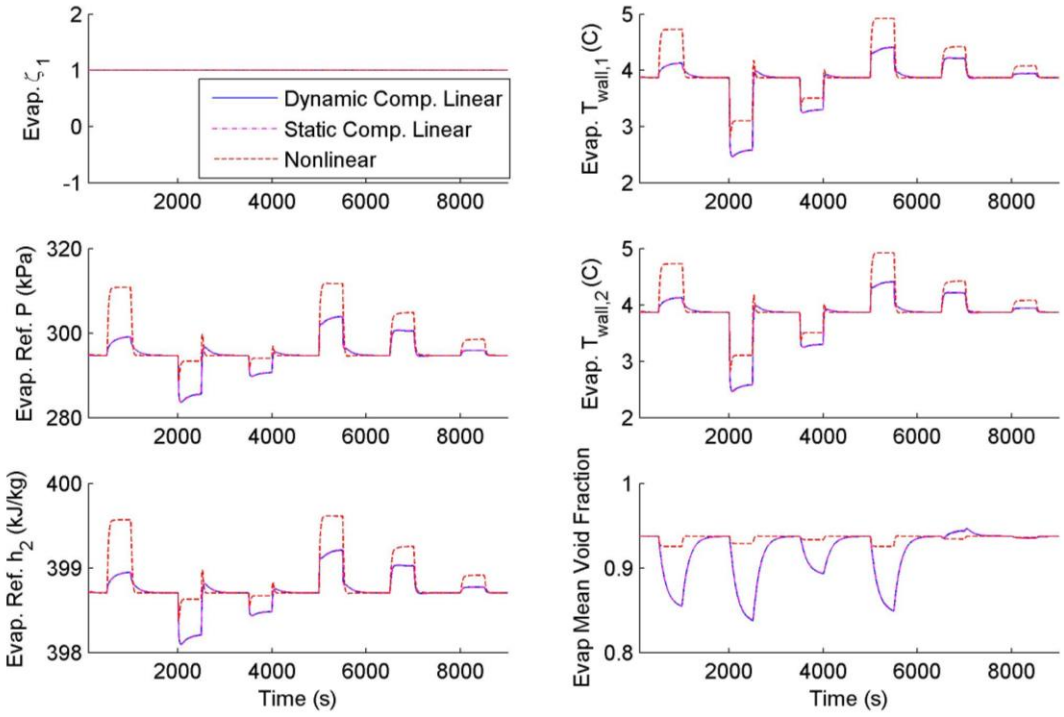

Figure 3.30 Nonlinear and Linear VCS Comparison—Evaporator States

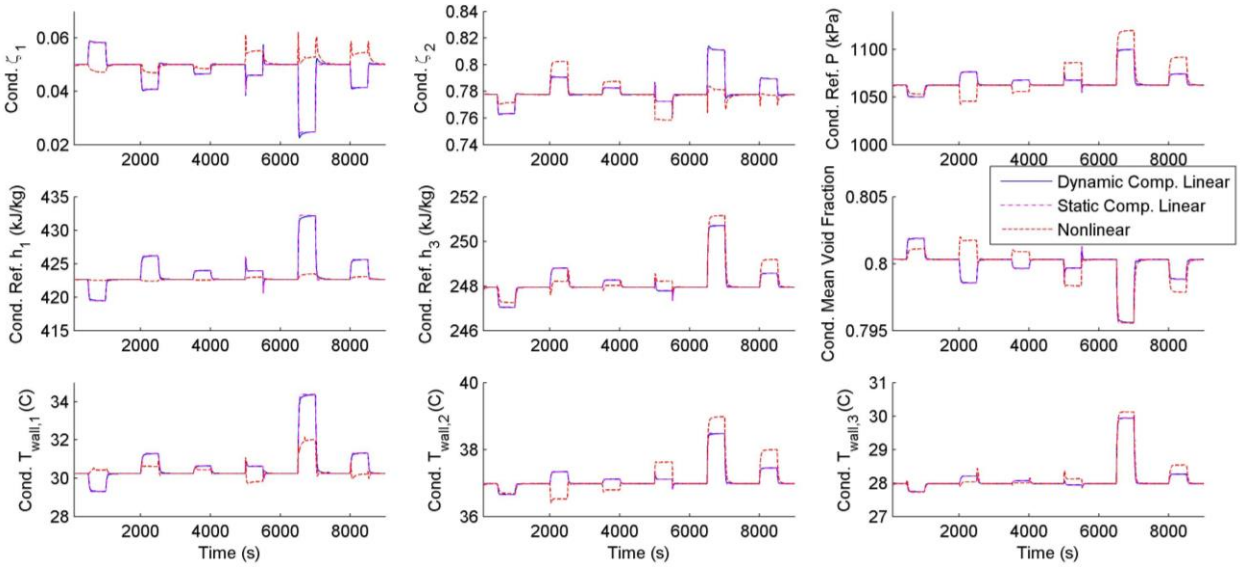

Figure 3.31 Nonlinear and Linear VCS Comparison—Condenser States

Chapter 4

Model Validation and Comparison

Model validation and accuracy comparison of the FV, SMB, and linear formulations was conducted using data from the experimental test stand described in [19]. This test stand has been used extensively for model and control validation in other work, including [14] and [17]. The stand was configured as a 4-component VCS consisting of a tube and fin evaporator, a compressor, a tube and fin condenser, and an EEV. Simulation of the models was implemented using the Thermosys™ toolbox for MATLAB/Simulink®, developed at the University of Illinois at Urbana-Champaign. Work included here has been published in [5]. Section 4.1 shows the actuator inputs provided to the experimental system. Section 4.2 shows the resulting validation data. Section 4.3 outlines the method of simulation and compares the data and simulation results. Section 4.4 compares the simulation speeds of each modeling approach. Lastly, section 4.5 summarizes the tradeoffs associated with each modeling approach.

4.1 Actuator Inputs

Figure 4.1 shows the steps in compressor speed and valve opening used to validate and compare the models. When collecting data, a sequence with one step of each actuator was repeated five times in order to observe the variability inherent in the experimental system. The speeds of the fans blowing air across each heat exchanger were held constant during data collection, and have been calibrated as corresponding to air mass flow rates of 0.29 kg/s for the condenser, and 0.121 kg/s for the evaporator.

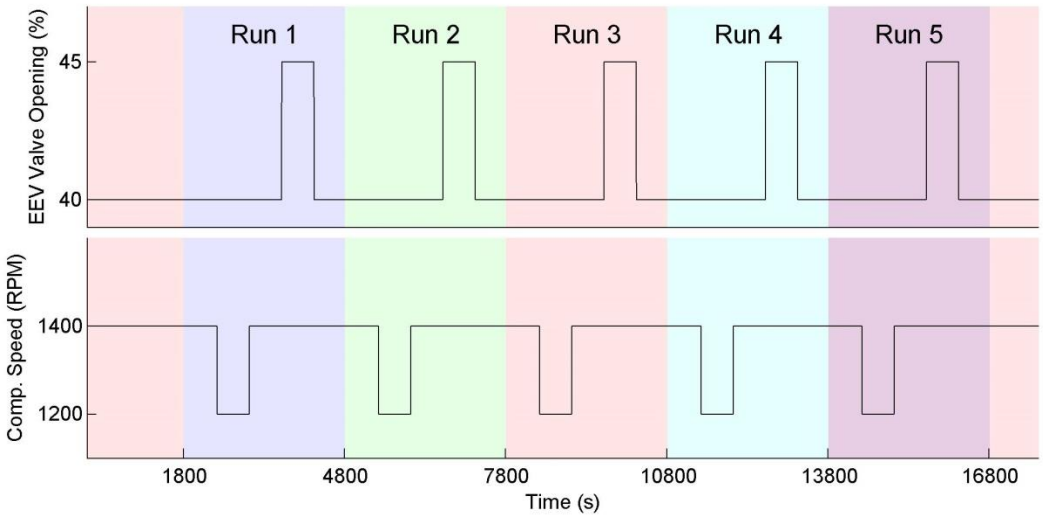

Figure 4.1 Actuator Step Inputs to Experimental System

4.2 Experimental Data

Figure 4.2 and Figure 4.3 show outputs measured from the experimental system for the condenser and evaporator, respectively. The outputs for each repetition of the actuator inputs have been superimposed. One can see that there appears to be a consistent drift in some of the outputs. For example, both the evaporator and condenser pressures increase slightly with each repetition. This drift is thought to be due to the gradual temperature change of large thermal masses in the experimental system, such as the metal body of the compressor, which evolves over a timescale of hours. Air inlet temperatures were also measured as part of the data collection, and are plotted in Figure 4.4. These were treated as disturbances to the models in simulation. The ambient relative humidity of the experimental facility was measured periodically throughout the duration of data collection, and found to remain constant at approximately 50%.

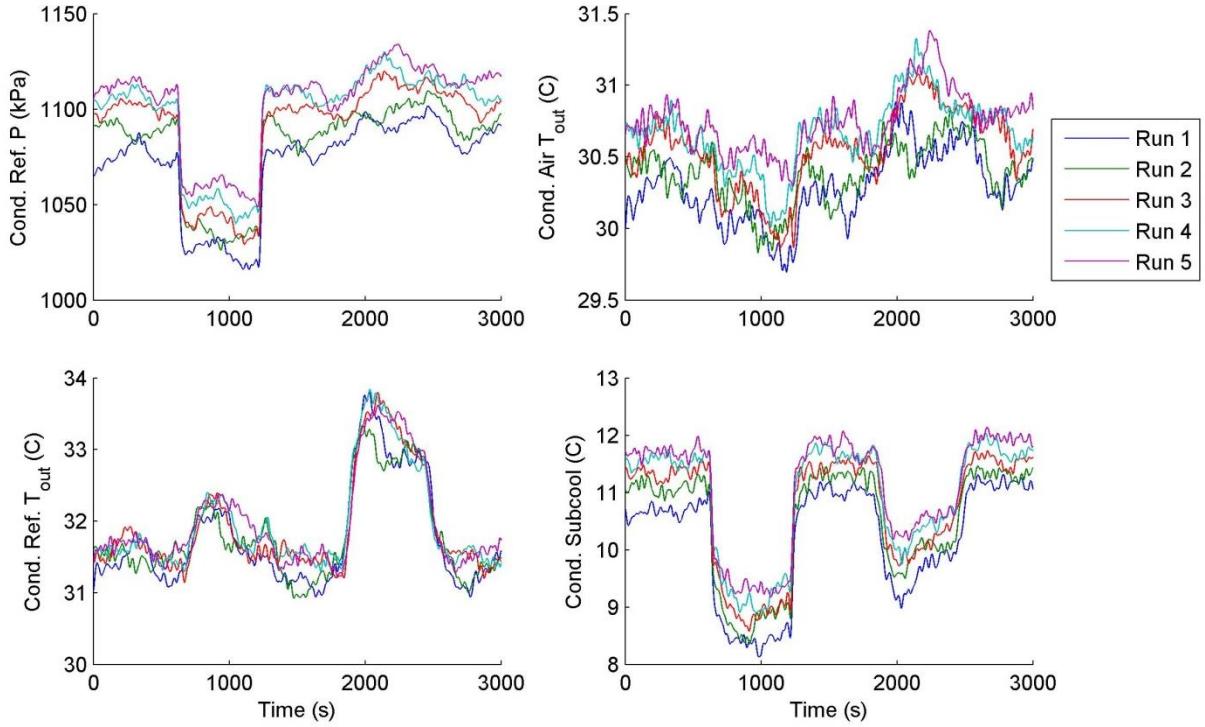

Figure 4.2 Condenser Data

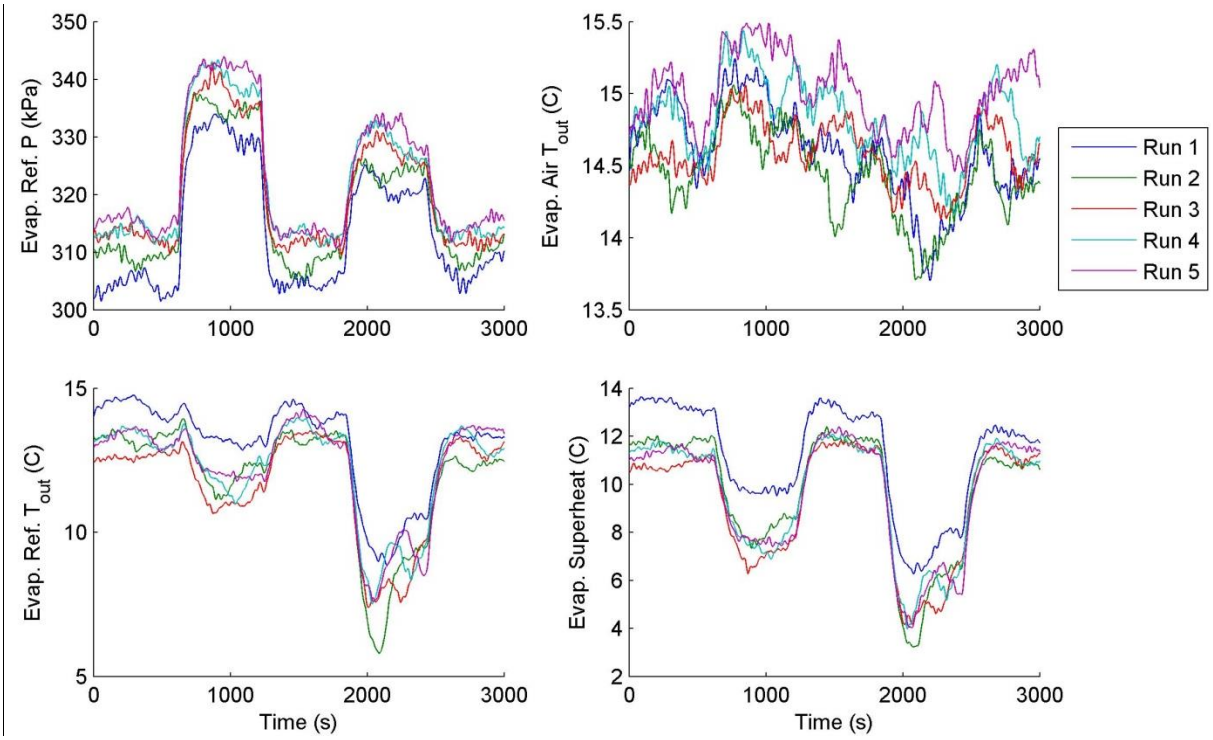

Figure 4.3 Evaporator Data

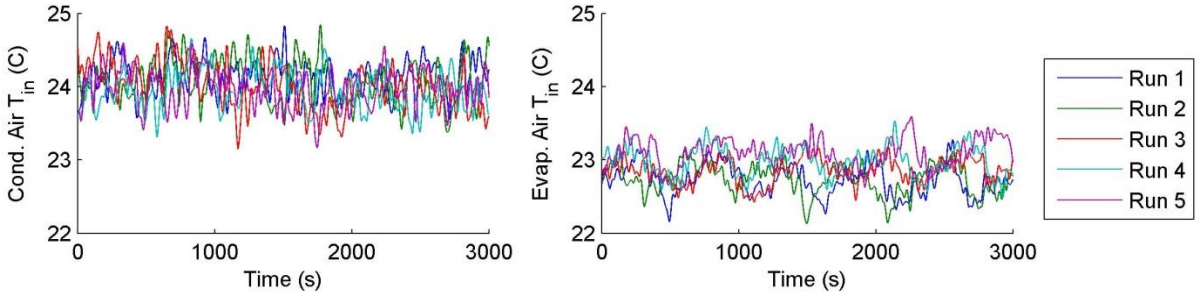

Figure 4.4 Air Inlet Temperatures

4.3 Simulation Results

Nonlinear models of the experimental system using both SMB and FV heat exchangers, as well as a linear VCS model, were simulated over the actuator inputs of Figure 4.1. The measured air inlet temperatures shown in Figure 4.4 were also provided to the heat exchanger models as disturbances. The linear model consisted of a 3-zone condenser and 2-zone evaporator and was linearized about the steady-state conditions exhibited by the SMB model when operating a valve opening of 40%, compressor speed of 1400 RPM, and at the average of the air inlet temperatures for each heat exchanger.

The simulations were sampled only every 5s in order to allow the variable step solver a maximum time step of the same value. To allow the heat exchanger models to better match their physical equivalents in the experimental system, tuning was conducted to account for unmodeled phenomenon such as fin configuration. This tuning consisted of constant scaling factors applied to the air HTC and the refrigerant HTCs for each refrigerant phase, which were determined empirically based on comparison of data and simulation results. SMB and FV models were tuned independently. The FV model was tuned using simulations with 200 CVs. Initial conditions for states that were measured in the experimental system (such as the refrigerant pressures) were taken from data. Initial conditions for states that were not measured (such as the refrigerant enthalpy of each CV) were extracted from profile assumptions on the initial flow characteristics given available measurements of inlet and outlet conditions. These initial conditions help to ensure that simulations begin with the proper amount of refrigerant charge.

Figure 4.5 and Figure 4.6 show simulation outputs for VCS models using both SMB and FV heat exchanger components. For the FV models, results from several different quantities of CVs are provided. These plots are superimposed over an envelope composed of the maximum and minimum values of the experimental data from all five runs at each time step. Figure 4.7 and

Figure 4.8 show simulation outputs of the SMB and linear models. The superheat and subcool of the heat exchangers was calculated from saturation temperature property tables for R134a and the model outputs of pressure and refrigerant outlet temperature.

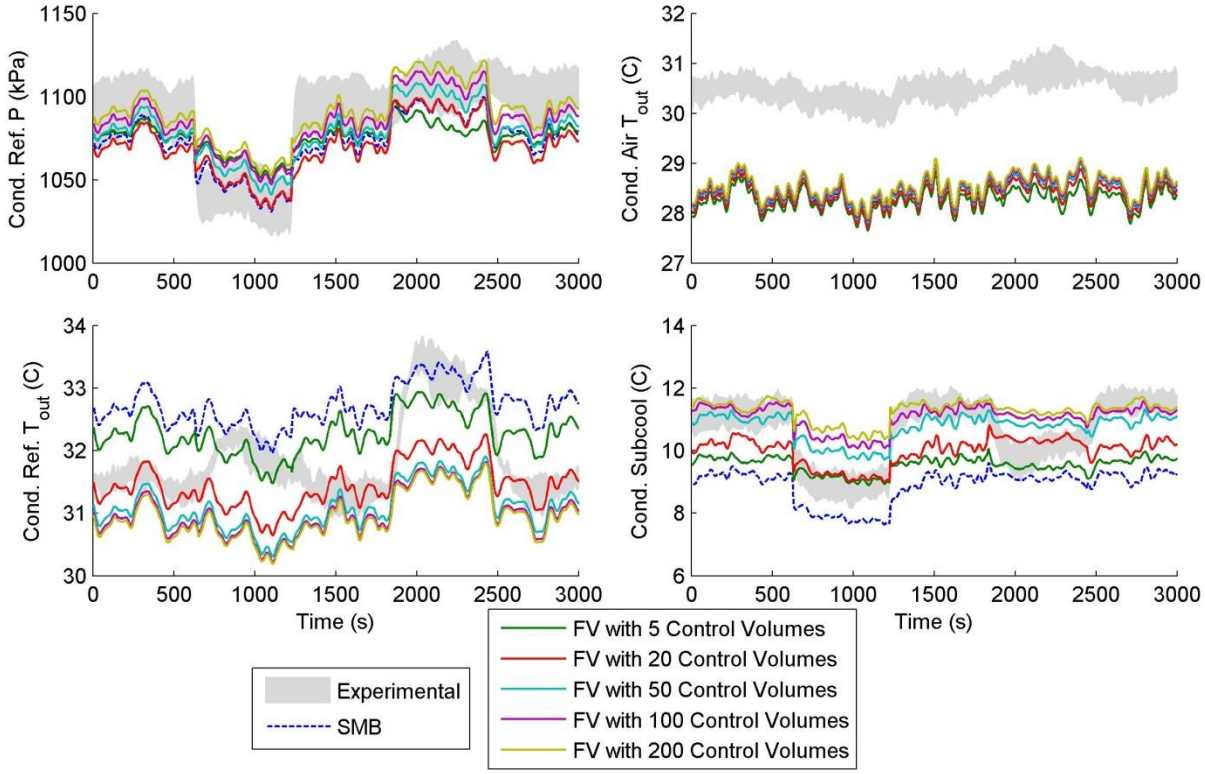

Figure 4.5 SMB/FV Condenser Outputs and Experimental Data

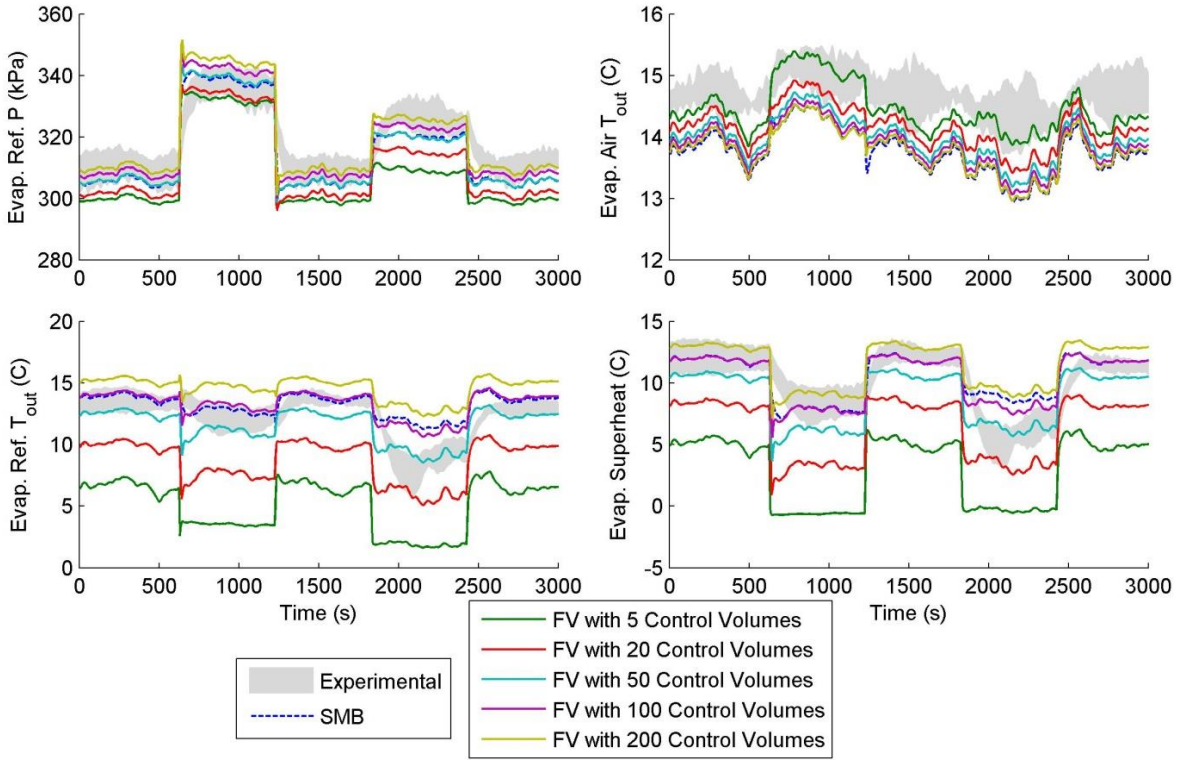

Figure 4.6 SMB/FV Evaporator Outputs and Experimental Data

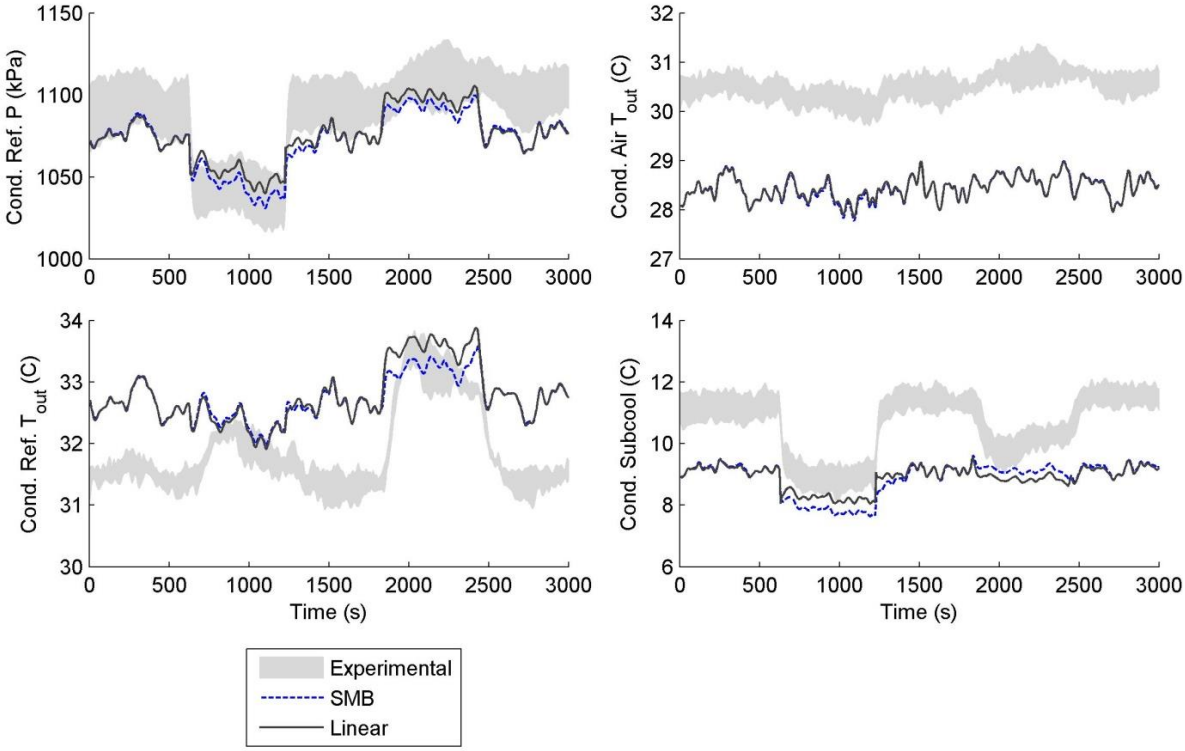

Figure 4.7 SMB/Linear Condenser Outputs and Experimental Data

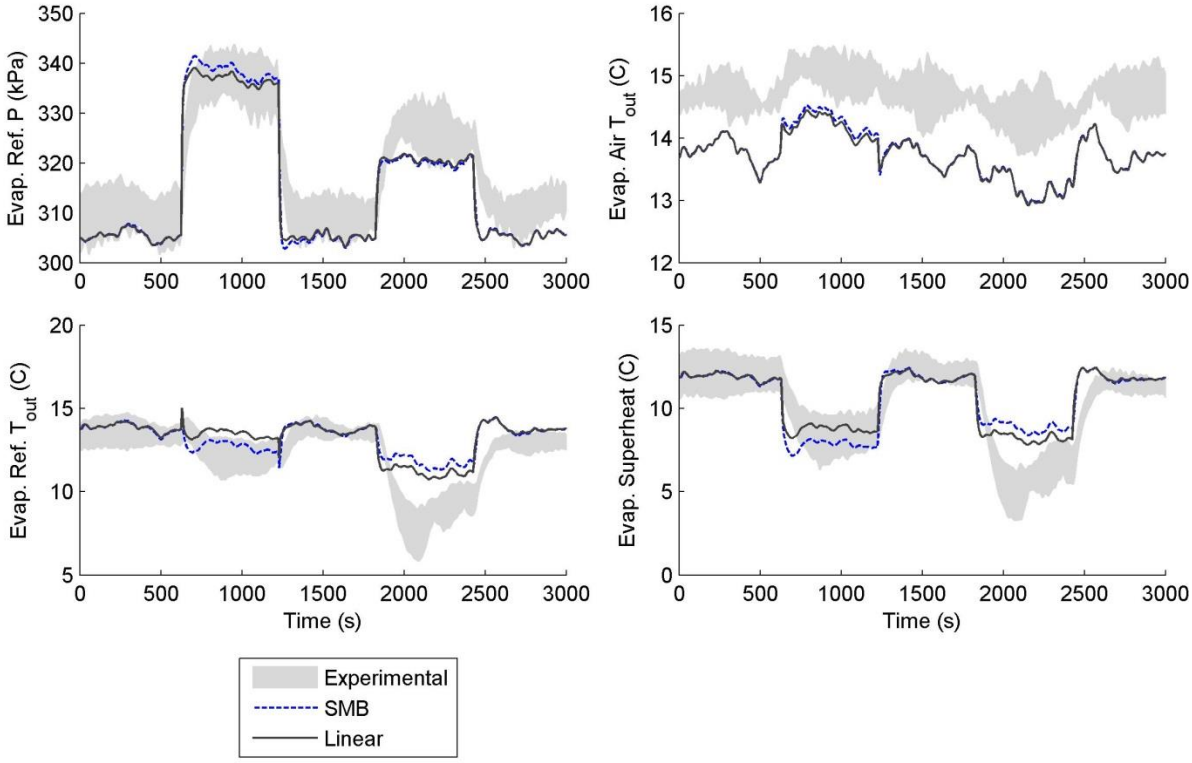

Figure 4.8 SMB/Linear Evaporator Outputs and Experimental Data

Figure 4.9 and Figure 4.10 show the normalized error residual of the simulation results as compared to the mean value at each time step of all five runs of the experimental data. This is computed by:

$$\text{Normalized Error Residual} = \frac{\sum_{k=1}^{end}\left(\text{simulation(k)-experimental(k)}\right)^2}{\sum_{k=1}^{end}\text{experimental(k)}^2}. \quad (4.1)$$

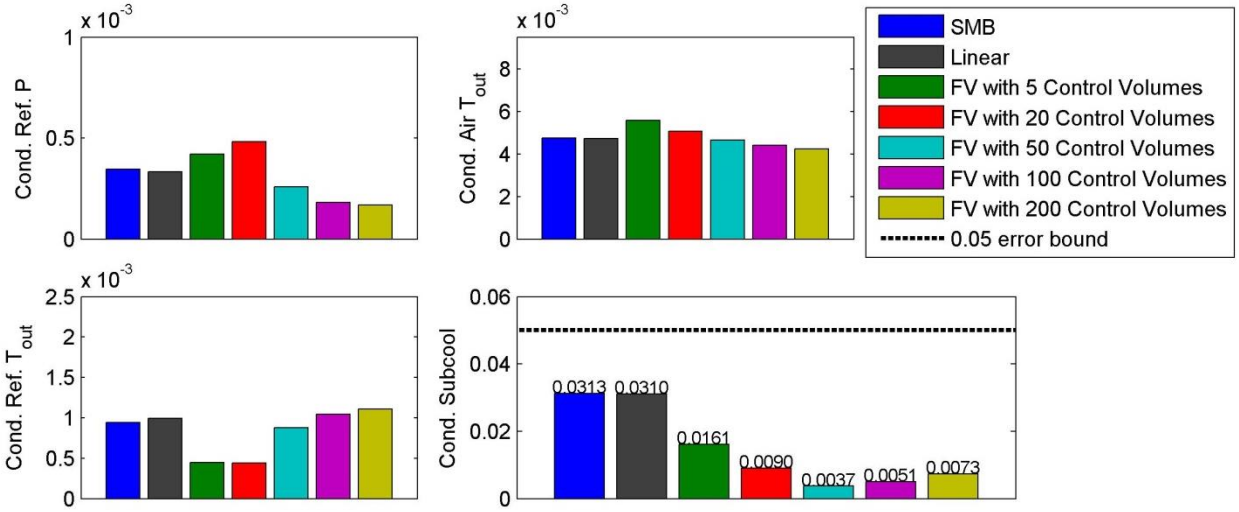

Figure 4.9 Normalized Error Residuals for Condenser Models

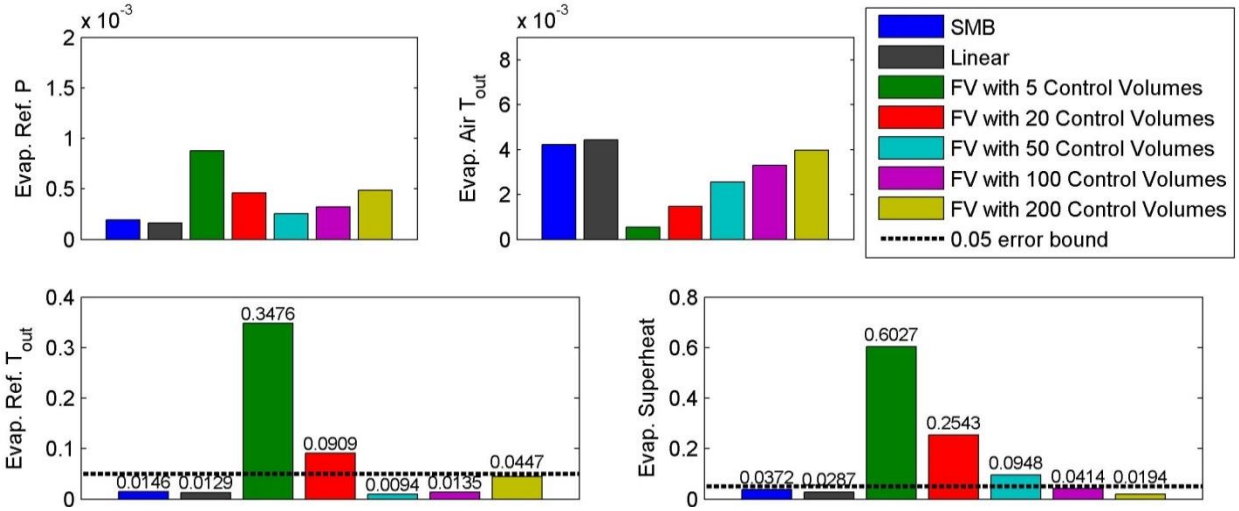

Figure 4.10 Normalized Error Residuals for Evaporator Models

While the acceptable degree of accuracy for any modeling attempt is application dependent, simulations with the FV, SMB, and linear models appear to match the data sufficiently well for most model-based control design purposes. This has been illustrated in Figure 4.9 and Figure 4.10 by the placement of a reference line at 0.05 in those subplots where the normalized residual errors are largest. It can be seen that the errors of the SMB, linear, and highly discretized FV models lie below the reference in these subplots, and are orders of magnitude less than 0.05 elsewhere. Where large errors occurred in FV models of low discretization, the error decreased as the discretization increased. This trend is exemplified by

evaporator superheat, in which significant improvements in accuracy occurred with increases in the number of CVs. Differences in error among models that lie well under the reference line can be treated as negligible, especially in light of the variability observed in the data from run to run.

The SMB and linear models are expected to match very closely, since the linear model formulation was derived directly from the SMB formulation and was linearized about the nominal operating conditions exhibited by the SMB model in this simulation. This expectation is met, as the differences between the SMB and linear models are well within the variability exhibited in the data from run to run. The SMB and 200 control volume FV models have a similar level of accuracy overall. A few exceptions are condenser subcooling, where the 200 control volume FV heat exchanger performs better, and evaporator refrigerant outlet temperature, where the SMB heat exchanger performs better.

Simulations of both the evaporator and the condenser air outlet temperatures have a constant offset from the data but follow the dynamics well. This can be confirmed by observation of Figure 4.11 in which the difference in mean between the data and simulations for this output has been added to the values for the simulations. We recall from Section 4.2 that the ambient relative humidity of the experimental facility was found to be approximately 50% during data collection, which is far from the 0% implicitly assumed in the SMB and FV models. As will be shown in Chapter 5, this air outlet temperature offset can be corrected by better accounting for the effects of air humidity on the system.

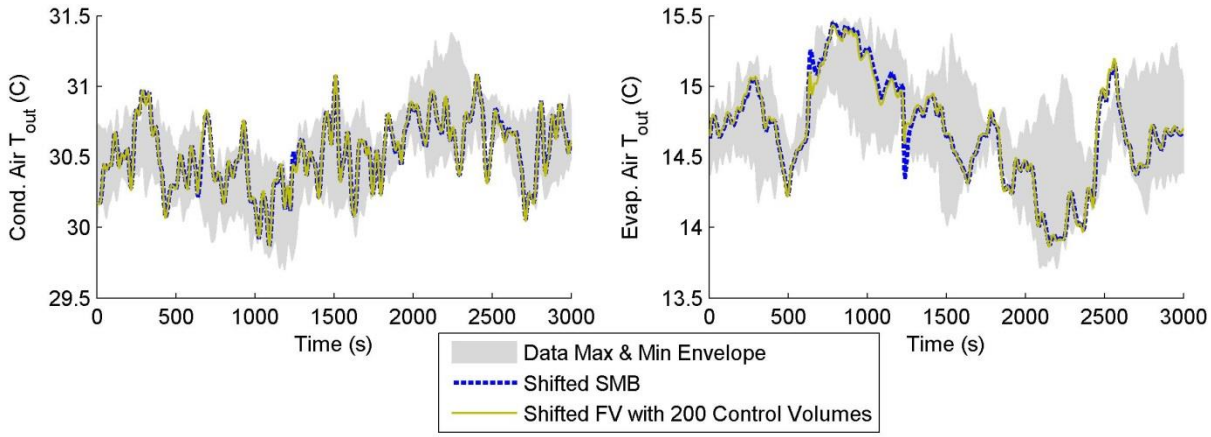

Figure 4.11 Mean-Adjusted Air Outlet Temperatures

4.4 Simulation Speed

Figure 4.12 shows the RTF of each simulation. The linear model is the fastest by orders of magnitude. This results from the computational advantages of simulating a time-invariant linear state-space model over the more complex nonlinear alternatives. It is also clear that the SMB model is much faster than the FV model, especially at higher numbers of FV control volumes. The simulation speeds of the nonlinear models represent order of magnitude improvements over the previous work cited in Section 2.1.3. This results from the use of a variable-step solver, from the implementation of a filter to increase the time constants of the mass flow rates (for the FV model only), and possibly also from the additional computational power available in current desktop PCs.

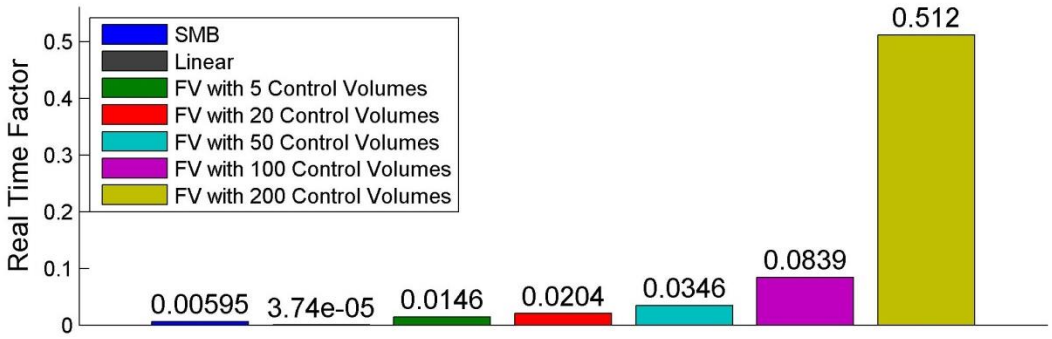

Figure 4.12 RTFs of VCS Simulations

4.5 Model Tradeoffs

Despite its slower simulation speed and similar accuracy, the FV approach does have advantages that may merit its use in favor of the SMB approach for several applications. The FV model is much simpler to derive and implement than the SMB model due to the complexity of variable CV lengths and the need to incorporate mean void fraction in the latter. As acknowledged in [6], these features also make it more difficult to extend the SMB approach to various heat exchanger types and geometries, while the simpler method of discretization used in the FV approach lends itself to reconfiguration. Furthermore, the FV approach may be more useful when conditions of the heat exchanger other than outlet properties and cooling capacity are desired. For example, if modeling frost formation on the exterior surface of the heat

exchanger, it may be useful to have access to the tube wall temperatures calculated by the FV model at uniform spacing along the length of the tube rather than only the lumped values for each refrigerant phase as calculated by the SMB model. Lastly, unlike the SMB approach, the FV approach can achieve different levels of fidelity as a tradeoff with simulation speed via modification of the number of CVs into which the heat exchanger is discretized.

After close evaluation, a more nuanced view of dynamic VCS simulation emerges from this work. Accuracy alone is not the sole forte of the highly discretized FV model. Instead, the intended use in target application, and the need for flexibility of implementation may be the driving factors for selection of the FV model. If simulation speed is paramount, a MB model can perform as accurately as a FV model while executing significantly faster. Therefore, in this simulation domain we can replace the conventional tradeoff picture of Figure 2.3 with the more realistic notions of Figure 4.13.

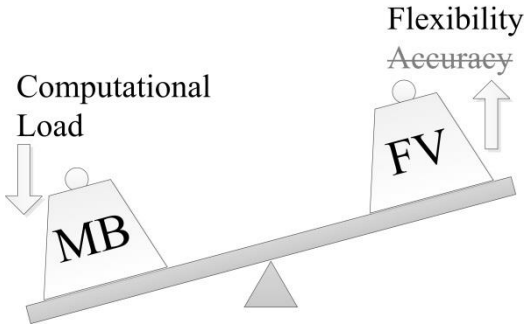

Figure 4.13 True Tradeoffs of FV vs. MB Approaches

A consideration of model tradeoffs would be remiss without including the linearized system models. The use of these models requires that a set of steady-state nominal operating conditions about which to linearize are found from the SMB model. Furthermore, the accuracy of the linear models decreases away from those nominal conditions. What the linear model does have is speed and, if one is satisfied with simulation results about a point of operation, then also sufficient accuracy. However, this is unlikely to be a tool used for system design or simulation. In Chapter 6, one very valuable asset of the linear model is shown to be its use in model-based estimation and control. In addition, the linear models are able to formally consider time scale separations by eigenvalue analysis; something that is challenging for the nonlinear SMB and FV model. This thesis does not advocate for one model approach over another. It is important to have all approaches available and utilize them in the appropriate situation.

Chapter 5
Humidity Modeling

In Section 4.3, it was suggested that including the effects of air humidity into heat exchanger models could improve the offset in air-side outlet temperature observed between the experimental data and models. In this chapter, we motivate and derive a method of incorporating humidity into the SMB modeling approach and demonstrate its effectiveness using experimental validation. Section 5.1 overviews the broad classes of applications for which this inclusion of humidity modeling can be impactful. Section 5.2 discusses the existing literature on humidity modeling for VCSs. Section 5.3 discusses the modeling platform used for simulation. Sections 5.4 and 5.5 present air-side modeling formulations with and without humidity modeling, respectively. Lastly, Section 5.6 demonstrates the improved accuracy of the model with humidity.

5.1 Motivation

For vehicles that translate between different climates or altitudes, the range of operational conditions experienced may include large differences in ambient air humidity. Stationary systems, such as heating, ventilation, and air conditioning (HVAC) systems for buildings, may also experience a wide range of ambient humidity conditions with the changing of the weather and seasons. In such cases, capturing how the humidity in the air at the inlet to the heat exchangers affects both refrigerant-side and air-side behavior is critical to predicting system performance. As a result, the inclusion of more accurate humidity modeling in model-based control designs will yield greater performance across the range of operational conditions for these systems.

In addition to using heat exchanger models with humidity to develop control designs that improve performance under changing ambient humidity conditions, there exist applications in

which a more accurate humidity model can be used to precisely control the air outlet humidity of heating and cooling systems [27]. For human environments, it has been shown that air of low humidity, also called “dry” air, is preferable for both comfort and health [28]. Manufacturing processes can also be affected by poor humidity control because undesirable humidity levels can decrease the lifespan of machinery, affect product quality, and impact safety [29].

5.2 VCS Humidity Modeling in the Literature

It is clear from [6] that relatively few existing approaches include modeling of humidity. In [30], a FV approach is taken for modeling heat exchangers with humidity, including modes with and without dehumidification. However, only the latter mode is validated with experimental data, and no measurements or simulation outputs of humidity are provided. In [31], a MB-derived state-space model and validation data are presented for a combined air-conditioning system and conditioned space. As stated in [6], this coupling of the VCS with a conditioned space prohibits direct validation of only the VCS model.

A state-space representation for a direct expansion air-conditioning system and corresponding multi-input multi-output controller of temperature and humidity are presented in [27] and [32]. The model in this work calculates no refrigerant-side conditions, and is also coupled to a conditioned space. System identification, neural networks, and fuzzy modeling approaches have been applied in developing models for humidity and temperature control of HVAC systems, including the work in [33], [34], and [35]. The generation of these models requires extensive data collection, which limits their applicability for systems other than those from which data was collected.

The MB evaporator with humidity modeling in [17] only includes a range in inlet relative humidity (RH) of approximately 4%, but was very influential to the work presented here, especially in the use of a log-mean humidity difference approach. Here, we contribute a model which has been thoroughly validated with both refrigerant-side and air-side measurements of a VCS across a wide range of humidity conditions.

5.3 Modeling Platform

The SMB heat exchangers of Section 2.2.2 serve as the baseline for this work, and will be modified to account for the effects of humidity on the system. This will require an additional

input of air inlet relative humidity ($RH_{a,\text{in}}$) and result in the calculation of the additional outputs of air outlet relative humidity ($RH_{a,out}$) and condensate mass flow rate ($\dot{m}_l$). The latter is the rate at which water vapor in the air mixture condenses into liquid water.

In order to compute properties of humid air, this work utilizes the CoolProp open-source library for fluid property generation [36]. The air is assumed to always be at standard atmospheric pressure (101.325 kPa). As previously in this work, all other fluid properties are interpolated from property lookup tables generated using the REFPROP database released by NIST [22].

5.4 Air-side Model without Humidity

We begin by presenting some additional details on the modeling of air-side conditions used in the SMB formulations of Section 2.2.2, which does not consider the effects of humidity. Instead, the effects of air humidity are treated as negligible, or the air is assumed to be sufficiently dry. Properties of the air are calculated as functions of the air inlet temperature, interpolated from property tables for dry air. For example, the constant pressure specific heat capacity of the air is found as:

$$c_{p,a} = fcn\left(T_{a,in}\right) \tag{5.1}$$

and the air-side heat transfer coefficient is found using the J-factor correlation data provided in [37] as:

$$\alpha_a = fcn\left(T_{a,in}, A_{a,cs}, \dot{m}_{a,dry}\right) . \tag{5.2}$$

Using the log mean air temperature difference (LMTD) and effectiveness number of transfer units (e-NTU) methods of [21], the air outlet temperature of each CV is calculated by:

$$T_{a,out,CV} = T_{wall,CV} + (T_{a,in} - T_{wall,CV})e^{-NTU} \tag{5.3}$$

where *NTU* is given by:

$$NTU = \frac{\alpha_a A_{a,s}}{\dot{m}_{a_{dry}} c_{p,a}} . \tag{5.4}$$

The heat transfer rate between the air and the heat exchanger wall, which appears in Z_2 of Eqs. (2.26) and (2.38), is given by:

$$\dot{Q}_{a,CV} = \zeta_{CV} \dot{m}_{a_{dry}} c_{p,a} (T_{a,in} - T_{a,out,CV}) \tag{5.5}$$

where $\zeta_{CV} \dot{m}_{a_{dry}}$ is the normalized length of the CV multiplied by the mass flow rate across the entire heat exchanger, giving the air mass flow rate across the CV only. The net heat transfer rate between the air and the wall is the sum of the heat transfer rate of each CV:

$$\dot{Q}_a = \sum_{j=1}^{\#CVs} \dot{Q}_{a,j} \tag{5.6}$$

and the bulk air outlet temperature is found by weighting the air outlet temperatures of each CV by their respective normalized lengths:

$$T_{a,out} = \sum_{j=1}^{\#CVs} \zeta_j T_{a,out,j} \ . \tag{5.7}$$

5.5 Air-Side Model with Humidity

The inclusion of humidity requires the additional input to the model of air inlet RH. This is defined as the ratio of the partial pressure of water vapor in the air mixture to the equilibrium vapor pressure of water at the temperature of the air mixture. As a percentage, this gives the percent of moisture present in the air mixture relative to saturation at a given temperature. In order to capture the dependence of air properties on both humidity and temperature in this model, $c_{p,a}$ and α_a are calculated individually for each CV, and at each time step are found as a function of the mean of the air inlet conditions of the current time step (k) and the air outlet conditions of the previous time step $(k-1)$:

$$\begin{aligned} (c_{p,a,CV})_k &= fcn\left(\frac{(RH_{in})_k + (RH_{out,CV})_{k-1}}{2}, \frac{(T_{a,in})_k + (T_{a,out,CV})_{k-1}}{2} \right) \\ (\alpha_{a,CV})_k &= fcn\left(\frac{(RH_{in})_k + (RH_{out,CV})_{k-1}}{2}, \frac{(T_{a,in})_k + (T_{a,out,CV})_{k-1}}{2}, \right. \\ &\qquad \left. A_{a,cs} \quad , \quad (\dot{m}_{a,dry})_k \right) \end{aligned} \ . \tag{5.8}$$

Note that this necessitates initial conditions of RH_{out} and $T_{a,out}$ to be specified for the model. The outlet air temperature of each CV is again calculated using Eqs. (5.3) and (5.4). However, now an individual *NTU* is calculated for each CV:

$$T_{a,out,CV} = T_{wall,CV} + (T_{a,in} - T_{wall,CV})e^{-NTU_{CV}} \tag{5.9}$$

where NTU_{CV} is given by:

$$NTU_{CV} = \frac{\alpha_{a,CV} A_{a,s}}{\dot{m}_{a_{dry}} c_{p,a,CV}}. \tag{5.10}$$

Using the CoolProp functions for moist air property generation, RH_{in} and $T_{a,in}$ are used to calculate the specific enthalpy ($h_{a,in}$) and specific humidity (ω_{in}) of the inlet air. The latter is defined as the ratio of the mass of water vapor in the air mixture to the mass of dry air in the air mixture:

$$\omega_{in} \equiv \frac{m_{vapor,in}}{m_{a_{dry},in}}. \tag{5.11}$$

The humidity model must determine if liquid water is being formed in each CV of the heat exchanger due to water vapor condensing out of the air mixture. The maximum temperature at which water vapor leaves a mixture of air is known as the dew point (T_d), and is a function of RH. Using CoolProp, T_d at each time step for each CV is calculated as a function of the mean of the inlet RH of the current time step (k) and the outlet RH of the previous time step $(k-1)$:

$$\left(T_{d,CV}\right)_k = fcn\left(\frac{\left(RH_{in}\right)_k + \left(RH_{out,CV}\right)_{k-1}}{2}\right). \tag{5.12}$$

It is common practice in the literature to assume that condensation occurs in a CV whenever its wall surface temperature is less than or equal to the air mixture dew point [17] [38].

$$\begin{aligned} T_{w,CV} &\le T_{d,CV} \rightarrow Condensing \\ T_{w,CV} &> T_{d,CV} \rightarrow Not\ Condensing \end{aligned}. \tag{5.13}$$

In each CV where condensation is found to not occur, the quantity of water vapor in the outlet air mixture remains unchanged from that of the inlet air mixture, so:

$$\begin{aligned} \omega_{out,CV} &= \omega_{in} \\ \dot{m}_{l,CV} &= 0 \end{aligned} . \tag{5.14}$$

For each CV in which condensation is found to occur, additional complexity is required in order to determine the quantity of water vapor that leaves the air mixture. This work uses the approach of [17], which begins with the log-mean humidity difference equation derived in [39]:

$$ln\left(\frac{\omega_{in} - \omega_{w,CV}}{\omega_{out,CV} - \omega_{w,CV}} \right) = \frac{\alpha_m A_{a,s} \eta}{\dot{m}_{a_{dry}}} \tag{5.15}$$

where $\omega_{w,CV}$ is the specific humidity of saturated air (RH of 100%) at $T_{w,CV}$ and α_m is the mass transfer coefficient, given by:

$$\alpha_m = \frac{\alpha_a}{\rho_{a_{dry}} c_{p,a_{dry}}} . \tag{5.16}$$

η is the surface effectiveness of the heat exchanger, which can be expressed as a function of fin efficiency. The equations used to calculate η are found in [17]. Solving Eq. (5.15) for $\omega_{out,CV}$ gives:

$$\omega_{out,CV} = \frac{\omega_{in} - \omega_{w,CV}}{e^{\left(\frac{\alpha_m A_{a,s} \eta}{\dot{m}_{a_{dry}}} \right)}} + \omega_{w,CV} . \tag{5.17}$$

In order to account for modeling errors in the above parameters for mass transfer and surface effectiveness, a constant parameter adjustment factor β is introduced to Eq. (5.17). While nominally unity, β can be hand-tuned by users to improve the model's match to experimental data. With the inclusion of this parameter, Eq. (5.17) becomes:

$$\omega_{out,CV} = \beta \frac{\omega_{in} - \omega_{w,CV}}{e^{\left(\frac{\alpha_m A_{a,s} \eta}{\dot{m}_{a_{dry}}} \right)}} + \omega_{w,CV} \tag{5.18}$$

The condensate mass flow rate is then found from conservation of mass for the water:

$$\dot{m}_{l,CV} = \zeta_{CV} \dot{m}_{a_{dry},CV} \left(\omega_{in} - \omega_{out,CV} \right) \tag{5.19}$$

Again, $\zeta_{CV} \dot{m}_{a_{dry},CV}$ is the normalized length of the CV multiplied by the dry air mass flow rate across the entire heat exchanger, giving the dry air mass flow rate across the CV only. To summarize the calculations to be made for each possible result of Eq. (5.13):

$$\begin{aligned} T_{w,CV} \le T_{d,CV} &\rightarrow \textit{Condensing} \quad \rightarrow \textit{use Eqs.(5.18) and (5.19)} \\ T_{w,CV} > T_{d,CV} &\rightarrow \textit{Not Condensing} \rightarrow \textit{use Eq. (5.14)} \end{aligned} \quad . \tag{5.20}$$

To this point, the three primary quantities that have been calculated for each volume are $T_{a,out,CV}$, $\omega_{out,CV}$, and $\dot{m}_{l,CV}$. The first two of these can be used in conjunction with CoolProp to calculate the air outlet specific enthalpy of each CV $(h_{a,\text{out,CV}})$. Conservation of energy for the air mixture and condensate then gives:

$$\dot{Q}_{a,CV} = \zeta_{CV} \dot{m}_{a_{dry}} (h_{a,in} - h_{a,out,CV}) - \dot{m}_{l,CV} \lambda_{l,CV} \tag{5.21}$$

where $\lambda_{l,CV}$ is the latent heat of condensation of water, approximated by:

$$\lambda_{l,CV} = 2500.8 - 2.36 T_{w,\text{CV}} + 0.0016 {T_{w,CV}}^2 - 0.00006 {T_{w,CV}}^3 \tag{5.22}$$

in which $T_{w,\text{CV}}$ takes units of $^{\circ}\text{C}$ and $L_{l,CV}$ is in J/g [40].

The net heat transfer rate between the air and the wall and the bulk air outlet temperature are again given by Eqs. (5.6) and (5.7), respectively. Other bulk outlet properties of the heat exchanger include:

$$\begin{aligned} \omega_{out} &= \sum_{j=1}^{\#CVs} \zeta_j \omega_{out,j} \\ \dot{m}_l &= \sum_{j=1}^{\#CVs} \dot{m}_{l\,j} \\ RH_{out} &= fcn(T_{a,out}, \omega_{out}) \end{aligned} \quad . \tag{5.23}$$

5.6 Model Validation

Model validation was conducted using the same experimental system as in Chapter 4. Two Measurement Specialties HTM2500LF humidity sensors were added to the data acquisition

system in order to measure the inlet and outlet humidity of a heat exchanger. These sensors are factory calibrated within ±2% RH. The stand was configured as a 4-component VCS consisting of a tube and fin evaporator, a compressor, a tube and fin condenser, and an electronic expansion valve. We present validation data here for only the evaporator.

A console evaporative humidifier was used to change the inlet humidity to the heat exchanger. In order to direct as much of the humidified air into the heat exchanger air inlet as possible, at some times during data collection a hood was added to enclose the humidifier outlet and heat exchanger air inlet. A schematic of the configuration with and without the hood is shown in Figure 5.1.

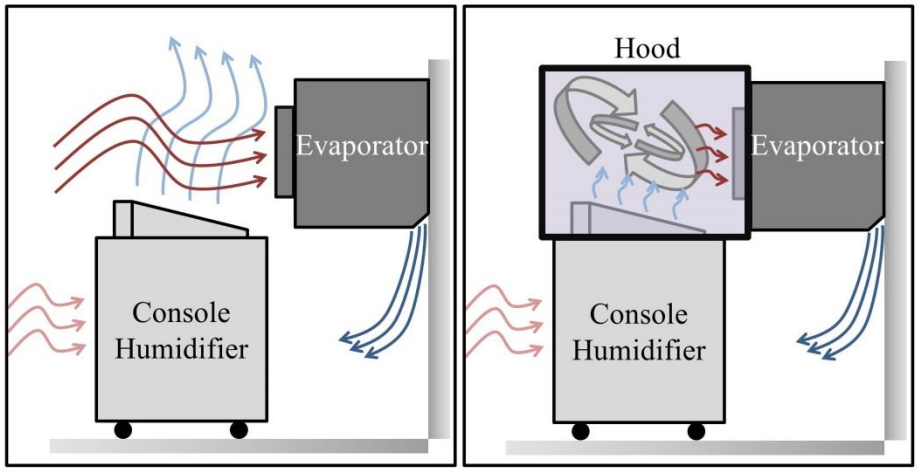

Figure 5.1 Evaporator with Hood (Left) and Without Hood (Right)

The validation data consists of a series of changes in inlet humidity. Because the humidification of the air also causes a decrease in its temperature, the inlet air temperature is also seen to vary. The actuators of the test stand (compressor speed, degree of EEV orifice opening, and fan speeds for each heat exchanger) were kept constant. Figure 5.2 shows the measured air-side and refrigerant-side inputs to the evaporator. Figure 5.3 shows several of the measured states and outputs of the evaporator.

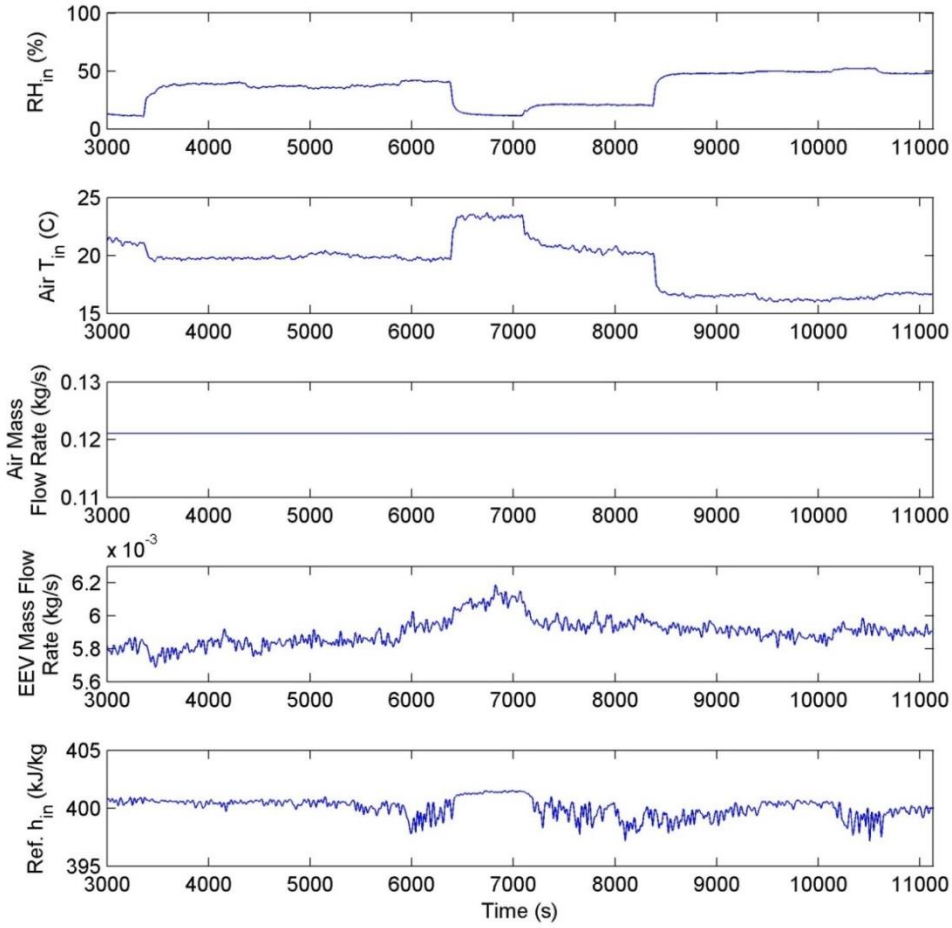

Figure 5.2 Evaporator Input Data

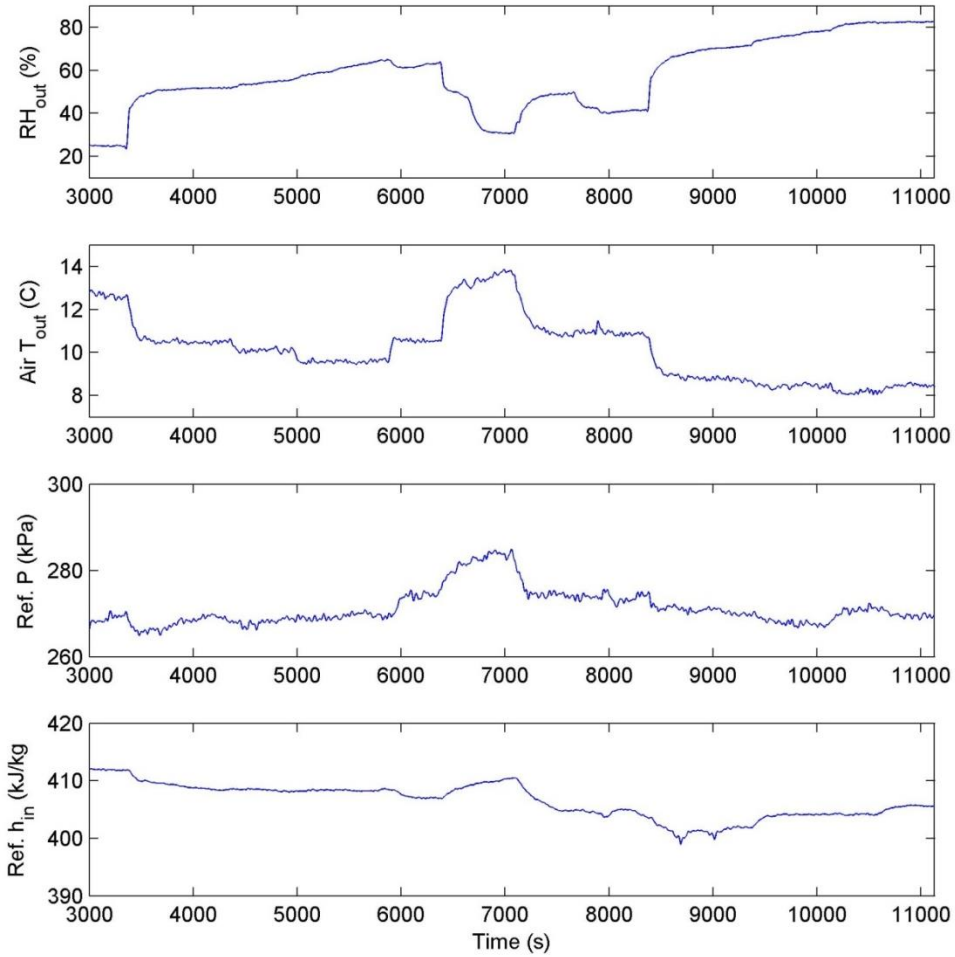

Figure 5.3 Evaporator Output Data

The measured inputs of Figure 5.2 were used as inputs to the evaporator models in simulation. Because no measurement of evaporator outlet refrigerant mass flow rate is available in the experimental system, this was calculated using the static compressor model described in Section 2.3.2. This technique was also used in [17] for heat exchanger model validation. The compressor model uses empirically generated maps of volumetric and isentropic efficiency to calculate mass flow rate as a function of the compressor speed command, heat exchanger pressures, and evaporator outlet enthalpy. The inputs of evaporator pressure and enthalpy were provided by the evaporator model, while all other inputs were taken from data. The closed-loop connection between P_e and $h_{r,out}$ from the evaporator as inputs to the compressor and $\dot{m}_{r,out}$ from the compressor as an input to the evaporator ensures that the inlet and outlet mass flow rates of the evaporator match at steady-state. Figure 5.4 shows this interconnection of the models.

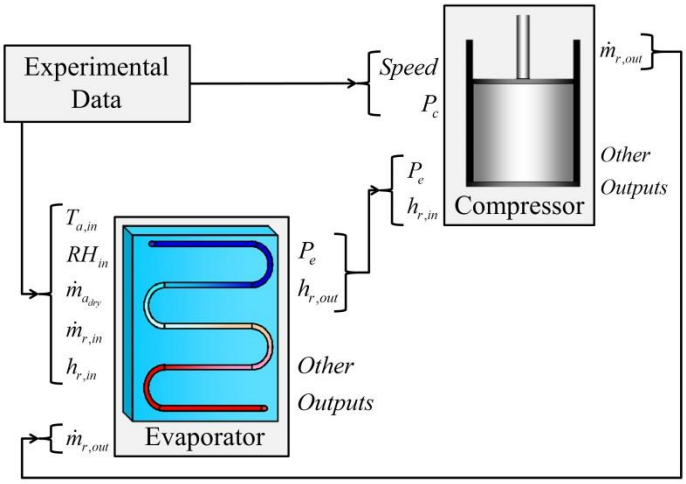

Figure 5.4 Inputs for Model Validation

To bring the heat exchanger models to better match their physical equivalents in the experimental system, tuning was conducted to account for model errors in heat and mass transfer coefficients. This tuning consisted of constant scaling factors applied to the air-side HTC and the refrigerant-side HTCs for each refrigerant phase, as well as selection of β in Eq. (5.18). These values were determined empirically based on comparison of data and simulation results.

Figure 5.5 shows simulation results for several of the model outputs as compared to the experimental data. Results for both the evaporator without humidity modeling and the evaporator with humidity modeling are provided.

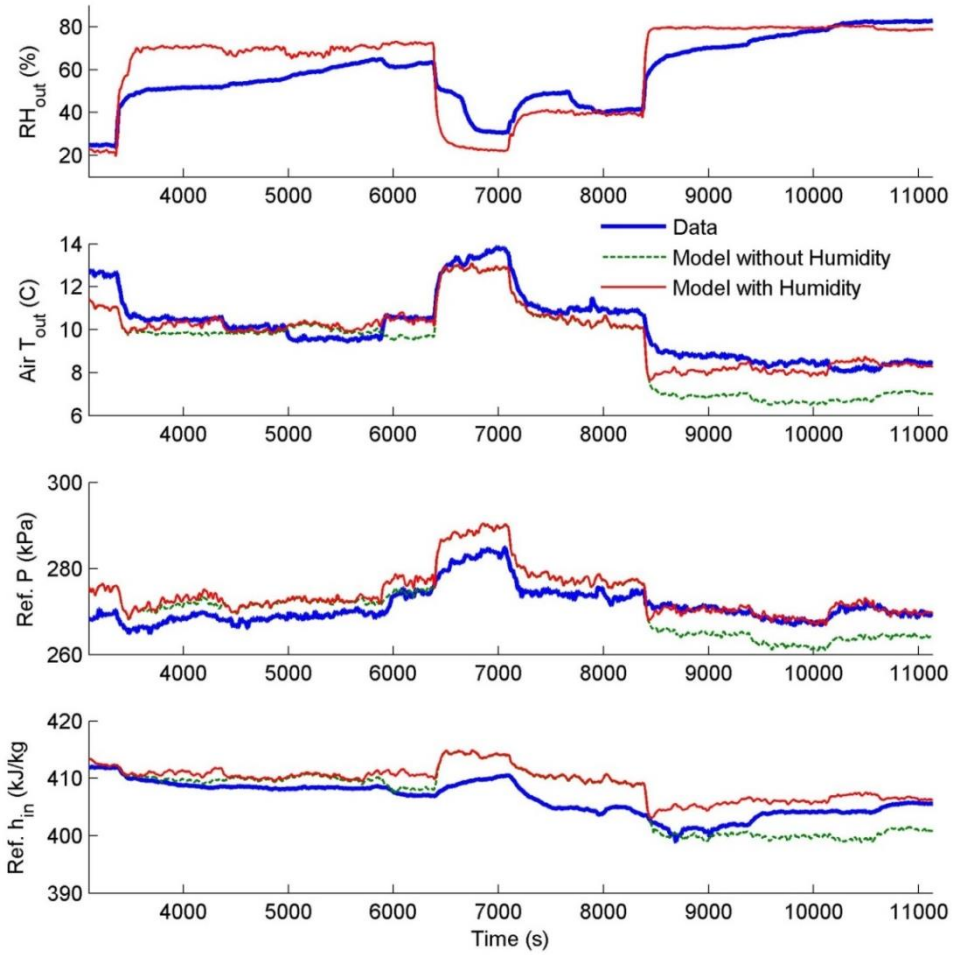

Figure 5.5 Data and Simulation Outputs

The clearest advantage of the model with humidity is that it calculates the output of RH_{out}, which the model without humidity cannot. As seen in the top subplot of Figure 5.5, the model and data reach very similar steady state values in this output; however there are differences in the transient behavior. This error is believed to be associated with the formation and evaporation of a film of liquid water on the heat exchanger tubes and fins. As stated in [38], the thermal resistance of a thin film of water is generally small in comparison to the air-side and refrigerant-side thermal resistances, and so its effect on the overall thermal resistance of the heat exchanger can be treated as negligible. However, this film represents a volume of water that is stored on the heat exchanger. Because Eq. (5.19) does not account for storage of liquid water on the heat exchanger, there is error when this film of liquid is being formed or evaporated away. As seen in Figure 5.5, this error manifests as higher-order dynamics and longer time constants

observed in the data. While incorporating a capacitance term to account for this liquid storage could be pursued as a means of attaining greater accuracy, the current model formulation demonstrates sufficient accuracy for its intended application in model-based control design.

The model with humidity is superior to the model without humidity in predicting air outlet temperature and refrigerant-side conditions across the range of air inlet conditions. We note that the primary difference in inlet conditions between the period of high humidity from 3500-6500s and that from 8500-11000s is that the air inlet temperature is several degrees lower in the latter, resulting in an increased rate of condensate formation. While the model with humidity is able to account for this more rapid condensate formation and accurately represent the experimental system under these conditions, the model without humidity exhibits significant steady-state errors. The two models match almost exactly during the period of low humidity from 6500-8500s. Here, the combination of low inlet relative humidity and high air inlet temperature result in no condensate formation.

Table 5.1 shows the normalized error residuals of the simulations as compared to the experimental data for each output. This is again computed by Eq. (4.1).

Table 5.1: Normalized Error Residuals

Output:	*Model:*	*NRE:*
RH_{out}	With Humidity	0.0322
$T_{a,out}$	Without Humidity	0.0132
	With Humidity	0.0038
P	Without Humidity	3.11e-4
	With Humidity	1.86e-4
$H_{r,out}$	Without Humidity	6.53e-5
	With Humidity	6.45e-5

While the acceptable degree of accuracy for any modeling effort is application dependent, the model with humidity appears to match the data sufficiently well across a wide range of humidity conditions for most control design oriented purposes.

Figure 5.6, Figure 5.7, and Figure 5.8 show the sensitivity of outputs of the model with humidity to disturbances in each of the air-side inputs. Of particular interest is the observation that RH_{out} has low sensitivity to these disturbances except during the simulation in which RH_{in} is decreased by 10% (the top subplot of Figure 5.9). The trigger of this sensitivity is whether the model determines that condensation is forming in the evaporator. As shown in Figure 5.9, the negative disturbance in RH_{in} causes $\dot{m}_l$ to fall to 0 for the first 8500s. When $\dot{m}_l = 0$, conservation of mass for the water requires that the decreased amount of water vapor in the air mixture at the inlet be accounted for by a decrease in its amount at the outlet, and RH_{out} decreases. However, when $\dot{m}_l \neq 0$ for the disturbance, as it does after 8500s, a change in air inlet humidity results in a change in the rate of condensate formation while the amount of water vapor exiting the heat exchanger remains relatively unchanged.

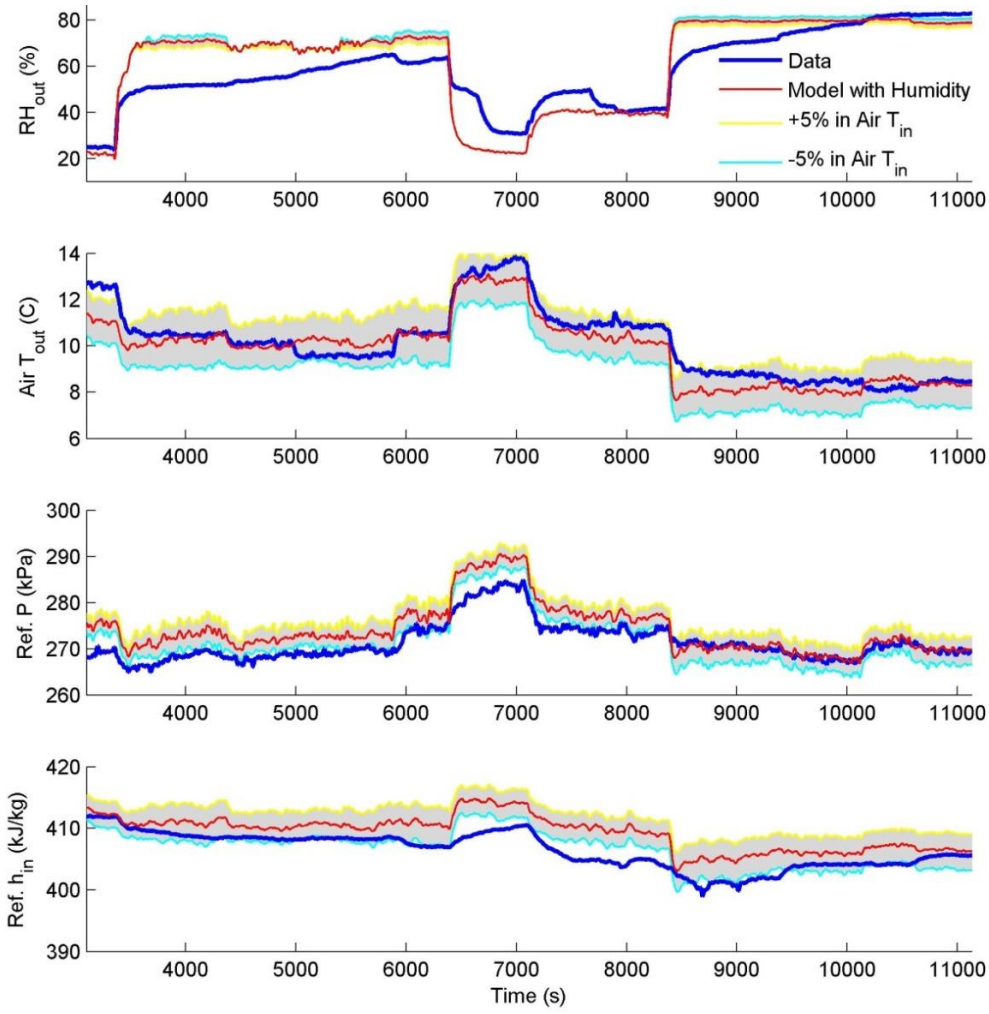

Figure 5.6 Sensitivity to $T_{a,in}$

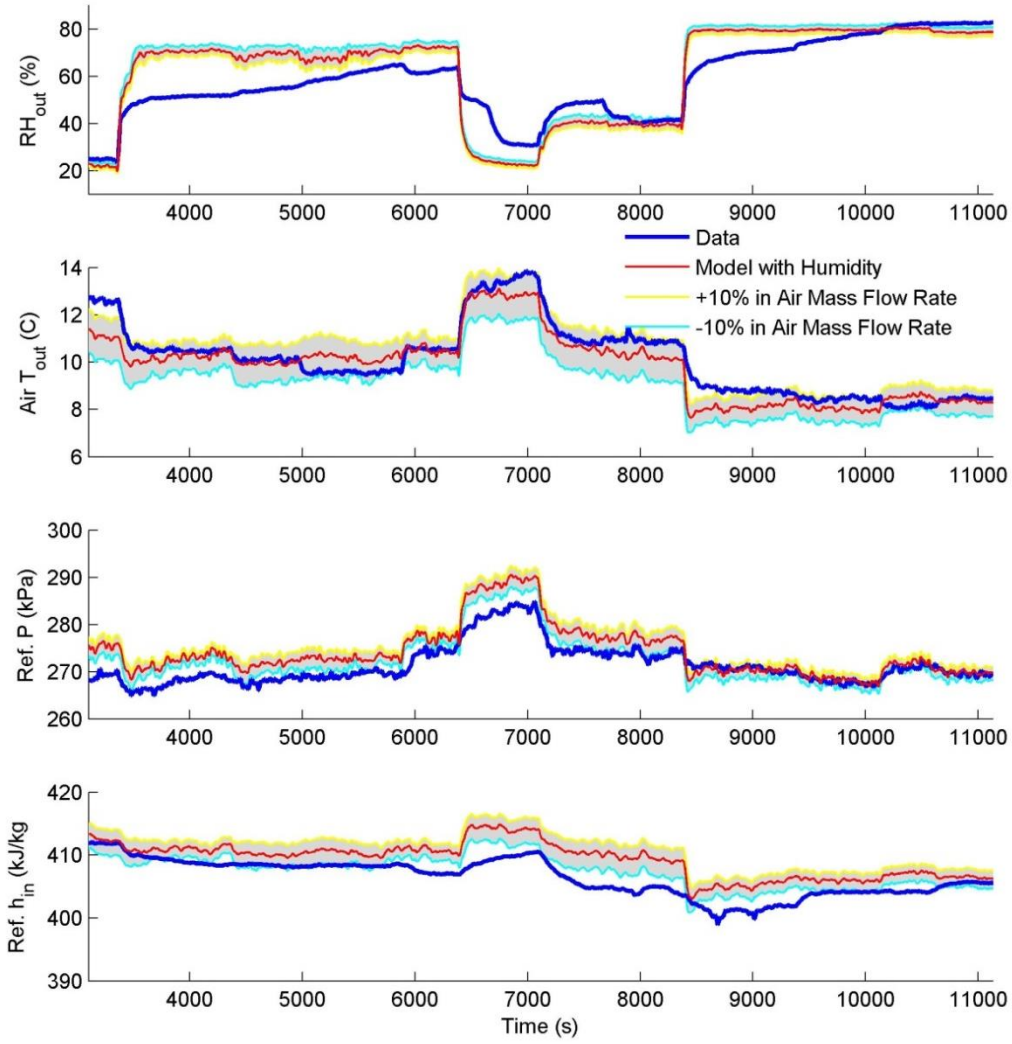

Figure 5.7: Sensitivity to $\dot{m}_a$

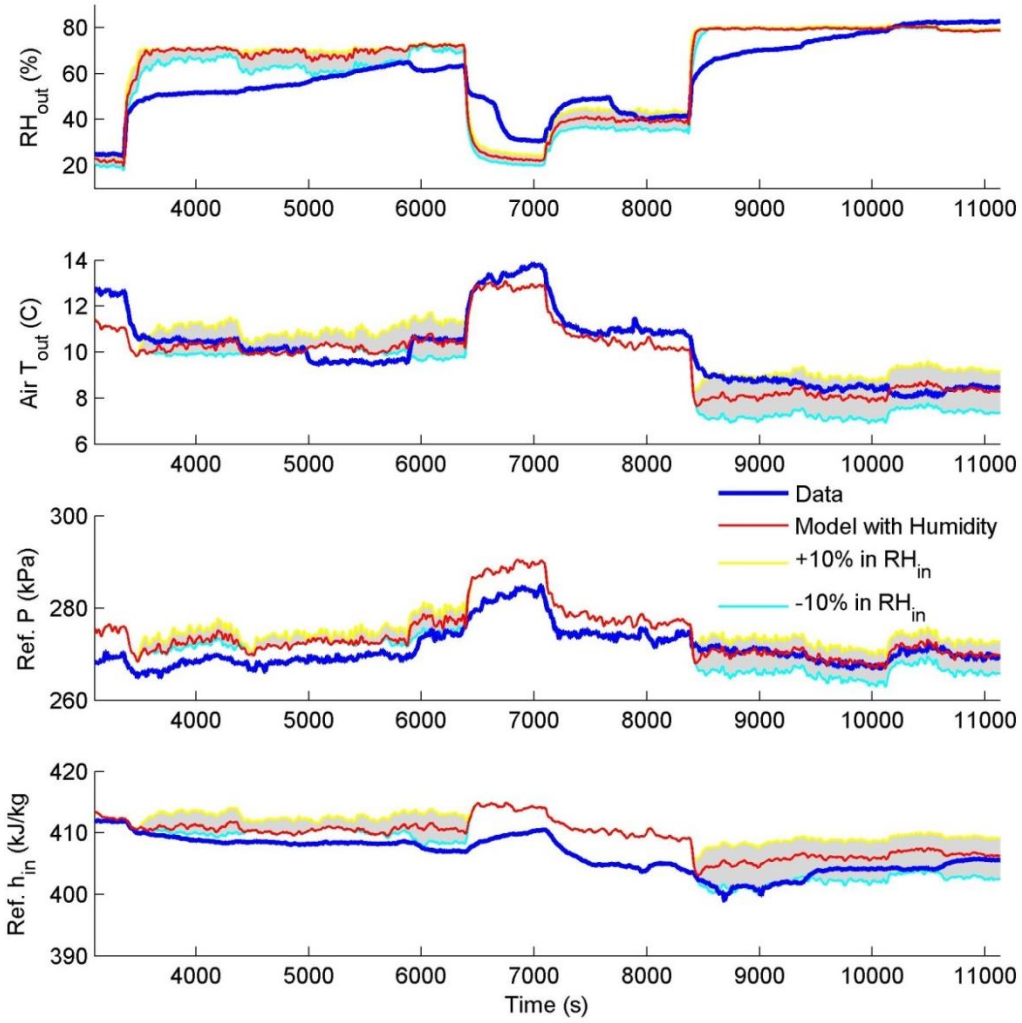

Figure 5.8: Sensitivity to RH_{in}

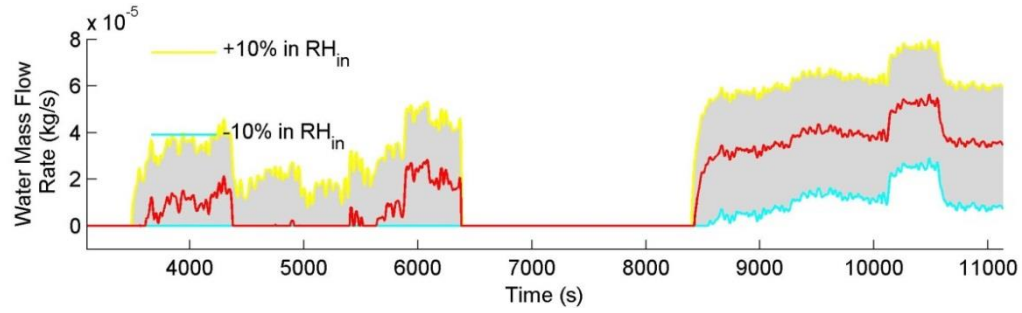

Figure 5.9: Sensitivity of $\dot{m}_l$ to RH_{in}

In a separate experimental test, the inlet humidity was raised as high as possible in order to initiate rapid condensate formation and then decreased until condensate formation ceased. From 3870s into the test, the total quantity of condensate that drained from the evaporator was

collected and measured. These measurements are plotted in Figure 5.10. Also shown is the integral of the $\dot{m}_{l,CV}$ output of the evaporator model with humidity when simulated over the input data. One can see that the model predicts condensate formation very accurately. While the general trend by which condensate formation slows is captured, the data shows a gradual reduction over time, while termination of condensate formation is seen to be a discrete change in the model with humidity at approximately 10500s.

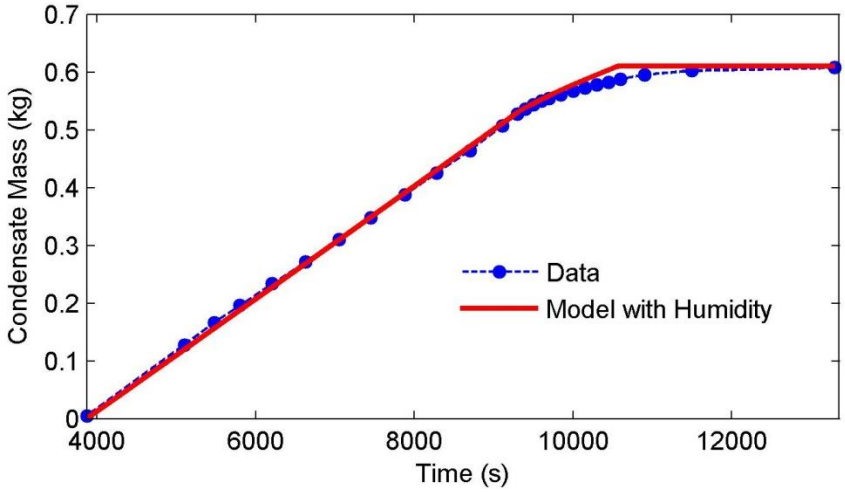

Figure 5.10 Data and Simulated Condensate Mass

Chapter 6

Switched Linear Control

In this chapter, we derive and validate a switched VCS control approach that uses the linear models of Chapter 3 to both estimate system states and determine actuator inputs that bring the system to a desired operating condition. The use of models for multiple modes of the system enables the controller to drive the system between these modes. Section 6.1 reviews the literature on switched control of VCSs. Section 6.2 gives an overview of the control framework. Section 6.3 describes the manager used to detect a mode switch in the plant. Section 6.4 provides some remarks on the notation used in the content that follows. Section 6.5 describes the observer used to estimate system states. Section 6.6 derives several LQR formulations for control of the system. Section 6.7 details the controllability and observability properties of the models used in demonstrating the control approach. Section 6.8 provides simulation results for the control framework, while Section 6.9 provides experimental results. Finally, Section 6.10 discusses the stability of the switched control framework.

6.1 Switched VCS Control in the Literature

Multivariable control of VCSs has been often studied in recent decades, including the early work in [45] and more recent work in [46]. Designing a controller that can be applied across a wide range of operational conditions has received recent attention, including the gain scheduled control in [47] and switched control strategies in [48]. However, these are not generally designed to operate the system at low or zero evaporator superheat. For example, the multivariable controller in [49] is shown to function well between 9.5°C and 22°C of superheat, but becomes unstable below 8.5°C. The switched LQR approach of [26] and [42] is able to regulate the system to operating conditions with both positive and zero superheat and subcool, and was very influential to the work presented here. This thesis builds upon the work in [26] and

[42] in three primary ways. First, a much greater level of detail is provided on the linear models and control formulation used. Second, the stability analysis of the switched control framework is revisited. Third, the control approach is demonstrated not only in simulation, but also experimentally.

6.2 Control Design Overview

In this work we assume that a model-based real time optimizer (RTO) receives desired performance specifications for the VCS (for example, a desired cooling capacity) along with appropriate constraints, and in turn calculates a set of nominal values that are provided to the controller as references. It is expected that the RTO updates on a timescale of minutes, while the controller updates several orders of magnitude faster. As indicated in Figure 6.1, which diagrams the basic control architecture, construction of a RTO falls outside the scope of this work. We instead focus on the design of an observer and controller framework that brings the system to track the desired reference values. Details on the construction of a RTO can be found in [42].

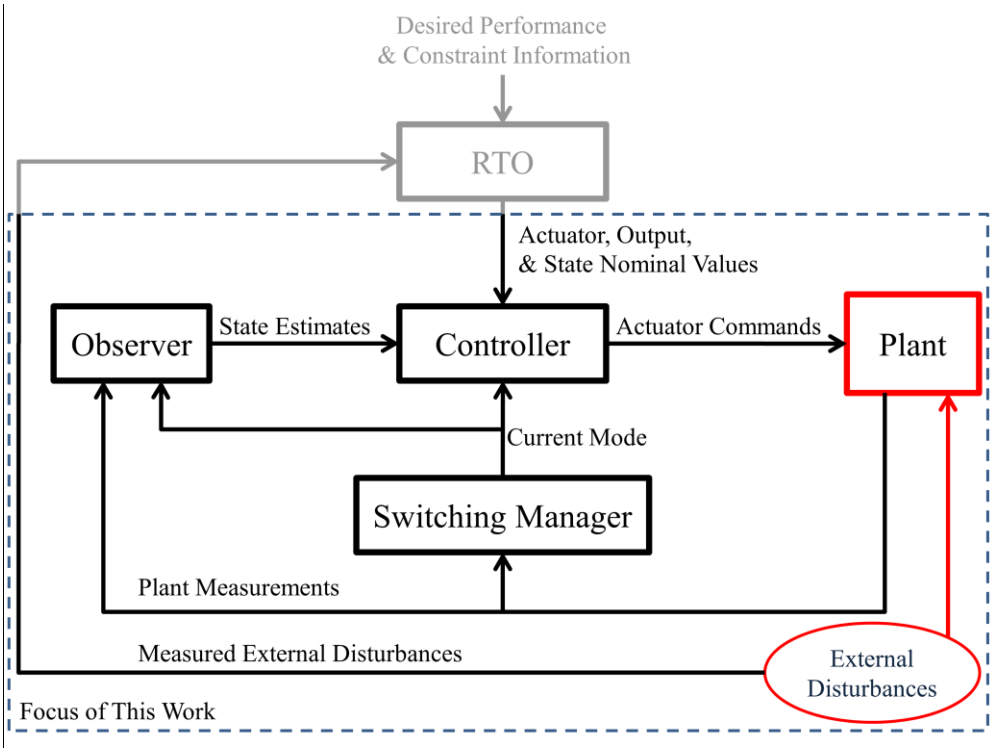

Figure 6.1 Control Design Diagram

As mentioned in Section 4.5, the linear VCS models derived in Chapter 3 will be used to estimate states of the system that cannot be directly measured in practice and to compute optimal

actuator commands to the plant given those estimates. Switching among linear models for each mode of operation of the VCS provides access to accurate models across the entire range of operation of the system and allows for the use of well-established theory on linear controller design and analysis. However, there are implications behind this switching between multiple models in estimation and control that must be carefully treated. Figure 6.2 shows how the internal mode selection of the controller and observer is based on the current mode of operation as determined by measurements of the plant.

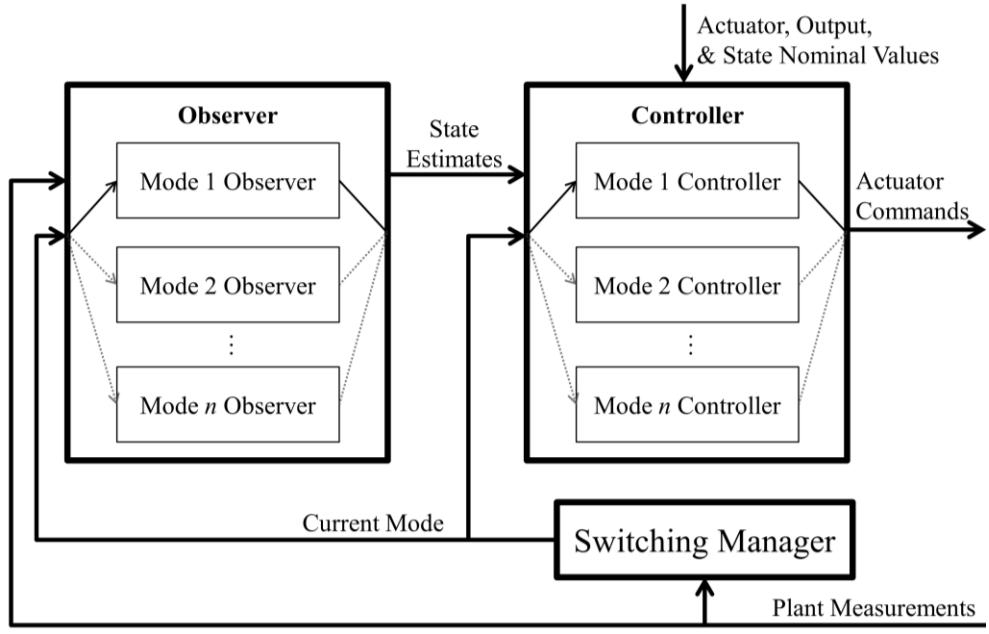

Figure 6.2 Switched Observer and Controller

Development of the control approach presented in this chapter is guided by the desire to satisfy a number of design objectives and constraints with the controller. The following overview of these criteria can therefore be used to motivate each feature of the design.

1. Set point tracking across modes

   For the RTO presented in [42], it is shown that for different desired cooling capacities the optimal set-point for a VCS may fall in different modes of the system (modes being distinguished as in previous chapters by the presence or absence of superheated refrigerant in the evaporator and subcooled refrigerant in the condenser). This motivates a need for the controller to not just be capable of regulating the system

within a single mode, but also to be able to drive the system between modes if need be as nominal values from the RTO change.

2. Disturbance rejection across modes

The desired ability of the controller to drive the system between modes is also valuable for the rejection of disturbances. In the event that a disturbance occurs which is large and rapid enough that neither the RTO nor the controller can prevent a mode switch from occurring, we would like the controller to able to drive the system back to the desired mode of operation, largely rejecting the effects of the disturbance.

3. Does not require data-based system identification

Many VCS control approaches in the literature make use of models developed by fitting experimental data. While this approach can yield successful control designs, it has several disadvantages. First, some identification processes do not preserve the physical interpretation of system parameters. This can make it difficult to understand the nature of the dynamics at play, inhibiting controller design and tuning. This can also limit the applicability of a particular model to only the exact plant on which data was collected, since there may be no clear way to adapt the model for a plant with different physical specifications. Also, identified models require access to an instrumented plant from which to collect data, the procurement of which can be a significant time and cost barrier to the control design in addition to the resources required to collect the data itself. By contrast, the model-based approach can be used with new system designs that are "still on the drawing board" and have yet to be physically realized. Lastly, the breadth of accuracy of an identified model is limited by the range of the data from which it is derived. It is possible to miss significant dynamic features of the plant simply because they were not triggered by the specific input sequence over which data was collected.

By contrast, the models used for control design in this work are derived mostly from physics-based modeling and linearization techniques. This simplifies the process of adapting and evaluating the controller for systems with different physical specifications. While not explored here, this also allows for co-design of the parameters of the physical

system with its controller, which could be used to construct VCSs that are better optimized for control.

4. Readily implementable on physical systems

Many critical states affecting the dynamic behavior of VCSs are extremely difficult to measure in practice. Such states include void fraction, the locations of phase transitions, and the refrigerant enthalpy along each phase zone. Clearly, a practically implementable feedback control design must be limited to measurements of the plant that are available to both experimental test stands and commercial systems. These may include air temperatures, refrigerant temperatures, and refrigerant pressures at the inlet or outlet of various components. As will be seen, the control design presented in this work uses models of the plant together with available measurements to estimate the values of states that are not readily measurable. Inherent in this estimation is the rejection of sensor noise.

Physically implementable control designs must also take into account the fact that no VCS actuators can produce a perfect step response. For example, it would be unreasonable to expect that the compressor speed can be decreased by 500 RPM instantaneously. In addition, small actuator steps occurring at high rates of change can cause wear on components, and as such are undesirable. Therefore, it is important that the control design provides reasonably smooth actuator commands over time, even in the presence of significant measurement noise. These commands must also be within the constraints of operation of the actuator.

6.3 Switching Manager

As shown in Figure 6.2, a switching manager uses measurements from the plant to determine the current mode of operation In this work, without loss of generality, we will present and demonstrate a control framework involving switching between the ‘3-2’ and ‘3-1’ modes of Chapter 3, corresponding to presence and absence of superheated refrigerant at the outlet of the evaporator, respectively. The condenser is assumed to maintain some amount of subcooled refrigerant at its outlet at all times. The degree of superheating in the evaporator is calculated from the pressure and refrigerant outlet temperature measured from the evaporator:

$$SH = T_{e,r,out} - T_g(P_e) \tag{6.1}$$

When the evaporator outlet temperature is nearly equal to the saturation temperature (i.e. the difference between the two is within the measurement noise), we assume that no superheat is present in the evaporator. In order to avoid rapid switching between modes as a result of sensor noise, hysteresis is added to the switching signal. The switching manager therefore behaves as depicted in Figure 6.3. Whenever the current mode is the '3-1' mode and more than 1.5°C of superheat are measured from the plant, the manager switches the current mode of operation to the '3-2' mode. Similarly, whenever the current mode is the '3-2' mode and less than 0.5°C of superheat is measured, the manager switches the current mode of operation to the '3-1' mode.

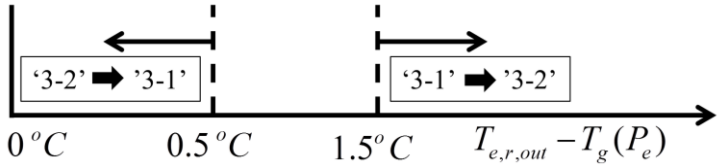

Figure 6.3 Switching Manager

6.4 Model Notation

To allow the desired mode of operation (assumed to be provided by a RTO) to be arbitrary, from this point forward we will refer to the two modes of the system as mode *'a'*, and mode *'b'*. We will always designate the desired mode of operation to which the controller regulates as mode *'b'*. The current mode of operation, which could be either *'a'* or *'b'*, will be denoted as mode *'j'*.

The linear models used for both the observer and controller take the form of Eq. (3.55). For mode *'j'*, we rewrite the system dynamics as:

$$\begin{aligned} \dot{x} &= A_j \Delta x_j + B_j \Delta u_j \\ \Delta y_j &= C_j \Delta x_j + D_j \Delta u_j \end{aligned} \tag{6.2}$$

Furthermore, we assume that the model for mode *'b'* is linearized about the nominal values from the RTO. In other words, $x_{b,o}$, $u_{b,o}$, and $y_{b,o}$ are exactly the references for the states, inputs, and outputs chosen by the RTO. In light of this, we see that regulation to the desired operating conditions involves driving Δx_b, Δu_b, and Δy_b to 0. Although achieving the references exactly corresponds to reaching the equilibrium of the linear model for mode *'b'*, due

to model error and disturbances the references are not likely to be an equilibrium of the plant as well. Therefore, one function of the controller will be to balance the errors of each state, input, and output from its reference in accordance with weights designating the importance of each. We note that the above assumption is easy to satisfy in implementation. Because the linear models of Chapter 3 can be numerically computed in just fractions of a second about arbitrary nominal operating conditions, a new linear model about the current nominal values can easily be generated with every update of the RTO.

6.5 Observer

In this work, a discrete linear Kalman filter estimates the states of the VCS using measurements from the plant and the linear VCS models for each mode. To adapt the linear models of Chapter 3 for use in the Kalman filter, their output vector is first reduced to a subset of outputs that are measurable in a physical system. The reduced output vector is:

$$y_{meas} = \begin{pmatrix} P_e & T_{e,r,out} & T_{e,a,out} & P_c & T_{c,r,out} & T_{c,a,out} \end{pmatrix}^T . \tag{6.3}$$

The input vector for the models used in the Kalman filter is reduced from Eq. (3.56) to include only actuator inputs and not the heat exchanger air inlet temperatures:

$$u_{meas} = \begin{pmatrix} o_{EEV} & \dot{m}_{e,a,in} & v_{comp} & \dot{m}_{c,a,in} \end{pmatrix}^T . \tag{6.4}$$

With this reduction, we assume that the heat exchanger air inlet temperatures do not change significantly between updates of the RTO, or that a sudden change would trigger an event-based update of the RTO, causing a new linear model about the current air inlet temperatures to be generated. Similarly to Eq. (3.55), the estimation model for mode *'j'* is given by:

$$\begin{aligned} \dot{x} &= A_j \Delta x_j + B_j \Delta u_{j,meas} \\ \Delta y_{j,meas} &= C_j \Delta x_j + D_j \Delta u_{j,meas} \end{aligned} \tag{6.5}$$

where

$$\begin{aligned} \Delta x_j &= x - x_{j,o} \\ \Delta u_{j,meas} &= u_{meas} - u_{j,o} \\ \Delta y_{j,meas} &= y_{meas} - y_{j,o} \end{aligned} . \tag{6.6}$$

Eq. (6.5) is next converted from a continuous to a discrete form:

$$\begin{aligned}\Delta x_j(k+1) &= \bar{A}_j \Delta x_j(k) + \bar{B}_j \Delta u_{j,meas}(k) \\ \Delta y_{j,meas}(k) &= \bar{C}_j \Delta x_j(k) + \bar{D}_j \Delta u_{j,meas}(k)\end{aligned} \tag{6.7}$$

where k is the time step index.

In addition to the system model, the Kalman filter also requires that a process noise Q (associated with model uncertainty and disturbances) and measurement noise R be defined. The relative weightings between Q and R determines the balance of "trust" that the Kalman filter places between the model and measurements, and can be treated as tuning parameters in this case. The filter also requires initial estimates of Δx_j and the covariance P. These are set to the zero and identity matrices of appropriate dimensions, respectively.

Following initialization, the basic Kalman filter algorithm consists of two steps, as shown in Figure 6.4.

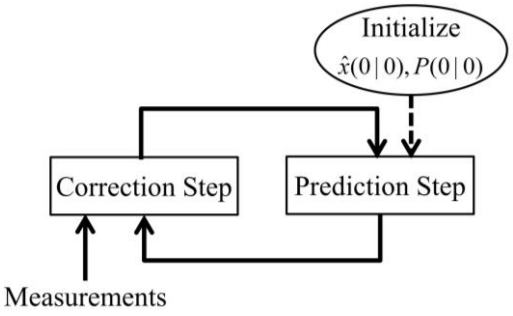

Figure 6.4: Kalman Filter Algorithm

The first step, often called the "prediction" step, predicts the states at the current time step by propagating the model forward from the predicted states, covariance, and inputs of the previous time step. Where $\hat{x}(k|k-1)$ represents the estimated states at time step k found using measurements up to time step k-1, the equations of the prediction step are:

$$\begin{aligned}\Delta\hat{x}_j(k|k-1) &= \bar{A}_j \Delta\hat{x}_j(k-1|k-1) + \bar{B}_j \Delta u_{j,meas}(k-1) \\ P(k|k-1) &= \bar{A}_j P(k-1|k-1) \bar{A}_j^T + Q\end{aligned}. \tag{6.8}$$

The second step of the Kalman filter, known as the "correction" step, updates the state estimates and covariance using the output measurements taken at the current time step. The equations of the correction step are:

$$
\begin{aligned}
K(k) &= P(k \mid k-1)\bar{C}_j^{\,T}\left[\bar{C}_j P(k \mid k-1)\bar{C}_j^{\,T} + R^T\right]^{-1} \\
P(k \mid k) &= \left[I - K(k)\bar{C}_j\right]P(k \mid k-1) \\
\Delta\hat{x}_j(k \mid k) &= \Delta\hat{x}_j(k \mid k-1) + K(k)\left[\Delta y_{j,meas}(k) - \bar{C}_j\Delta\hat{x}_j(k \mid k-1)\right]
\end{aligned}
\qquad . \qquad (6.9)
$$

$K(k)$ in Eq. (6.9) is known as the "Kalman Gain."

As shown in Figure 6.5, in this work the linear system matrices and errors from the linearization conditions of the current mode of operation are fed into the Kalman filter. This ensures that the states of the system are always predicted using the linear model that is expected to be most accurate given the current mode of operation.

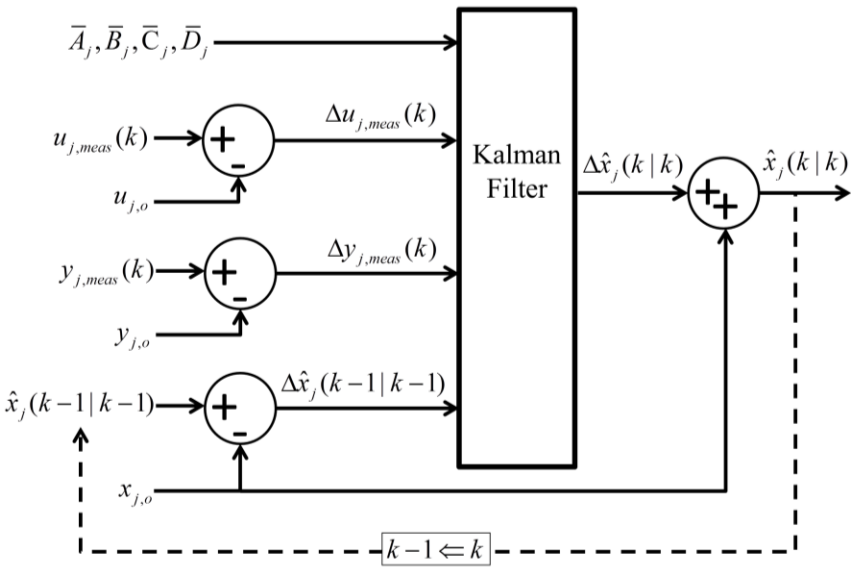

Figure 6.5: Switching Kalman Filter

Whenever a mode switch occurs, we can treat the estimation that follows as a new process with initial estimates of $\Delta\hat{x}_j$ and P as given by the last values found prior to the mode switch. The trajectories of the estimates therefore exhibit switching dynamics as the estimates converge to values based on the current mode's model from the initial conditions based on the previous mode's model. However, as will be demonstrated in the simulations and experiments of Sections 6.8 and 6.9, respectively, these switching dynamics do not significantly impede the performance of the controller. Further development of observers for linear switched systems has been conducted in the literature, such as that in [50], but is not explored here.

6.6 Controller

We now discuss the linear quadratic regulator (LQR) that uses a system model to calculate actuator inputs to the VCS in order to drive to zero the errors between the system's current operating conditions and the nominal conditions received from the RTO.

6.6.1 Error Dynamics

It is necessary to begin by describing the error dynamics of the regulation problem. First, we consider the case when the current mode of operation matches desired mode, defined as mode *'b'* in Section 6.4. Since we assumed, also in Section 6.4, that the linearization conditions of mode '*b'* match exactly the nominal values from the RTO, the error dynamics of the linear model for mode *'b'* are simply:

$$\begin{aligned} \dot{x} &= A_b \Delta x_b + B_b \Delta u_b \\ \Delta y_b &= C_b \Delta x_b + D_b \Delta u_b \end{aligned} \tag{6.10}$$

where Δx_b, Δu_b, and Δy_b are the differences between the current operating conditions and the nominal values. We note that $\dot{x}_b = 0$ because the nominal operating condition is assumed to be at steady-state.

Next, we consider the case when the current mode of operation does not match the desired mode. In other words, we wish to describe the dynamics of the linear model for mode *'a'*:

$$\begin{aligned} \dot{x} &= A_a \Delta x_a + B_a \Delta u_a \\ \Delta y_a &= C_a \Delta x_a + D_a \Delta u_a \end{aligned} \tag{6.11}$$

in terms of the errors from the nominal values: $\Delta x_b = x - x_b$, $\Delta u_b = u - u_b$, and $\Delta y_b = y - y_b$. Doing so, we find that:

$$
\begin{aligned}
\dot{x} &= A_a \Delta x_a + B_a \Delta u_a \\
&= A_a(\Delta x_b + x_b) + B_a(\Delta u_b + u_b) - (A_a x_a + B_a u_a) \\
&= A_a \Delta x_b + B_a \Delta u_b + \begin{pmatrix} A_a & B_a & 0 \end{pmatrix} \begin{pmatrix} (x_b - x_a)^T \\ (u_b - u_a)^T \\ (y_b - y_a)^T \end{pmatrix}
\end{aligned}
$$

$$
\begin{aligned}
\Delta y_a &= y - y_a \\
&= C_a(\Delta x_b + x_b) + D_a(\Delta u_b + u_b) - (C_a x_a + D_a u_a) \\
\Rightarrow y &= C_a \Delta x_b + D_a \Delta u_b + \begin{pmatrix} C_a & D_a & I \end{pmatrix} \begin{pmatrix} (x_b - x_a)^T \\ (u_b - u_a)^T \\ y_a{}^T \end{pmatrix} \\
\Rightarrow y - y_b &= \Delta y_b = C_a \Delta x_b + D_a \Delta u_b + \begin{pmatrix} C_a & D_a & -I \end{pmatrix} \begin{pmatrix} (x_b - x_a)^T \\ (u_b - u_a)^T \\ (y_b - y_a)^T \end{pmatrix}
\end{aligned} \tag{6.12}
$$

The above equations can be written in the compact form:

$$
\begin{aligned}
\dot{x} &= A_a \Delta x_b + B_a \Delta u_b + Vd \\
\Delta y_b &= C_a \Delta x_b + D_a \Delta u_b + Wd
\end{aligned} \tag{6.13}
$$

where the terms Vd and Wd represent constant disturbances associated with the differences in linearization conditions between modes *'a'* and *'b'*.

We can combine the two cases above by considering the arbitrary current mode of operation *'j'* with error dynamics:

$$
\begin{aligned}
\dot{x} &= A_j \Delta x_b + B_j \Delta u_b + V_j d_j \\
\Delta y_b &= C_j \Delta x_b + D_j \Delta u_b + W_j d_j
\end{aligned} \tag{6.14}
$$

where:

$$W_j = \begin{pmatrix} A_j & B_j & 0 \end{pmatrix}$$
$$V_j = \begin{pmatrix} C_j & D_j & -I \end{pmatrix} \tag{6.15}$$
$$d_j = \begin{pmatrix} \left(x_b - x_j\right)^T \\ \left(u_b - u_j\right)^T \\ \left(y_b - y_j\right)^T \end{pmatrix}$$

Clearly, when the current mode of operation matches that of the nominal values (i.e. *'j'='b'*), we find that $d_j = 0$ and see that the system model has an equilibrium at the origin. Otherwise, the equilibrium is typically nonzero.

6.6.2 LQR Formulations

As in the observer, the linear models from Chapter 3 will be used in computing the control. In Chapter 3 the air inlet temperatures to the heat exchangers were treated as an input to the system. However, from the perspective of control these are viewed as an external disturbance. Therefore, the input vector for the models used in the LQR formulation is reduced from that in Eq. (3.56) to include only the four actuator inputs:

$$u = \begin{pmatrix} o_{EEV} & \dot{m}_{e,a,in} & v_{comp} & \dot{m}_{c,a,in} \end{pmatrix}^T. \tag{6.16}$$

We also note that determining a weight in the cost function for each of the 14 outputs of Eq. (3.56) may be excessive. We therefore reduce the output vector of the models used in the LQR formulation to:

$$\begin{pmatrix} \dot{m}_{EEV} & P_e & h_{e,r,out} & SH & \dot{Q}_e & \dot{m}_{comp} & P_c & h_{c,r,out} & SC & \dot{Q}_c \end{pmatrix}^T \tag{6.17}$$

and will further remove the output of superheat when determining a control for a VCS mode that does not include a superheated zone in the evaporator.

In the remainder of this section, we derive two state-feedback LQR formulations to be compared in simulation in Section 6.8. Formulation 1 includes the following features to be covered in detail:

- Normalization of signal errors for ease in defining relative weightings in the cost function

- Weights against errors from nominal values in outputs and inputs
- A constant feedforward term associated with differences between the current and desired mode of operation

In this formulation, the cost function takes the form:

$$J(\Delta u_b) = \int_{t_o}^{\infty} L_j \left(\Delta y_b(t), \Delta u_b(t) \right) dt \,. \tag{6.18}$$

Formulation 2 includes the same features as Formulation 1, with the addition of a weighting against the derivative of the actuator inputs. This can be used to slow the rate of change of the actuator commands, improving the feasibility of the control design for implementation on physical systems (see the second paragraph of the 4th item of Section 6.2). In Formulation 2, the cost function takes the form:

$$J(\Delta u_b) = \int_{t_o}^{\infty} L_j \left(\Delta y_b(t), \Delta u_b(t), \dot{u}(t) \right) dt \,. \tag{6.19}$$

6.6.2.1 Formulation 1: Output Weighting with Feedforward

This formulation can be seen as a modification of the LQR derivation in [43] to incorporate an output-weighted cost and extend to a system with a constant disturbance. It can also be considered also a special case of [44], also with the additional modification of an output weighted cost. The running cost L_j in Eq. (6.18) is given by:

$$L_j = \Delta y_b{}^T Q_j \Delta y_b + \Delta u_b{}^T R_j \Delta u_b \,. \tag{6.20}$$

where Q_j and R_j are diagonal matrices of the weights assigned to each signal. As stated above, we first normalize the errors Δy_b and Δu_b by the nominal values of each signal. This is done to make selection of the elements of Q_j and R_j more user-friendly in light of the wide range of magnitudes occurring across the outputs and inputs. For example, pressures can be on the order of 1000 in kPa, while refrigerant mass flow rates are on the order of 0.01 in kg/s. Therefore, a weight of '1' associated with a 10% error in pressure contributes orders of magnitude more to the cost than the same weight associated with a 10% error in air mass flow rate. By augmenting the system such that the error signals are all on the same order of magnitude, the weights chosen as

entries in Q_j and R_j in the resulting augmented cost function do not have to be user-adjusted so significantly for differences in signal magnitudes. A weight of '1' associated with a 10% error in pressure contributes approximately the same to the cost function as the same weight associated with a 10% error in mass flow rate.

To achieve this normalization, we define:

$$\begin{aligned}\Delta x_b &= diag(\mathrm{x}_{j,o})\Delta\bar{x}_b = w_{j,1}\Delta\bar{x}_b \\ \Delta u_b &= diag(u_{j,o})\Delta\bar{u}_b = w_{j,2}\Delta\bar{u}_b \\ \Delta y_b &= diag(y_{j,o})\Delta\bar{y}_b = w_{j,3}\Delta\bar{y}_b\end{aligned} \tag{6.21}$$

so that the overbarred signals are scaled by their nominal values. Substituting into Eq. (6.14) and noting that $\dot{x}_j = w_1\dot{\bar{x}}_j$, we find:

$$\begin{aligned} w_1\dot{\bar{x}} &= A_j w_1\Delta\bar{x}_j + B_j w_2\Delta\bar{u}_j + V_j d_j \\ &\Rightarrow \dot{\bar{x}} = w_1^{-1}A_j w_1\Delta\bar{x}_j + w_1^{-1}B_j w_2\Delta\bar{u}_j + w_1^{-1}V_j d_j \\ w_3\Delta\bar{y}_j &= C_j w_1\Delta\bar{x}_j + D_j w_2\Delta\bar{u}_j + W_j d_j \\ &\Rightarrow \Delta\bar{y}_j = w_3^{-1}C_j w_1\Delta\bar{x}_j + w_3^{-1}D_j w_2\Delta\bar{u}_j + w_3^{-1}W_j d_j \end{aligned} \tag{6.22}$$

Eq. (6.22) can be rewritten as the augmented system:

$$\begin{aligned}\dot{x} &= \bar{A}_j\Delta\bar{x}_b + \bar{B}_j\Delta\bar{u}_b + \bar{V}_j d_j \\ \Delta\bar{y}_b &= \bar{C}_j\Delta\bar{x}_b + \bar{D}_j\Delta\bar{u}_b + \bar{W}_j d_j\end{aligned} \tag{6.23}$$

with

$$\begin{aligned}\bar{A}_j &= w_{j,1}^{-1}B_j w_{j,1} \\ \bar{B}_j &= w_{j,1}^{-1}B_j w_{j,2} \\ \bar{V}_j &= w_{j,1}^{-1}V_j \\ \bar{C}_j &= w_{j,3}^{-1}C_j w_{j,1} \\ \bar{D}_j &= w_{j,3}^{-1}D_j w_{j,2} \\ \bar{W}_j &= w_{j,3}^{-1}W_j\end{aligned} \tag{6.24}$$

We then replace Eq. (6.20) with:

$$L_j = \Delta\bar{y}_b^{\,T}Q_j\Delta\bar{y}_b + \Delta\bar{u}_b^{\,T}R_j\Delta\bar{u}_b\,, \tag{6.25}$$

completing the normalization of signals in the cost function.

We next substitute $\Delta\bar{y}_b$ above with the second line of Eq. (6.23):

$$L_j = \left(\bar{C}_j \Delta x_b + \bar{D}_j \Delta\bar{u}_b + \bar{W}_j d_j\right)^T Q_j \left(\bar{C}_j \Delta x_b + \bar{D}_j \Delta\bar{u}_b + \bar{W}_j d_j\right) + \Delta\bar{u}_b{}^T R_j \Delta\bar{u}_b \ . \tag{6.26}$$

For simplicity of notation, from this point forward we will omit the subscripts and overbars of Eq. (6.26), leaving it to the reader to understand that these should be carried over from Eq. (6.26) into the equations that follow. Expanding Eq. (6.26) and using the equalities:

$$\begin{aligned} \Delta x^T \left(C^T Q D\right)\Delta u + \Delta u^T \left(D^T Q C\right)\Delta x &= 2\Delta u^T \left(D^T Q C\right)\Delta x \\ \Delta x^T \left(C^T Q W\right) d + d^T \left(W^T Q C\right)\Delta x &= 2 d^T \left(W^T Q C\right)\Delta x \\ \Delta u^T \left(D^T Q W\right) d + d^T \left(W^T Q D\right)\Delta u &= 2 d^T \left(W^T Q D\right)\Delta u \end{aligned} \ , \tag{6.27}$$

we find that

$$\begin{aligned} L = {} & \Delta x^T \left(C^T Q C\right)\Delta x + \Delta u^T \left(R + D^T Q D\right)\Delta u + d^T \left(W^T Q W\right) d \\ & + 2\Delta u^T \left(D^T Q C\right)\Delta x + 2 d^T \left(W^T Q C\right)\Delta x + 2 d^T \left(W^T Q D\right)\Delta u \end{aligned} . \tag{6.28}$$

We first consider the finite time horizon case in which the upper limit of the cost function is given by some $t_f > t_o$. This will later be extended to the infinite horizon case by taking t_f to infinity in the limit. The Hamiltonian is given by:

$$\begin{aligned} H &= \langle \lambda, \dot{x} \rangle - L \\ &= \lambda^T \left(A\Delta x + B\Delta u + V d\right) - \Delta x^T \left(C^T Q C\right)\Delta x - \Delta u^T \left(R + D^T Q D\right)\Delta u - d^T \left(W^T Q W\right) d \\ &\quad - 2\Delta u^T \left(D^T Q C\right)\Delta x - 2 d^T \left(W^T Q C\right)\Delta x - 2 d^T \left(W^T Q D\right)\Delta u \end{aligned} . \tag{6.29}$$

We denote x, u, and λ along the optimal trajectory as x^*, u^*, and λ^*. Along this trajectory, λ^* satisfies the adjoint equation:

$$\begin{aligned} \dot{\lambda}^* &= -H_{x^*} \\ &= -A^T \lambda^* + 2\left(C^T Q C\right)\Delta x^* + 2\left[\Delta u^{*T} \left(D^T Q C\right)\right]^T + 2\left[d^T \left(W^T Q C\right)\right]^T \\ &= -A^T \lambda^* + 2\left(C^T Q C\right)\Delta x^* + 2\left(C^T Q D\right)\Delta u^* + 2\left(C^T Q W\right) d \end{aligned} \tag{6.30}$$

with $\lambda^*(t_f) = 0$.

We next define λ as:

$$\lambda^* = -2\left(P_1^*\Delta x + P_2^* d\right) \tag{6.31}$$

with $P_1^*(t_f) = 0$ and $P_2^*(t_f) = 0$.

Taking the derivative of (6.31) and noting that $\dot{d} = 0$ and $\Delta\dot{x} = \dot{x}$, we find:

$$\dot{\lambda}^* = -2\left(\dot{P}_1^*\Delta x + P_1^*\dot{x}^* + \dot{P}_2^* d\right). \tag{6.32}$$

Substituting Eqs. (6.31) and (6.32) into Eq. (6.30), dividing by two, and expanding yields:

$$\begin{aligned} &-\dot{P}_1\Delta x^* - P_1 A\Delta x^* - P_1 B\Delta u^* - P_1 V d - \dot{P}_2 d \\ &= A^T\left(P_1\Delta x^* + P_2 d\right) + \left(C^T QC\right)\Delta x^* + \left(C^T QD\right)\Delta u^* + \left(C^T QW\right)d \end{aligned}. \tag{6.33}$$

By the Maximum Principle, we know that:

$$\begin{aligned} H_{u^*} &= 0 \\ &= B^T\lambda^* - 2\left(R + D^T QD\right)\Delta u^* - 2\left(D^T QC\right)\Delta x^* - \left[2d^T\left(W^T QD\right)\right]^T \\ &= B^T\lambda^* - 2\left(R + D^T QD\right)\Delta u^* - 2\left(D^T QC\right)\Delta x^* - 2\left(D^T QW\right)d \end{aligned}. \tag{6.34}$$

Rearranging Eq. (6.34) and assuming that $R + D^T QD$ is invertible, we find that:

$$\Delta u^* = \left(R + D^T QD\right)^{-1}\left(\frac{1}{2}B^T\lambda^* - \left(D^T QC\right)\Delta x^* - \left(D^T QW\right)d\right). \tag{6.35}$$

Substituting Eq. (6.31) into Eq. (6.35), we get:

$$\Delta u^* = -\left(R + D^T QD\right)^{-1}\left(B^T\left(P_1^*\Delta x^* + P_2^* d\right) + \left(D^T QC\right)\Delta x^* + \left(D^T QW\right)d\right). \tag{6.36}$$

We then substitute Eq. (6.36) into Eq. (6.33):

$$\begin{aligned} &-\dot{P}_1^*\Delta x^* - P_1^* A\Delta x^* - P_1^* V d - \dot{P}_2^* d \\ &-P_1^* B\left[-\left(R + D^T QD\right)^{-1}\left(B^T\left(P_1^*\Delta x^* + P_2 d\right) + \left(D^T QC\right)\Delta x^* + \left(D^T QW\right)d\right)\right] \\ &= A^T\left(P_1^*\Delta x^* + P_2^* d\right) + \left(C^T QC\right)\Delta x^* + \left(C^T QW\right)d \\ &+\left(C^T QD\right)\left[-\left(R + D^T QD\right)^{-1}\left(B^T\left(P_1^*\Delta x^* + P_2^* d\right) + \left(D^T QC\right)\Delta x^* + \left(D^T QW\right)d\right)\right] \end{aligned}. \tag{6.37}$$

Expanding and regrouping terms by Δx^* and d we get:

$$\begin{aligned}
&\dot{P}_1^*\Delta x^* + P_1^* A\Delta x^* + A^T P_1^*\Delta x^* + \left(C^T QC\right)\Delta x^* - P_1^* B\left(R + D^T QD\right)^{-1} B^T P_1^*\Delta x^* \\
&\qquad - P_1^* B\left(R + D^T QD\right)^{-1}\left(D^T QC\right)\Delta x^* \\
&\qquad - \left(C^T QD\right)\left(R + D^T QD\right)^{-1} B^T P_1^*\Delta x^* \\
&\qquad - \left(C^T QD\right)\left(R + D^T QD\right)^{-1}\left(D^T QC\right)\Delta x^* \\
&+\dot{P}_2^* d + P_1^* V d + A^T P_2^* d + \left(C^T QW\right)d - \left(C^T QD\right)\left(R + D^T QD\right)^{-1} B^T P_2^* d \\
&\qquad - \left(C^T QD\right)\left(R + D^T QD\right)^{-1}\left(D^T QW\right)d \\
&\qquad - P^*{}_1 B\left(R + D^T QD\right)^{-1} B^T P_2^* d \\
&\qquad - P_1^* B\left(R + D^T QD\right)^{-1}\left(D^T QW\right)d \\
&= 0
\end{aligned} \quad . \qquad (6.38)$$

Since Δx^* and d can be arbitrary, we find that:

$$\begin{aligned}
&\dot{P}_1^*\Delta x^* + P_1^* A\Delta x^* + A^T P_1^*\Delta x^* + \left(C^T QC\right)\Delta x^* - P_1^* B\left(R + D^T QD\right)^{-1} B^T P_1^*\Delta x^* \\
&\qquad - P_1^* B\left(R + D^T QD\right)^{-1}\left(D^T QC\right)\Delta x^* \\
&\qquad - \left(C^T QD\right)\left(R + D^T QD\right)^{-1} B^T P_1^*\Delta x^* \\
&\qquad - \left(C^T QD\right)\left(R + D^T QD\right)^{-1}\left(D^T QC\right)\Delta x^* = 0
\end{aligned} \qquad (6.39)$$

and

$$\begin{aligned}
&\dot{P}_2^* d + P_1^* V d + A^T P_2^* d + \left(C^T QW\right)d - \left(C^T QD\right)\left(R + D^T QD\right)^{-1} B^T P_2^* d \\
&\qquad - \left(C^T QD\right)\left(R + D^T QD\right)^{-1}\left(D^T QW\right)d \\
&\qquad - P^*{}_1 B\left(R + D^T QD\right)^{-1} B^T P_2^* d \\
&\qquad - P_1^* B\left(R + D^T QD\right)^{-1}\left(D^T QW\right)d = 0
\end{aligned} \quad . \qquad (6.40)$$

Regrouping terms in (6.39) yields:

$$\dot{P}_1^* + P_1 A + A^T P_1^* - \left(P_1^* B + C^T QD\right)\left(R + D^T QD\right)^{-1}\left(B^T P_1^* + D^T QC\right) + \left(C^T QC\right) = 0 \; . \qquad (6.41)$$

This is just a Riccati differential equation:

$$\dot{P}_1^* + P_1^* A + A^T P_1^* - (P_1^* B + \tilde{N})\tilde{R}^{-1}(B^T P_1^* + \tilde{N}^T) + \tilde{Q} = 0 \qquad (6.42)$$

where:

$$\begin{aligned}\tilde{N} &= C^T QD \\ \tilde{R} &= R + D^T QD \\ \tilde{Q} &= C^T QC\end{aligned} \quad . \tag{6.43}$$

In the infinite horizon case (i.e. when $t_f \to \infty$), Eq. (6.42) admits a unique steady-state solution for P_1^* if (*A*, *B*) is stabilizable and

$$\begin{pmatrix} \tilde{Q} & \tilde{N} \\ \tilde{N}^T & \tilde{R} \end{pmatrix} > 0 . \tag{6.44}$$

Since positive definite matrices are invertible, this also enforces the assumption stated for Eq. (6.35).

We can also regroup terms in Eq. (6.40) and substitute in terms from Eq. (6.43) to find that:

$$\begin{aligned}&\dot{P}_2^* + \left[A^T - \tilde{N}\tilde{R}^{-1}B^T - P_1 B\tilde{R}^{-1}B^T \right] P_2^* \\ &+ P_1^* \left[V - B\tilde{R}^{-1}\left(D^T QW \right) \right] \\ &- \tilde{N}\tilde{R}^{-1}\left(D^T QW \right) + \left(C^T QW \right) = 0\end{aligned} \quad . \tag{6.45}$$

In the infinite horizon case, as long as Eq. (6.45) admits a unique steady-state solution we can solve for P_2^* as:

$$P_2^* = -\left[A^T - \tilde{N}\tilde{R}^{-1}B^T - P_1^* B\tilde{R}^{-1}B^T \right]^{-1} \left\{ P_1^* \left[V - B\tilde{R}^{-1}\left(D^T QW \right) \right] - N\tilde{R}^{-1}\left(D^T QW \right) + \left(C^T QW \right) \right\} . \tag{6.46}$$

We note that a steady-state solution to Eq. (6.45) does not necessarily exist in the absence of additional assumptions. For example, if P_1^* is not full rank, then the differential equation of Eq. (6.45) may not reach a steady-state solution. This can also cause the terms in the first set of brackets of Eq. (6.46) to not be invertible. We assume that Eq. (6.45) does admit the steady-state solution as given by Eq. (6.46).

Returning to Eq. (6.36), we find that:

$$\begin{aligned}\Delta u^* &= -\tilde{R}^{-1}\left(B^T\left(P_1^*\Delta x^* + P_2^* d\right) + \tilde{N}^T\Delta x^* + \left(D^T Q W\right)d\right) \\ &= -\tilde{R}^{-1}\left(B^T P_1^* + \tilde{N}^T\right)\Delta x^* - \tilde{R}^{-1}\left[B^T P_2^* + \left(D^T Q W\right)\right]d\end{aligned}. \tag{6.47}$$

Recalling that we were working with the augmented system of Eq. (6.23) and adding back in the notation that was omitted for convenience, we see that we have actually calculated the optimal feedback gain and feedforward term for the normalized inputs and states:

$$\Delta\bar{u}_b^*(t) = -\bar{k}_{j,x}\Delta\hat{\bar{x}}_b(t) - \bar{k}_{j,d}d_j \tag{6.48}$$

with

$$\begin{aligned}\bar{k}_{j,x} &= \bar{\tilde{R}}_j^{-1}\left(\bar{B}_j^T\bar{P}_{j,1}^* + \bar{\tilde{N}}_j^T\right) \\ \bar{k}_{j,d} &= \bar{\tilde{R}}_j^{-1}\left[\bar{B}_j^T\bar{P}_{j,2}^* + \left(\bar{D}_j^T Q_j\bar{W}_j\right)\right]\end{aligned}. \tag{6.49}$$

Using Eq. (6.21), we find that the optimal inputs to the plant are given by:

$$u^*(t) = -k_{j,x}\Delta\hat{x}_b(t) - k_{j,d}d_j + u_b \tag{6.50}$$

with

$$\begin{aligned}k_{j,x} &= w_2\bar{k}_{j,x}w_1^{-1} \\ k_{j,d} &= w_2\bar{k}_{j,d}\end{aligned}. \tag{6.51}$$

6.6.2.1.1 Special Cases

Since the above formulation essentially combines several simpler and well documented LQR augmentations, under appropriate assumptions it should be possible to recover these results. First, we assume that $W = 0$ and $V = 0$. In this case, $\bar{P}_1^*$ and $\bar{k}_{j,x}$ are calculated exactly as before, but we find that $\bar{k}_{j,d} = 0$. This implies that there should be no feedforward term when the disturbance does not enter the system dynamics. The formulation then matches the MATLAB function 'lqr', which computes an output weighted LQR state-feedback gain.

As a second special case, we assume that $\bar{C} = I$, $\bar{D} = 0$, and $\bar{W} = 0$. This reduces the running cost of Eq. (6.25) to:

$$L_j = \Delta x_j^T Q_j\Delta x_j + \Delta\bar{u}_j^T R_j\Delta\bar{u}_j, \tag{6.52}$$

giving a state-based weighting. Again omitting the subscripts and overbars of the normalized system for notational simplicity, the Riccati equation of Eq. (6.42) reduces to:

$$P_1^* A + A^T P_1^* - P_1^* B R^{-1} B^T P_1^* + Q = 0 \tag{6.53}$$

and P_2^* is given by:

$$P_2^* = -\left(A^T - P_1^* B R^{-1} B^T\right)^{-1} P^*{}_1 V \,. \tag{6.54}$$

The normalized optimal control inputs are then given by Eq. (6.48) with

$$\begin{aligned} \bar{k}_{j,x} &= R_j^{-1} \bar{B}_j^T \bar{P}_{j,1}^* \\ \bar{k}_{j,d} &= -R_j^{-1} \bar{B}_j^T \left(\bar{A}_j^T - \bar{P}_{j,1}^* \bar{B}_j R_j^{-1} \bar{B}_j^T\right)^{-1} \bar{P}_{j,1}^* \bar{V}_j \end{aligned} \tag{6.55}$$

This is the LQR formulation for a state-based weighting with a constant disturbance, which can also be found as a special case of the result in [44].

6.6.2.2 Formulation 2: Additional Input Derivative Weighting

As previously stated, in Formulation 2 we seek to penalize against the instantaneous rate of change of the control inputs, $\dot{u}$, as a means of smoothing the controller commands in time. Since we would like to keep the control inputs in the neighborhood of their nominal values as well, we will also continue to penalize against Δu_j directly. We first define the running cost L_j in Eq. (6.19) as:

$$L_j = \Delta y_b{}^T Q_j \Delta y_b + \Delta u_b{}^T R_j \Delta u_b + \dot{u}^T S_j \dot{u} \,. \tag{6.56}$$

This can be rewritten as:

$$L_j = \begin{pmatrix} \Delta y_b{}^T & \Delta u_b{}^T \end{pmatrix} \begin{pmatrix} Q_j & 0 \\ 0 & R_j \end{pmatrix} \begin{pmatrix} \Delta y_b \\ \Delta u_b \end{pmatrix} + \dot{u}^T S_j \dot{u} \,. \tag{6.57}$$

We next take the system model of Eq. (6.14) and combine it into an augmented system in which $\dot{u}$ is also part of the state vector:

$$\begin{pmatrix}\dot{x}\\ \dot{u}\end{pmatrix}=\begin{pmatrix}A_j & B_j\\ 0 & 0\end{pmatrix}\begin{pmatrix}\Delta x_b\\ \Delta u_b\end{pmatrix}+\begin{pmatrix}V_j\\ 0\end{pmatrix}d_j+\begin{pmatrix}0\\ I\end{pmatrix}\dot{u}$$
$$\begin{pmatrix}\Delta y_b\\ \Delta u_b\end{pmatrix}=\begin{pmatrix}C_j & D_j\\ 0 & I\end{pmatrix}\begin{pmatrix}\Delta x_b\\ \Delta u_b\end{pmatrix}+\begin{pmatrix}W_j\\ 0\end{pmatrix}d_j+\begin{pmatrix}0\\ 0\end{pmatrix}\dot{u} \tag{6.58}$$

The running cost and system dynamics can then be expressed compactly as:

$$\begin{aligned}L_j &= \Delta\tilde{y}_b{}^T\tilde{Q}_j\Delta\tilde{y}_b+\dot{u}^T\tilde{R}_j\dot{u}\\ \dot{\tilde{x}} &= \tilde{A}_j\Delta\tilde{x}_b+\tilde{B}_j\dot{u}+\tilde{V}_j d_j\\ \Delta\tilde{y}_b &= \tilde{C}_j\Delta\tilde{x}_b+\tilde{D}_j\dot{u}+\tilde{W}_j d_j\end{aligned} \tag{6.59}$$

with

$$\begin{aligned}&\dot{\tilde{x}}=\begin{pmatrix}\dot{x}\\ \Delta\dot{u}_b\end{pmatrix},\ \Delta\tilde{x}_b=\begin{pmatrix}\Delta x_b\\ \Delta u_b\end{pmatrix},\ \Delta\tilde{y}_b=\begin{pmatrix}\Delta y_b\\ \Delta u_b\end{pmatrix},\ \tilde{Q}_j=\begin{pmatrix}Q_j & 0\\ 0 & R_j\end{pmatrix},\ \tilde{R}_j=S_j,\\ &\tilde{A}=\begin{pmatrix}A_j & B_j\\ 0 & 0\end{pmatrix},\ \tilde{B}_j=\begin{pmatrix}0\\ I\end{pmatrix},\ \tilde{V}_j=\begin{pmatrix}V_j\\ 0\end{pmatrix},\ \tilde{C}_j=\begin{pmatrix}C_j & D_j\\ 0 & I\end{pmatrix},\ \tilde{D}_j=\begin{pmatrix}0\\ 0\end{pmatrix},\ \tilde{W}_j=\begin{pmatrix}W_j\\ 0\end{pmatrix}\end{aligned} \tag{6.60}$$

Therefore, we see that we can directly make use of Formulation 1 from Section 6.6.2.1 by using the augmented equations above as the cost function and system model. This allows us to calculate the derivative of the optimal inputs as a function of state and input feedback:

$$\dot{u}^*(t)=-k_{j,x}\begin{pmatrix}\Delta\hat{x}_b(t)\\ \Delta u_b(t)\end{pmatrix}-k_{j,d}d_j\,. \tag{6.61}$$

Integrating Eq. (6.61) then gives the optimal inputs to the plant:

$$u^*(t)=\int_{t_o}^{t}\left[-k_{j,x}\begin{pmatrix}\Delta\hat{x}_b(t)\\ \Delta u_b(t)\end{pmatrix}-k_{j,d}d_j\right]dt+u_b\,. \tag{6.62}$$

6.7 Controllability and Observability

In Chapter 3, linear model formulations both with and without a compressor outlet enthalpy dynamic are presented. While including the compressor outlet enthalpy dynamic does improve the accuracy of the linear models in some cases, the difference is small enough that for most applications this added accuracy is not worth the model complexity that the inclusion of an

additional state brings. Therefore, linear models without this dynamic are used in the estimation and control. The full vector of these models consists of 6 evaporator states and 9 condenser states:

$$x = \begin{pmatrix} \zeta_{e,1} & P_e & h_{e,r,2} & T_{e,w,1} & T_{e,w,2} & \bar{\gamma}_e & \zeta_{c,1} & \zeta_{c,2} & P_c & h_{c,r,1} & h_{c,r,3} & \bar{\gamma}_c & T_{c,w,1} & T_{c,w,2} & T_{c,w,3} \end{pmatrix}. \quad (6.63)$$

In Chapter 3, it was sufficient for the purpose of open-loop accuracy comparison that the linear models be stable. However, to use these models in control and estimation, they must exhibit suitable controllability and observability properties as well. In order to achieve these, the following five states from Eq. (6.63) are removed from the model: $\bar{\gamma}_e$, $\zeta_{c,1}$, $\zeta_{c,2}$, $h_{c,r,1}$, and $T_{c,w,1}$. These correspond to dynamics that were either observed to vary little from their nominal values during the evaluation in Section 3.5.3.1 or were observed to have little effect on the refrigerant or air-side outputs that we seek to control. The resulting reduced state vector is:

$$x = \begin{pmatrix} \zeta_{e,1} & P_e & h_{e,r,2} & T_{e,w,1} & T_{e,w,2} & P_c & h_{c,r,3} & \bar{\gamma}_c & T_{c,w,2} & T_{c,w,3} \end{pmatrix}. \quad (6.64)$$

Following this state reduction, the models used in the observer of Section 6.5 were found to be fully observable for the '3-2' model and have three unobservable modes in the '3-1' model. Following the additional augmentations made to the linear models for use in control as detailed in Section 6.6, the '3-2' model was found to have one uncontrollable mode and the '3-1' model was found to have two uncontrollable modes. The uncontrollable modes are stable. As will be seen in the simulation and experimental results that follow, the controller and observer both perform well despite the presence of these few uncontrollable and unobservable modes.

6.8 Simulation Results

Before implementing the control design experimentally, its salient features can be evaluated in simulation. All simulations in this section use the nonlinear VCS models with SMB heat exchangers of Chapter 2 (experimentally validated in Chapter 4) as the plant to which the controller is applied. We perform the following comparisons:

- Section 6.8.1 — Compare the switched LQR Formulation 1 of Section 6.6.2.1 (which includes output and input-based weightings) with Formulation 2 of Section 6.6.2.2 (which includes output, input, and input derivative-based weightings) for a superheat

recovery process. This demonstrates how the inclusion of output derivative-based weightings improves the feasibility of the control approach for experimental application.

- Section 6.8.2 — Compare the switched LQR formulation with a decentralized proportional-integral (PI) controller to demonstrate the advantage of model-based control.
- Section 6.8.3 — Compare LQR formulations with and without mode switching in estimation and control. This demonstrates the benefits of the switched framework.

To better simulation experimental conditions, white Gaussian noise of similar standard deviation to that which occurs in the experimental system is added as measurement noise to the plant outputs received by the switching manager and observer. These standard deviations are $\sqrt{3}$ kPa on pressure measurements and 0.1°C on temperature measurements. The observer and switching manager operate at 10Hz.

6.8.1 LQR Formulation 1 vs. LQR Formulation 2

Here, we compare LQR Formulation 1 of Section 6.6.2.1 with LQR Formulation 2 of Section 6.6.2.2 for a superheat recovery process. Recall that the difference between these approaches is that Formulation 2 includes a weighting against the derivative of the actuator inputs in its cost function, while Formulation 1 weights only against errors from nominal in outputs and inputs. The system is first brought to a steady-state operating condition without superheat by supplying constant actuator inputs in open loop. Figure 6.6 shows this initial operating condition on a P-h diagram.

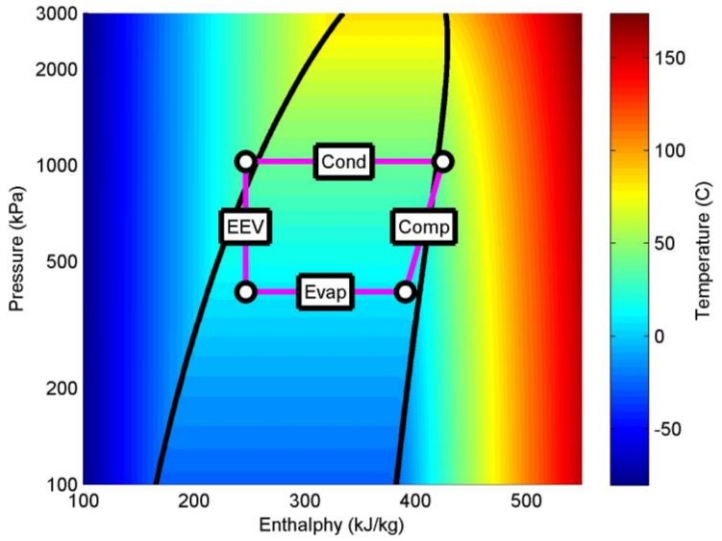

Figure 6.6: Initial Operating Condition

At 200s, the controller is turned on and closed-loop regulation to a nominal operating condition with approximately 14°C of superheat begins. Figure 6.6 shows this desired nominal operating condition on a P-h diagram.

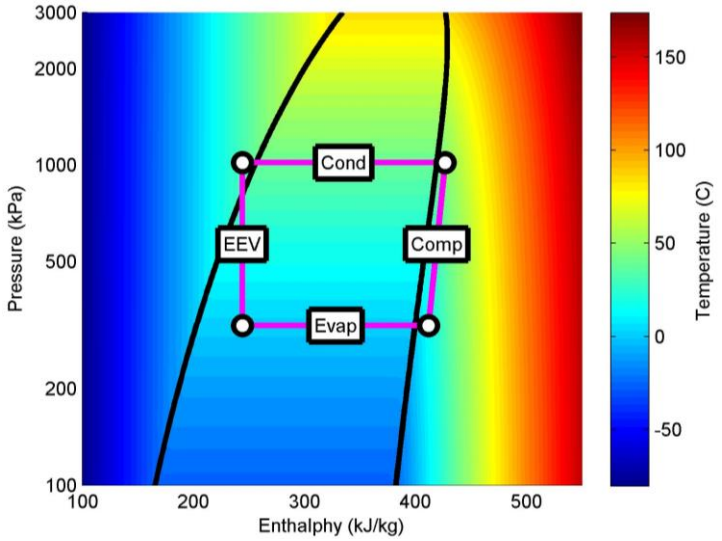

Figure 6.7: Nominal Operating Condition

Figure 6.8 shows several outputs of the simulated VCS for the process of superheat recovery. Simulations using controllers of both Formulation 1 and Formulation 2 are shown. The

switching time at which the observer and controller change modes from the '3-1' model to the '3-2' model is plotted as a dashed vertical line for each formulation.

The formulations bring the system to recover superheat at similar times, however Formulation 2 results in a longer settling time to the nominal conditions. The reason for this is clear from Figure 6.9, which shows the actuator inputs from each formulation. The use of weighting against the derivative of the outputs in Formulation 2 essentially rate limits the actuator commands, smoothing the inputs. This limits the ability of the Formulation 2 controller to bring the system to rapidly reach the nominal conditions. However, this smoothing is advantageous in practice because the rates of changes available to real-world actuators are inherently limited and because the smooth actuator commands would result in less component wear than the noisy commands of Formulation 1.

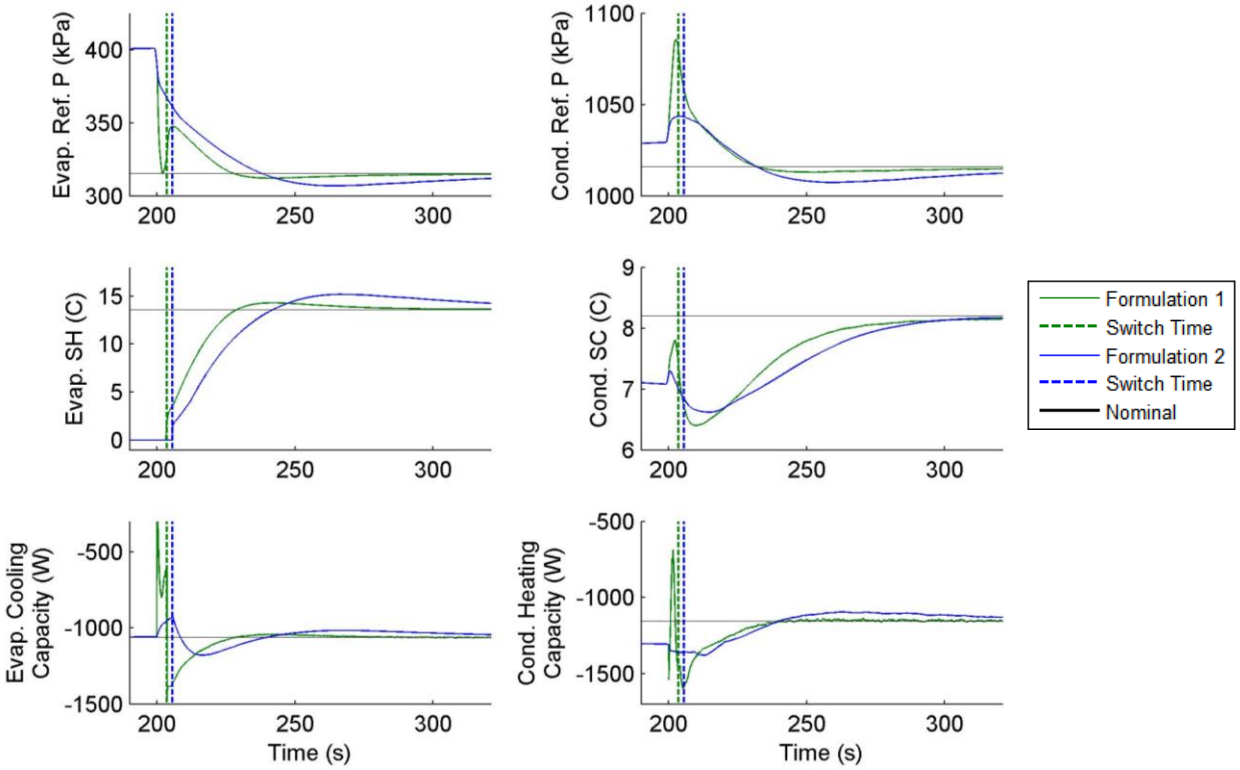

Figure 6.8: Simulation Outputs

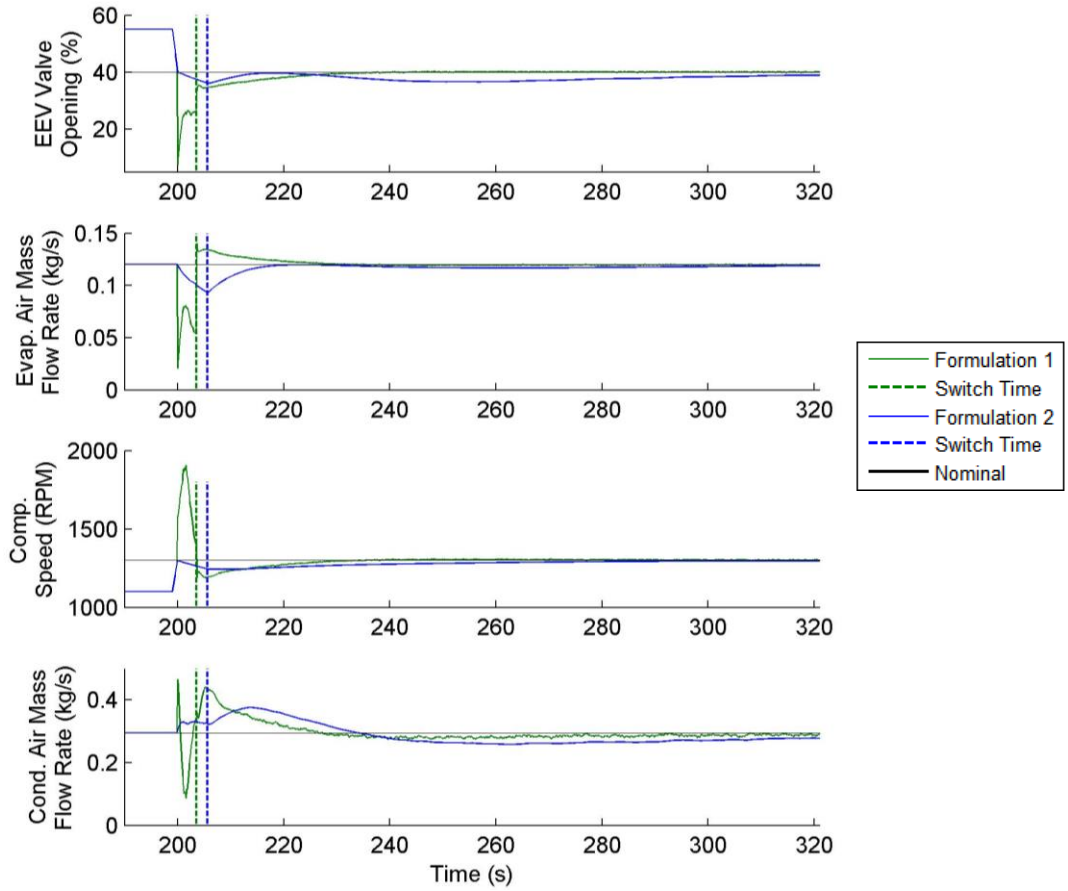

Figure 6.9: Actuator Inputs

Figure 6.10 and Figure 6.11 show the actual and estimated states under use of Formulations 1 and 2, respectively. From these, it is clear that the Kalman filter provides reasonably accurate esimates of the system states. Those errors that do occur are relatavely small and generally appear in states that are not critical to the refrigerant-side dynamics, such as the condenser wall temperatures. The system outputs received by the observer (from which the estimates of Figure 6.10 and Figure 6.11 are computed) are plotted as Figure 6.12, in which the white Gaussian noise added to simulate experimental measurement can be seen. Comparing these measurements with the estimated states, one can see that the observer rejects some but not all of the measurement noise. This further motivates the choice of Formulation 2 as the better controller, since it produces smooth actuator commands despite the presence of noise in some estimated states.

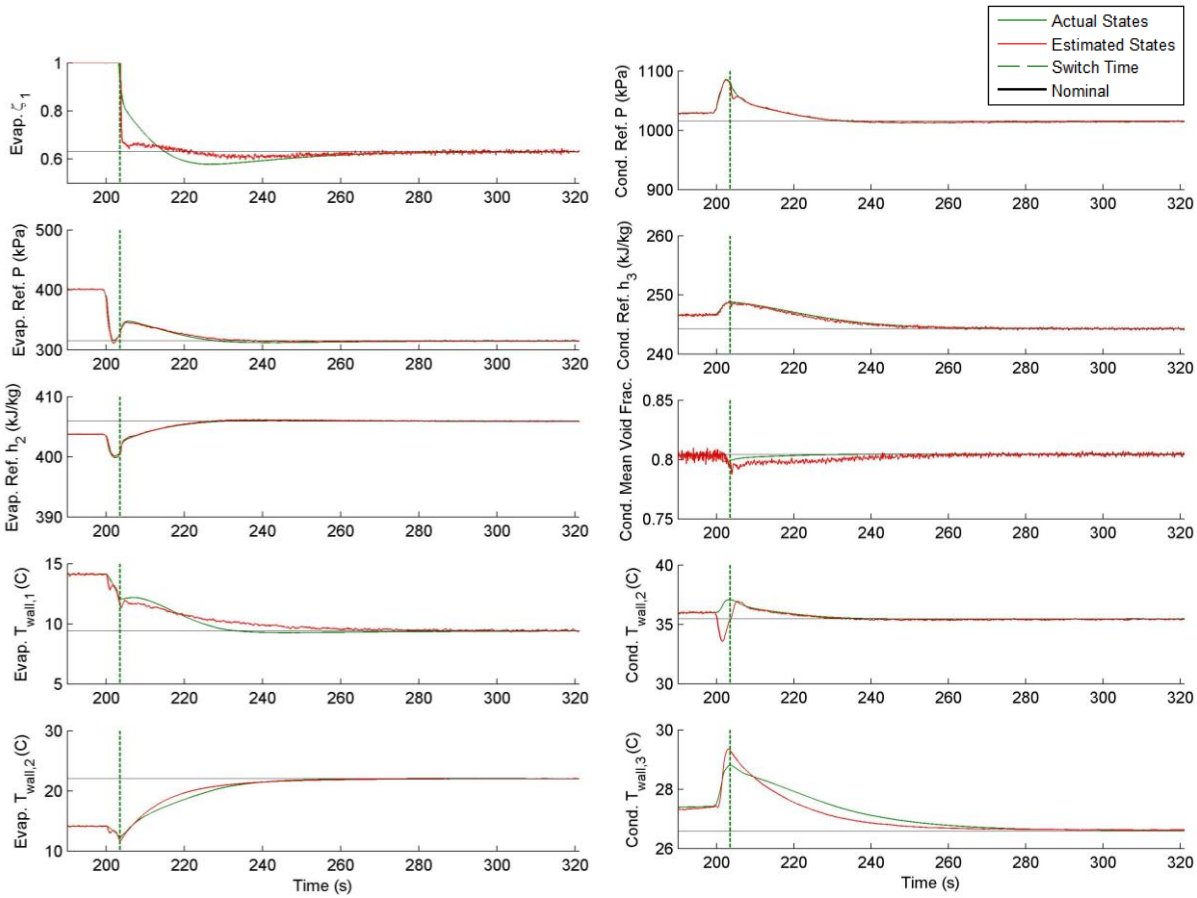

Figure 6.10: States Under Formulation 1

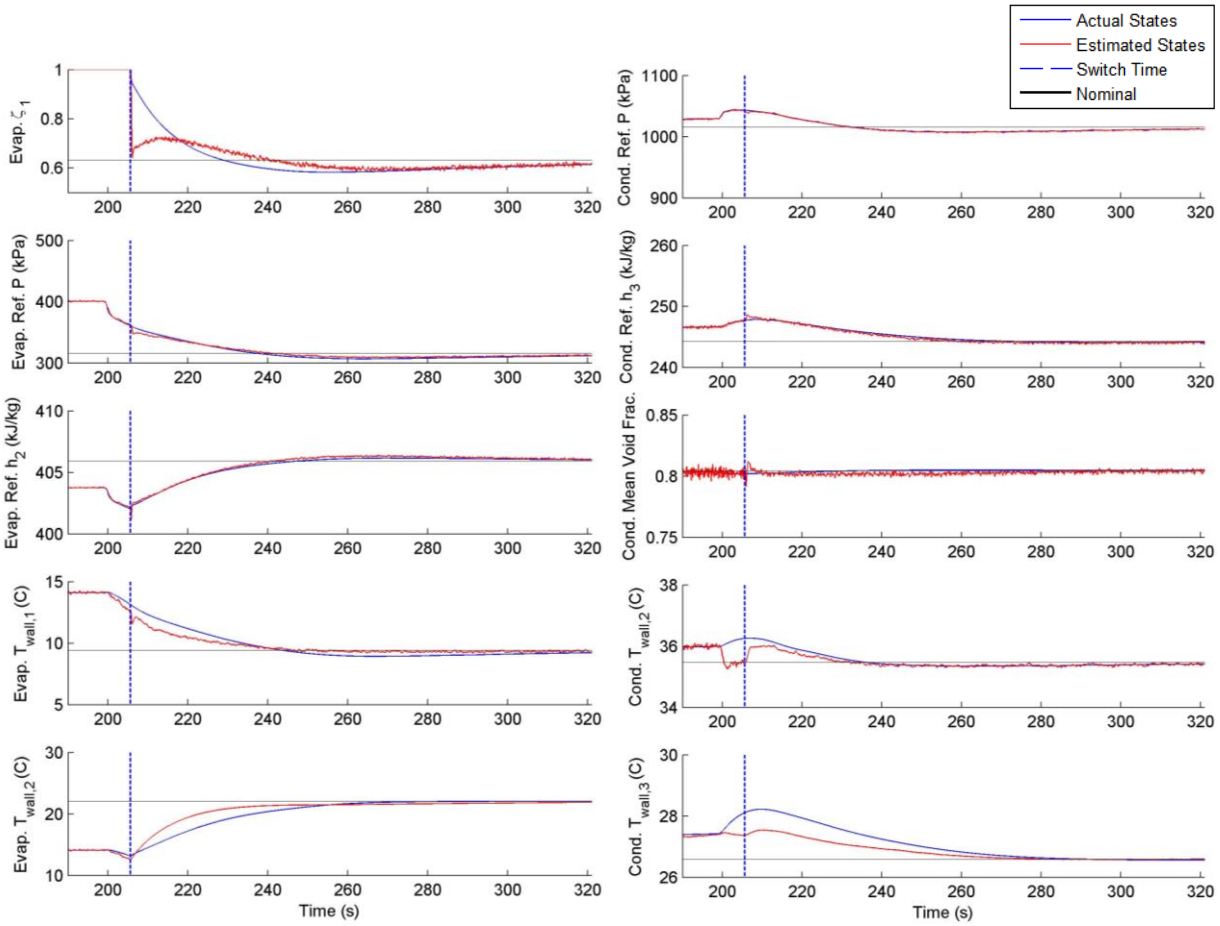

Figure 6.11: States Under Formulation 2

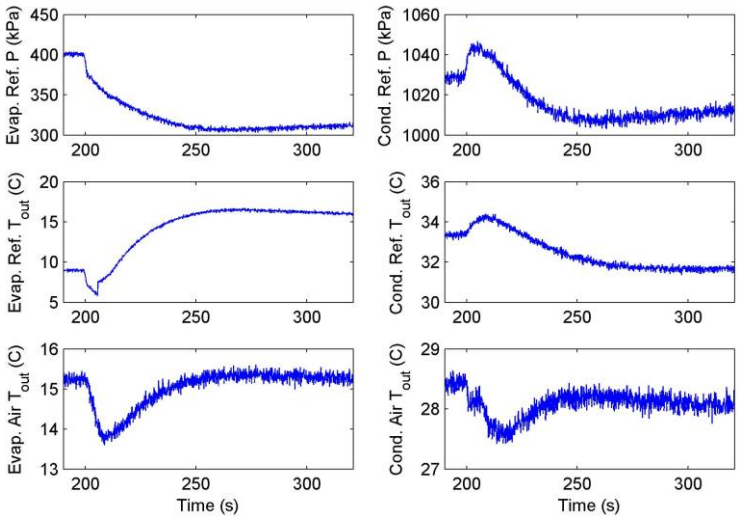

Figure 6.12: Measurements Received By Observer

Figure 6.13 shows the actual and estimated outputs of the system. The latter are calculated by:

$$\hat{y} = C_j(\hat{x} - x_j) + D_j \Delta u_j + y_j \tag{6.65}$$

where j coincides with the current mode of the observer and controller (either *'a'* or *'b'*) at each instant in time. One can see that, excluding some mismatch as a result of switching dynamics in the observer, the outputs are accurately estimated.

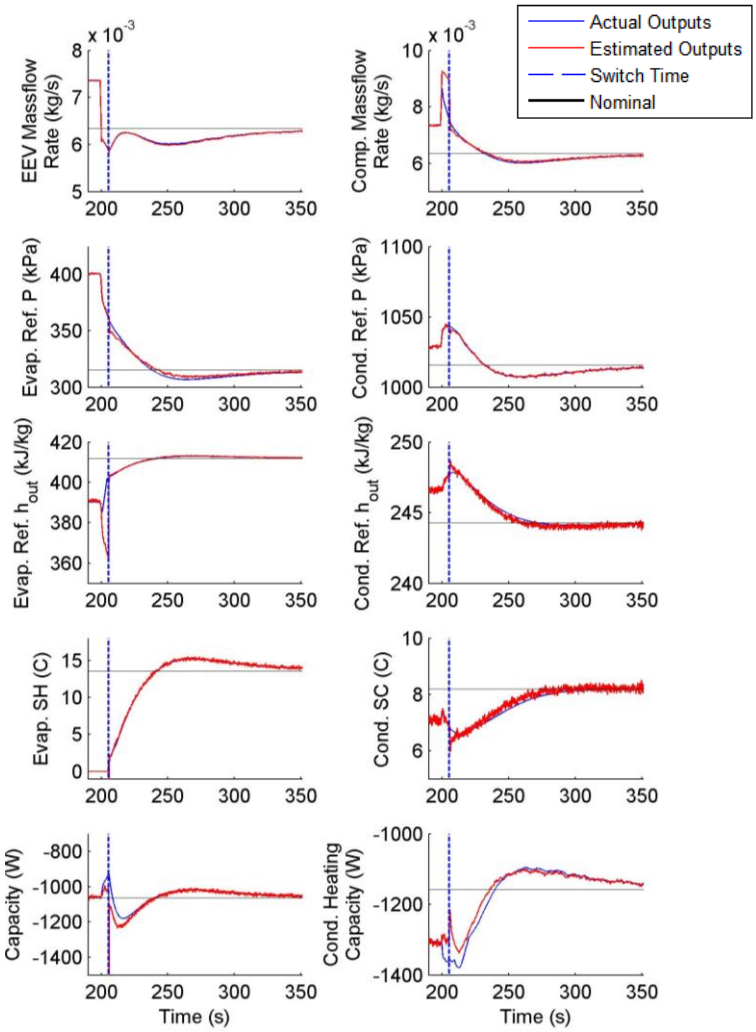

Figure 6.13: Formulation 2 True and Estimated Outputs Under Formulation 2

6.8.2 Switched LQR vs. Decentralized PI

In [26], a switched LQR controller and a decentralized PI approach are compared for reference tracking under loss and recovery of condenser subcool. The switched LQR approach is

shown to have significantly less overshoot and faster settling time than decentralized PI approach. We now demonstrate a similar comparison for superheat recovery, from the initial operating condition shown in Figure 6.6 to the desired operating condition shown in Figure 6.7. The decentralized PI controller used here is similar to that in [26] and [51]. As described in Eq. (6.66), one PI loop is used for each actuator input, with all signals as errors from the nominal values:

$$\begin{aligned}
\Delta o_{EEV} &= k_{p,1}\Delta T_{comp,r,out} + k_{i,1}\int \Delta T_{comp,r,out}\,dt \\
\Delta m_{e,a,in} &= k_{p,2}\Delta T_{e,a,out} + k_{i,2}\int \Delta T_{e,a,out}\,dt \\
\Delta v_{comp} &= k_{p,3}\Delta P_{diff} + k_{i,3}\int \Delta P_{diff}\,dt \\
\Delta m_{c,a,in} &= k_{p,4}\Delta P_{c} + k_{i,4}\int \Delta P_{c}\,dt
\end{aligned} \quad , \tag{6.66}$$

where the errors are defined as the reference value minus the measured value and $P_{diff} = P_c - P_e$. In [26], superheat is used as the feedback signal for the EEV orifice opening. In the present case we instead use the compressor discharge temperature as the EEV orifice opening feedback signal. This ensures that a nonzero error signal remains available to that PI loop under loss of superheat. The gains, in most cases identical to those in [26], are given by Table 6.1.

Table 6.1: Decentralized PI Gains

$k_{p,1} = 1$	$k_{p,2} = 0.005$	$k_{p,3} = 1$	$k_{p,4} = -0.001$
$k_{i,1} = 0.02$	$k_{i,2} = 0.009$	$k_{i,3} = 0.4$	$k_{i,4} = -0.0001$

The decentralized PI controller is compared to the switched LQR framework with feedback and feedforward as computed by Formulation 2 of Section 6.6.2.2, for which simulation results have already been shown in Section 6.8.1. At 200s, the controller is turned on and closed-loop regulation to a nominal operating condition with approximately 14°C of superheat begins. Figure 6.14 shows several outputs of a simulated VCS for the process of superheat recovery for both the decentralized PI and switched LQR approaches. Figure 6.15 shows the corresponding actuator inputs. Figure 6.16 shows the VCS states under the PI controller. The states and estimated states of the switched LQR approach were previously shown

in Figure 6.11. From these figures, one can see that the PI and LQR approaches both bring the system to recover superheat and reach the nominal values. Although the difference in performance between the two approaches is small in this simulation, the differences are shown to be much greater when the controllers are evaluated experimentally in Section 6.9. Since no filtering is done to the measurements used as feedback by the PI loops, the actuator inputs reflect the presence of measurement noise. As has previously been discussed, this does not occur in the LQR approach as a result of a combination of noise rejection in the Kalman filter and the output derivative weighting of LQR Formulation 2. A benefit of the LQR approach is inherent in its model and cost function-based architecture. This design allows the user to tune the controller directly to achieve a desired balance between the nominal outputs, inputs, and input derivatives, making the tuning process much more intuitive than selection of the eight gains of the decentralized PI approach.

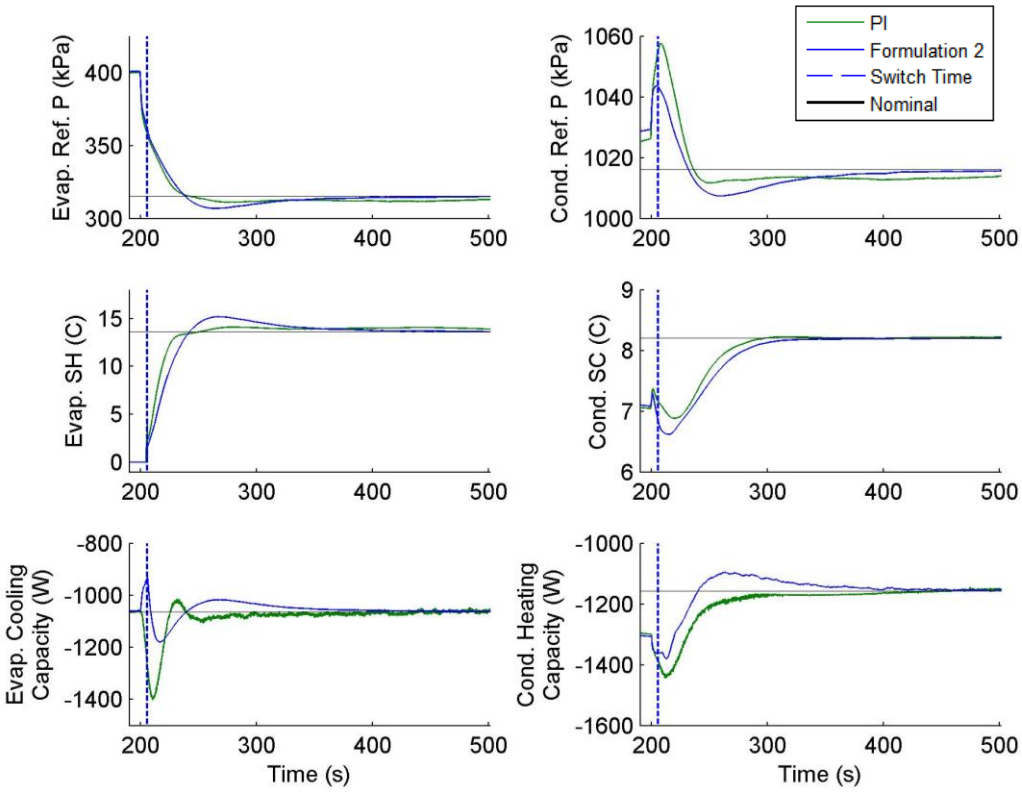

Figure 6.14: Simulation Outputs

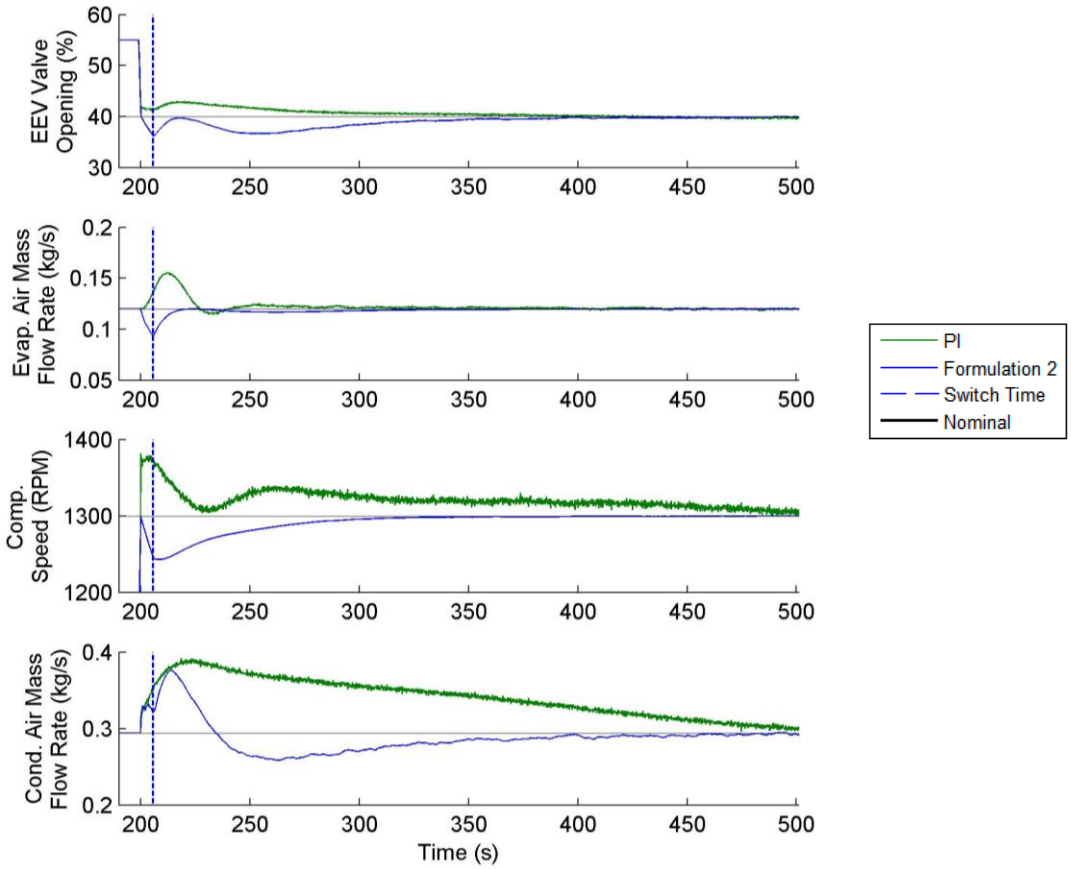

Figure 6.15: Actuator Inputs

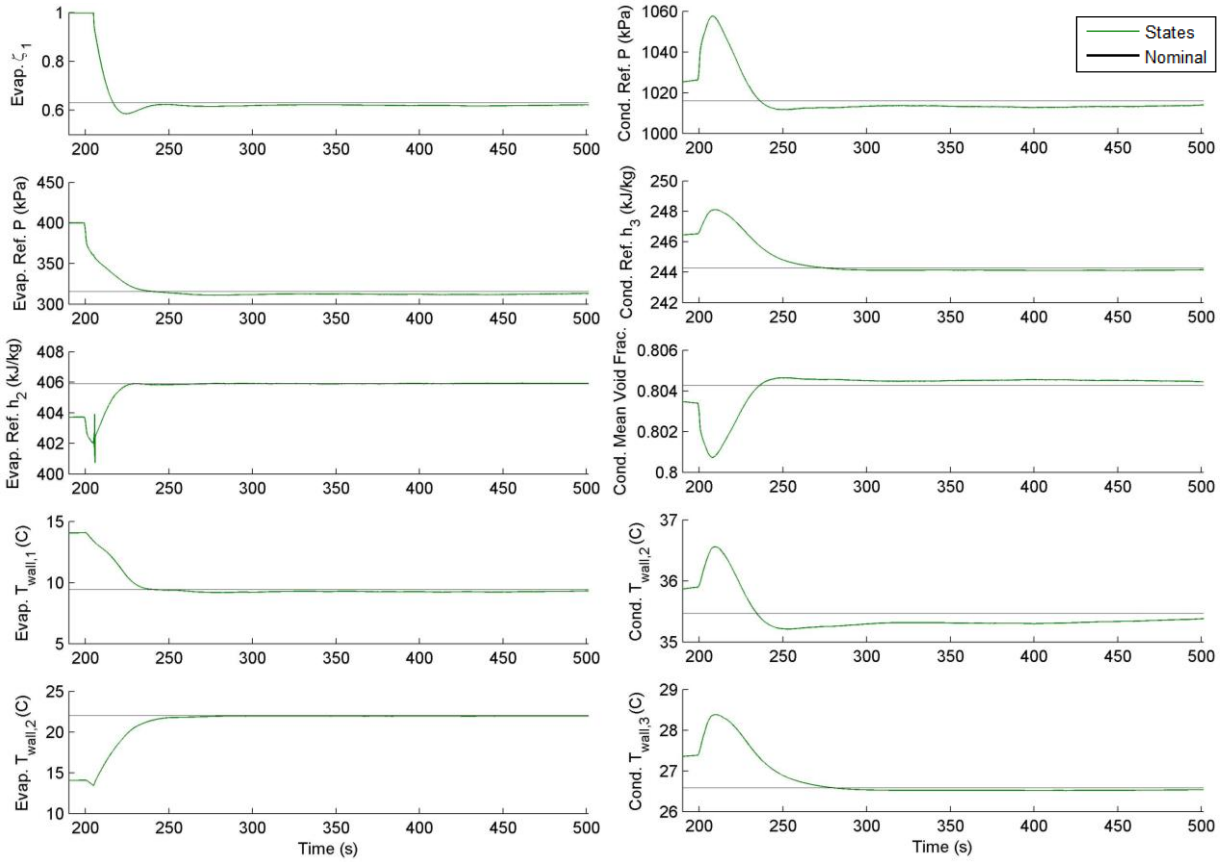

Figure 6.16: States Under PI Control

6.8.3 Switched vs. Non-Switched

In this simulation study, we demonstrate the benefits of using a switched framework instead of a single non-switched controller and observer. In particular, we show that attempting to use a linear model to control system operation in a different mode from that in which the model was linearized can result in poor performance. We consider the case of regulating from the operating condition with superheat of Figure 6.8 to the operating condition without superheat of Figure 6.7 and compare two control approaches. Both approaches use feedback and feedforward gains as computed by Formulation 2 of Section 6.6.2.2. In the first approach, as in the previous examples, the observer and controller switch between linear models of the '3-2' and '3-1' modes. However, the second approach uses only the '3-2' mode, with no switch occurring when superheat is lost.

At 200s, the controller is turned on and closed-loop regulation begins. Simulation outputs under each control approach are shown in Figure 6.17, and the corresponding actuator inputs are

shown in Figure 6.18. The actual and estimated states of the first and second approach are shown in Figure 6.19 and Figure 6.20, respectively. As these figures show, the two approaches are identical up to about 225s, at which time the switching manager detects that the plant has lost superheat. After this time, the switched approach changes to a controller and observer mode based on the '3-1' linear model, while the non-switched approach continues to use the '3-2' model. The significant model error between the linear '3-2' model and nonlinear '3-1' model manifests in large steady-state tracking and estimator errors of the non-switched control approach. The linear and nonlinear '3-1' modes match much more closely, especially near the nominal operating condition about which linearization was performed, and so for the switched approach, the tracking error approaches zero.

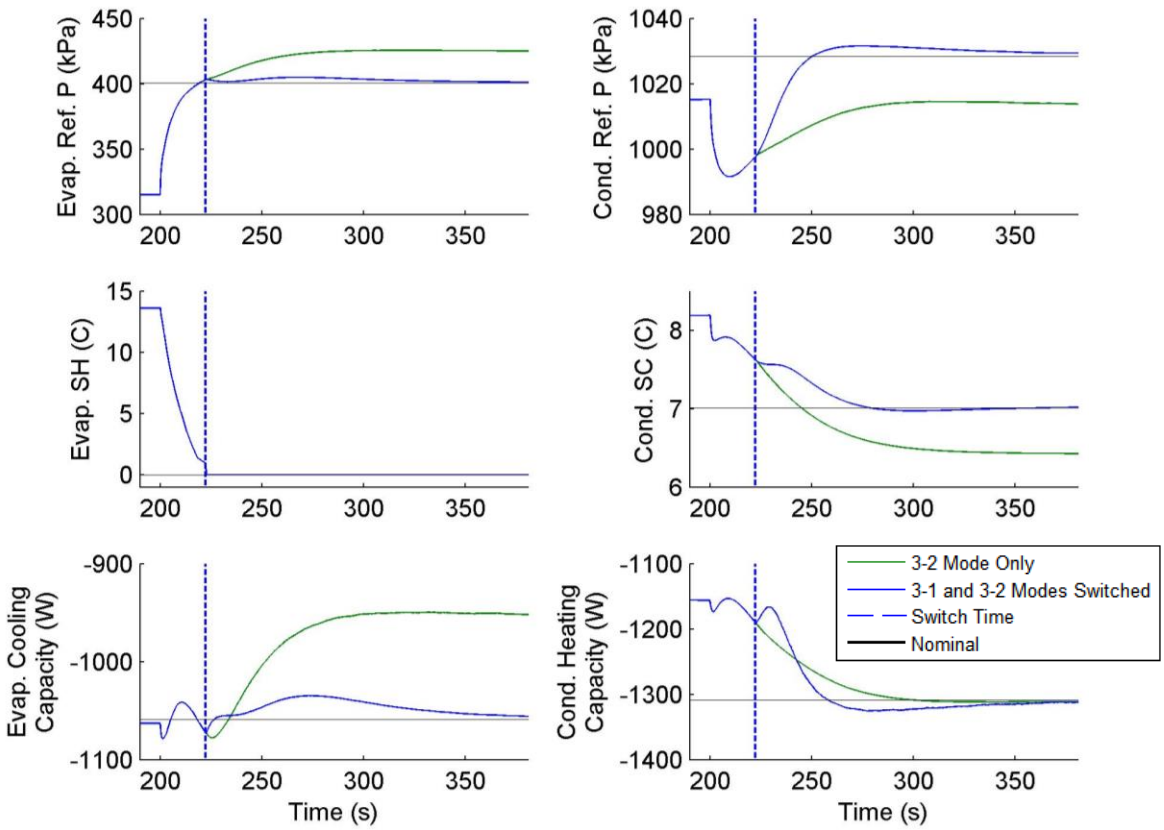

Figure 6.17: Simulation Outputs

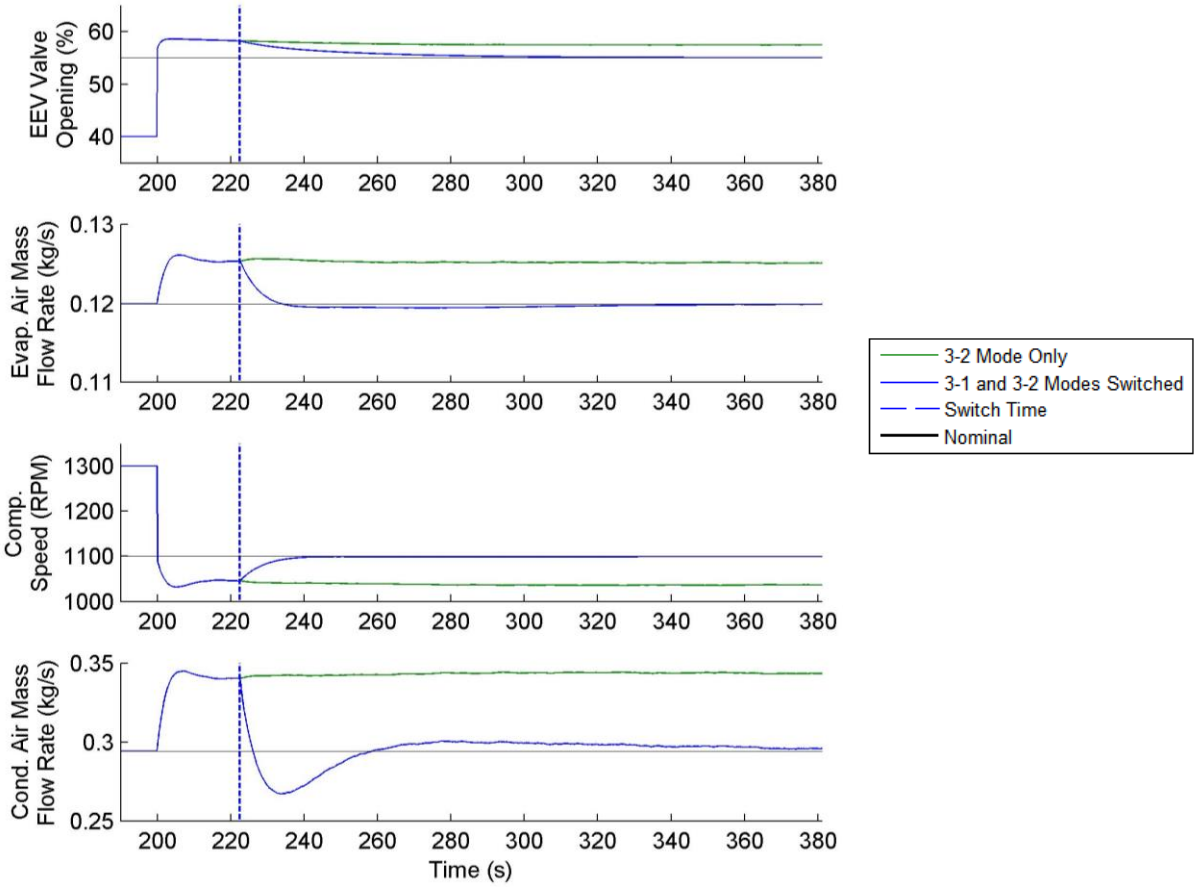

Figure 6.18: Actuator Inputs

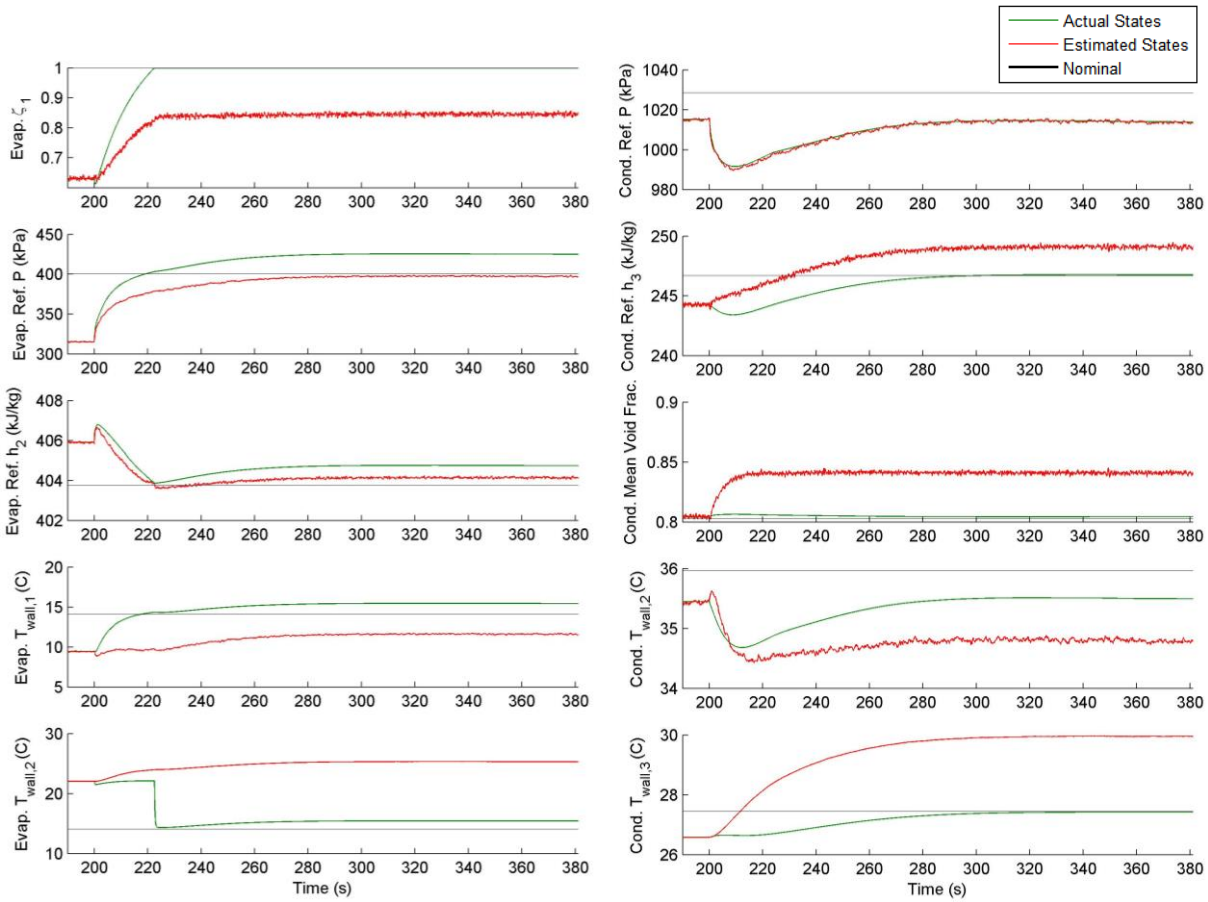

Figure 6.19: States Under Non-Switched Control

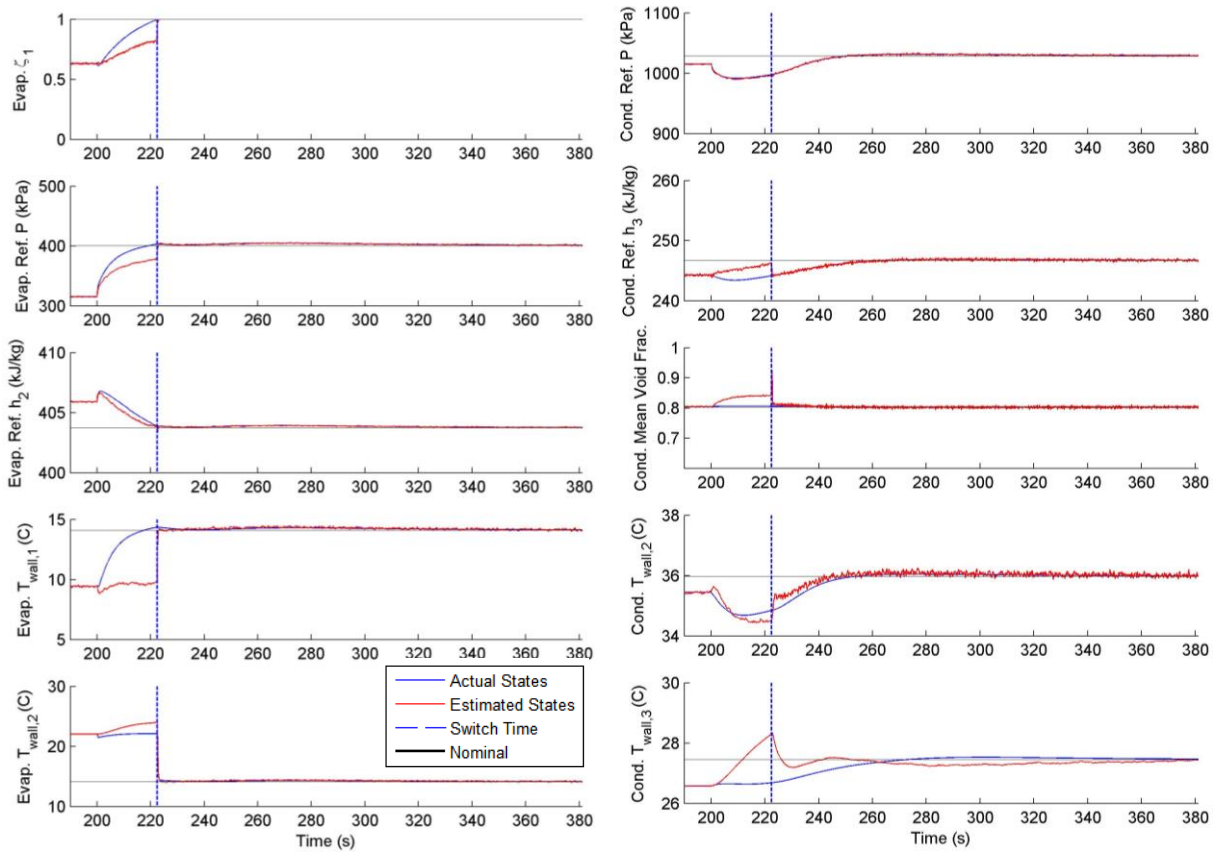

Figure 6.20: States Under Switched Control

6.9 Experimental Results

Although the simulation results of Section 6.8 are promising, there is no substitute in validation for real-world application. Because the linear models are expected to have far greater model error with respect to a real-world plant than with respect to nonlinear models—in particular with regard to steady-state operating conditions—experimental validation is ultimately a test of the robustness of the control design with respect to model error. With this understanding, the experimental test stand used in Chapter 4 and Chapter 5 for open-loop model validation is now used to demonstrate the applicability of the switched control approach to real-world systems. We note that the data shown in Chapter 4 and Chapter 5 was downsampled and low-pass filtered to reduce the presence of measurement noise and make the trends in the data more visible. However, since the handling of this noise in real time is a significant feature of the control approach, in this chapter the raw data is plotted exactly as measured, with a sample rate of 10Hz and no filtering. The observer and switching manager also operate at 10Hz.

6.9.1 LQR Formulation 2

In Section 6.8.1, LQR Formulation 2 was shown in simulation to be able to bring the system to recover superheat and regulate to a desired operating condition while providing smooth actuator commands. This capability is now demonstrated experimentally. Figure 6.21 shows the outputs of the experimental system, from which the recovery of superheat and regulation to the nominal conditions can be seen.

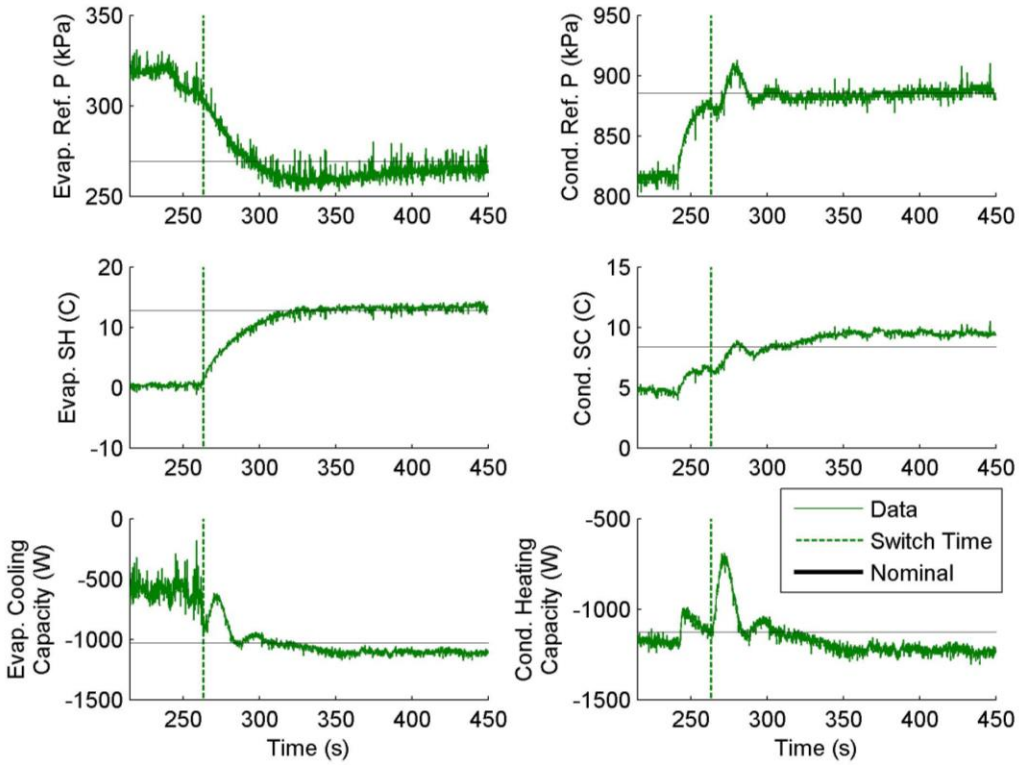

Figure 6.21: Experimental System Outputs

Although zero steady-state error cannot be achieved in every output of interest, the error that persists is generally small. While the steady-state errors in pressures, superheat, and subcool are clearly acceptable, it must be justified that the steady-state errors in cooling capacities are allowable. These errors in cooling capacity are approximately 10% from nominal in the evaporator and 20% from nominal in the condenser. Since typically no direct measurement of cooling capacity is available to VCSs, the most tractable way to ensure that the system still tracks global objectives with zero steady-state error would be through the use of integrator dynamics in the RTO. For example, if the input to the RTO is the desired temperature of an air-conditioned space, using an integral controller for the tracking of that temperature would cause

the nominal cooling capacity demand from the RTO to be adjusted until the temperature is tracked exactly, regardless of small errors in the tracking of the cooling capacity itself.

Figure 6.22 shows the actuator inputs. We note for this figure that the controller is turned on at approximately 240s. Figure 6.23 shows the Kalman filter estimates for those states that can be measured in the experimental system. Although much of the measurement noise is rejected from the estimates of pressure, it is not rejected from the estimate of the condenser's third zone enthalpy. However, the actuator inputs remain smooth despite this noise in the state estimates as a result of the input-smoothing built into LQR Formulation 2. Figure 6.24 shows the system output measurements used by the observer to generate these state estimates.

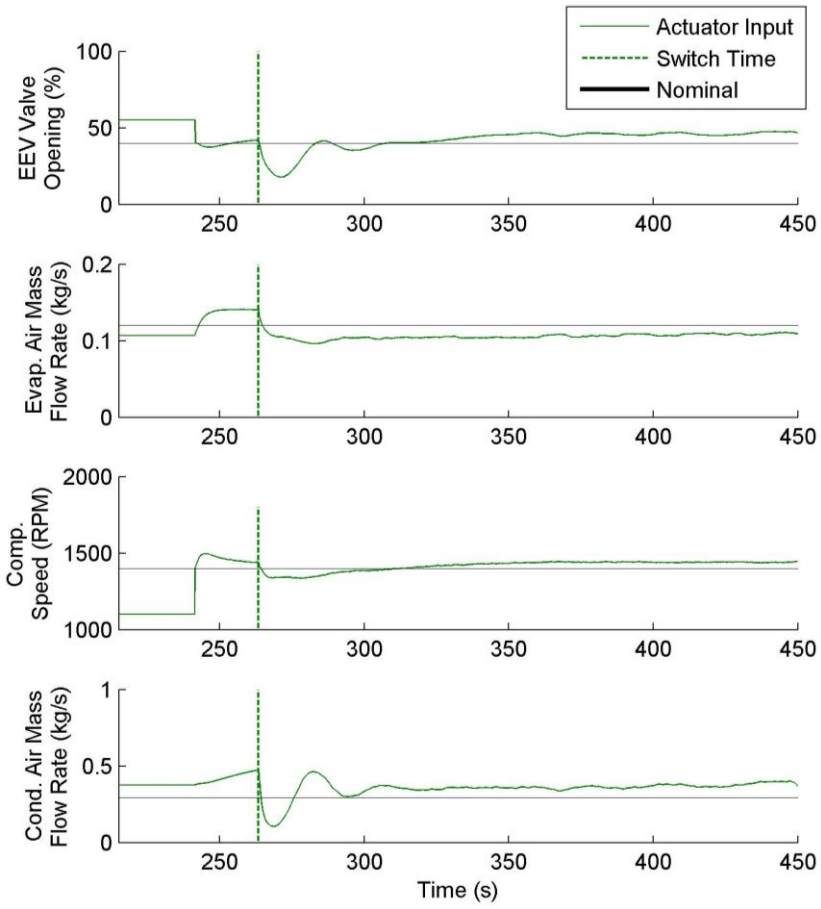

Figure 6.22: Experimental System Actuator Inputs

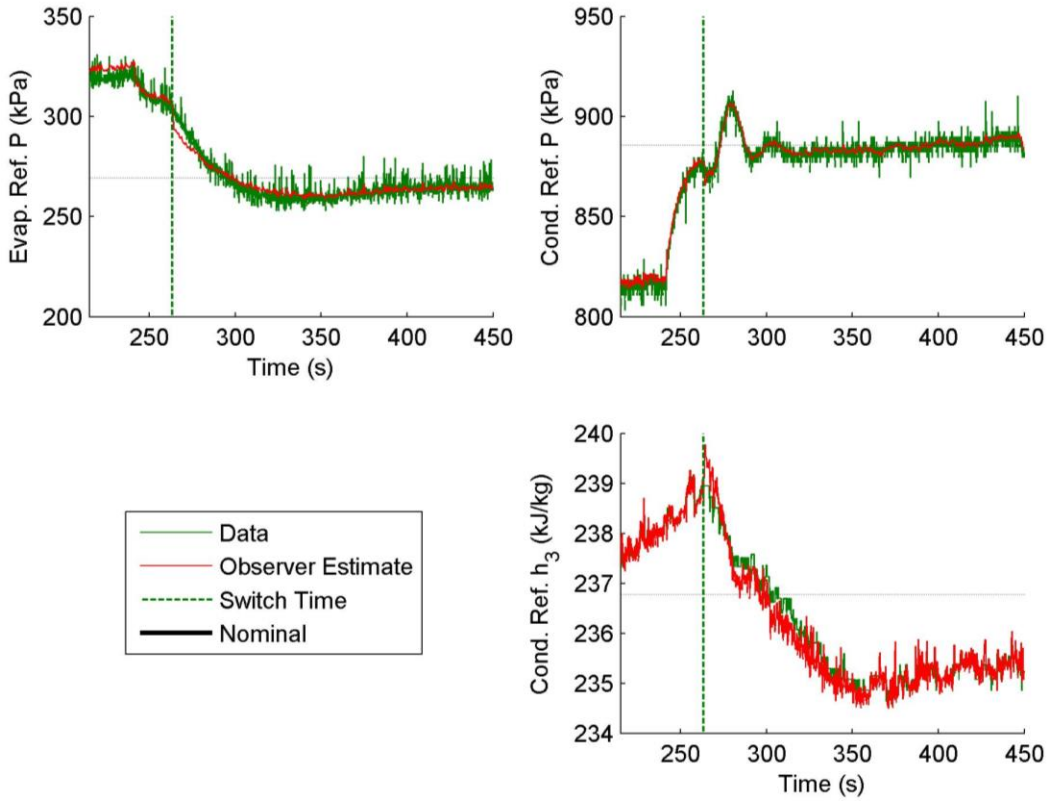

Figure 6.23: Experimental System Estimated States

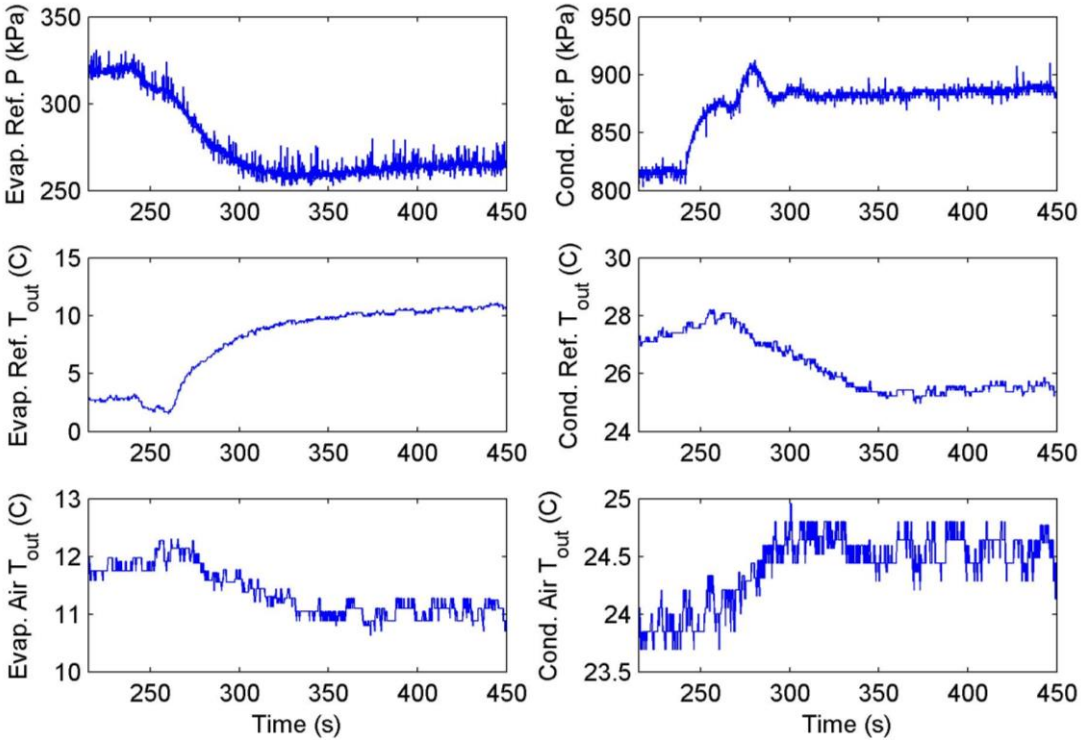

Figure 6.24: Experimental System Measurements Received By Observer

Figure 6.25 shows the estimated and measured outputs of the system. Note that measurements for the evaporator outlet enthalpy and compressor mass flow rate are not provided. This is because the evaporator enthalpy is not measurable at zero superheat, and no sensor is present in the experimental system for the measurement of compressor mass flow rate. The estimated outputs are calculated as shown in Eq. (6.65). While there is some steady-state offset in the estimation of evaporator cooling capacity and dynamic mismatch in both cooling capacities, the other outputs are estimated very well.

Figure 6.26 shows the measured heat exchanger air inlet temperatures, which are seen to deviate from the nominal value about which the linear models were linearized by about 1°C at most.

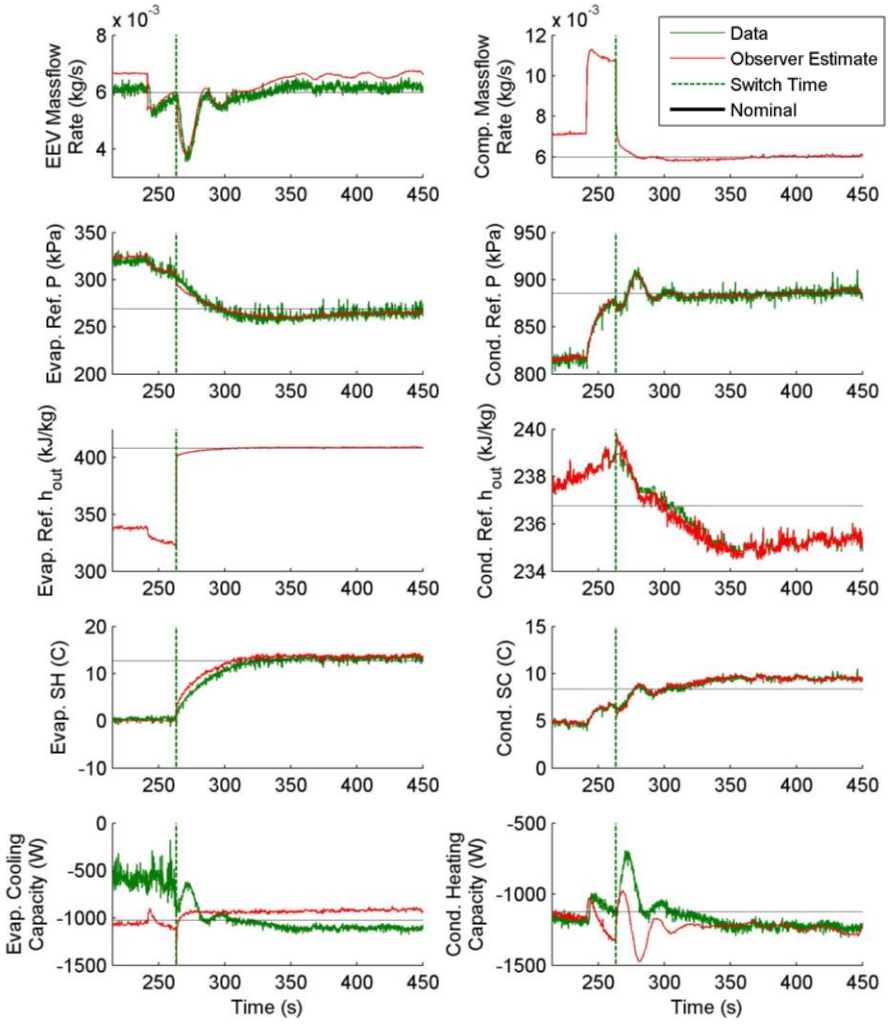

Figure 6.25: Measured and Estimated Outputs

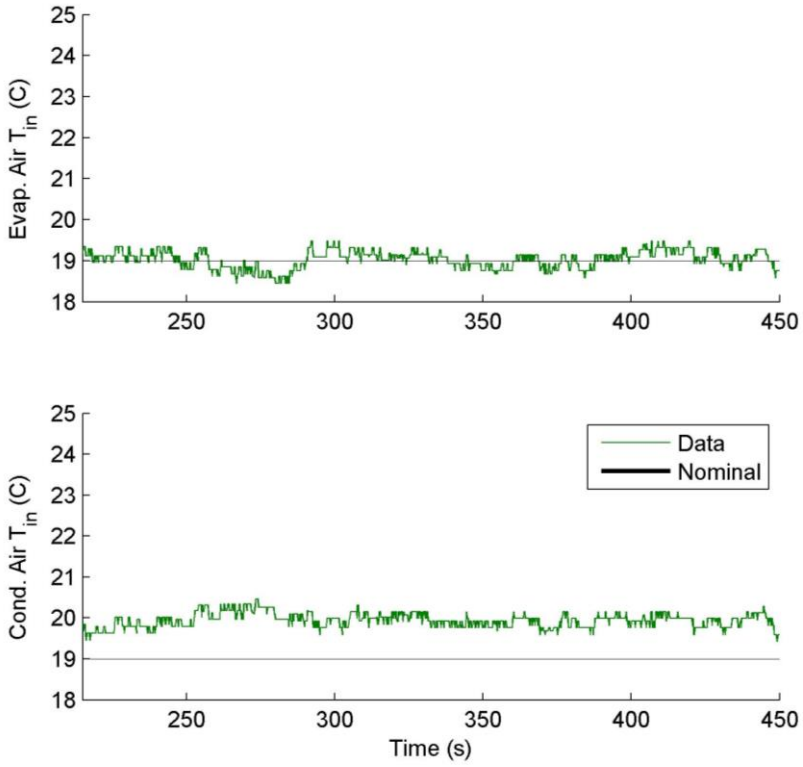

Figure 6.26: Experimental System Air Inlet Disturbances

6.9.2 Decentralized PI

In Section 6.8.2, a decentralized PI control approach was shown in simulation as exhibiting comparable performance to LQR Formulation 2 for a superheat recovery and regulation process. We now show experimentally that this result does not carry over to the experimental system. For application to the experimental system, two modifications were made to the decentralized PI controller shown in Section 6.8.2. First, a low-pass filter was added to each feedback signal used by the controller. This removed the measurement noise, ensuring that the resulting actuator outputs would be smooth. Second, the gains of the controller were reduced based on the observation that the original gains rapidly saturated the actuators to their maximum or minimum bounds when the controller was applied to the experimental system. The gains on the EEV orifice opening were reduced to 10% of their original value. The evaporator air mass flow and compressor speed gains were reduced by half, and the condenser air mass flow gains were reduced to 75% of their original value.

Figure 6.27 shows the resulting outputs of the experimental system, from which one can see that the system fails to reach the nominal conditions, never regaining a significant amount of superheat and eventually even losing subcooling. Figure 6.28 shows the actuator inputs, the first three of which are eventually saturated to either maximum or minimum bounds. From Figure 6.28, one can also see that the controller is turned on at approximately 3425s.

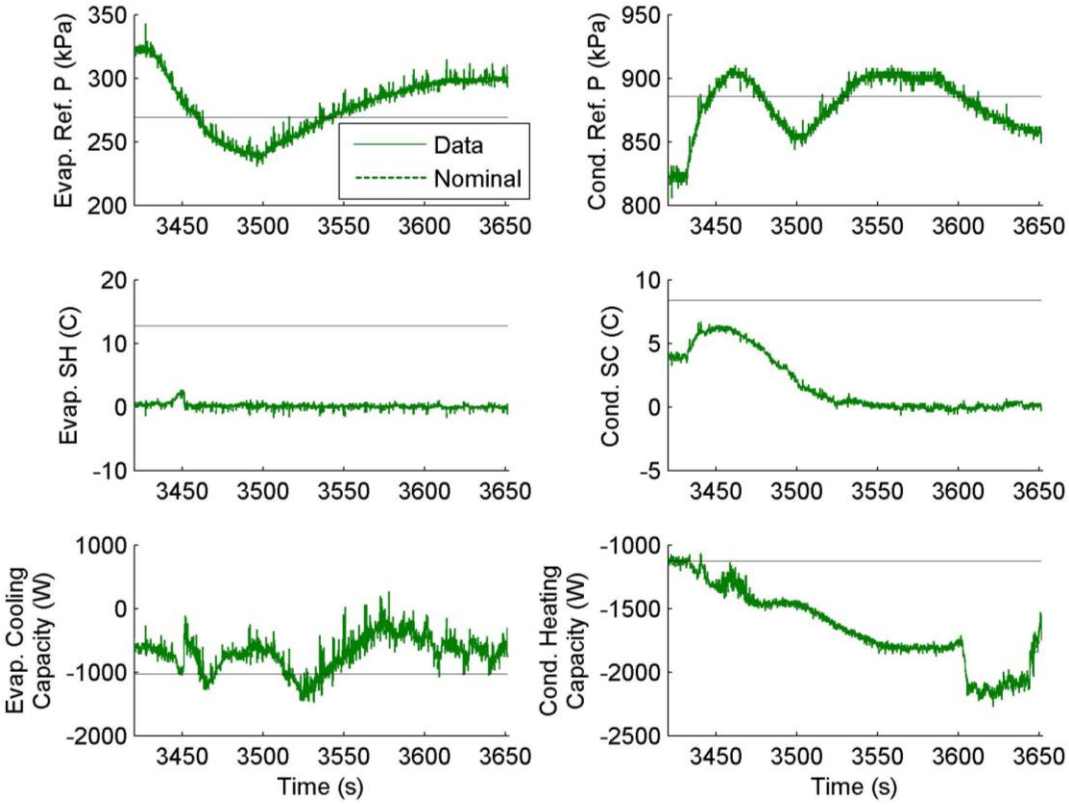

Figure 6.27: Experimental System Outputs

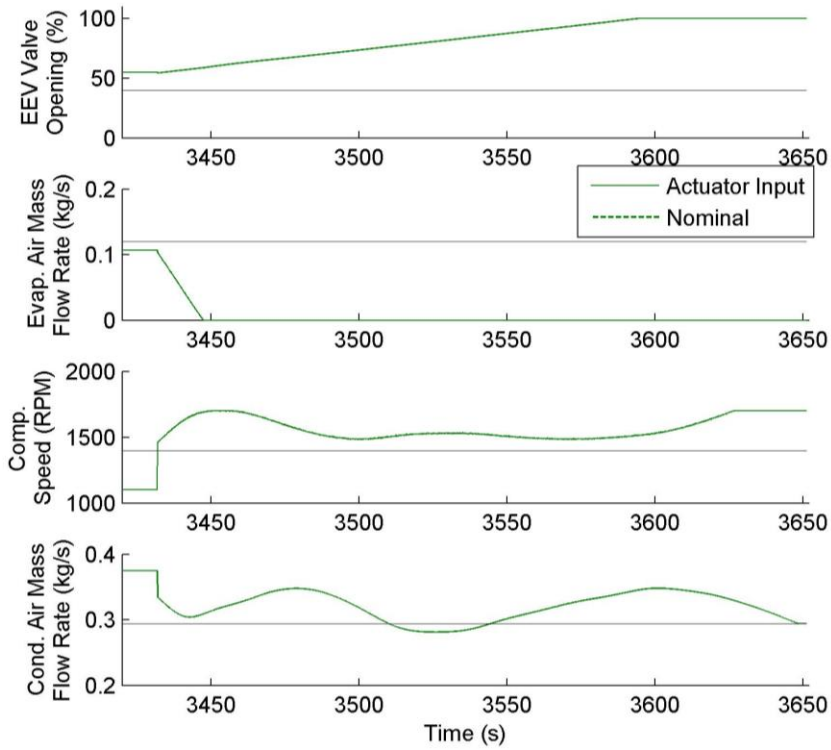

Figure 6.28: Experimental System Actuator Inputs

This experimental behavior of the decentralized PI approach is very different from that observed in simulation in Section 6.8.2. The cause of this difference is believed to be a phenomenon called Minimum Stable Superheat (MSS), which is known to occur in real-world evaporators but is not captured by the models in this work. MSS occurs when evaporators exhibit erratic behavior at low superheat due to the phase transition undergone by the refrigerant at the outlet, and is characterized by a rapid loss of measured superheat [52], dropping from 5-10°C to 0°C in a few seconds. This is seen to occur in the superheat subplot of Figure 6.27 at approximately 3450s, at which time the few degrees of superheat that the controller had managed to achieve are rapidly lost. In the switched LQR approach, a high weighting placed in the cost function against errors from nominal in superheat brings the controller to drive the system through this instability into a rapid superheat recovery. However, the same cannot be said of the decentralized PI approach.

6.10 Discussion of Stability

While the stability of the switched LQR approach has been demonstrated both in simulation and in experimental testing, it is beneficial to discuss theoretical guarantees of stability that can be made. Writing the control from Formulation 2 as:

$$\Delta u_b = \int_{t_o}^{t} \left[-k_{j,x} \Delta \hat{x}_b(t) - k_{j,d} d_j \right] dt \,, \tag{6.67}$$

we can approximate the closed-loop system by considering the control applied to the linear error system of (6.14) as:

$$\begin{aligned} \dot{x}_j &= A_j \Delta x_b + B_j \int_{t_o}^{t} \left[-k_{j,x} \Delta \hat{x}_b(t) - k_{j,d} d_j \right] dt + V_j d_j \\ &= \left(A_j \Delta x_b - B_j k_{j,x} \int_{t_o}^{t} \Delta \hat{x}_b(t) dt \right) + \left(V_j - B_j k_{j,d} (t - t_o) \right) d_j \end{aligned} \,. \tag{6.68}$$

Because it is generally not possible to define $k_{j,d}$ such that the term multiplied by d_j of Eq. (6.68) evaluates to exactly 0, we see that the set of closed-loop switched systems includes multiple equilibrium points among the modes. This would also hold true if the control from Formulation 1 was used. The existence of multiple equilibria must be carefully considered in stability analysis, since much of the literature on stability of switched systems assumes that all modes share a common equilibrium.

The work in [26] and [42] presents a similar switched linear control framework. In order to rigorously prove the stability of the framework, the LQR problem is first represented in a linear mixed inequality (LMI) form. In [26], a set of multiple Lyapunov function matrices is said to result from solution of this LMI-based LQR problem, proving closed-loop stability of the control framework. In [42], a common Lyapunov function is said to result from this solution. However, in neither case is the presence of multiple equilibrium points among modes discussed. We designate further review of this approach as a topic for future exploration, and instead pursue a different reasoning, albeit with less rigorous claims.

We first note that most literature on the stability of switched systems with multiple equilibria imposes either state-based or time-based switching constraints on the system. A state-based approach is proposed in [53] and [54], where the state-space is divided into convex polyhedral cells defining the spaces where each mode of the switched system is active. A

Lyapunov function is then defined piecewise for each cell. However, such an approach cannot be used for the linear models in this work because it would require that the switching be defined purely by the states. We could not, for example, use the current model formulation to detect a switch from the '3-1' mode to the '3-2' mode based on states alone, since the evaporator's first zone length and second zone enthalpy for the '3-1' mode are represented using non-physical pseudo-state equations and therefore cannot be used to determine whether superheat has been recovered in the evaporator. In order to take a state-based approach to detecting a switch, the signals used to detect switching in the nonlinear models (see Figure 2.7) would have to be included in the state-space of the linear models.

A time-based approach to ensuring stability is proposed in [55], where it is shown that for a collection of individually exponentially stable systems with different equilibrium points, a conservative lower bound on the switching dwell time can be computed which ensures that the switched system globally converges to a superset containing the individual equilibria. An approach along these lines is much more tractable for the models used in this work. With appropriate assumptions on the frequency and magnitude of disturbances and by limiting the interval at which the RTO is permitted to intentionally direct the controller to change the mode of operation of the plant, an arbitrary minimum dwell time can be achieved. While this at least ensures that the system states will remain bounded, it does not guarantee convergence to the desired nominal values. Returning to the nomenclature of Section 6.4, if the closed-loop equilibrium associated with mode *'a'* is achieved prior to the switch into mode *'b'*, the closed-loop equilibrium of *'b'* will obviously not be achieved. This is similar to the simulation result shown in Section 6.8.3 for a non-switched LQR formulation, however in that instance the controller and observer were prevented from switching modes even though a mode switch did occur in the plant. We leave it to future work to explicitly calculate the minimum dwell time described in [55], and to investigate analytical methods that reveal necessary conditions for convergence to the desired equilibrium. At present, we point to the simulation and experimental results as showing promise that such conditions exist.

Chapter 7
Conclusion

7.1 Summary of Research Contributions

This thesis traces the complete process of model-based control design for VCSs, from nonlinear model development to linearization and control formulation. Addressing gaps in the previous literature, the equations behind each model and control approach are clearly stated and emphasis is placed on conducting experimental validation at every stage.

In Chapter 2, FV and SMB heat exchanger models are derived, illustrating the key differences in method of discretization between these approaches. Practical considerations for the numerical implementation of these approaches in simulation are also provided. A detailed linearization of the SMB approach is then presented in Chapter 3, culminating in the creation of a family of four-component linear models for different modes of operation of a VCS.

Chapter 4 compares both the nonlinear and linear modeling approaches with experimental data to reveal the tradeoffs of each. The intended use in target application, and the need for flexibility of implementation may be the driving factors for selection of the FV model. If simulation speed is paramount, a MB model can perform as accurately as a FV model while executing significantly faster. While both the nonlinear approaches are primarily used to evaluate system dynamics in simulation as a stand-in for a real-world plant, the linear models serve very different purposes. First, these allow well-known linear model analysis tools to be used, such as the examination of eigenvalues. Second, they can be directly embedded into model-based control formulations.

The validation data of Chapter 4 was collected at an ambient air relative humidity of approximately 50%. The humidity is suggested as a cause of the constant offset from experimental data observed in the air outlet temperature predictions of the models. Chapter 5 addresses this claim by incorporating the modeling of air-side humidity into the SMB

formulation. When provided with an input of air inlet humidity, the augmented SMB evaporator model is shown to more accurately predict both air-side and refrigerant-side outputs in addition to providing accurate predictions of liquid condensate formation and air outlet humidity.

Returning to the linear models of Chapter 3, Chapter 6 demonstrates how linear models for multiple modes of operation can be embedded into model-based control. Emphasis is placed on developing a framework suited to real-world implementation. A switched observer and LQR approach are shown in both simulation and experimental application to be able to effectively drive the system between modes in order to regulate about a desired nominal operating condition. In particular, the experiments demonstrate that the switched LQR approach is more robust at low evaporator superheat than a decentralized PID approach. In addition to providing more explicit model and controller formulations and demonstrating the success of the control design through experimental testing, Chapter 6 improves upon the previous literature by providing new insight on stability analysis of the switched LQR approach.

7.2 Future Work

Future work should include development in modeling, validation, and control of vapor compression systems.

7.2.1 Modeling

In Section 3.2.3, it was shown that the 2-zone linear condenser model in Section 3.2.2 was far from matching the nonlinear model. Developing a working linearization for this mode of the condenser (such as that discussed but not derived in [26]) will in turn allow the controller of Chapter 6 to be extended to operating conditions where the refrigerant exiting the condenser is two-phase.

Just as the SMB heat exchanger models without humidity were linearized in Chapter 3, the models with humidity of Chapter 5 can also be linearized. This modeling will facilitate the investigation of control techniques that achieve a performance objective of air outlet humidity in addition to the objectives explored in this thesis. Including a humidity objective is especially important given the impact that humidity is known to have on human health and comfort in conditioned spaces [28]. Furthermore, the heat exchanger models with humidity of Chapter 5 can

be extended from the current modeling of only liquid condensate formation to also capture frost formation and melting on the external surfaces of the heat exchanger.

Lastly, the methods used to generate individual linear component models and combine them into a complete four-component linear VCS model can be extended to include additional components and arbitrary system architectures, such as receivers, accumulators, or multi-evaporator configurations. This would provide a very effective and time-efficient method of creating accurate linear models for a variety of applications of VCSs, which can be used to better understand the underlying dynamics of such systems and to extend the applicability of the control framework of Chapter 6.

7.2.2 Validation

Open-loop experimental data was used in Chapter 4 and Chapter 5 to aid in the comparison of several VCS modeling approaches. However, this validation data only includes conditions in which both the evaporator and condenser are operating in 'Mode 1' as defined in Figure 2.6. While the broad conclusions regarding the tradeoffs associated with different modeling approaches would be expected to hold in other modes of operation, this can be verified with experimental data. We note that, unlike the SMB and linear models, the FV formulation does not require the derivation of a distinct formulation for each combination of phases in the heat exchangers, since each CV is able to switch between superheated, two-phase, and subcooled phases as model inputs and states change. In addition, the humidity modeling of Chapter 5 should be validated with condenser data to verify that the conclusions of validation with evaporator data hold true for the condenser as well.

7.2.3 Switched Control

In addition to the advancements in VCS control that follow from the future work in modeling discussed in Section 7.2.1, there exist opportunities to further explore and compare switched linear model-based control approaches. As discussed in Section 6.10, this includes a more detailed analysis of the conditions required under the switched LQR framework to ensure that the system is not only stable, but also converges to the desired equilibrium.

As an additional point of comparison, a Model Predictive Control (MPC) approach could be developed and compared with the switched LQR approach in this thesis. Because MPC uses a

dynamic model of the system to predict the system behavior over a time horizon, embedding linear models for multiple modes into the MPC design could allow the controller to better chart a system trajectory to the desired operating conditions when a mode switch is required to reach those conditions. This would require that a method of predicting the occurrence of a mode switch for the linear models in closed loop be developed in order to propagate them over the time horizon in solving for the optimal control.

References

[1] "Residential Energy Consumption Survey," U.S. Energy Information Administration, 2009.

[2] "Energy Saver 101 Infographic: Home Cooling," U.S. Department of Energy, 2014.

[3] "Buildings Energy Data Book," U.S. Department of Energy, 2012.

[4] International Institute of Refrigeration, "Refrigerated Transport: What's New?" *International Journal of Refrigeration*, vol. 25, pp. 501–503, 2002.

[5] H. Pangborn and A.G. Alleyne "A Comparison Between Finite Volume and Switched Moving Boundary Approaches for Dynamic Vapor Compression System Modeling," *International Journal of Refrigeration*, vol. 53, pp. 101-114, 2015.

[6] B.P. Rasmussen, "Dynamic Modeling for Vapor Compression Systems — Part I: Literature Review," *HVAC&R Research*, vol. 18:5, pp. 934-955, 2012.

[7] J.W. MacArthur, "Transient Heat Pump Behavior: A Theoretical Investigation," *International Journal of Refrigeration*, vol. 7:2, pp.123-132, 1984.

[8] W.D. Gruhle, and R. Isermann, "Modeling and Control of a Refrigerant Evaporator," *ASME Journal of Dynamic Systems, Measurement, and Control*, vol. 107:4, pp. 235–240, 1985.

[9] J.W. MacArthur, G.D. Meixel, and L.S. Shen, "Application of Numerical Methods for Predicting Energy Transport in Earth Contact Systems," *Journal of Applied Energy*, vol. 13, pp. 121-156, 1983.

[10] S. Bendapudi, J.E. Braun, and E.A. Groll, "Dynamic Model of a Centrifugal Chiller System—Model Development, Numerical Study, and Validation," *ASHRAE Transactions*, vol. 111:1, pp. 132-148, 2005.

[11] G.L. Wedekind, B.L. Bhatt, and B.T. Beck, "A System Mean Void Fraction Model for Predicting Various Transient Phenomena Associated with Two-Phase Evaporating and Condensing Flows," *Int. J. Multiphase Flow*, vol. 4:1, pp. 97-114, 1978.

[12] S.M. Zivi, "Estimation of Steady-State Steam Void-Fraction by Means of the Principle of Minimum Entropy Production," *Journal of Heat Transfer*, vol. 85:2, pp. 247–251, 1964.

[13] T.L. McKinley and A.G. Alleyne, "An Advanced Nonlinear Switched Heat Exchanger Model for Vapor Compression Cycles Using the Moving-Boundary Method," *International Journal of Refrigeration*, vol. 31:7, pp. 1253-1264, 2008.

[14] B. Li and A.G. Alleyne, "A Dynamic Model of a Vapor Compression Cycle with Shut-Down and Start-Up Operations," *International Journal of Refrigeration*, vol. 31:7, pp. 1253-1264, 2008.

[15] S. Bendapudi, J.E. Braun, and E.A. Groll, "A Comparison of Moving-Boundary and Finite-Volume Formulations for Transients in Centrifugal Chillers," *International Journal of Refrigeration*, vol. 31:8, pp. 1437-1452, 2008.

[16] B. P. Rasmussen and B. Shenoy, "Dynamic Modeling for Vapor Compression Systems — Part II: Simulation Tutorial," *HVAC&R Research*, vol. 18:5, pp. 956-973.

[17] B.D. Eldredge and A.G. Alleyne, "Improving the Accuracy and Scope of Control-Oriented Vapor Compression Cycle System Models," *Air Conditioning and Refrigeration Center*, TR-246, 2006.

[18] W. Zhang, C. Zhang, and G. Ding, "On Three Forms of Momentum Equation in Transient Modeling of Residential Refrigeration Systems," *International Journal of Refrigeration*, vol. 33:3, pp. 538-552, 2010.

[19] B.P. Rasmussen, "Dynamic Modeling and Advanced Control of Air Conditioning and Refrigeration Systems," Ph.D. Dissertation, Dept. Mech. Eng., Univ. Illinois Urbana–Champaign, Urbana, IL, 2005.

[20] J.M. Fasl, "Modeling and Control of Hybrid Vapor Compression Cycles," M.S. Thesis, Dept. Mech. Eng., Univ. Illinois Urbana–Champaign, Urbana, IL, 2013.

[21] F.P. Incropera and D.P. DeWitt, Fundamentals of Heat and Mass Transfer 6th ed., New York: John Wiley and Sons Inc., 2007.

[22] E.W. Lemmon, M.L. Huber, and M.O. McLinden, NIST Reference Fluid Thermodynamic and Transport Properties—REFPROP, *NIST*, 2013.

[23] V. Gnielinski, "New Equations for Heat and Mass Transfer in the Turbulent Flow in Pipes and Channels," NASA STI/Recon Technical Report A, vol. 752, pp. 22028, 1975.

[24] M. Dobson and J. Chato, "Condensation in Smooth Horizontal Tubes," *Journal of Heat Transfer*, vol. 120, pp. 193, 1998.

[25] J.P. Wattelet et al, "Heat Transfer Flow Regimes of Refrigerants in a Horizontal-Tube Evaporator, *Air Conditioning and Refrigeration Center*, TR-55, 1994.

[26] B. Li, "Dynamic Modeling, Simulation, and Control of Transportation HVAC Systems," Ph.D. Dissertation, Dept. Mech. Eng., Univ. Illinois Urbana–Champaign, Urbana, IL, 2013.

[27] Q. Qi and S. Deng, "Multivariable Control of Indoor Air Temperature and Humidity in a Direct Expansion (DX) Air Conditioning (A/C) System," *Building and Environment*, vol. 44:8, pp. 1659-1667, 2009.

[28] P.O. Fanger, "Human Requirements in Future Air-Conditioned Environments," *International Journal of Refrigeration*, vol. 24, pp. 148-153, 2001.

[29] E. Bracken, "Combating Humidity—The Hidden Enemy in Manufacturing". *Sensor Review*, vol. 17:4, pp. 291-298, 1997.

[30] D. Ndiaye and M. Bernier, "Transient Modeling of Refrigerant-to-Air Fin-and-Tube Heat Exchangers," *HVAC&R Research*, vol. 16:3, pp. 335-381, 2010.

[31] M. Kumar, I.N. Kar, and A. Ray, "State Space Based Modeling and Performance Evaluation of an Air-Conditioning System," *HVAC&R Research*, vol. 15:5, pp. 797-816, 2008.

[32] Q. Qi and S. Deng, "Multivariable Control-Oriented Modeling of a Direct Expansion (DX) Air Conditioning (A/C) System," *International Journal of Refrigeration*, vol. 31, pp. 841-849, 2008.

[33] F. Scotton et al., "Physics-Based Modeling and Identification for HVAC Systems," *2013 European Controls Conference*, pp. 1404-1409, 2013.

[34] K.S. Yigit and H.M. Ertunc, "Prediction of the Air Temperature and Humidity at the Outlet of a Cooling Coil Using Neural Networks," *International Communications in Heat and Mass Transfer*, vol. 33:7, pp. 898–907, 2006.

[35] S. Soyguder and H. Alli, "An Expert System for the Humidity and Temperature Control in HVAC Systems Using ANFIS and Optimization with Fuzzy Modeling Approach," *Energy and Buildings*, vol. 41:8, pp. 814-822, 2009.

[36] I. Bell et al., "Pure and Pseudo-pure Fluid Thermophysical Property Evaluation and the Open-Source Thermophysical Property Library CoolProp," *Industrial and Engineering Chemistry Research*, vol. 53:6, pp. 2498-2508, 2014.

[37] W.M. Kays and A.L. London, Compact Heat Exchangers, McGraw-Hill, NY, 1964.

[38] S.G., Kandlikar, Thermal Design Theory for Compact Evaporators, Hemisphere, NY, 1990

[39] F.C. McQuiston, "Fin Efficiency with Combined Heat and Mass Transfer," *ASHRAE Transactions*, vol. 81:1, pp. 350-355, 1975.

[40] R.R. Rogers, and M.K. Yau, A Short Course in Cloud Physics, 3rd ed., Pergamon, 1989.

[41] M. Keir, "Dynamic Modeling and Fault Detection in Vapor Compression Systems," M.S. Thesis, Dept. Mech. Eng., Univ. Illinois Urbana–Champaign, Urbana, IL, 2005.

[42] B. Li, N. Jain and A.G. Alleyne, "LMI Control Design for Nonlinear Vapor Compression Cycle Systems," *Dynamic Systems and Controls Conference*, 2012.

[43] D. Liberzon, Calculus of Variations and Optimal Control Theory, Princeton University Press, 2012

[44] T. Gongyou, Z. Yandong, and Z. Baolin, "Feedforward and Feedback Optimal Control for Linear Time-Varying Systems with Persistent Disturbances," *Journal of Systems Engineering and Electronics*, vol. 16:2, pp. 350-354, 2006.

[45] X. He, et al, "Multivariable Control of Vapor Compression Systems," *HVAC&R Research*, vol. 4, pp. 205-230, 1998.

[46] L.C. Schurt, C.J.L. Hermes, and A.T. Neto, "A Model-Driven Multivariable Controller for Vapor Compression Refrigeration Systems," *International Journal of Refrigeration*, vol. 32, pp. 1672-1682, 2009.

[47] B.P. Rasmussen and A.G. Alleyne, "Gain Scheduled Control of an Air Conditioning System Using the Youla Parameterization," *IEEE Transactions on Control Systems Technology*, vol. 18:5, 2010.

[48] V. Oliveira, A. Trofino, and C.J.L. Hermes, "A Switching Control Strategy for Vapor Compression Refrigeration Systems," *Applied Thermal Engineering*, vol. 31, pp. 3914-3921, 2011.

[49] L.C. Schurt, C.J.L. Hermes and A.T. Neto, "Assessment of the Controlling Envelope of Model-Based Multivariable Controller for Vapor Compression Refrigeration Systems," *Applied Thermal Engineering*, vol. 30:13, pp. 1538-1546, 2010.

[50] A. Tanwani, H. Shim, and D. Liberzon, "Observability for Switched Linear Systems: Characterization and Observer Design," *IEEE Transactions on Automatic Control*, vol. 58:4, pp. 891-904, 2013.

[51] N. Jain, et al, "Decentralized Feedback Structures of a Vapor Compression Cycle System," *IEEE Transactions on Control Systems Technology*, vol. 18:1, pp. 185-193, 2010.

[52] W. Chen et al, "Experimental Investigation of a Minimum Stable Superheat Control System of an Evaporator," *International Journal of Refrigeration*, vol. 25, pp. 1137-1142, 2002.

[53] M. Johansson and A. Rantzer, "Computation of Piecewise Quadratic Lyapunov Functions for Hybrid Systems," *IEEE Transactions on Automatic Control*, vol. 43:4, pp. 555-559, 1998.

[54] M. Johansson, "Piecewise Linear Control Systems," *Lecture Notes in Control and Information Sciences*, vol. 284, Springer, 2003.

[55] T. Alpcan and T. Basar, "A Stability Result for Switched Systems with Multiple Equilibria," *Dynamics of Continuous, Discrete and Impulsive Systems*, vol. 17:6a, pp. 949-958, 2010.